

University of Wollongong - Research Online

Thesis Collection

Title: Analysis of lepton contamination in high energy x-ray beams

Author: Nyanpen Damrongkijudom

Year: 2007

Repository DOI:

Copyright Warning

You may print or download ONE copy of this document for the purpose of your own research or study. The University does not authorise you to copy, communicate or otherwise make available electronically to any other person any copyright material contained on this site.

You are reminded of the following: This work is copyright. Apart from any use permitted under the Copyright Act 1968, no part of this work may be reproduced by any process, nor may any other exclusive right be exercised, without the permission of the author. Copyright owners are entitled to take legal action against persons who infringe their copyright. A reproduction of material that is protected by copyright may be a copyright infringement. A court may impose penalties and award damages in relation to offences and infringements relating to copyright material.

Higher penalties may apply, and higher damages may be awarded, for offences and infringements involving the conversion of material into digital or electronic form.

Unless otherwise indicated, the views expressed in this thesis are those of the author and do not necessarily represent the views of the University of Wollongong.

Research Online is the open access repository for the University of Wollongong. For further information contact the UOW Library: research-pubs@uow.edu.au

University of Wollongong Thesis Collections

University of Wollongong Thesis Collection

University of Wollongong

Year 2007

Analysis of lepton contamination in high energy x-ray beams

Nyanpen Damrongkijudom
University of Wollongong

Damrongkijudom, Nuanpen, Analysis of lepton contamination in high energy x-ray beams, PhD thesis, School of Engineering Physics, University of Wollongong, 2007.
<http://ro.uow.edu.au/theses/738>

This paper is posted at Research Online.
<http://ro.uow.edu.au/theses/738>

NOTE

This online version of the thesis may have different page formatting and pagination from the paper copy held in the University of Wollongong Library.

UNIVERSITY OF WOLLONGONG

COPYRIGHT WARNING

You may print or download ONE copy of this document for the purpose of your own research or study. The University does not authorise you to copy, communicate or otherwise make available electronically to any other person any copyright material contained on this site. You are reminded of the following:

Copyright owners are entitled to take legal action against persons who infringe their copyright. A reproduction of material that is protected by copyright may be a copyright infringement. A court may impose penalties and award damages in relation to offences and infringements relating to copyright material. Higher penalties may apply, and higher damages may be awarded, for offences and infringements involving the conversion of material into digital or electronic form.

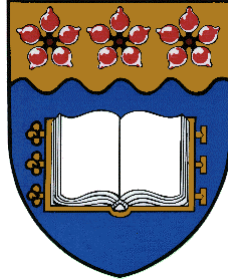
ANALYSIS OF LEPTON CONTAMINATION IN HIGH ENERGY X-RAY BEAMS

A thesis submitted in fulfillment of the requirements for the award of
the degree

DOCTOR OF PHILOSOPHY

from

UNIVERSITY OF WOLLONGONG



by

Nuanpen Damrongkijudom, M.S. (Medical Physics)

School of Engineering Physics

University of Wollongong

Wollongong, Australia

August 2007

CERTIFICATION

I, Nuanpen Damrongkijudom, declare that this thesis, submitted in fulfilment of the requirements for the award of Doctor of Philosophy, in the School of Engineering Physics, University of Wollongong, is wholly my own work unless otherwise referenced or acknowledged. The document has not been submitted for qualifications at any other academic institution.

Nuanpen Damrongkijudom

6 August 2007

ABSTRACT

The objectives of this study were to improve our understanding of the contamination arising in conventional radiotherapy treatment from the various principal processes involved. The evolution of the contamination was investigated in two main ways: i) experimental measurements; and ii) the Monte Carlo method.

The magnetic field strengths in this improved design were intended to result in more uniform magnetic flux densities in the area of interest, with the prediction of a greater volume where the electron contamination was effectively removed by our magnetic deflector device. The magnetic field strengths obtained by the magnetic deflector will theoretically give rise to electron deflection radii that should cause the majority of electron contamination to exit the treatment field. An enhancement of the electron dose was never experimentally observed in the irradiated area, and a percentage reduction of the skin and subcutaneous dose up to 34 % with the NdFeB magnetic device was seen for a 20 x 20 cm² field size. The elimination of significant electron doses due to contaminant electrons down to a depth of a few millimetres was obtained with this newly designed magnetic deflector device.

In the study, the experiments were verified by an Attix chamber and radiographic film. The surface dose was increased as the field size was increased in an open field and when a Perspex tray was placed in the beam, with the increase especially significant in the case where there was both a Perspex tray and a larger field size. The Perspex tray or a wedge filter eliminate secondary electrons and generate new electrons at the same time, however, when combined with magnetic field the surface dose is reduced significantly. Results are also shown for the surface dose profile in two dimensions (x and y-axis) with the surface dose showing a decrease at all sites within the treatment field due to the magnetic deflector device, not only for an open field, but also when a wedge or a Perspex tray is in the beam.

Calculation and analysis of spectra of deflected electrons in photon beams from the linear accelerator treatment head were investigated. Calculating such spectra with more accuracy requires knowledge of the characteristics of the electron beam incident on the target as well as better equipment for modelling the linear accelerator. We used the

Monte Carlo method performed with BEAMnrc and DOSXYZnrc code to derive estimates for the average energy deposited in the system. Monte Carlo modelling of photon beams was achieved and adjusted for two parameters: $AE = ECUT = 0.521 \text{ MeV}$ and $AE = ECUT = 0.700 \text{ MeV}$ by matching the Monte Carlo calculated depth dose and beam profile data with the measured data.

The capability of the Monte Carlo program in evaluating dose distribution has been verified by comparison with measurements in a water phantom and with radiographic film. The comparisons were performed for percentage of the build-up dose for various field sizes. Ionisation measurements were made in a solid water phantom by means of an Attix chamber for experiments to determine the dose in the build-up region. The measurement of skin dose uses an Attix parallel plate ionisation chamber, which is primarily used as the benchmark chamber in solid-water phantom dose build-up measurements.

Monte Carlo simulations were performed to generate data to predict the dose distribution for 6 MV x-rays. Investigation of dose components of electron spectra are compared between calculated and measured dose distributions. From the Monte Carlo calculations and measurements on the surface and in the build-up region for 6 MV x-ray beams based on our results, we conclude that our optimised simulation model represents the beam emerging from the treatment head and the calculated percentage depth doses in such a way that there is a satisfactory match with the experimental measurements for the same irradiation set-ups.

TABLE OF CONTENTS

CERTIFICATION	i
ABSTRACT	ii
LIST OF FIGURES	x
LIST OF TABLES	xxi
ACKNOWLEDGEMENTS	xxiii
CHAPTER 1 INTRODUCTION	1
1.1. Lepton contamination in high-energy x-ray beams	1
1.2. The statement of problems from the contamination electrons	2
1.3. Consideration of a proposed technique	3
1.4. Aim and objectives	4
1.5. Scope	4
CHAPTER 2 SURFACE DOSE IN HIGH ENERGY X-RAY BEAMS	6
2.1. Introduction	6
2.1.1. Surface dose	7
2.1.2. Build-up region	8
2.1.3. D_{\max} (The Maximum Dose)	10
2.1.4. d_{\max} (The Depth of Maximum Dose)	10
2.1.5. PDD (Percentage depth dose)	11
2.2. High-energy x-ray beams from linear accelerators	11
2.3. High energy x-ray beams Interactions	13
2.3.1. Photoelectric Effect Interaction	13
2.3.2. Compton Effect Interaction	14

2.3.3. Pair production Interaction	15
2.3.4. Thomson scattering	16
2.3.5. Photodisintegration	16
2.4. Contamination Electrons	16
2.4.1. Source from treatment head materials	19
2.4.2. Source from treatment setup parameters	19
2.5. Skin dose	19
2.6. Surface dose from high energy x-ray beams for different clinical set-up parameters	20
2.6.1. Using beam modifying and accessory devices	21
2.6.2. Source to Surface Distance	22
2.6.3. Angle of incident beam	23
2.7. Magnetic field	24
2.8. Electron deflection in magnetic field	25
2.8.1. Motion of a charged particle in a magnetic field	25
2.8.2. Direction of particle's motion is changed	26
2.8.3. Speed unchanged in the magnetic field	26
2.8.4. Uniform circular motion in a magnetic field	26
2.8.5. Helical motion in a magnetic field	27
CHAPTER 3 MATERIALS AND METHODS	31
3.1. Linear accelerator	31
3.1.1. Linear accelerator treatment head	33
3.2. Ionisation chambers	34
3.2.1. The Attix chamber	36

3.3. Phantom materials	37
3.3.1. Solid Water phantom	37
3.4. Beam modifying device	39
3.4.1. Wedges	39
3.4.2. Perspex tray	40
3.5. Film dosimetry	41
3.5.1. Radiographic film	43
3.5.2. Types of radiographic film	44
3.5.3. Radiographic film density	45
3.6. Film digitiser	46
3.7. Hall Effect Teslameter	48
3.8. Neodymium iron boron magnetic deflector	50
3.9. Monte Carlo technique	52
3.9.1. Monte Carlo technique for modelling linear accelerator	53
CHAPTER 4 RESULTS AND DISCUSSION	55
4.1. Magnetic Deflection Model	55
4.1.1. Magnetic deflector device	56
4.1.2. Simulation of magnetic fields around magnetic deflector device	57
4.1.3. Measurement of magnetic fields around magnetic deflector device	59
4.1.4. Simulation and measurement of the magnetic field	61
4.1.5. Dose in the build up region with magnetic deflector device	65
4.1.6. Conclusions on magnetic fields produced by deflector device	68

4.2. Electron deflection in magnetic field	69
4.2.1. Analytical Theory	70
4.2.2. Electron deflection using magnetic deflection device	75
4.2.3. Conclusion on magnetic deflection	82
4.3. Surface dose measurement in magnetic field	82
4.3.1. Film dosimetry and calibration method	83
4.3.2. Extrapolation Technique	83
4.3.3. Extrapolated surface dose of 6 MV x-rays with magnetic device	94
4.3.4. Conclusion on surface dose measurement	100
CHAPTER 5 LEPTON CONTAMINATION IN 6 MV X-RAYS	101
5.1. Electron contamination from high-energy x-ray beams	105
5.2. Source of electron contaminate	106
5.3. Experimental set up	107
5.4. Results and discussion of measurement	109
5.4.1. Dose build up region	109
5.4.2. Field size	112
5.4.3. Beam modifying devices	118
5.4.4. Surface dose from Attix chamber and radiographic film	125
5.5. Conclusions	126
CHAPTER 6 MONTE CARLO CALCULATIONS	128
6.1. Introduction	128
6.2. Monte Carlo approach to electron contamination sources in Varian Clinac 2100C	128

6.3. METHODS and MATERIALS	131
6.3.1. Monte Carlo method	131
6.3.2. Linear accelerators	134
6.3.3. Monte Carlo simulation	139
6.4. Results and Discussion	141
6.4.1. Linear accelerator head	141
6.4.2. Contaminant particles	149
6.5. Characteristics of radiation from a linear accelerator head	151
6.5.1. Methods and Materials	153
6.5.2. Results and Discussion	154
6.6. Monte Carlo Depth dose distribution	158
6.6.1. Methods and Materials	158
6.6.2. Results and Discussion	161
6.7. Conclusions	169
CHAPTER 7 EXPERIMENTS AND MONTE CARLO CALCULATION	171
7.1. Experimental setup	172
7.1.1. Dose build-up region	172
7.1.2. Radiographic film with magnetic deflection device	173
7.2. Monte Carlo method	174
7.2.1. Water phantom	175
7.2.2. Radiographic film	175
7.3. Results and Discussion	177
7.3.1. Dose in the build-up region	177

7.3.2. Surface dose	189
7.3.3. Electron and contamination doses	194
7.4. Conclusions	200
CHAPTER 8 CONCLUSIONS	201
8.1. Magnetic field model	201
8.2. Electron contamination from 6 MV x-ray beams	202
8.3. Monte Carlo Simulation	206
8.3.1. Monte Carlo simulation model	206
8.3.2. Determination of the transport model parameters	209
REFERENCES	212

LIST OF FIGURES

Figure 2.1	Some of the characteristics from a general central axis percent depth dose curve	7
Figure 2.2	Build-up curves in polystyrene for 10 x 10 cm ² open fields for the photon beams studied	9
Figure 2.3	Dose build-up curves for Clinac 6 MV x-ray beams at 100 cm SSD for fields of 5 x 5 cm ² to 40 x 40 cm ²	9
Figure 2.4	Depth of d _{max} as a function of field size for 6, 10 and 18 MV x-rays	10
Figure 2.5	Percentage depth dose of 10 and 25 MV x-ray beams for field sizes of 10 x 10 cm ² and 35 x 35 cm ² at 100 cm SSD	11
Figure 2.6	The diagram illustrates the structure of the linear accelerator treatment head	13
Figure 2.7	The Photoelectric Effect interaction process	14
Figure 2.8	The Compton Effect interaction process	14
Figure 2.9	The pair production interaction process	15
Figure 2.10	Relative absorbed dose at phantom surface for 21 MV x-rays, with filter thickness of 2 g / cm ² for field sizes of 10 x 10 cm ² , 20 x 20 cm ² , and 40 x 40 cm ²	16
Figure 2.11	The diagram illustrates the structure of the linear accelerator treatment head and the regions where electron contamination is produced	17
Figure 2.12	Cross-section of the skin anatomy shows the main structures in the epidermis and dermis layers	20
Figure 2.13	The electron contribution from the portion of the ERS determining the surface dose from the incident photon beams	23
Figure 2.14	The magnetic field lines between the poles of two bar magnets, displayed using the Vizimag program	25
Figure 2.15	The direction of the magnetic force is always at right angle to the plane formed by the velocity vector (v) and the magnetic field (B) for positive and negative charged particles	26

Figure 2.16	A charged particle moving parallel to the magnetic field will travel with a uniform velocity, and there is no work on the charged particle	27
Figure 2.17	Trigonometry is used to resolve the velocity of a charged particle into components parallel to (\hat{v}_p) and perpendicular to (\hat{v}_\perp) the magnetic field lines	28
Figure 2.18	The path of a charged particle with components of velocity both parallel and perpendicular to the field direction in a uniform magnetic field is helical	28
Figure 2.19	The radius as a function of electron energy from 0.5 to 6 MeV in different magnetic field strengths	29
Figure 3.1	Diagram of the medical linear accelerator system used to produce x-ray beams	32
Figure 3.2	Picture of Varian Clinac 2100C linear accelerator. This machine is capable of producing 6 and 18 MV x-ray beams and 6, 9, 12, 16, and 20 MeV electron beams	32
Figure 3.3	Diagram showing the structure of a medical linear accelerator treatment head	34
Figure 3.4	Picture of the Attix model 449 chamber (Gammex RMI Model 457) used for the experiments in solid water	36
Figure 3.5	The ratio of the mass energy-absorption coefficient relative to water of Solid Water as a function of x-ray beam energy	38
Figure 3.6	Solid Water phantoms with various slab thicknesses used for the experiments	39
Figure 3.7	Picture of wedges with 15, 30, 45, and 60 degree angles that were used in the experiments	40
Figure 3.8	Picture of 6 mm thickness Perspex tray used in the experiments	41
Figure 3.9	The ratio of the mass energy-absorption coefficient of photographic emulsion to that of water as a function of the x-ray beam energy	42
Figure 3.10	Dose profile of radiographic film compared with dose to water	43
Figure 3.11	A cross-sectional view of radiographic film layers	45
Figure 3.12	Pictures of X Omat V films for the measurement of dose	46

Figure 3.13	The major components of the film digitiser	47
Figure 3.14	Picture of Vidar VXR-12 Plus film digitiser for scanning film	47
Figure 3.15	The Hall Effect for magnetic field measurement	48
Figure 3.16	The Hall Effect probe is direction dependent, and the output is greatest when the flux lines are perpendicular to it	49
Figure 3.17	Pictures of the DTM-132 Digital Teslameter and Hall probe	50
Figure 3.18	Picture of Neodymium Iron Boron (NdFeB) lanthanide ceramic magnet each of dimensions 5 x 5 x 5 cm and 5 x 5 x 1.25 cm were selected for placement in an Aluminium holding frame as the magnetic deflector device	51
Figure 3.19	NdFeB magnetic deflector device inserted directly into an accessory mount in a linear accelerator head	52
Figure 4.1	The magnetic deflector in location for simulated clinical measurements	55
Figure 4.2	Schematic diagram of the details of the magnetic deflector device with a photograph of the actual device	56,57
Figure 4.3	(a) Magnetic field lines through the central plane of our magnetic deflector as determined by Vizimag. (b) Greyscale colour-intensity image of the magnetic field intensity (magnitude) around the magnetic deflector	58
Figure 4.4	The 3D assumption made by Vizimag	59
Figure 4.5	(a) The measurement performed at a distance of $x = -7.5$ cm, (b) at the central plane ($x = 0$), and (c) performed at distance of $x = 7.5$ cm away from the central plane.	60,61
Figure 4.6	Simulation of Y-component magnetic field strength using Vizimag within the 10 cm pole separation along the y-axis on the magnetic deflector central plane	62
Figure 4.7	Measurement of magnetic field strength along the y-axis on the magnetic deflector central plane within the 10 cm pole separation. Curves represent data taken at different depths along the z-axis, down to 10 cm	62
Figure 4.8	The central measurement and simulation plane and a 3D surface mesh plot of the Y-components	63

Figure 4.9	Variation between the experimental data and the Vizimag prediction in the central plane	64
Figure 4.10	Y-direction magnetic field strength between the magnet banks on axes other than the central one	65
Figure 4.11	Measurements for open field (without deflector) and with the field when the magnetic deflector device in place for 6 MV x-ray beams in the build-up region	67,68
Figure 4.12	Diagram of the locations of the component modules in medical linear accelerator machine with magnetic deflector device	70
Figure 4.13	Magnetic deflector device with the magnetic field (\vec{B}) parallel to the y-axis	71
Figure 4.14	The diagram for the deflection of an electron after passing through the magnetic field region	74
Figure 4.15	The experimental set-up, with the magnetic device attached to the treatment head of the linear accelerator by placement under the block tray location and with the radiographic film placed perpendicular to the beam axis	76
Figure 4.16	(a) The deflection distance and angle of electrons as a function of electron energy from 0.5 to 20 MeV in different magnetic field strengths using simplified model of uniform magnetic field distribution calculated by Vizimag	77
	(b) The deflection distance and angle of electrons as a function of electron energy from 0.5 to 20 MeV in different magnetic field strengths measured data of the magnetic field strength of magnetic deflector device	78
Figure 4.17	Radiographic images used to determine deflection distances of electron beams from 6 MeV up to 20 MeV after passing through the magnetic deflector device	80
Figure 4.18	Surface dose can be obtained from a second order polynomial extrapolation from radiographic film for field size 10 x 10 cm ² , 15 x 15 cm ² and 20 x 20 cm ² with and without magnetic field	84,85
Figure 4.19	Dose profiles measured cross-plane without (open field) magnetic deflection for a field size of 10 x 10 cm ² at the surface and at 0.38, 1.14, and 1.9 mm depths	86
Figure 4.20	Dose profiles measured cross-plane with magnetic deflection for a field size of 10 x 10 cm ² at the surface and at 0.38, 1.14, and 1.9	87

mm depths

Figure 4.21	Dose profiles measured in-plane without (open field) magnetic deflection for a field size of $10 \times 10 \text{ cm}^2$ at the surface and at 0.38, 1.14, and 1.9 mm depths	88
Figure 4.22	Dose profiles measured in-plane with magnetic deflection for a field size of $10 \times 10 \text{ cm}^2$ at the surface and at 0.38, 1.14, and 1.9 mm depths	89
Figure 4.23	Dose profiles measured cross-plane without (open field) magnetic deflection for a field size of $20 \times 20 \text{ cm}^2$ at the surface and at 0.38, 1.14, and 1.9 mm depths	90
Figure 4.24	Dose profiles measured cross-plane with magnetic deflection for a field size of $20 \times 20 \text{ cm}^2$ at the surface and at 0.38, 1.14, and 1.9 mm depths	91
Figure 4.25	Dose profiles measured in-plane without (open field) magnetic deflection for a field size of $20 \times 20 \text{ cm}^2$ at the surface and at 0.38, 1.14, and 1.9 mm depths	92
Figure 4.26	Dose profiles measured in-plane with magnetic deflection for a field size of $20 \times 20 \text{ cm}^2$ at the surface and at 0.38, 1.14, and 1.9 mm depths	93
Figure 4.27	Radiographic images of 6 MV beams of the three layers of film for field sizes of $10 \times 10 \text{ cm}^2$, $15 \times 15 \text{ cm}^2$, and $20 \times 20 \text{ cm}^2$ illustrate that the electron contamination is swept away by the magnetic field	94
Figure 4.28	Surface dose can be obtained from a second order polynomial extrapolation from radiographic film	95
Figure 4.29	Extrapolated surface dose profile at central axis for 6 MV, measured cross-plane and in-plane with and without (open field) magnetic field from the deflector for a radiation field size of $10 \times 10 \text{ cm}^2$	97
Figure 4.30	Extrapolated surface dose profile at central axis for 6 MV, measured cross-plane and in-plane with and without (open field) magnetic field from the deflector for a radiation field size of $15 \times 15 \text{ cm}^2$	98
Figure 4.31	Extrapolated surface dose profile at central axis for 6 MV, measured cross-plane and in-plane with and without (open field) magnetic field from the deflector for a radiation field size of $20 \times 20 \text{ cm}^2$	99

Figure 5.1	(a) Radiographic image with Surface and Profile plots present the lepton contamination of an open field (without deflection or beam-modifying devices) of $10 \times 10 \text{ cm}^2$ (b) Radiographic image with Surface and Profile plots present the lepton contamination with magnetic field. Electrons and positrons are swept in opposite directions following the Lorentz force rule	102,103 104,105
Figure 5.2	Source size and location of electron contamination in a linear accelerator head; ΔY is the upper jaw opening and ΔX is the lower jaw opening	107
Figure 5.3	Diagram of the linear accelerator with magnetic deflector device and radiographic film as used in the experiments	108
Figure 5.4	Percentage dose build up for 6 MV x-rays from an Attix chamber (open field) and in magnetic field for field sizes of $10 \times 10 \text{ cm}^2$, $15 \times 15 \text{ cm}^2$, and $20 \times 20 \text{ cm}^2$	110
Figure 5.5	Percentage contamination dose reduction for 6 MV x-rays from an Attix chamber with a magnetic field applied to a linear accelerator treatment head for $10 \times 10 \text{ cm}^2$, $15 \times 15 \text{ cm}^2$, and $20 \times 20 \text{ cm}^2$ field sizes	111
Figure 5.6	Extrapolated surface doses from radiographic films are shown for profiles measured in-plane and cross-plane of 6 MV x-ray beam for open field, tray in place, and magnetic field and tray in place with magnetic field for field sizes of (a) $5 \times 5 \text{ cm}^2$, (b) $10 \times 10 \text{ cm}^2$, (c) $20 \times 20 \text{ cm}^2$, and (d) $30 \times 25 \text{ cm}^2$	113,114 115,116
Figure 5.7	Relative surface dose from radiographic film of 6 MV x-rays for open field and 6 mm Perspex tray with and without magnetic field for $5 \times 5 \text{ cm}^2$, $10 \times 10 \text{ cm}^2$, $20 \times 20 \text{ cm}^2$, and $30 \times 25 \text{ cm}^2$ field sizes	119
Figure 5.8	Extrapolated surface doses are shown for profiles measured in-plane and cross-plane for 6 MV x-ray beam with magnetic field for wedge field with a wedge angle of (a) $W15^\circ$, (b) $W30^\circ$, (c) $W45^\circ$, and (d) $W60^\circ$ compared with open field	120,121 122,123
Figure 6.1	Schematic drawing of linear accelerator components modelled in Monte Carlo simulations	137
Figure 6.2	Schematics of the geometry illustrating the accelerator head components	138

Figure 6.3	Influence of AE on the spectrum for a 6 MV beam for a) all particles and photons after passing through mirror, b) electrons after passing through mirror	143
Figure 6.4	Influence of AE on the spectrum for a 6 MV beam for a) all particles and photons, b) electrons at SSD5100 cm	144
Figure 6.5	Influence of AE on the fluence along the X-axis for a 6 MV beam for a) all particles and photons after passing through the mirror, b) electrons after passing through mirror	146
Figure 6.6	Influence of AE on the fluence along the X-axis for a 6 MV beam for a) all particles and photons after passing through air at 100 cm, b) electrons after passing through air at 100 cm	147
Figure 6.7	Mean energy distribution of a 10 x 10 cm ² 6 MV photon beam simulated along the x-axis after passing through the linear accelerator treatment head at 100 cm for a) all particles and photons, b) electrons	148
Figure 6.8	Influence of AE values on spectral distribution and fluence of particle and electron contamination along the X-axis of 6 MV beam at 100 cm SSD for 10 x 10 cm ² field size: a) spectral distribution of particle and electron contamination, b) fluence of particle and electron contamination	150
Figure 6.9	Influence of AE values on fluence of contaminant particles along the X-axis of 6 MV beam at a) scoring plane after mirror material, b) 100 cm SSD for 10 x 10 cm ² field size	151
Figure 6.10	Schematic representation of a linear accelerator with the photon radiation originating from the accelerator head, passing through the air, and propagating this radiation down to the phantom	152
Figure 6.11	A schematic of the modelling process for each scoring plane for the phase-space information for Monte Carlo calculations of radiation from a linear accelerator treatment head	153
Figure 6.12	Spectral distribution of all particles and photons in (a), (c), (e), (g), (h), (i), (j), (k), electrons and contamination in (b), (d), (f) from a Varian Clinac 2100 C with a 6 MV beam	157
Figure 6.13	Schematic drawing of linear accelerator for the DOSXYZnrc simulation	159

Figure 6.14	Spectral distribution from BEAMnrc phase-space data (AE = 0.700 MeV) of linear accelerator head at 100 cm from the target using BEAMDP calculations of field sizes 5 x 5 cm ² , 10 x 10 cm ² , 20 x 20 cm ² , and 30 x 30 cm ² for a) photon fluence, b) electron fluence	160
Figure 6.15	Monte Carlo calculations using AE = 0.700 MeV to calculate the percent dose build-up distribution for 6 MV Clinac 2100 C for field sizes: a) 5 x 5 cm ² , b) 10 x 10 cm ² , c) 20 x 20 cm ² , d) 30 x 30 cm ²	161
Figure 6.16	Monte Carlo calculation (AE = 0.700 MeV) in the build-up region for 6 MV Clinac 2100 C for field sizes of 5 x 5 cm ² , 10 x 10 cm ² , 20 x 20 cm ² , and 30 x 30 cm ²	162
Figure 6.17	Surface dose profile plot calculated from Monte Carlo (AE = 0.700 MeV) results with field sizes 5 x 5 cm ² , 10 x 10 cm ² , 20 x 20 cm ² , and 30 x 30 cm ² in: (a) distance along the X –axis, and (b) distance along the Y-axis	164
Figure 6.18	Dose distribution on central axis of 6 MV Clinac 2100 C for field size of 10x10 cm ² at AE = 0.521 and 0.700 MeV in a water phantom: a) depth dose distribution, b) dose in the build-up region	165
Figure 6.19	Electron dose distribution on central axis of 6 MV Clinac 2100 C for field size of 10x10 cm ² for AE = 0.521 and AE = 0.700 MeV in a water phantom: a) electron distribution in the build-up region, b) electron depth dose distribution	166
Figure 6.20	Total dose profile plot at different depths in a water phantom for AE = 0.521 and 0.700 MeV from 6 MV Clinac 2100 C for field size of 10 x 10 cm ² along the X and Y-axes	168
Figure 6.21	Electron dose profile plot at different depths for AE = 0.521 and 0.700 MeV for 6 MV beam in a water phantom along the X and Y-axes	168
Figure 7.1	Schematic drawing of linear accelerator for the DOSXYZnrc simulation in a water phantom	176
Figure 7.2	Schematic drawing of the size of scoring voxels for the DOSXYZnrc simulation in the radiographic film on a water phantom	176
Figure 7.3	Match between experimental data and Monte Carlo calculation in the build-up region for a 6 MV beam in a water phantom for AE	178

and ECUT = 0.700 MeV for field sizes of: a) 10 x 10 cm², b) 15 x 15 cm², c) 20 x 20 cm²

Figure 7.4	Match between experimental data and Monte Carlo calculation in the build-up region for 6 MV beam in a water phantom for a field size of 10 x 10 cm ² for AE = 0.521 and 0.700 MeV	182
Figure 7.5	Dose values measured with Attix chamber and Monte Carlo calculations with AE = 0.700 MeV in the build-up region for 6 MV beam in a water phantom for field size of 10 x 10 cm ² : a) Comparison of open (without magnetic field) and magnetic field results for all particles and photons, b) Difference between open and magnetic field results compared to difference between all particles and photons, and percentage of contamination of the total dose	184
Figure 7.6	Dose values measured with Attix chamber and Monte Carlo calculations with AE = 0.700 MeV in the build-up region for 6 MV beam in a water phantom for a field size of 20 x 20 cm ² : a) Open and magnetic field results are compared for all particles and photons, b) Difference between open and magnetic field results compared to difference between all particles and photons, and percentage contamination from the total dose	185
Figure 7.7	Depth dose curves from Monte Carlo results on simulated radiographic film for the energy cut-offs and AE = 0.521 MeV for 6 MV beam and field size of 10 x 10 cm ² : a) depth dose curves of all particles, b) dose distribution of electrons	186
Figure 7.8	Depth dose curves from Monte Carlo calculations on simulated radiographic film for the energy cut-offs and AE = 0.700 MeV for 6 MV beam with field size of 10 x 10 cm ² : a) depth dose curves of all particles, b) dose distribution of electrons	187
Figure 7.9	Comparison of depth dose curves from Monte Carlo calculations on simulated radiographic film using the different AE for 6 MV beam for field size of 10 x 10 cm ² : a) depth dose curves of all particles, b) dose distribution of electrons	188
Figure 7.10	Simulated dose profiles compared between using AE = 0.700 MeV in a water phantom and radiographic film for 6 MV Clinac 2100 C with a field size of 10 x 10 cm ² at different depths along X and Y – axis directions	190
Figure 7.11	Simulated dose profiles compared between using AE = 0.521 MeV in a water phantom and radiographic film for 6 MV Clinac 2100 C for field size of 10 x 10 cm ² at different depths along the X and Y – axes	190

Figure 7.12	Simulated dose profiles compared between using AE = 0.521 MeV and AE = 0.700 MeV on a water phantom for 6 MV Clinac 2100 C for a field size of 10 x 10 cm ² at different depths along the X and Y – axes	191
Figure 7.13	Simulated profiles compared between using AE = 0.521 MeV and AE = 0.700 MeV for radiographic film on a water phantom for 6 MV Clinac 2100 C for a field size of 10 x 10 cm ² for different depths along the X and Y – axes	191
Figure 7.14	Surface dose profiles comparing the MC calculations with measurements on radiographic film using AE = 0.700 MeV for a 6 MV beam along the X and Y– axes for field sizes of: a) 5 x 5 cm ² , b) 10 x 10 cm ² , and c) 15 x 15 cm ²	192
Figure 7.15	Surface dose profiles comparing the MC calculations with measurements on radiographic film using AE = 0.521 and 0.700 MeV for a 6 MV beam along the X and Y– axes for a field size of 10 x 10 cm ²	193
Figure 7.16	Comparison of electron and contamination depth dose curves from Monte Carlo calculations on radiographic film using the different AE for a 6 MV beam with a field size of 10 x 10 cm ² : a) AE = 0.521 MeV, b) AE = 0.700 MeV, c) AE = 0.521 and 0.700 MeV	196
Figure 7.17	Comparison of electron and contamination depth dose curves from Monte Carlo calculations on radiographic film using the different AE for a 6 MV beam with a field size of 20 x 20 cm ² : a) AE = 0.521 MeV, b) AE = 0.700 MeV, c) AE = 0.521 and 0.700 MeV	197
Figure 7.18	Comparison of electron depth dose curves from Monte Carlo calculations on radiographic film using the different AE: a) AE = 0.521 MeV for F.S. 10 x 10 and 20 x 20 cm ² , b) AE = 0.700 MeV for F.S.10 x 10 and 20 x 20 cm ² , c) AE = 0.521 and 0.700 MeV for F.S.10 x 10 and 20 x 20 cm ²	198
Figure 7.19	Comparison of contamination dose distribution curves from Monte Carlo calculations on radiographic film using the different AE: a) AE = 0.521 MeV for F.S. 10 x 10 and 20 x 20 cm ² , b) AE = 0.700 MeV for F.S.10 x 10 and 20 x 20 cm ² , c) AE = 0.521 and 0.700 MeV for F.S.10 x 10 and 20 x 20 cm ²	199
Figure 8.1	Extrapolated surface dose profile at central axis for 6 MV beam, measured cross-plane and in-plane: a) without (open field) magnetic field from the deflector for field sizes of 5 x 5 cm ² , 10 x	205

10 cm², 20 x 20 cm², and 30 x 25 cm², b) with magnetic field from the deflector for field sizes of 5 x 5 cm², 10 x 10 cm², 20 x 20 cm², and 30 x 25 cm²

- | | | |
|------------|-------------------------------------------------------------------------------------------------------------------------------------------------------------------------------------------------------------------|-----|
| Figure 8.2 | Schematic diagram of the Monte Carlo model used to simulate the Varian Clinac 2100 C for 6 MV x-ray beams | 207 |
| Figure 8.3 | The geometry of the Clinac 2100 C accelerator head for 6 MV photon beam as shown by EGS_Windows 4.0 using 150-200 histories. Photons are represented by yellow lines, and electrons are represented by blue lines | 208 |

LIST OF TABLES

Table 2.1	Comparison of surface dose as a function of field size for several linear accelerator models	7
Table 2.2	Percentage surface dose for linear accelerators measured at SSD 100 cm for 10 x 10 cm ² field size using an extrapolation chamber	8
Table 2.3	Percentage skin dose of 8 and 18 MV x-ray beams for different field sizes and wedge angles	22
Table 2.4	The sources of electron contamination in the 25 MV Clinac-35 photon beam for different SSD distances	23
Table 4.1	The electron deflection in magnetic field for electron energies ranging from 6 MeV up to 20 MeV	82
Table 4.2	Surface dose measurements by the extrapolation technique from radiographic film compared to the Attix chamber results for 6 MV x-rays with and without (open field) magnetic field from the deflector	100
Table 5.1	Surface doses for field sizes of 15 x 15 cm ² and 20 x 20 cm ² for 6 MV x-rays using radiographic film combined with a wedge and magnetic field	124
Table 5.2	Surface dose for field size of 20 x 20 cm ² with a Perspex tray and with different wedges used with and without magnetic field	125
Table 5.3	Surface dose measurements by an Attix chamber and extrapolated from radiographic film for field sizes of 10 x 10 cm ² , 15 x 15 cm ² , and 20 x 20 cm ²	126
Table 6.1	The description of the accelerator geometry is provided by the manufacturer	136
Table 6.2	Fluence-averaged quantities for first-time crossing of the scoring plane normalised per incident particles	155
Table 6.3	Number and energy fluence distributions of 6 MeV electron beams from Varian Clinac 2100 C linear accelerator	156
Table 6.4	Angular distributions of photons and particles	156

Table 6.5	The depth dose distribution on the central axis of 6 MV Clinac 2100 C for field size of 10 x 10 cm ² using AE = 0.521 and 0.700 MeV at the same depth in a water phantom	167
Table 6.6	The dose profile distribution of 6 MV Clinac 2100 C for field size of 10 x 10 cm ² using AE = 0.521 and 0.700 MeV at the same depth in a water phantom along the X and Y-axes	169
Table 7.1	DOSXYZnrc simulation parameters	177
Table 7.2	(a) Percentage of the dose in the build-up region between experimental data and Monte Carlo calculations for 6 MV beam in a water phantom and radiographic film for AE = 0.700 MeV of field size 10 x 10 cm ² and 20 x 20 cm ²	180
	(b) Percentage of the dose in the build-up region between experimental data and Extrapolated surface dose of Monte Carlo calculations for 6 MV beam in a water phantom for AE = 0.700 MeV of field size 10 x 10 cm ² and 20 x 20 cm ² .	180
Table 7.3	Percentage of the surface dose from Monte Carlo calculations compared to the measurements on radiographic film	194
Table 8.1	Percentage of dose from the contamination and the percentage reduction for field sizes of 10 x 10 cm ² , 15 x 15 cm ² , and 20 x 20 cm ² with the magnetic deflector device in place for a 6 MV x-ray beam in the build-up region	203
Table 8.2	Percentage of dose absorbed at the surface for field sizes of 10 x 10 cm ² , 15 x 15 cm ² , and 20 x 20 cm ² with the use of beam modifying devices and the magnetic deflector device in place for 6 MV x-ray beam from radiographic film	204

ACKNOWLEDGEMENTS

My sincere thanks go to everyone who has assisted and supported me throughout the three and a half years of this PhD project.

To The Royal Thai Government for providing me scholarships.

To my supervisors, Professor Anatoly Rosenfeld and A/Prof. Martin Butson, for your encouragement and guidance throughout the difficult situations. I am very grateful and appreciative for your tremendous academic and personal support, without you this work would not be possible. Also, I would like to thank Professor Peter Metcalfe and Dr George Takacs, for your support and advice.

Thanks to Puangpen Tangboonduangjit, Brad Oborn and friends in the Centre for Medical Radiation Physics and also friends in School of Engineering for the support and friendship.

Finally, to my dad and mum and my sister with highly respect who have greatly cared, constantly supported, and been next to me no matter what circumstances. This thesis is dedicated to them.

CHAPTER 1

INTRODUCTION

A high-energy x-ray beam from a medical linear accelerator is one of the main options in radiotherapy treatment. A particularly advantageous feature of high-energy x-ray beams is the skin-sparing effect, but this effect may be reduced or lost under certain conditions of treatment. Furthermore, high-energy x-ray beams will always produce lepton contamination. Leptons are by-product particles, such as electrons and positrons, which have no strong interactions. A certain amount of electrons always originate from Compton scattering and pair production, whereas a small percentage of positrons are generated from the pair production process. The absorption of radiation therapy is mainly due to the Compton Effect interaction process. High energy x-ray beams are used to treat cancers that occur at various depths underneath the skin, and the aim for radiotherapy treatment is to deliver the maximum homogeneous radiation dose to the tumour target while minimising the dose to the surrounding normal tissues. Recent technological advances are expected to continue to demonstrate the value of the technique we have developed to diminish electron contamination on the skin surface when a high-energy photon beam is used for the treatment of deep-seated tumours. The present thesis work was based on theoretical study of the transport of charged particles in the photon beam. The theoretical qualitative and quantitative results of the dose enhancements were calculated for the surface and the build-up region. We also made efforts to experimentally confirm the theoretical amount of electron deflection by monitoring the paths of the electron beams and the motions of electrons as well as the electron distributions from the linear treatment head and along the x, y, and z-directions in a water phantom, which had been simulated by the Monte Carlo method.

1.1 Lepton contamination in high-energy x-ray beams

A particularly advantageous feature of high-energy x-ray beams is the skin sparing effect, but this effect may be reduced or lost under certain conditions of treatment such as when using large field sizes or obliquely incident beams (Khan et al., 1973, Gerbi et al., 1987). Furthermore, high-energy x-ray beams will always produce lepton contamination. Leptons are by-product particles, such as electrons and positrons, which

have no strong interactions. A certain amount of electrons originate from Compton scattering and pair production, whereas a small percentage of positrons are generated from the pair production process. The absorption of radiation therapy is mainly due to the Compton Effect interaction process. Thus, electron particles are the main contaminants that need to be studied. These numerous electron contaminants are produced by the interaction of x-rays with materials in objects such as the flattening filter, monitor ion chamber, collimators, wedges, compensators, and blocks and block trays in the treatment head of the medical linear accelerator (Petti et al., 1983, Krithivas and Rao, 1985, Sjogren and Karlsson, 1996). As well as the fluence, these contamination electrons vary with parameters such as field size, photon energy, and source to surface distance (Petti et al., 1983, Nilsson, 1985, Sjogren and Karlsson, 1996). The electron contaminants produced by high-energy x-ray beams have a long range in air, generate their dose deposition on the surface, and shift the position of the maximum dose towards the surface (Jursinic and Mackie, 1996). When the magnitude of these contamination electrons increases the skin-sparing effect is degraded by increasing surface doses.

High energy x-ray beams are used to treat cancers that occur at various depths underneath the skin, and the aim for radiotherapy treatment is to deliver the maximum homogeneous radiation dose to the tumour target while minimising the dose to the surrounding normal tissues. On the contrary, the electron contamination contributes an unwanted dose to the patient by increasing the skin dose and the dose to organs close to skin. Consequently, if patients are treated with high-energy x-ray beams containing a large amount of electron contamination, the energy absorbed by the skin is greatly increased and may result in severe skin reactions.

As an overview of this research, the problems and techniques considered are first described, and the aims and scope of the research are established as a research framework.

1.2 The statement of problems from the contamination electrons

Electron contamination enhances damage to the skin and subcutaneous tissues. As a result, the skin reactions have always been of concern for radiation oncologists. A

patient's skin reactions may lead to treatment interruptions, because high surface doses are undesirable in many clinical situations for an accessible optimal treatment. However, it is complicated to determine the depth of skin thickness for skin doses; ICRP 60 recommends for practical purposes that the dose be measured at a depth of 0.07 mm. This depth is in the basal cell layer, which is the critical layer for carcinogenesis (ICRP 60).

Consequently, elimination of electron contaminations from high-energy x-ray beams has been proposed to minimise skin reactions while not affecting the dose at depth or the beam symmetry in the process. The recommended methods to remove electron contamination from medical linear accelerator beams include using electron filters and magnetic fields (Nilsson, 1985, Rao et al., 1988, Butson et al., 1996).

1.3 Consideration of a proposed technique

The method that is going to be used in this research depends on a magnetic deflector device, and the required properties of this magnetic deflector would include a high strength magnetic field and light weight for easy manual insertion into the medical linear treatment head. The advantage of magnetically sweeping electrons is that all electron contamination from the medical linear accelerator treatment head is removed without the production of extra contaminants and with no requirement of a correction factor for the beam attenuation, as well as no significant distortion in beam flatness or beam symmetry that might come from interfering magnetic fields (Jursinic and Mackie, 1996, Butson, 1997).

The focus of the present research is the design of a method to reduce skin dose by using magnetic deflection to sweep the electron contamination away from the radiation treatment field. The effects of magnetic fields on the high-energy x-ray dose distribution are thus studied in this research. Calculation and analysis of spectra of deflected electrons and motion of electrons in magnetic fields are investigated. By using such magnetic fields in combination with the radiation field, this method will be expected to provide surface dose reductions for significant improvement of the quality of radiotherapy treatment. Furthermore, high-energy x-ray beams have spectra or various quantities based on them that are used in many advanced treatment planning systems.

Calculating such spectra with more accuracy requires knowledge of the characteristics of the electron beam incident on the target as well as better equipment for modelling the linear accelerator. We used the Monte Carlo method to derive best estimates for the average energy deposited in the system, the photon and electron spectra, and the dose build-up data, especially at the surface and in the dose build-up region for the high-energy x-ray beam. The investigation systematically tested the validity of this proposed method for the 6 MV photon beam from a Varian 2100 C accelerator.

Monte Carlo (MC) modelling of photon beams

- achieved by matching MC depth dose and beam profile data with measured data

MC calculations

- performed with BEAMnrc / DOSXYZnrc code

- adjusted for two parameters: $AE = ECUT = 0.521 \text{ MeV}$ and $AE = ECUT = 0.700 \text{ MeV}$

- based on a model of the Varian 2100 C

1.4 Aim and objectives

The aim of this study is to investigate the feasibility of a magnetic deflector design for the clinical application of high-energy x-ray beams. The specific objectives of this research are:

- (a) To develop a magnetic deflector design that can be expected to reduce large doses of electron contamination in the treatment field.
- (b) To determine the effect of strong magnetic field on the high-energy x-ray beam dose distribution.
- (c) To investigate whether the measured distributions are in agreement with the theoretical prediction.
- (d) To achieve and determine the applicability for the radiotherapy treatment field.

1.5 Scope

To achieve the objectives, the study will include:

- (a) Develop a strong and uniform magnetic deflector for clinical application. Neodymium Iron Boron (NdFeB) rare earth lanthanide magnets are chosen to construct the magnetic deflector.

- (b) Experimental verification by an Attix chamber and radiographic film. The measurement of skin dose uses an Attix parallel plate ionisation chamber, which is primarily used as the benchmark chamber in solid-water phantom dose build-up measurements.
- (c) Monte Carlo simulations are performed to generate data to predict the dose distribution for 6 MV x-rays.
- (d) Investigation of dose components of electron spectra. A comparison will be made between calculated and measured dose distributions.

CHAPTER 2

SURFACE DOSE IN HIGH ENERGY X-RAY BEAMS

2.1 Introduction

Radiation therapy has become increasingly available and in demand for cancer treatment. Whereas there is increasing concern about the hazards of radiation, when used properly, the risks are small and are greatly outweighed by the benefits. This radiation can either be given from outside the body as external beam radiotherapy or teletherapy, or from inside the body. The radiation sources include beams of x-rays, gamma rays, or electrons. The radiation sources applied to the patient from a distance consist of megavoltage machines such as Cobalt 60 and linear accelerator equipment. The energy is higher and varies depending on the machine specifications, but has a usual range of 4-25 MeV. There is greater penetrability for more deeply seated tumours due to the higher energy and a uniform dose deposition in bone and soft tissue. The dose build-up region is such that the maximum dose is not deposited until a few centimetres below the skin surface, resulting in what is termed a "skin-sparing" effect. For higher energies there is an even greater skin-sparing effect with the maximum dose deposited at a depth related to the energy of the photons. The source-to-skin distance is typically 100 cm, and the relatively large source-to-skin distance allows treatment of large fields. It is also possible to treat large volume tumours more uniformly due to the depth dose characteristics.

High-energy x-ray beams in radiotherapy treatment have some characteristics of photon beams, such as surface dose, build-up region, D_{\max} (the maximum dose), d_{\max} (the depth of maximum dose) and PDD (the percentage depth dose), which are important considerations in the radiation therapy planning treatment system. The high doses given for deep tumours may require carefully deliberation of dose distributions to avoid permanent damage to the skin and subcutaneous tissues that are outside the treatment area. Some of these characteristics from a general central axis percent depth dose curve as shown in Figure 2.1 are:

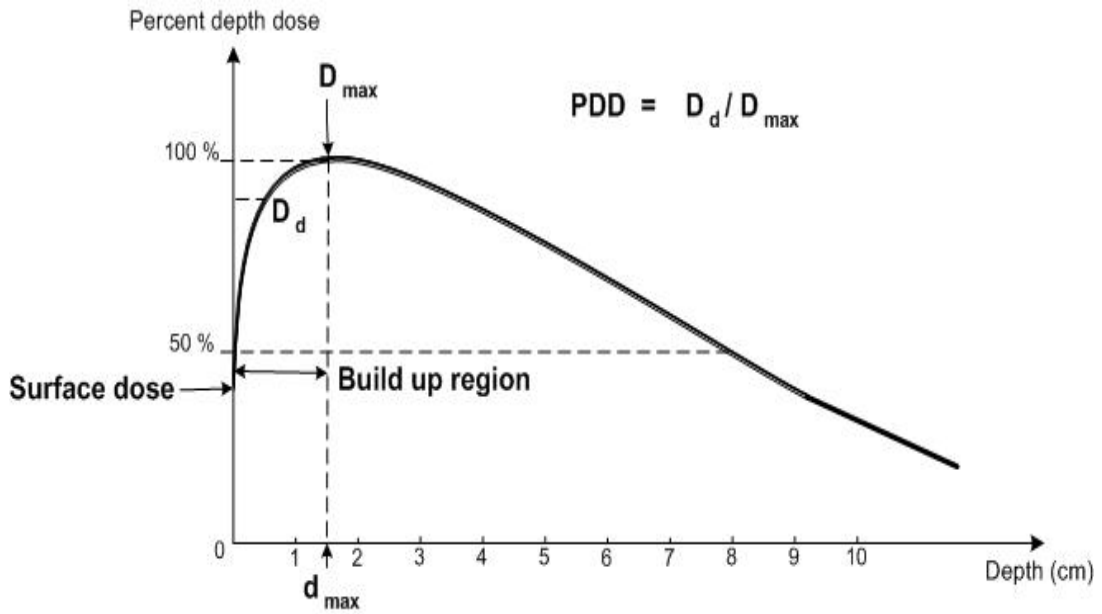


Figure 2.1. Some of the characteristics from a general central axis percent depth dose curve.

2.1.1 Surface dose

The surface dose is the dose on the incident skin surface of the patient. It could be high or low depending on its energy. The surface dose decreases as energy increases because scattered radiation is of higher energy within the forward direction. On increasing the field size, the surface dose is increased because more scattered radiation is present, which is of lower energy and less penetrating. The surface dose is dependent on variations in scattered radiation in the form of electrons and photons streaming from the treatment machine configuration. Examples are shown in Table 2.1 and 2.2.

Table 2.1. Comparison of surface dose as a function of field size for several linear accelerator models (Purdy, 1986).

Field size (cm ²)	Therac 6 (Tannous et al., 1981)	Mevatron 67 (Horton, 1983)	Clinac 6 /100 (Coffey et al., 1980)	Clinac 6 /100 (Purdy, 1986)
5 x 5	8%	7.0%	10.0%	7.5%
10 x 10	13%	12.1%	16.0%	12.5%
20 x 20	23%	22.1%	25.0%	22.6%
30 x 30	33%	31.0%	33.0%	31.4%
40 x 40	39%	36.1%	39.0%	36.0%

Table 2.2. Percentage surface dose for linear accelerators measured at SSD 100 cm for 10 x 10 cm² field size using an extrapolation chamber (Gerbi et al., 1987).

Linear accelerator	Energy (MV)	Surface dose (%DD)
Varian Clinac 6/100	6	15.0
Varian Clinac-2500	6	14.6
Philips SL 75-20	10	10.3
Philips SL 75-20	18	12.5
Varian Clinac-2500	24	13.9

2.1.2 Build-up region

The build-up region is a region near the incident surface where the dose rapidly increases within the first few millimetres and gradually attains its maximum value at the depth of the peak dose. The dose in this build-up region is comprised of the primary photon beam, as well as backscattered radiation from the patient and contamination electrons. The shape of the build-up curve depends on many factors and may even be different for the same conditions with two different radiation machines of the same type (Figures 2.2 and 2.3). It has been demonstrated that with increasing field size, the ratio of the dose due to electrons and photons increases rapidly. Build-up doses near the surface are liable to discrepancies in scattered radiation in the form of electrons and photons coming from the treatment head and thus are dependent on the treatment machine configuration. Under these circumstances, dose to the build-up regions must be accurately calculated by the treatment planning system.

2.1.3 D_{\max} (The Maximum Dose)

The D_{\max} is the maximum dose along the central axis, which is often used as a reference dose. For high-energy x-ray beams, the region where D_{\max} occurs is below the skin and is the place at which an equal number of secondary electrons are set in motion from a volume element as are stopped in that volume element. The region where electronic equilibrium is established is defined as the region of maximum absorbed dose (D_{\max}). The depth at which electronic equilibrium occurs is dependent upon such factors as the primary photon energy, the field size, the irradiated medium, and the particular machine.

2.1.4 d_{\max} (The Depth of Maximum Dose)

The d_{\max} is the depth of the maximum dose. It starts near or at the surface and increases as the electron range increases with energy. The d_{\max} decreases as the field size increases because the increasing amounts of scattered radiation shift the depth of the maximum dose closer to the surface. The d_{\max} of megavoltage x-ray beams was studied (Sixel and Podgorsak, 1994), as a function of beam energy and field size for 6, 10 and 18 MV x-ray beams and field sizes ranging from 1 x 1 cm² to 30 x 30 cm². Their results showed that the magnitude of the d_{\max} shift depends on photon beam energy, for a given beam energy, d_{\max} , increases rapidly with increasing field size at small fields, reaches a maximum around 5 x 5 cm² and then gradually decreases with increasing field size for large fields (Figure 2.4).

Please see print copy for figure 2.4

2.1.5 PDD (Percentage depth dose)

The PDD is the dose along the central axis of the beam as a percentage of the d_{\max} dose. For high-energy x-ray beams, it is known that the percentage depth dose increases considerably with field size in the build-up region, resulting in a shift in the apparent position of d_{\max} (Figure 2.5).

Please see print copy for figure 2.5

2.2 High-energy x-ray beams from linear accelerators

Linear accelerators produce high-energy beams of x-rays (also referred to as photons) or electron beams. They use high-frequency electromagnetic waves to accelerate charged particles such as electrons to high energies through a tube; the electrons can then be extracted from the unit and used for the treatment of superficial lesions, or they can be directed to strike a target to produce high-energy x-rays for treatment of deep-seated tumours. The linear accelerator also has been a standard part of radiotherapy equipment with its energy depending on the machine specifications. When a beam of electrons is generated and accelerated through a waveguide their energy is increased to the megavoltage range. These electrons strike a tungsten target and produce x-rays. For the x-ray beams to conform to a certain field size, high atomic number collimators are set up in the machine. They can vary the field size from $4 \times 4 \text{ cm}^2$ to $40 \times 40 \text{ cm}^2$ at a distance of 100 cm from the target, which is the distance at which most treatments are

performed. The collimators consist of a conical fixed primary collimator and two pairs of adjustable secondary collimator jaws. The secondary collimator jaws confine the beam in the x and y directions and define a rectangular radiation field. The collimators are opened to the field size that covers the tumour within the treatment field. Further restrictions of the field are accomplished by placing blocks in the path of the beam. In this way, normal tissues are shielded, and the dose can be delivered to the tumour at a higher level than if the normal structures were in the field. These individually constructed blocks are used in high-energy x-ray beam treatments. A modern technique involves multileaf collimators (MLCs) mounted inside the gantry, which has allowed precise shaping of the radiation beam to match the irregular shape of most tumours instead of having to construct a new block for each treatment area.

The linear accelerator is capable of rotating around a patient lying on a treatment couch, treating the tumour from several angles. This allows the delivery of high doses of radiation to the tumour whilst reducing the dose to the normal surrounding tissues. Figure 2.6 is a schematic drawing of a linear accelerator treatment head. Radiotherapy by a linear accelerator is usually given in one treatment per day with the standard dose between 1.8 – 2.0 Gy per day, 9 – 10 Gy per week. Treatment is given 5 days per week, with 2 days off from the preceding week's treatment to allow time for the normal cells to recover. The number of treatments depend on several factors, including age and general health, and the site and type of cancer being treated. A course of treatment can take 6 – 7 weeks to complete. Although the radiation is directly administered to cancerous cells by this machine, potential damage can occur to normal tissues that are caught unavoidably in the radiotherapy field. This will cause hair loss or a skin reaction when there are hair follicles or skin inside the treatment field.

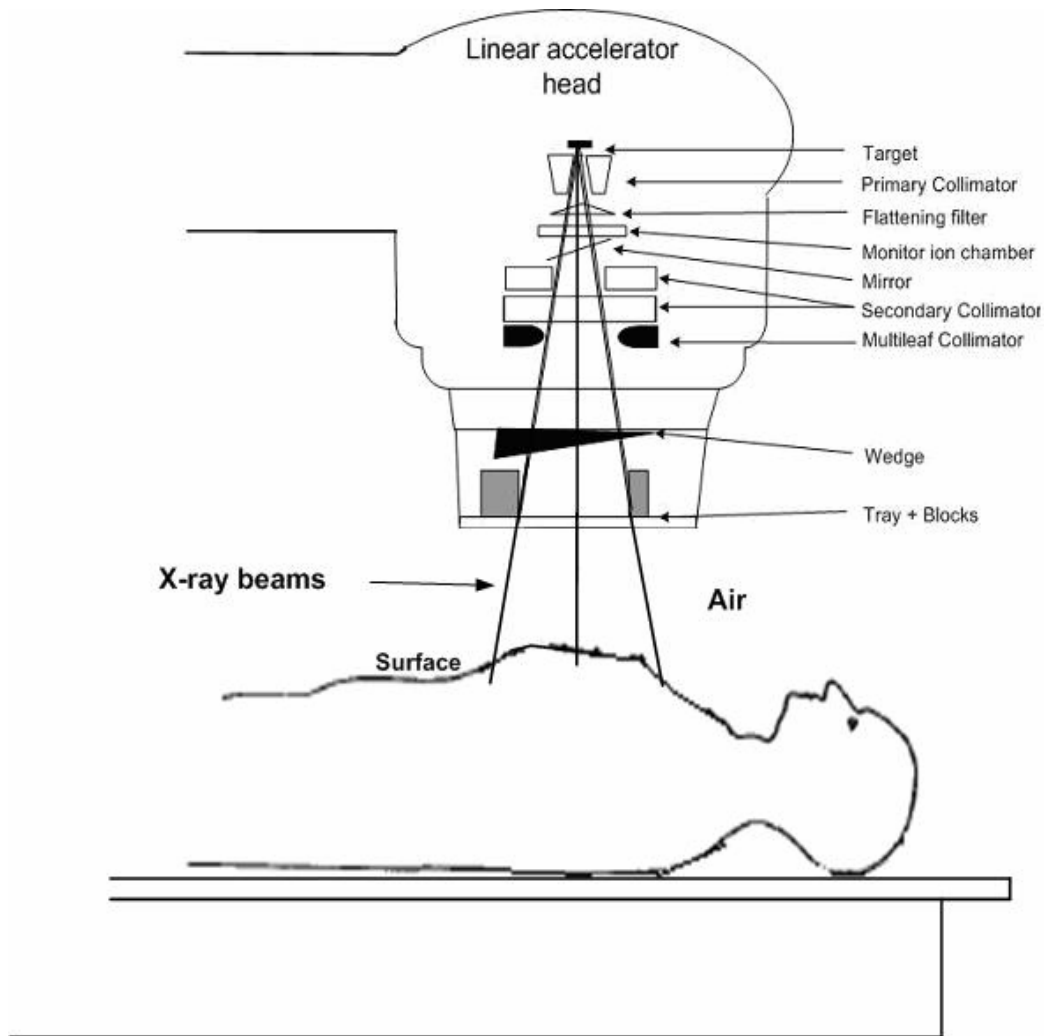


Figure 2.6. The diagram illustrates the structure of the linear accelerator treatment head.

2.3 High energy x-ray beams Interactions

Interaction between incident radiation and matter is not a simple process in which the primary x-ray beams are altered to some other pattern of energy by absorption or scattering from the incident beam in a single event. There are different photon interaction mechanisms that affect the radiation beam properties, such as the photoelectric effect, incoherent scattering, and pair production.

2.3.1 Photoelectric Effect Interaction

This interaction process occurs between bound atomic electrons and an absorbed x-ray photon. When the x-ray photon is absorbed electrons are ejected from the outer shell of the atom, resulting in the ionisation of the atom as shown in Figure 2.7. Consequently,

the ionised atom returns to the neutral state with the emission of an x-ray that is characteristic of the atom. Photoelectron absorption is the dominant process for x-ray absorption up to energies of about 100 keV. Photoelectron absorption is also dominant for atoms of high atomic numbers.

2.3.2 Compton Effect Interaction

This also known as an incoherent scattering and occurs when the incident x-ray photon ejects an electron from an atom, resulting in the scattering of an x-ray photon of lower energy as shown in Figure 2.8. Relativistic energy and momentum are conserved in this process, and the scattered x-ray photon has less energy and therefore greater wavelength than the incident photon. The Compton Effect is important for low atomic number materials. At energies of 100 keV - 10 MeV, the absorption of radiation therapy is mainly due to the Compton Effect interaction process.

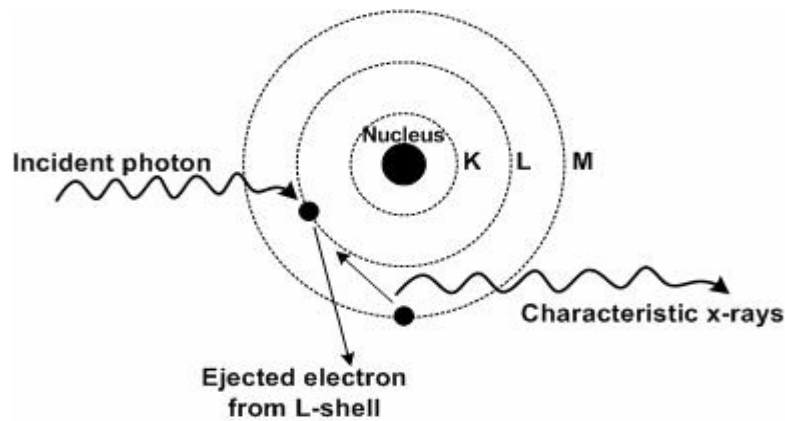


Figure 2.7. The Photoelectric Effect interaction process.

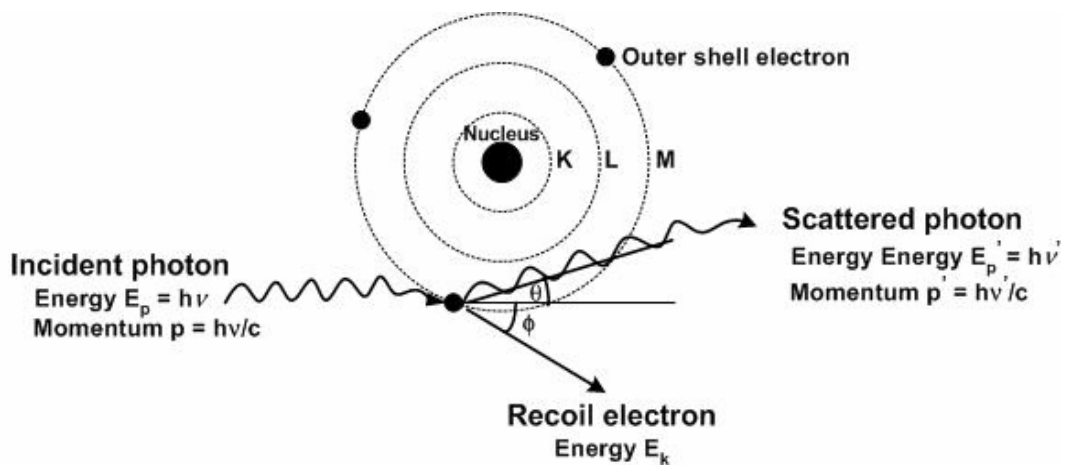


Figure 2.8. The Compton Effect interaction process.

2.3.3 Pair production Interaction

This process can occur with an x-ray photon energy greater than 1.022 MeV, when an electron and positron are produced with the annihilation of the x-ray photon in the coulomb field of a nucleus. Positrons are very short lived and fade away (positron annihilation) with the formation of two photons of 0.511 MeV energy. Pair production is of particular importance when high-energy photons pass through materials of a high atomic number, provided that the photon energy is greater than 1.022 MeV. Triplet production also can occur when the x-ray photon energy is greater than 2.044 MeV in the coulomb field of an electron (Figure 2.9). The result of this interaction process is a newly created positron and electron, while the original electron is also expelled from the atom. The positron produced interacts with matter by ionising and exciting atoms through the same process as electrons, thus it loses energy until it reaches a state of rest. At this point, the positron combines with an electron to produce two 0.511 MeV photons in an annihilation process.

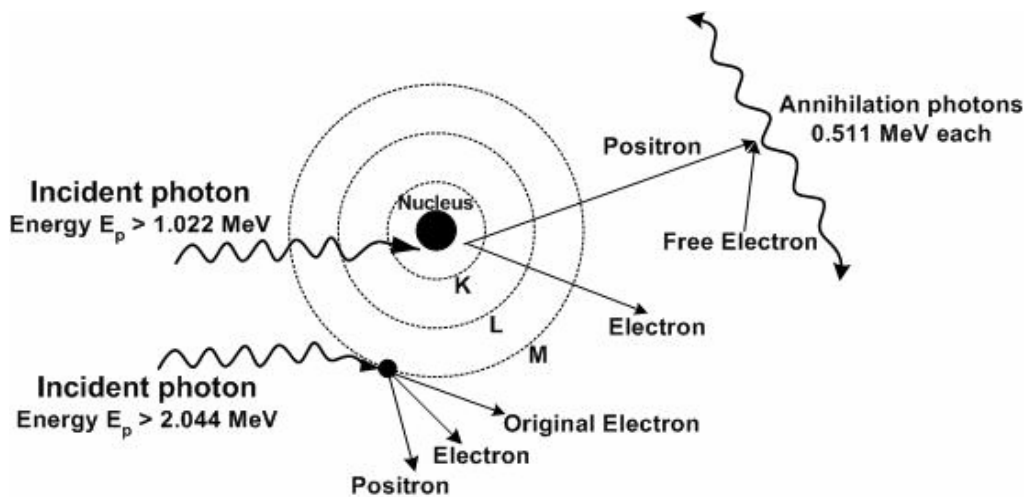


Figure 2.9. The pair production interaction process.

The variation of absorbed dose with different parameters such as atomic number and field size has been studied. Figure 2.10 shows the results for absorbed dose along the central axis at the phantom surface for 21 MV x-rays with a filter thickness of 2 g / cm^2 . For small field sizes, there is a small variation in surface absorbed dose with atomic number, but for large field sizes there is an increase with atomic number because of the pair production.

Please see print copy for figure 2.10

There are other photon interaction mechanisms, such as Thomson scattering and photodisintegration, which also affect the radiation beam properties.

2.3.4 Thomson scattering

It also known as Coherent, Rayleigh, or Classical scattering, this occurs when the x-ray photon interacts with the whole atom, so that the photon is scattered with no change in internal energy to the scattering atom, nor to the x-ray photon. The scattering occurs without the loss of energy. Scattering is mainly in the forward direction.

2.3.5 Photodisintegration

This is the process by which the x-ray photon is captured by the nucleus of the atom with the ejection of a particle from the nucleus when all the energy of the x-ray is given to the nucleus. This process involves high energies of x-ray beams.

2.4 Contamination Electrons

High-energy x-ray beams, which are used to treat deep-seated tumours, have a skin-sparing effect. This is an advantage for using the high-energy x-ray beam therapy

(Sjogren and Karlsson, 1996). It means that larger doses can be given to tumours located deep inside the body. These high-energy beams not only spare the superficial tissues but also enhance the dose delivered at depths. However, secondary electrons generated in the patient or contaminating electrons produced outside the patient, in air or structures in the linear accelerator head, may reduce this effect (Khan, 1994). Figure 2.11 illustrates how the various components of the linear accelerator's treatment head act as sources of electron contamination. The interaction of the x-ray beam with the mechanical parts of the linear accelerator and the air below the linear accelerator head produces a continuous electron spectrum (Malataras et al., 2001).

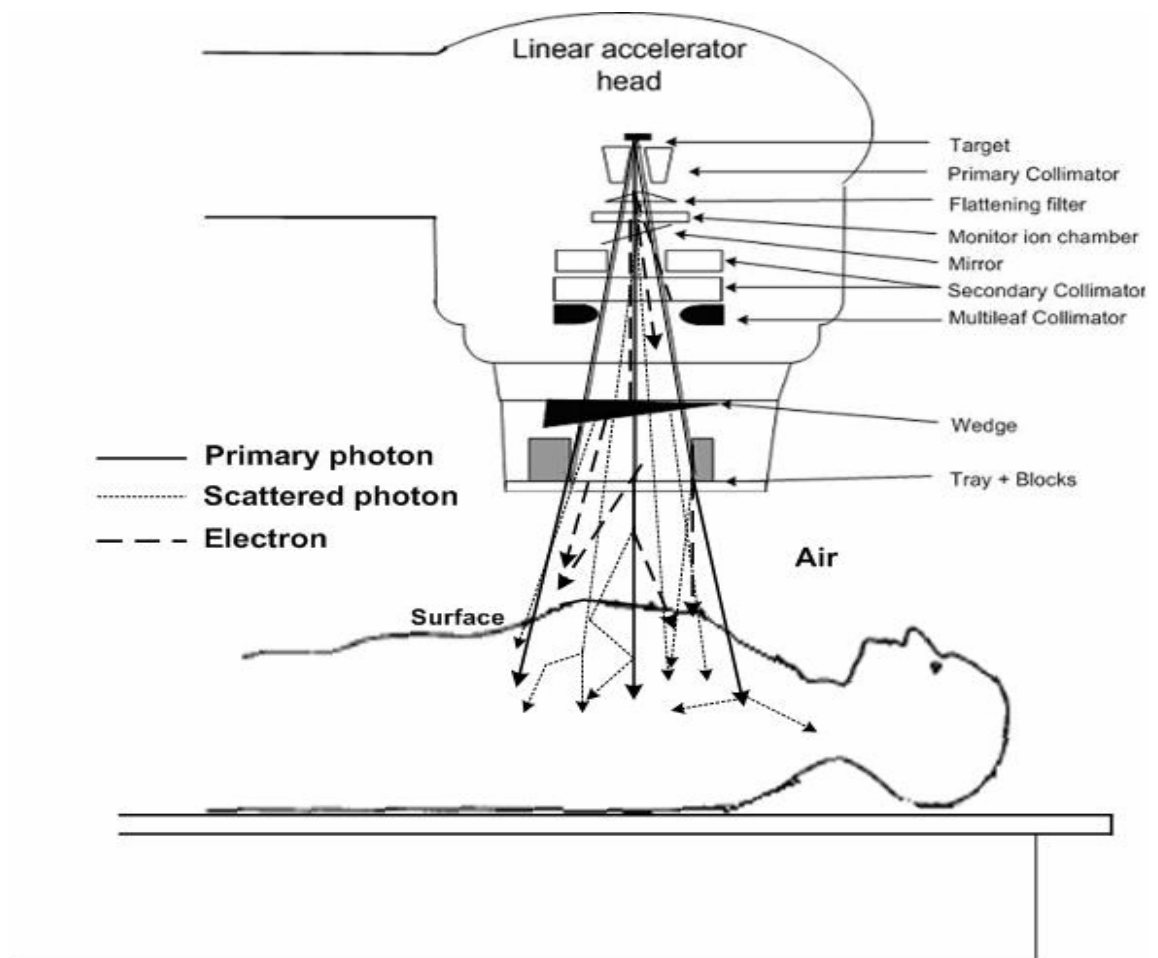


Figure 2.11. The diagram illustrates the structure of the linear accelerator treatment head and the regions where electron contamination is produced.

The dose distribution of the electron contamination in a phantom has been investigated by a number of authors. Many of them (Biggs and Ling, 1979, Biggs and Russel, 1983, Rogers et al., 1985, Sixel and Podgorsak, 1994, Sjogren and Karlsson, 1996, Jursinic

and Mackie, 1996, Zhu and Palta, 1998, Butson et al., 2002a, Butson et al., 2002b) have performed experiments to measure the increased surface dose and the shift of the depth of the maximum dose (d_{\max}) to shallower depths by increasing the field size or decreasing the source-to surface distance (SSD).

The experimental evidence indicates that electrons are the major contaminant (Padikal and Deye, 1978). Petti et al. (1983) employed Monte Carlo simulation to identify the sources of the electron contamination of a 25 MV Clinac-35 photon beam at SSD 80-100 cm. 70 % of contaminant electrons were produced in the flattening filter and monitor chamber, 13 % from the fixed primary collimators and the adjustable photon jaw, and 17 % of these electrons were produced in air. Biggs and Russell (1983) have observed that this electron contamination is produced by the interaction of the primary beam, not only with the collimating system, but also with the beam-shaping device and with the intervening air volume between the patient and the treatment head. The radiation fields are contaminated by electrons and at higher energies also by positrons. These leptons are produced by x-ray interactions in the treatment head, in the air and in different accessories located in the beam path. This contamination increases the surface dose and degrades the build up in the field compared to when the field is clean from leptons (Sjogren and Karlsson, 1996).

It is important to accurately know the dose in the build-up area because high surface doses, which are undesired in many clinical situations, can enhance damage to the skin. Therefore, knowledge of the dose at the skin surface of the patient is essential for proper treatment decisions (Kim et al, 1998). Sjogren and Karlsson (1996) have investigated some sources of electron contamination in different geometries with two 20 MV beams and found that the air generated electrons were comparatively negligible in standard fields at SSD between 80 and 120 cm. There is a large variation with field size in electron contamination, depending on collimator positioning and treatment head design. Perspex or lead in the beam path will act as a scatterer and absorber. The sources for electron contamination may vary depending on the treatment head materials and treatment set-up parameters.

2.4.1 Source from treatment head materials

Treatment head materials such as the target, flattening filter, beam monitor chambers, and collimator jaws (Petti et al, 1983, Nilsson and Brahme, 1986) are sources of contamination electrons because these electrons are produced from x-ray beam interactions with air, collimator jaws, and any other scattering material. Nizin (1993) reported two sources of electrons for x-ray interactions, one from the primary interaction and the other from multiple scattering within the medium.

2.4.2 Source from treatment setup parameters

Treatment set-up parameters such as field size, wedge, tray, block and source-to-surface distance (SSD) (Mellenberg, 1995) have an influence on how these contamination electrons affect the surface dose (Mackie and Scrimger, 1982). It is not practical to alter the effect of treatment head materials, except that the skin dose can be changed by using special treatment set-up parameters in clinical applications.

2.5 Skin dose

High-energy x-ray beams in radiotherapy treatment will always produce electron contamination, and these electrons have a long range in air and produce dose deposition at the patient skin surface (Figure 2.11). The unwanted electrons increase the skin dose and dose to organs close to the skin when an accessory tray is placed in the x-ray field and the source to surface distance is decreased (Klein and Purdy, 1993). Patients are treated with high-energy x-ray beams containing a large number of contaminant electrons; the energy absorbed by the skin is greatly increased and may result in severe skin reactions. Patients' skins are burnt by the incident radiation because of the inherent limitations of the treatment procedure. The definition of the surface dose is related to the depth at which the radiation sensitive layer begins and is underneath the epidermis at about 0.15 mm depth (Klevenhagen et al, 1991). The thickness of the epidermis is between 0.07 – 0.12 mm (Maximow and Bloom, 1942). The dermis can extend from this depth down to 1- 4 mm. Figure 2.12 shows the main structures in the dermis. The dermis layer plays an important role in the change observed after irradiation, which suggests the appropriateness of the term "skin dose". The skin reactions such as erythema, desquamation and telangiectasia are effects of excessive doses delivered to the skin and subcutaneous tissue, which is often not the site of treatment. Erythema, a redness of the skin caused by congestion of capillaries in the lower layer of the skin, is

an early reaction, which occurs when the basal layer is subjected to a high dose. Whereas telangiectasia, which appears as spidery red lines across in the skin due to damaging fibrosis of the blood vessels, is a late reaction, which occurs when the dermal layer has a high dose. These reactions will result in the area experiencing poor healing. Therefore, skin reactions can develop and permanent damage is possible. The side effects from radiation are usually caused by irradiation of normal tissue in the treatment area. Nevertheless, cancer cells are particularly sensitive to radiation and are damaged far more after being exposed to it. To minimise these unwanted reactions we wish to eliminate electron contamination from the entry beam whilst not affecting dose at depth or beam symmetry in the process.

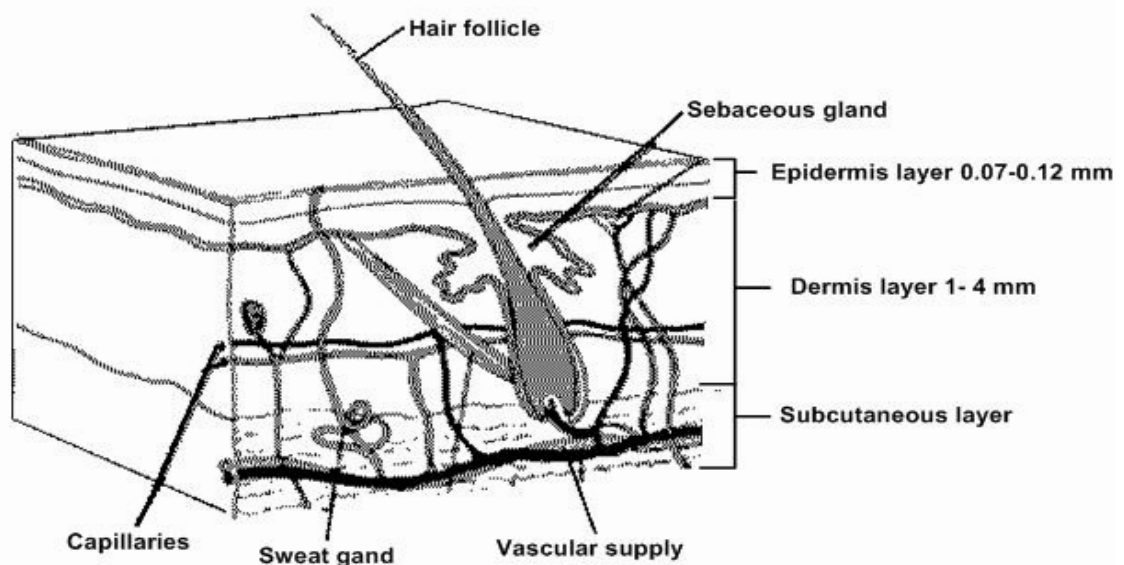


Figure 2.12. Cross-section of the skin anatomy shows the main structures in the epidermis and dermis layers.

2.6 Surface dose from high energy x-ray beams for different clinical set-up parameters

One of the most advantageous features of high-energy x-ray beams is the skin sparing effect, but in some situations, this effect may be reduced or even lost if the beam is excessively contaminated with secondary electrons. Parameters affecting skin surface

doses include those associated with using beam modifying and accessory devices, the source to surface distance (SSD), and the angle of the incident beam.

2.6.1 Using beam modifying and accessory devices

When patients are treated with radiation beams, various skin reactions have been noted. Doses delivered in the skin surface are often dominated by electron contamination and can vary quite considerably within the first few millimetres of depth due to the build-up characteristics of x-ray beams. These electrons arise from photon interactions with the collimating system and with any other scattering medium in the beam path. The problem, however, arises when low atomic number absorbers such as Perspex in the tray for supporting the shielding blocks, compensators, or physical wedges are introduced into the beam. This is important, especially in the isocentric method of treatment in which these absorbers are brought close to the skin. Rao et al. (1973) studied the effect of the tray and found that it caused considerable contamination of the beam for 6 MV x-rays from a Varian Clinac-6, leading to an increase in surface dose of up to approximately 48 % of the local dose for large fields, while using a lead filter can eliminate this contamination. Kim et al. (1998) measured skin doses for 8 MV and 18 MV photon beams for various clinical set-ups including a dynamic wedge, and blocked and multileaf collimator (MLC) fields. The skin dose with a wedge showed a much more complex tendency. It was generally lower than the dose for an open field, but higher in the case of large fields and higher degree wedges. When both a wedge and a block tray were used, the tray was a major contributor to the skin dose because some of the contaminant electrons from the wedge were absorbed by the block tray. Field-shaping blocks increased the skin dose, but, interestingly, the block tray reduced the skin dose for small blocked fields treated with a high-energy photon beam. The effect of an MLC on skin dose was very similar to that of a block, but its magnitude was less. The skin dose was higher for dynamic wedge fields than it was for standard wedge fields. As can be seen from Table 2.3, the skin dose for wedge fields increases as the field size increases. The skin dose for different wedge angles is similar regardless of the energy of the beam.

Table 2.3. Percentage skin dose of 8 and 18 MV x-ray beams for different field sizes and wedge angles (Kim et al., 1998).

F.S. (cm ²)	8 MV				18 MV			
	15°	30°	45°	60°	15°	30°	45°	60°
5 x 5	5	4	3	3	3	3	3	3
10 x 10	10	9	9	9	9	9	9	10
15 x 15	15	15	14	15	16	17	17	18
20 x 20	20	20	20	-	24	24	25	-
15 x 40	24	24	25	27	28	29	30	34

Normally, a patient is treated either supine or prone. If anterior and posterior beams are used, usually one of the beams must traverse through the linear accelerator treatment couch. The linear accelerator couch is normally made from carbon fibre in a tennis string formation with a Mylar covering for comfort. The introduction of this material into the beam path will increase the dose delivered to the patient's skin during treatment. In addition, patient support devices such as the Alpha Cradle and the graphite in the table can increase the surface dose to as much as 92 % (Klein and Purdy, 1993). Thus the pattern of behaviour of the skin dose can be attributed to variations in electron contamination caused by using accessory devices in radiotherapy treatment.

2.6.2 Source to Surface Distance

Several studies have focus on the source of dose build-up for high-energy x-ray beams and found that the surface dose is highly dependent on electrons scattered from accelerator structures and from the air above the measurement surface. Nilsson and Brahme (1979) have predicted that electron contamination increases with increasing SSD due to electron production in air. Petti et al. (1983) investigated the sources of electron contamination for the 25 MV photon beams of the Clinac-35 linear accelerator. Their results showed that at a distance of less than 100 cm SSD, most electron contributions occurred from the flattening filter and beam monitor chamber. The large contribution of contaminant electrons from the flattening filter and monitor chamber is dependent on the experimental increase in build-up dose with field size, since for larger fields, fewer electrons from the flattening filter and beam monitor are blocked by the primary collimators and secondary jaws. Thus, at large SSD, air was the dominant source of electron contamination as can be seen in Table 2.4. Biggs and Russell (1983) also confirmed that at 400 cm, there are more electrons in the beam than at 100 cm.

Table 2.4. The sources of electron contamination in the 25 MV Clinac-35 photon beam for different SSD distances (Petti et al., 1983).

SSD (cm)	80	100	200	300	400
Flattening filter and monitor chamber	70 %	66 %	49 %	40 %	34 %
Collimation system downstream from monitor chamber	13 %	11 %	8 %	6 %	5 %
Air above the measurement surface	17 %	23 %	43 %	54 %	61 %

2.6.3 Angle of incident beam

Beam incident angle is another parameter that affects surface dose. The surface dose for using obliquely incident beams is a function of both the scattered electrons from the air and the accelerator, and the forward scattered electrons produced by interactions of the incident x-ray beams with the material of the phantom. Angle of incidence is defined by ICRU No. 24 as the angle between the beam axis and the normal to the irradiated surface. Jackson (1971) has explained that the skin dose increases with increasing angle of the beam incidence at the entrance surface through the concept of electron range surface (ERS). This ERS is a three dimensional representation of the secondary electron range and distribution caused by the interaction of a pencil beam of photons with the irradiated material, as illustrated in Figure 2.13. Increasing the angle of incidence of the photon beam results in more secondary electrons being ejected in a direction toward the skin surface, resulting in an increased skin dose.

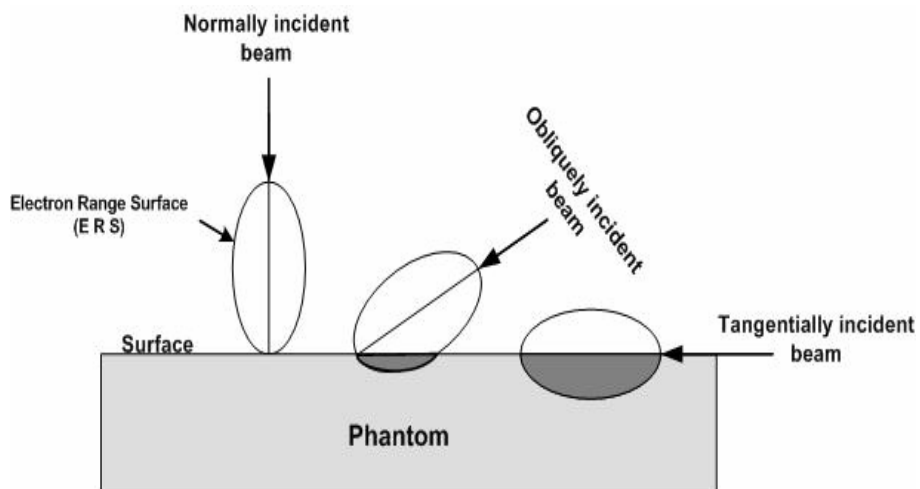


Figure 2.13. The electron contribution from the portion of the ERS determining the surface dose from the incident photon beams.

Investigations dealing with obliquely incident high energy x-ray beams have shown that skin sparing with oblique beams is reduced from what is observed for normally incident photon beams, and that the depth of D_{\max} moves closer to the surface with increasing angle of obliquity. Gerbi et al. (1987) measured the dose in the build-up region using a plane-parallel ionisation chamber in a polystyrene phantom with obliquely incident 6, 10, 18 and 24 MV x-ray beams angled at 0° to 84° . Results indicate that the obliquity factor (the ratio of ionisation charge collected at a point for a particular angle of incidence to that collected at the same point at normal incidence) is highly dependent on the beam energy, the angle of incidence, the collimator opening, and the source-skin distance. Thus the determination of the absorbed dose at the surface and in the build-up region is important, not only for normally incident beams, but also for obliquely incident beams in the clinical application of radiotherapy.

2.7 Magnetic field

Regarding skin reactions caused by the unwanted electrons from radiotherapy treatment, a procedure to minimise skin reactions by elimination of electron contamination from the x-ray beams whilst not affecting dose at depth or beam symmetry in the process is proposed. The technique selected is to reduce skin dose using magnetic deflection to sweep the electron contamination away from the radiation treatment field. Permanent magnets, which are produced from materials such as steel and various alloys, can have a large amount of magnetism. Regardless of the size or shape of a magnet, it always has two poles, called north and south poles. When two poles are brought close together, the like poles repel each other and unlike poles attract each other. In the region around a magnet there is a magnetic field. This is described by a vector quantity whose direction at any point is given by a line running from the north pole of the magnet and then continuing back through the magnet from the south pole to the north. Magnetic field has both direction and strength (or magnitude). The direction of the field lines indicates the direction of the field at a particular point, while the density of the field lines indicates the magnitude of the field. The magnetic field lines always begin on the north pole and end on the south pole. So the magnetic field lines are continuous, will form closed loops, and never cross one another (Figure 2.14).

Please see print copy for figure 2.14

2.8 Electron deflection in magnetic field

Contamination electrons are produced by the interaction of x-rays with materials placed in the linear accelerator beam path during the radiating process. The amount of contamination affects the dose to the skin and subcutaneous tissue. To minimise these reactions and the dose delivered to the build-up region we wish to eliminate or at least minimise electron contamination from the entry beam whilst not affecting any other important beam qualities. The deflection and removal of electrons produced by a medical linear accelerator has been attained using a magnetic field device. The deflection of contamination via a magnetic field following the Lorentz force rule is explained below.

2.8.1 Motion of a charged particle in a magnetic field

When a charged particle q has velocity \vec{v} moving in a magnetic field \vec{B} , there is a magnetic force \vec{F} on it that is proportional to q and v . The force is perpendicular to both the velocity and the magnetic field for positive and negative charged particles (Figure 2.15). The magnetic force \vec{F} on the charge is

$$\vec{F} = q \vec{v} \times \vec{B}. \quad (2.1)$$

The magnitude of the magnetic force has the value

$$F = qvB \sin \theta. \quad (2.2)$$

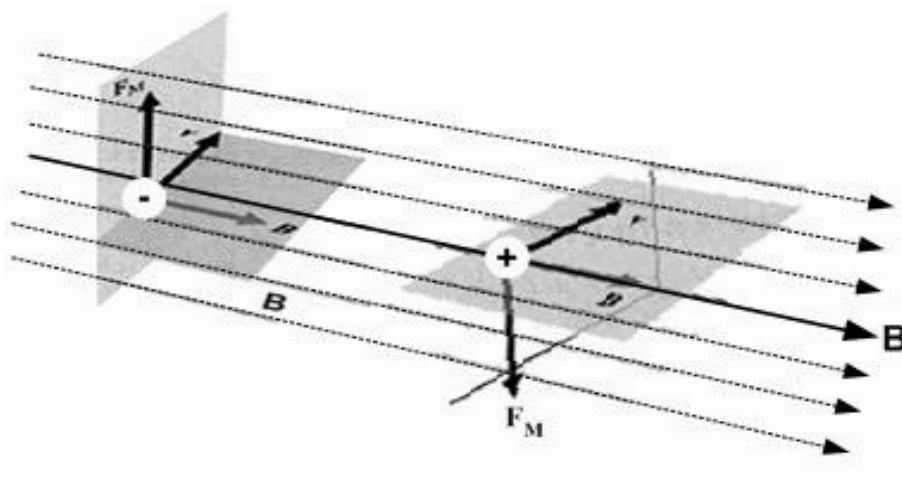


Figure 2.15. The direction of the magnetic force is always at right angle to the plane formed by the velocity vector (v) and the magnetic field (B) for positive and negative charged particles.

2.8.2 Direction of particle's motion is changed

The magnetic force on a charged particle moving through a magnetic field is always perpendicular to the velocity of the charged particle. If the charged particle moves in the direction perpendicular to the magnetic field vector, the charged particle will move in a circle. Hence, the magnetic field changes the direction of the velocity, but not its magnitude, and the direction of the magnetic force is always at 90° to the direction of motion of the charged particle.

2.8.3 Speed unchanged in the magnetic field

The magnetic force acting on a charged particle moving in a magnetic field is always perpendicular to the velocity of the charged particle. The magnetic force thus changes the direction of the velocity. When a charged particle moves with a velocity, an applied magnetic field can alter the direction of the velocity vector, but a magnetic field cannot speed up or slow down a moving charged particle. It can only change the direction in which a charged particle is moving.

2.8.4 Uniform circular motion in a magnetic field

When the velocity of a charged particle is perpendicular to a uniform magnetic field, the particle moves in a circular orbit. The magnetic force provides the centripetal force necessary for the centripetal acceleration v^2/r in circular motion. Newton's second law is used to relate the radius of the circle to the magnetic field and the speed of the

particle. The magnitude of the net force is qvB . When \vec{v} and \vec{B} are perpendicular. Newton's second law gives

$$F = ma = m \frac{v^2}{r}$$

$$qv_{\perp}B = m \frac{v^2}{r}$$

$$r = \frac{mv_{\perp}}{qB} \quad (2.3)$$

Where r is the orbital radius. For uniform circular motion, the angular speed ω is given by

$$\omega = \frac{v_{\perp}}{r}. \quad (2.4)$$

2.8.5 Helical motion in a magnetic field

When the initial velocity of a charged particle is parallel to the magnetic field lines, the force exerted on a charged particle by the magnetic field is zero. The relationship for the force, $F \propto \sin \theta$, shows that $\theta = 0^\circ$, thus $F = 0$. So this charged particle will travel with constant velocity parallel to the magnetic field lines (Figure 2.16).

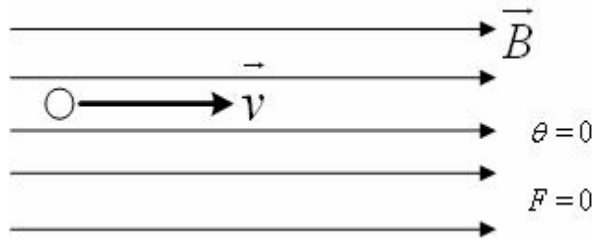


Figure 2.16. A charged particle moving parallel to the magnetic field will travel with a uniform velocity, and there is no work on the charged particle.

When a charged particle moves at some angle to the magnetic field, the velocity will split into two components. One is the component parallel to the magnetic field, and the other is perpendicular to the magnetic field (Figure 2.17).

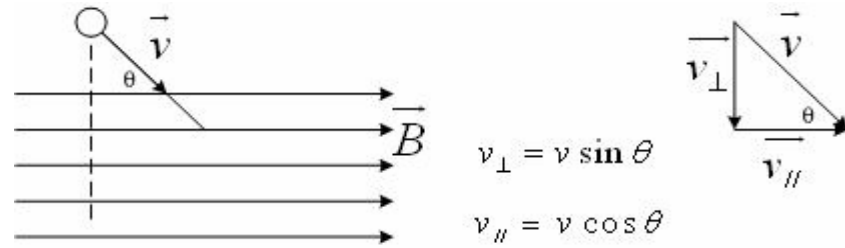


Figure 2.17. Trigonometry is used to resolve the velocity of a charged particle into components parallel to (\vec{v}_{\parallel}) and perpendicular to (\vec{v}_{\perp}) the magnetic field lines.

Figure 2.18 illustrates that when a charged particle moves in a uniform magnetic field with its velocity at some angle to the magnetic field, its path is a helix.

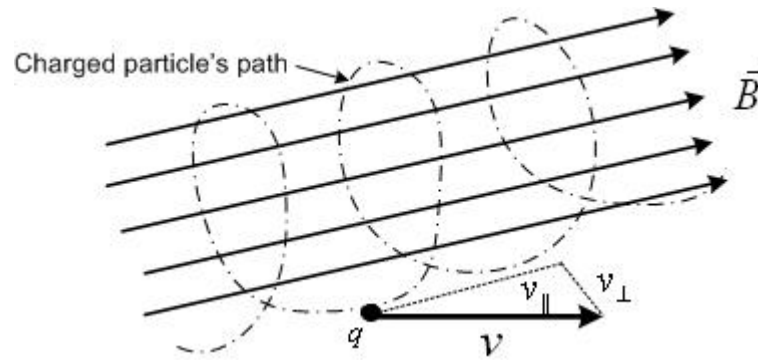


Figure 2.18. The path of a charged particle with components of velocity both parallel and perpendicular to the field direction in a uniform magnetic field is helical. The radius of the motion will alter with changing magnetic induction.

Newton's second law is used to relate the radius of the circle to the magnetic field and the speed of the particle. When (\vec{v}) and (\vec{B}) are perpendicular,

From equation (2.3),
$$r = \frac{mv_{\perp}}{qB}.$$

Generally, the motion of an electron in a uniform magnetic field whose velocity is in a perpendicular direction to the direction of the magnetic field is always circular. Thus contamination electrons produced by a clinical linear accelerator can be considered as relativistic particles, whose energy (E) with kinetic energy (KE) is

$$E = E_0 + KE. \quad (2.5)$$

When P_{rel} is the momentum of the electron and c is the speed of light

$$P_{rel} = \frac{\sqrt{E^2 - E_0^2}}{c}. \quad (2.6)$$

If the magnetic field (\vec{B}) is parallel to the Y-axis with its direction out of page, the radius (r) of the electron path from equations (2.3) and (2.6) for an electron with relativistic energy in a magnetic field is given by

$$r = \frac{mv}{qB} = \frac{P_{rel}}{qB} = \frac{\sqrt{E^2 - E_0^2}}{qBc} \quad (2.7)$$

as shown in Fig. 2.19.

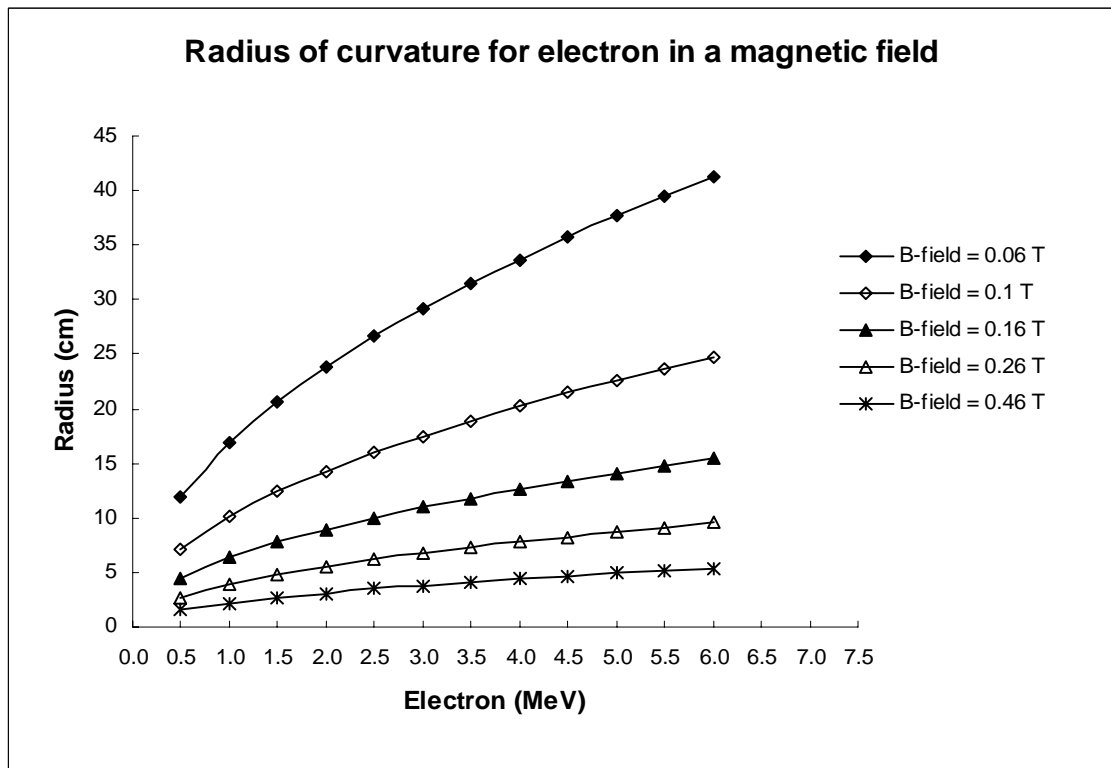


Figure 2.19. The radius as a function of electron energy from 0.5 to 6 MeV in different magnetic field strengths.

The procedure utilises a magnetic deflector device with a high strength magnetic field and light weight for clinical insertion into the medical linear accelerator treatment head. The magnetic field strengths obtained by the magnetic deflector will theoretically give rise to electron deflection radii that should promote the majority of electron contamination to exit the treatment field. The device can be located at any position between the target and the patient, depending on the deflector design, size

and purpose. In theory the ideal location tends to be closer to the patient surface than the x-ray source as this potentially allows for removal of more contamination electrons, i.e. the only remaining contamination arises from the air column between the lowest part of the deflector and the patient surface. A simple magnetic field applied across the beam with direction perpendicular to the beam axis will generate a sweeping action of any electrons passing through the region as described by the Lorentz Force rule. Such a magnetic field can be set up by a simple arrangement of permanent magnets that are mounted on either side of the x-ray beam.

CHAPTER 3

MATERIALS AND METHODS

3.1 Linear accelerator

A linear accelerator is a device that generates high-energy x-ray and electron beams for radiotherapy treatment. It is the most common type of radiotherapy machine used to deliver external beam radiation, with its energy depending on the machine specifications. X-rays and electrons can both be generated by the same linear accelerator, but at different times. The high-energy x-ray beams penetrate deep into the body and spare more superficial tissues, whereas electrons penetrate superficially and spare deeper structures. When the radiation is produced, electrons are directed from an electron gun into a waveguide, so that the electrons will be accelerated and guided by the waveguide towards the linear accelerator machine head. For an electron beam treatment, the narrow beam of electrons then passes through a scattering foil, which spreads the beam out so it can cover the desired treatment area. For an x-ray beam treatment, high energy electrons strike a metal target to produce x-ray beams. The x-rays are pointed towards the patient and can cover a treatment area of up to 40 x 40 cm². If particular treatment areas are desired, the x-rays can be shaped into a rectangular or square field by adjustable metal jaws or collimators.

The Varian Clinac 2100C offers several energy options for treating patients, depending on tumour size and location. To shield the regions around the tumour that need to be protected from the radiation it contains a computer-controlled device called a multileaf collimator, which permits specific beam shaping. This function has no need for alloy blocks and allows treatments to be performed more quickly and efficiently. The multileaf collimators use numerous leaves to create specific radiation field shapes that can be delivered to the patient. The Clinac 2100 C is capable of producing high-energy x-ray beams as well as a range of electron energies that are suitable for treating both deep and shallower tumours. The machine is capable of rotating around a patient lying on a treatment couch and irradiating from several angles. This allows the delivery of high doses of radiation to the tumour whilst reducing the dose to the normal surrounding tissues. Figure 3.1 shows a diagram of a medical linear accelerator system to produce x-ray beams. A beam of electrons is generated and accelerated through a

waveguide that increases their energy to the megavoltage range, and then these electrons pass through a bending magnet and strike a target to produce x-rays. A photograph of the Varian Clinac 2100 C is shown in Figure 3.2. This machine is capable of producing 6 and 18 MV x-ray beams and 6, 9, 12, 16, and 20 MeV electron beams.

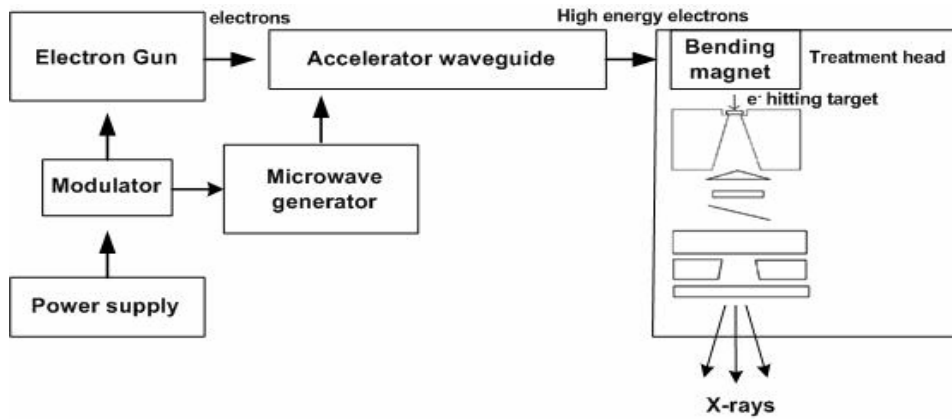


Figure 3.1. Diagram of the medical linear accelerator system used to produce x-ray beams.



Figure 3.2. Picture of Varian Clinac 2100C linear accelerator. This machine is capable of producing 6 and 18 MV x-ray beams and 6, 9, 12, 16, and 20 MeV electron beams.

3.1.1 Linear accelerator treatment head

The production of x-ray and electron beams originates in the head of a linear accelerator. This treatment head contains high-density shielding materials with an x-ray target, scattering foils, a flattening filter, ion monitor chambers, a mirror, a primary and secondary collimator, a multileaf collimator and a light-localiser device. The distance from the target to the distal end of the collimator surface must be large enough to limit geometrical penumbra and also be small enough to leave room for a beam-modifying device such as a wedge-filter or a block and tray accessory mount while providing adequate clearance for the patient and the treatment couch. It is desirable that the distance between the block and the tray be large enough to minimise the scattering of radiation to the patient.

The primary collimator, which is cone shaped, can be fixed in the treatment head and defines the maximum angular spread of the x-ray beam. The adjustable collimators consist of two pairs of jaws and are located as an upper and lower set to define the radiation beam in x-ray beam treatment. The inner surfaces of these jaws are designed to be almost tangential to the radiation beam to reduce the geometrical penumbra. Jaws can move independently or in pairs. The field size is defined by these motorised collimating jaws. For electron beam treatment, they combine with the electron applicator below these jaws. Generally, the jaws are coupled to move about the isocentre.

Modern linear accelerators are also equipped with a multileaf collimator (MLC). The MLC was developed to encompass irregularly shaped tumours. The number of leaves and the leaf spacing differ for different linear accelerator manufacturing designs. The field-defining light and range finder in the treatment head provide visual methods for patient positioning using reference field sizes or distance indicators. The centre of the radiation beam is marked on the beam axis on a Mylar window that is illuminated by a light source. The lamp is located in the treatment head outside the radiation beam. Its light is reflected by a mirror that is positioned at an appropriate location and angle with respect to the beam axis. A mirror fixed on the beam axis is used as a field light reflector for x-ray beam treatment. The range finder is placed on the outer front or back edge of the treatment head. It provides a centimetre scale that indicates the distance of the patient's skin from the target. The field size can vary up to $40 \times 40 \text{ cm}^2$ at a distance

of 100 cm from the target, which is the distance at which most treatments are performed. Figure 3.3 shows the structure of a medical linear accelerator treatment head.

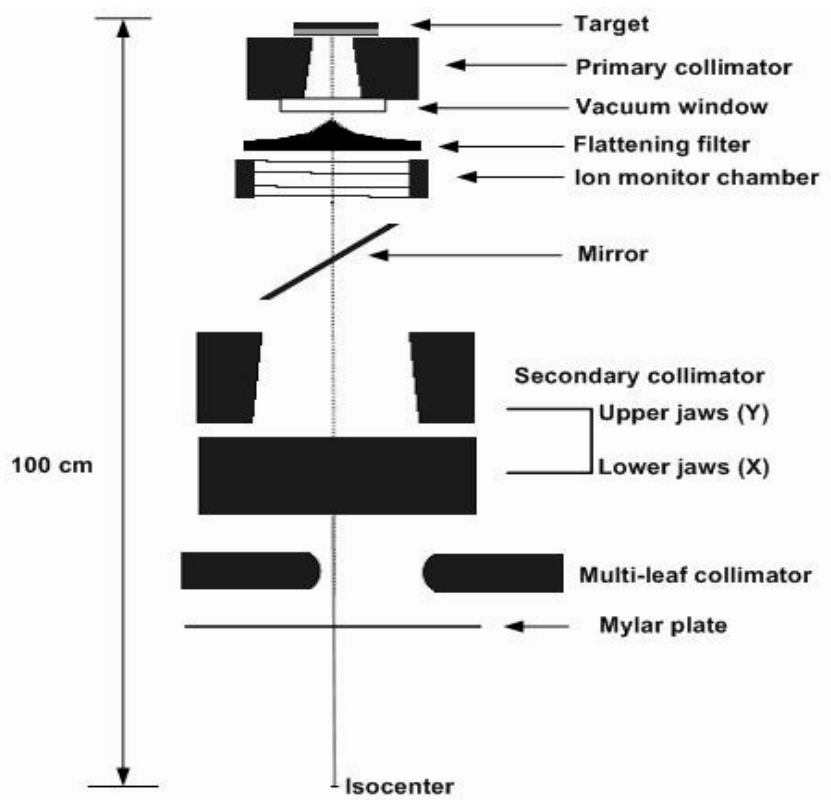


Figure 3.3. Diagram showing the structure of a medical linear accelerator treatment head.

3.2 Ionisation chambers

The measurement of the dose at the surface of a phantom and in the build-up region is a difficult task. Because of the steep dose gradient in the build-up region, the size of the dosimeter should be as small as possible. Several instruments have been used to measure the dose in the build-up region, or region of non-electronic equilibrium, including at the surface (Velkley et al., 1975, Nilsson and Montelius, 1986, Gerbi and Khan, 1990). The instruments of choice for these measurements are extrapolation chambers because of their high accuracy in the non-electronic equilibrium situation, but few institutions have these instruments.

In ionometric measurements, the beam has to pass through the ionisation volume before it is recorded. A detector should be designed to cause as little perturbation as possible of the electron fluence. Ionisation chambers with parallel plane geometry have this characteristic. A plane parallel-plate ionisation chamber consists of two plane walls, one serving as an entry window and polarising electrode, and the other as the back wall and collecting electrode, as well as a guard ring system. The back wall is a block of a non-conducting material, with a thin conducting layer of graphite forming the collecting electrode and the guard ring system on top. Some types of plane parallel designs (e.g. the Markus chamber) overestimate surface dose due to design limitations, Velkley et al. have proposed an empirical method to correct fixed volume ionisation values to values at the zero chamber volume measured with a variable volume extrapolation chamber. The corrected percentage of maximum ionisation, P' , is defined by Velkley as

$$P'(d) = P(d) - \xi(E, d/d_{\max}) l$$

Where $P'(d)$ is the corrected percentage build up as a function of depth (d) to the front surface of the chamber. For the skin-dose data ($d \sim 0$) $P(d)$ is the uncorrected percentage build up obtained in the fixed volume chamber with the electrode or plate separation (l) and the correction factor in percent per mm of plate separation (ξ). The correction factor (ξ) is a function of energy (E) and the ratio of depth of measurement (d) to the electronic equilibrium distance d_{\max} . It reduces to zero at the depth of the maximum dose. It is obtained from the slope of the plot of percent of maximum ionisation versus plate separation (l).

Tannous et al. (1981) used this empirical method with a fixed volume PTW parallel-plate ionisation chamber and corrected to the zero-chamber volume. The results were found to be regular with similar measurements to those taken with a variable volume extrapolation chamber. It is known that fixed separation plane parallel ionisation chambers overestimate the surface dose due to a finite window thickness and electrons scattered from the walls of the chamber (Gerbi and Khan, 1990). To minimise this problem requires using a smaller plate separation and wider guard ring (Khan, 1994). The chamber window thickness is important, and when measuring the surface dose the front window of the chamber should be at least 0.1 mm thick, because the surface dose is related to the depth at which the radiation sensitive layer begins, about 0.1 – 0.5 mm underneath the epidermis (Klevenhagen, 1993). Currently, a new chamber based on solid water has become available which is particularly designed for surface dose

measurements. When these corrections are applied to an Attix chamber, correction less than 1 % are required due to the separate design of the Attix chamber.

3.2.1 The Attix chamber

The Attix model 449 chamber is a plane parallel ionisation chamber with dimensions of 6.0 cm x 1.4 cm (diameter x height). The body is made from RMI solid water, model 457, and nylon screws. The front electrode is made of 0.025 mm Kapton conductive film, and the collecting electrode insulator is 0.13 mm thick polyethylene. Its thinness allows measurements of dose build up starting almost at the surface of a phantom. The conducting surfaces are minimal thickness colloidal graphite. The guard ring diameter is 4.0 cm, and the collecting electrode is 1.27 cm in diameter. The air gap is 1 mm, giving an ion-collecting volume of approximately 0.127 cm^3 vented to the atmosphere. A disadvantage is that it is not waterproof. Therefore, it is used to perform measurements in solid water (Gammex RMI Model 457). The design of the Model 449 eliminates errors due to the Velkley effect in photon dose build-up measurements. A photograph of the Attix model 449 chamber used for the experiments is shown in Figure 3.4.



Figure 3.4. Picture of the Attix model 449 chamber (Gammex RMI Model 457) used for the experiments in solid water.

Due to its construction, an Attix chamber's over-response near the surface will be minimal, and therefore it gives more accurate results for the surface dose than the

Markus chamber. For a surface dose of 6 MV x-rays Butson et al. (1994) found that the Markus over-responded by 10.7 % while the Attix chamber over-responded by 0.7 %. The over-response of the Markus chamber compared to the Attix chamber shows that the over-response dose is due to the finite window thickness and the electrons scattered from the walls of the chamber. The Attix chamber is larger, but also has a thin entrance window similar to that of the Markus chamber. The angular response is reported to be more stable than for the Markus chamber, and the response is similar to that of an extrapolation chamber. In our experiments, the surface dose measurements (for x-ray beams) were obtained using an Attix Model 449 parallel plate ionisation chamber in a solid water phantom. Reproducibility of measurements for this configuration was found to be ± 0.5 %. The over-response of this type of chamber was calculated to be less than 1% (Rawlinson, 1992) as such no corrections to data were applied. For the build-up dose measurements at a constant SSD of 100 cm, thin solid water slabs were taken from below the chamber and placed on top of varying thicknesses in front of the chamber to measure the build-up doses.

3.3 Phantom materials

Dose distribution data are derived from measurements in phantoms that closely approximate the radiation absorption and scattering properties of muscle and soft tissues (Khan, 1994). Water is the phantom material usually recommended for measurements, but in some situations, this can give rise to problems because a chamber then requires a waterproof sheath. These can also be uncertainties in depth positioning near the surface due to meniscus pressure. For relative measurements, it is convenient to use non-water phantoms. Constantinou et al. (1982) designed a solid water phantom, which is made from an epoxy resin-based solid substitute for water, to use for radiation dosimetry.

3.3.1 Solid Water phantom

The Solid Water phantom of dimensions 30 cm x 30 cm (Constantinou et al., 1982) that was used in the present research is manufactured by the RMI Company with various slab thicknesses as used. It matches tissue composition in percentage of mass composition, consisting of H (8.09 %), C (67.22 %), N (2.4 %), O (19.84 %), and Ca (0.13 %), while the dimensions of the phantom provide enough scattering material for

most field sizes without adding too much weight (Metcalf et al., 1997). It eliminates the problem of transporting, setting up, and filling water tanks. It scatters and attenuates in the same way as water. It can be used for both photon and electron beam calibrations, including relative ionisation and depth dose measurements, without the need for correction and scaling factors. Ionisation readings obtained in solid water are virtually the same as those in liquid water for the same depth and exposure duration. The ratio of mass energy-absorption coefficient for Solid Water is close to unity for the entire energy range (Figure 3.5), only being slightly higher below approximately 0.1 MeV. For polystyrene and PMMA, in contrast, the ratio below 0.1 MeV is less than unity. Thus, water absorbs more low energy photons than either polystyrene or PMMA and slightly less than Solid Water (Palm and LoSasso, 2004). A photograph of Solid Water phantoms with various slab thicknesses that were used for experiments is shown in Figure 3.6.

Please see print copy for figure 3.5



Figure 3.6. Solid Water phantoms with various slab thicknesses used for the experiments.

3.4. Beam modifying device

Radiotherapy beams sometimes require changes to their properties to provide an accurate dose delivery distribution within the patient. This can be performed with the use of beam modifying devices. Examples of these devices are given below.

3.4.1. Wedges

Wedges are used to modify the intensity distribution in a radiation beam because wedges generate a reduction in beam transmission, resulting in tilted dose profiles. Wedges may be used to compensate for body thickness changes and increase the uniformity of radiation treatment for the shaped body parts. Wedges are blocks of material constructed such that the thickness varies continuously or in steps in the shape of a wedge. The thick end of the wedge transmits less of the initial beam, and the thin end transmits more. Wedges are usually made of high atomic number materials to minimise space in the machine head or above the blocking tray holder. A standard set provides wedges with wedge angles of 15, 30, 45, and 60 degrees. The effect of a wedge on the beam is to attenuate the lower energies of x-ray beams so the depth dose

distribution can be changed, especially at large depths (Khan, 1994). Photographs of wedges used in the experiments are shown in Figure 3.7.

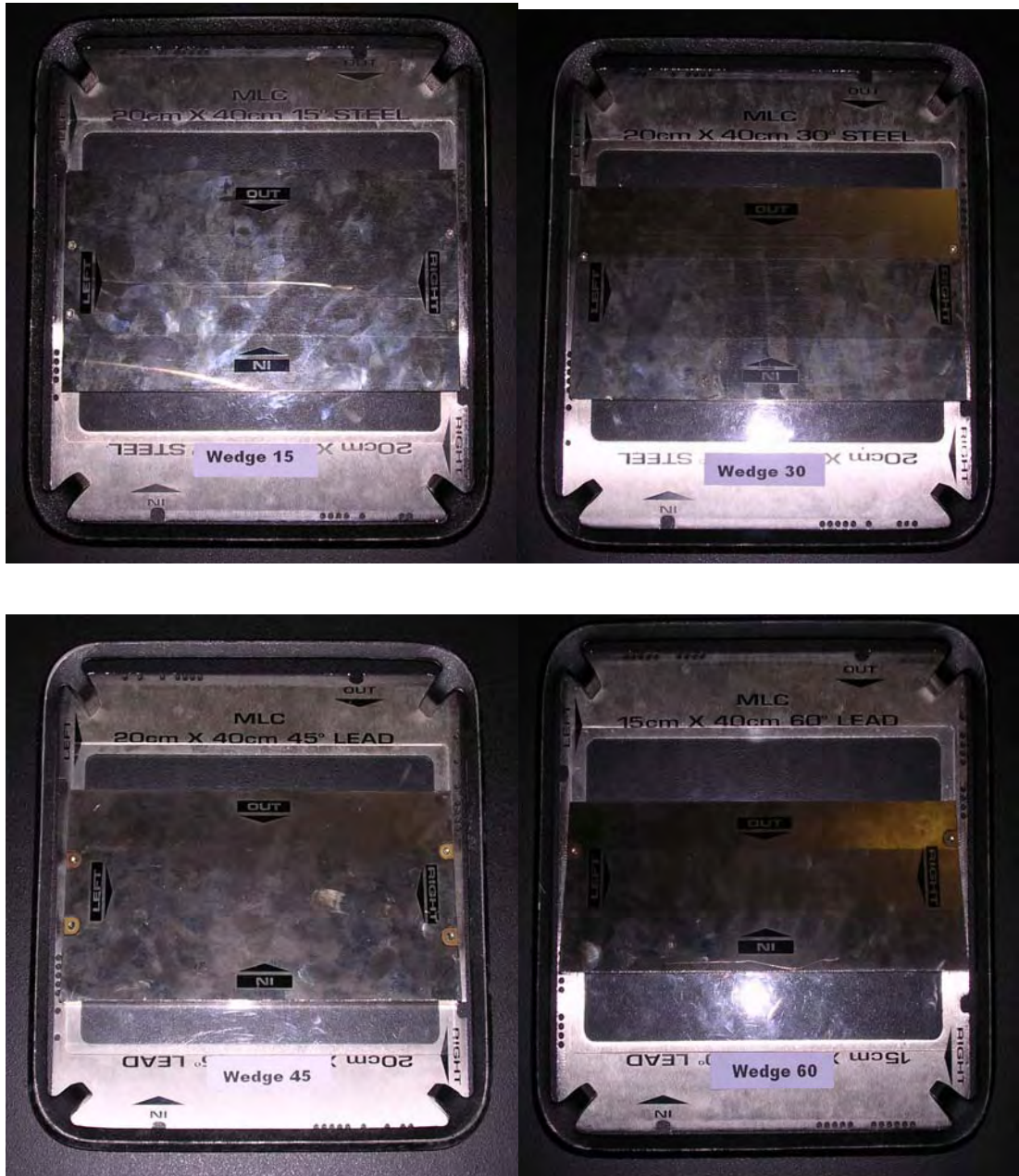


Figure 3.7. Picture of wedges with 15, 30, 45, and 60 degree angles that were used in the experiments.

3.4.2. Perspex tray

During external beam radiation therapy, radiation is directed through the skin to a tumour and the surrounding area in order to eradicate the tumour cells. The treatment field size is defined with the collimating jaws. Thus, x-rays can be shaped into a

rectangular or square field. For normal tissue in the treatment field that needs to be protected from the radiation we use blocks for shielding. Shielding blocks are most commonly made of lead. The thickness of the block required to provide sufficient protection of the shielding areas depends on the beam quality and the allowed transmission throughout the block. The block is placed above the patient and supported in the beam on a transparent tray, such as is shown in Fig. 3.8, in the linear accelerator head. The tray intercepts the treatment beam and attenuates the beam, reducing the dose to the patient. Therefore, we need to consider attenuation for calculation of the prescribed dose to the patient.



Figure 3.8. Picture of 6 mm thickness Perspex tray used in the experiments.

3.5 Film dosimetry

Film dosimetry has become a widespread method for quality assurance and dose verification because it is attractive due to its high spatial resolution, great convenience, and flexibility with regards to placing films in the phantom. Film dosimetry provides intrinsically two-dimensional image data with a short measuring time and at low cost as

well. Although radiographic film is known to have an energy-dependent response, because of the high atomic number of silver, photoelectric interactions in film become important for photon energies below 200 keV (Williamson et al., 1981, Muench et al., 1991), resulting in increased sensitivity of the film. Consequently, film sensitivity increases with field size and depth due to an increasing contribution of low energy Compton scattered photons. Film dosimetry also requires a densitometer to analyse the darkening of the film and to relate the darkening to the radiation received. Despite some limitations, film offers a convenient medium for easily generating profiles and two-dimensional distributions. Due to the photoelectric effect, the high atomic number of the silver in silver halide film emulsion means a greater cross section for low-energy photons (Figure 3.9), causing the ratio of the mass-energy absorption coefficient for photographic film relative to water to vary with photon energy.

Please see print copy for figure 3.9

It is known that the sensitivity of the film increases as the scatter-to-primary ratio increases due to increased scatter fluence. For a uniform radiation field, the scatter photon fluence is higher near the centre and decreases outwards, whereas the primary photon fluence is uniform within the field. Palm et al. (2004) found that radiographic film will under-respond from the centre of the irradiated field while it will over-respond outside the field if the film calibration curve is based on data derived from the central

axis (Figure 3.10). Radiographic film is not an ideal detector for measurement of x-ray since it involves changing spectrum. However this film was still used as a crucial part of this experiment and results were analysed for the study. Alternative to radiographic film for 2D dose verification have their limitations. Radiochromic film is considered tissue equivalent and energy independent, but it is limited in size, expensive, and it still requires higher dose. Electronic portal imagers have the advantage of being available in many modern therapy centers; but by design, they measure and verify fluence patterns, not dose distributions in phantoms, and therefore interpretations of delivery errors could be difficult. While many therapy centers have experience with radiographic film, there is presently improved interest in film dosimetry as it provides a very convenient two-dimensional, integrating system with high spatial resolution suitable for mapping the dose distributions. Film can be used to make good relative dose measurements in phantoms. An alternative approach is to accept the limitations of film and use it within those limitations.

Please see print copy for figure 3.10

3.5.1 Radiographic film

Radiographic film consists of a base of thin plastic with a radiation sensitive emulsion containing silver halide grains up to 1 micrometre in diameter, which is coated uniformly on one or both sides of the base. The thickness of the emulsion ranges from 10 to 20 micrometres. The ionisation of silver halide grains, as a result of radiation interaction, forms a latent image in the film. This image only becomes visible (film blackening) and permanent subsequently to processing. The high silver content in the

film enhances the photoelectric interactions when compared to biological tissue, resulting in an over-response of the film to low-energy photons. The dosimetric response is also influenced by surrounding material, such as air gaps (Suchowerska et al., 2001), film orientation (Danciu et al., 2001), and development conditions (Bos et al., 2002).

Danciu et al.(2001) have studied the influence of parameters on the sensitometric curve (net optical density versus dose) such as the effect of beam energy and film plane orientation on OD (optical density) for two types of film, Kodak X-Omat V and Agfa Structurix D2 using different x-ray beams of 6,15,18, and 45 MV. It was found that the differences in OD with depth are less than 2 % and the difference in sensitivity between parallel and perpendicular exposure was small except in the region of dose maximum.

However, radiographic film gives excellent 2-D spatial resolution and, in a single exposure, provides information about the spatial distribution of radiation in the area of interest. Typically, film is used for qualitative dosimetry, but with proper calibration, as well as careful use and analysis, film can also be used for dose evaluation. Various types of film are available for radiotherapy work as discussed in the following section.

3.5.2 Types of radiographic film

Several special types of radiographic film have been designed for the radiography of materials, such as direct exposure non-screen films for field size verification, phosphor screen films used with simulators, and metallic screen films used in portal imaging. Radiographic films are commonly coated with emulsion on one or both sides of the film base in order to increase the sensitivity. Figure 3.11 shows a cross-sectional view of radiographic film layers.

Cross-section of radiographic film layers

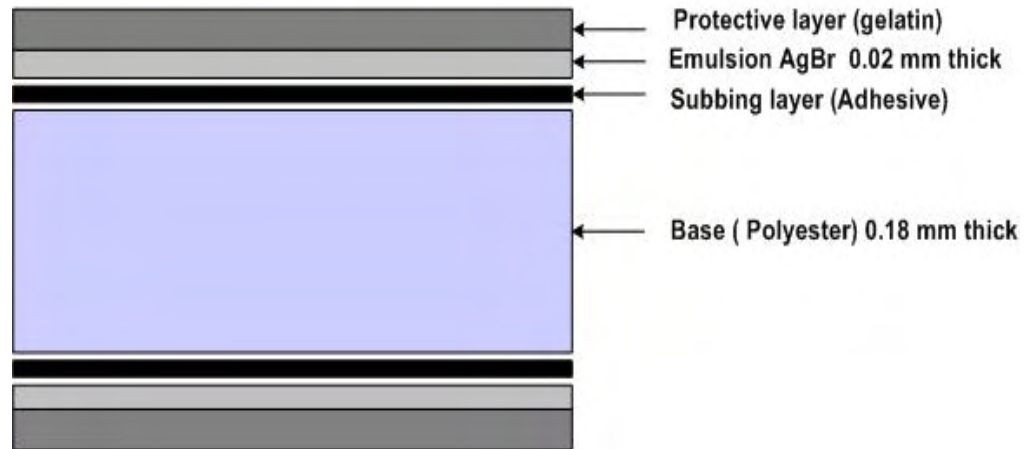


Figure 3.11. A cross-sectional view of radiographic film layers.

3.5.3 Radiographic film density

Radiographic film density refers to a quantitative measure of film blackening. Density is defined by the equation:

$$D = \log \frac{I_0}{I_1}$$

where D is the density, I_0 is the intensity incident on the film and I_1 is the intensity transmitted after passage through the film. Curves that relate optical density to film exposure are known as characteristic curves or H & D curves. It is common practice to plot film dose on a logarithmic scale. The characteristic curve of a film is the relationship between the logarithm of the radiation exposure and the optical density. The important part of the curve is the approximately linear region between the toe and the shoulder where the density is proportional to the logarithm of the exposure. The condition of the processor at the time the film passes through makes the greatest difference in the characteristic curve. Thus, all the films used for the curve and the experimental determination of the output must come from the same batch and be processed together. Normally, applications of a radiographic film in radiotherapy work are qualitative and quantitative measurements, including electron beam dosimetry, quality control of radiotherapy machines, verification of treatment techniques in various phantoms, and portal imaging. In our study we selected the ready-pack radiographic film X-Omat V for the film dosimetry. The X-Omat V Film has emulsion applied to both sides of the film base to increase the sensitivity and features the ready-pack, which

removes the need for loading screen cassettes. It is a relatively low-speed film designed for verifying the orientation and for approximating patient dosage in radiation therapy procedures. Kodak X-Omat V radiographic films were used for the assessment of surface dose measurements in our research. All radiographic films were from the same batch, avoiding confounding effects by inter-batch differences (Bos et al. 2002). A photograph of the X-Omat V film used for measurements is shown in Figure 3.12. X-Omat V films were processed in an automatic X-Omat processor. Optical density to dose conversions was performed on the experimental films using results supplied from the calibration curve. In each case, the optical density was measured at the centre of each film piece to minimise the effects of variations in measured dose near the edge of the film. Using the optical density calibration function of the Vidar VXR-12 Plus visible light densitometer and Scion imaging software scanner results from H and D curves produced a calibration curve adequately fitted over the range from 5 to 100 monitor units (MU) by a third order polynomial.



Figure 3.12. Pictures of X Omat V films for the measurement of dose.

3.6 Film digitiser

The Vidar VXR-12 Plus film digitiser translates hard-copy x-ray films to digital images. The resulting data matrix can be electronically transmitted, viewed, and stored. This film digitiser is used for film dosimetry such as with X-Omat V film. The major

components of the digitiser (Figs. 3.13 and 3.14) are a light source from a fluorescent lamp with the light crossing the light diffusion plate and passing through the scrolling film to be digitised. The vertical and horizontal shutters collimate this light beam to a rectangular field that covers the film length. The transmitted light is reflected by a stationary mirror, focused by the lens, and detected by a linear CCD detector. The CCD detector reads line by line at 300 dots per inch (dpi) over its full length of 14 inches. A 12-bit analogue-to-digital converter digitizes the signal and uses conversion tables to translate data. Then the matrix data is transferred to the computer.

Please see print copy for figure3.13



Figure 3.14. Picture of Vidar VXR-12 Plus film digitiser for scanning film.

3.7 Hall Effect Teslameter

All sources of magnetism have at least two poles that are linked by invisible lines of force, called flux lines. Flux lines are generally viewed as exiting the north pole and returning to the south pole. The total number of flux lines passing perpendicularly through a given area is the flux density (B) or magnetic induction. In the centimetre-gram-second (CGS) system, a gauss (G) is one flux line passing through one square centimetre. In the international system (SI) system, the tesla (T) is 1×10^4 lines per square centimetre. Thus the relationship is $1 \text{ T} = 1 \times 10^4 \text{ G}$. The force within the magnet that produces the flux lines is the magnetic field strength (H). It must be known that flux density and magnetic field strength are related but not equal. The intrinsic characteristics of the magnetic material must be considered. Only in free space (air) are flux density and field strength considered equal. The Hall Effect device consists of a thin square or rectangular plate or film. The plate or film is affixed to a ceramic substrate that provides mechanical support, thermal stability, and wiring nodes. When an electric current flows through a conductor in a magnetic field, the magnetic field produces a transverse force on the moving charge carriers, which tends to push them to one side of the conductor. Then an increasing charge at the sides of the conductor will balance this magnetic influence, producing a voltage between the two sides of the conductor. The presence of this transverse voltage is called the Hall Effect. The Hall Effect can be used to measure magnetic fields with a Hall probe, as shown in Figure 3.15.

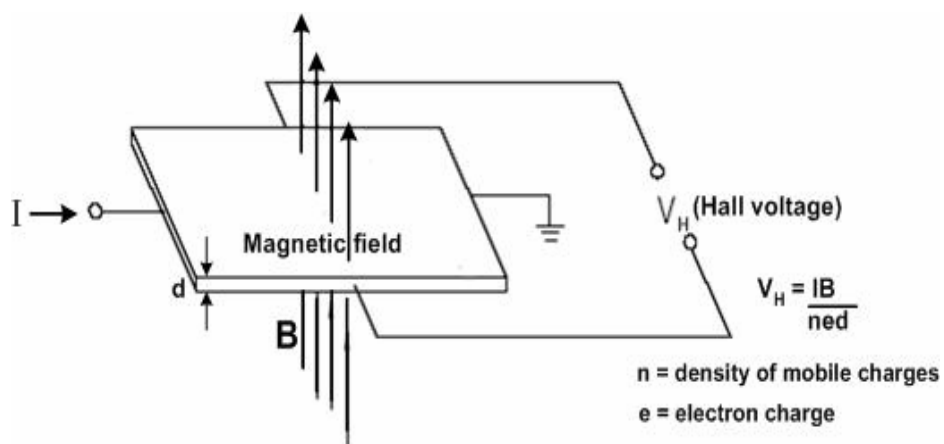


Figure 3.15. The Hall Effect for magnetic field measurement.

The Hall voltage is directly proportional to the flux density. A Hall generator's output is related to the angle at which flux lines pass through it. Maximum output is achieved when the lines are perpendicular to the sensor (Figure 3.16).

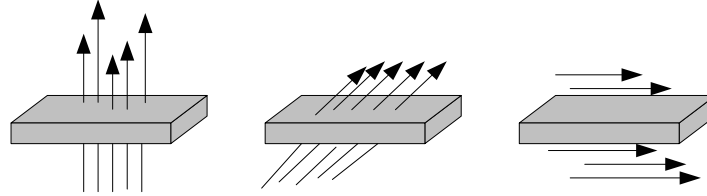


Figure 3.16. The Hall Effect probe is direction dependent, and the output is greatest when the flux lines are perpendicular to it.

Measurements of the magnetic field strength in the volume between the magnet banks are performed with a Digital Hall Effect Teslameter (DTM-132). The probe of the Teslameter is direction dependent, and so caution was taken to ensure that the field measured was comprised entirely of the given directional component at any given point (Figure 3.17). The DTM-132 Digital Teslameter offers accurate well-resolved measurements of magnetic flux densities with a precision of ± 0.005 T for mapping or precise field control, with the active area of 1.0×0.5 mm housed in a probe head size of $14 \times 5 \times 2$ mm³.



Figure 3.17. Pictures of the DTM-132 Digital Teslameter and Hall probe.

3.8 Neodymium iron boron magnetic deflector

Neodymium Iron Boron (NdFeB) is an alloy of the Lanthanide group of elements. It is a strong and powerful rare-earth permanent magnetic material with good characteristics in terms of high-energy product and high coercive force. The basic and typical shapes of the magnets used are block (square shape), disc, ring, and tile. The surface is usually coated with zinc, nickel, or epoxy resin. Neodymium Iron Boron (NdFeB) permanent magnets were selected as the magnetic deflection device due to their high magnetic field properties, being approximately 16 times greater than those of iron ferromagnetic devices per unit mass, as well as being lighter in weight. A deflector device with an Aluminium holding frame (Fig. 3.18) can be inserted directly into an accessory mount or similar in a linear accelerator head (Fig. 3.19). The magnets in the device are two large banks of 4 NdFeB lanthanide ceramic permanent magnets each having dimensions

of $5 \times 5 \times 5 \text{ cm}^3$ and 16 smaller NdFeB magnets of $5 \times 5 \times 1.2 \text{ cm}^3$ (AMF Magnetics). This design improvement can increase the volume of space that has a strong magnetic field strength.

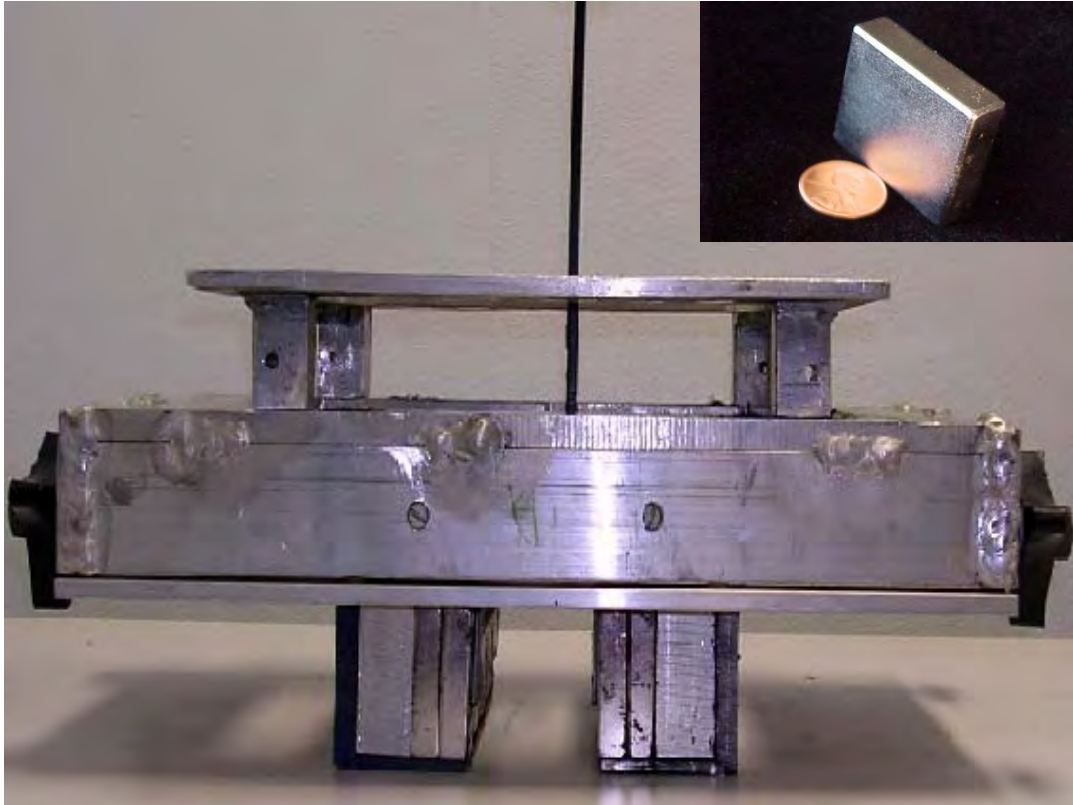


Figure 3.18. Picture of Neodymium Iron Boron (NdFeB) lanthanide ceramic magnet each of dimensions $5 \times 5 \times 5 \text{ cm}$ and $5 \times 5 \times 1.25 \text{ cm}$ were selected for placement in an Aluminium holding frame as the magnetic deflector device. Inset shows some of the actual magnets.

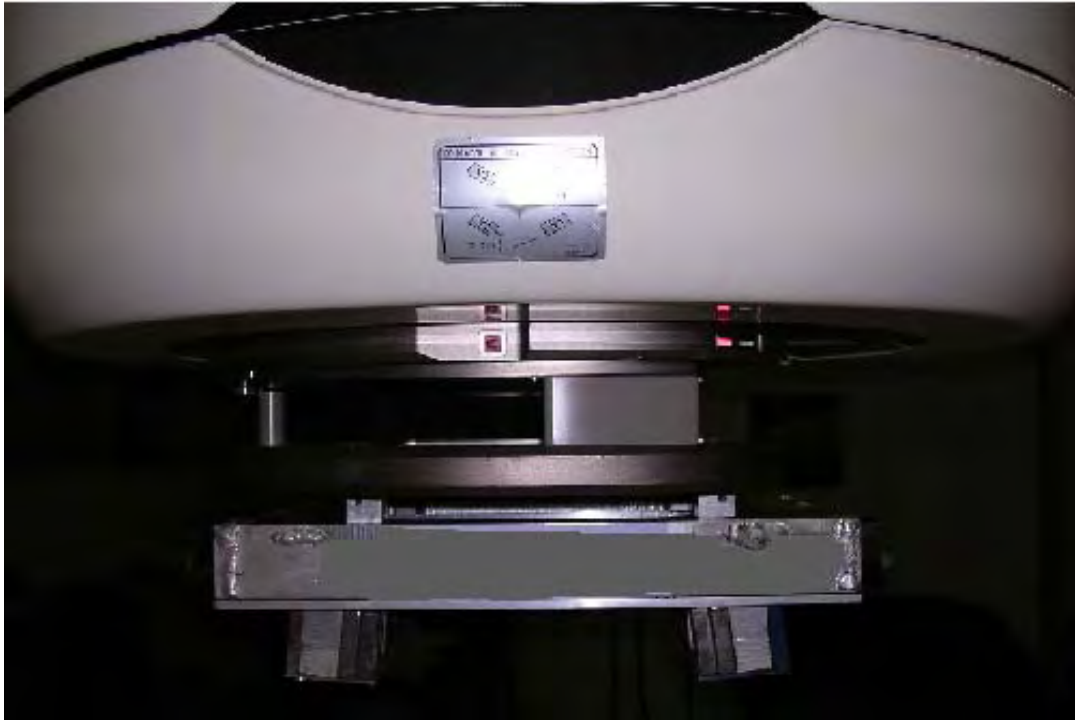


Figure 3.19. NdFeB magnetic deflector device inserted directly into an accessory mount in a linear accelerator head.

3.9 Monte Carlo technique

Monte Carlo methods for modelling linear accelerators are able to determine doses accurately for the entire range of situations encountered in the treatment of cancer. These methods are able to correctly characterise beams of photons or electrons emerging from medical linear accelerators. Calculated information on beam characteristics can be very useful for a variety of radiation dosimetry problems, such as studies of electron contamination in photon beams and accurate estimation of quantities difficult or impossible to measure in clinical physics. This is because the Monte Carlo method uses basic physical interaction probabilities to determine the behaviour of the particles to be studied. The interactions between each particle and the surrounding media are simulated.

The particles reaching the patient are generated in the accelerator head, in the collimating jaws or the multileaf collimators, and in any beam modifiers such as wedges, blocks, compensators, and trays, as well as in the air column between the accelerator and the patient. The Monte Carlo method tracks individual particle histories

and is specifically employed to calculate the tracks of particles, including secondary particles that they may be generated between the accelerator head and the patient. All of the energy introduced into the system comes from the initial particles. These particles are absorbed by or escape from the system. Then a map of the energy deposition throughout the system is created and iterated for a very large number of particles. The result is an estimate of the average energy deposited in the system per particle due to the radiation source. The obtained data for each simulated particle at any location in the system consist of the dose deposited per initial particle, the dose deposited per electron/photon, the particle fluence, the energy spectrum, and the electron and photon spectra. The Monte Carlo technique used for dose calculations produces accurate results and provides an accurate method for the simulation of patient dose distributions.

3.9.1 Monte Carlo technique for modelling linear accelerator

Monte Carlo techniques to calculate radiotherapy beams have been studied in various groups. It is recognised that the various components of the accelerator treatment head present as sources of contaminating electrons. The interaction of the x-ray beam with the mechanical part of the linear accelerator and the air below the machine head produces a continuous spectrum. High-energy x-ray beams have the advantage of a skin-sparing effect, whereas the presence of contaminating electrons reduces this advantage. Study of the electron contamination sources offers important knowledge for developing methods for detection of electron contamination. The influence of electron contamination on the dose distribution in a phantom has been investigated by a number of authors (Biggs and Ling, 1979, Biggs and Russel, 1983, Sixel and Podgorsak, 1994, Rogers et al., 1985, Attix et al., 1983, Jursinic and Makie, 1996, Zhu and Palta, 1998). They performed experiments to measure the increase in the surface dose and the shift of the depth of the maximum dose to nearer the surface by increasing the field size or decreasing the source-to-surface distance (SSD). In some experimental studies a magnet was used below the treatment head to sweep the electrons coming from the linear accelerator head (Biggs and Russel, 1983, Jursinic and Mackie, 1996, Sjogren and Karlsson, 1996).

It is known that the energy and dose distributions of photons and contaminant charged particles, such as electrons and positrons, from medical accelerators are important

characteristics of radiotherapy with high-energy x-ray beams. Thus information on clinical beams is essential for dosimetry and the development of a new accurate treatment planning system. Sometimes experimentally it is difficult to obtain detailed information because of various limitations in the clinical environment and detectors. One of the major advantages of the Monte Carlo technique is that it allows detailed information about each particle's history to be identified. Our study aims to provide information on radiotherapy x-ray beams and contaminating electrons in a radiotherapy beam from a medical linear accelerator. The code BEAMnrc was used to simulate 6 MV radiotherapy photon beams emerging from an accelerator. The position, energy, angle, charge, and weight of simulated particles were stored in a phase space file. The stored phase space files were used repeatedly for analysing the beam or as input to the EGSnrc user code DOSXYZnrc to calculate the dose distribution in a water phantom. This investigation presents simulated 6 MV beams from a Varian Clinac-2100 C linear accelerator.

CHAPTER 4

RESULTS AND DISCUSSION

4.1 Magnetic deflection model

Conventional linear accelerator high energy x-ray beams used in radiotherapy treatment will always produce electron contamination because of the inelastic scattering interactions of x-rays with materials such as the flattening filter, monitor ion chamber, collimators, Mylar cross hairs, wedges, compensators, blocks, and block trays, and in the interactions with air molecules in the column of air between the source and the patient surface. The purpose of this research is to design a magnetic deflector device with a high strength magnetic field and light weight for easy manual insertion into the medical linear accelerator treatment head. In this work, to create a strong magnetic field, the improvements to the magnetic deflector, which is clinically mounted below the block tray of the linear accelerator head, is shown in position for a simulated clinical procedure in Figure 4.1.

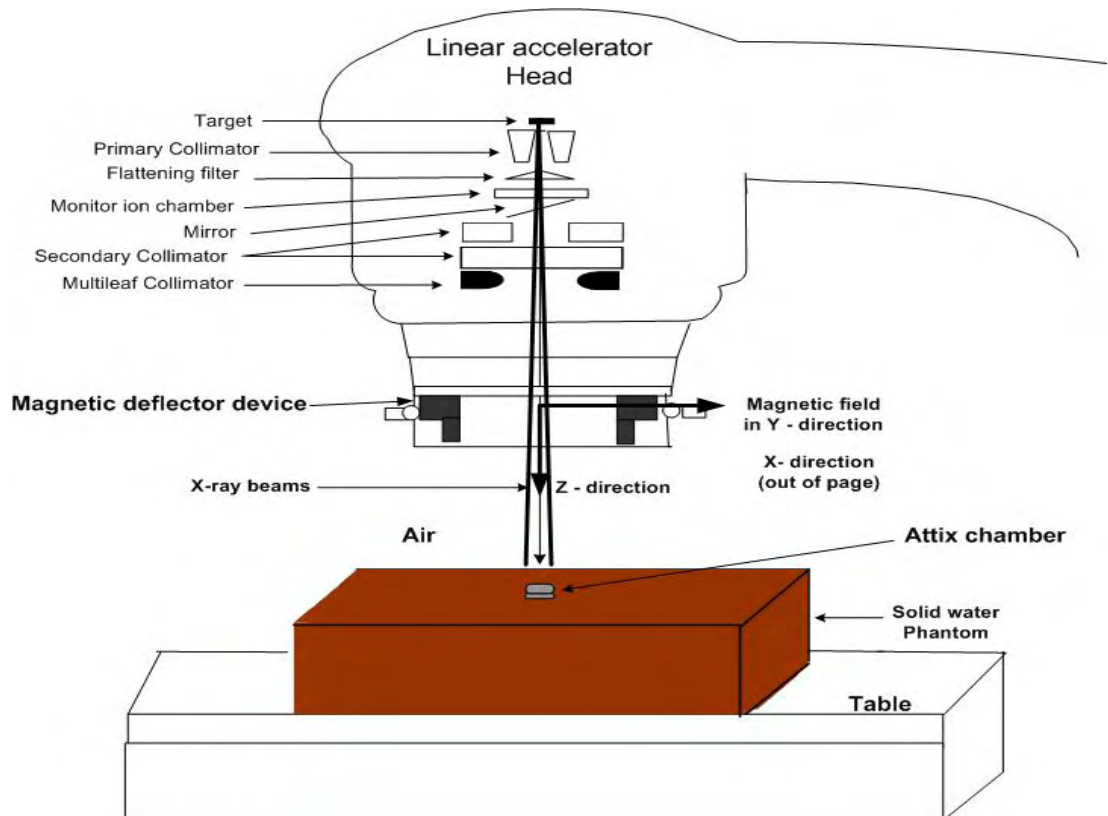
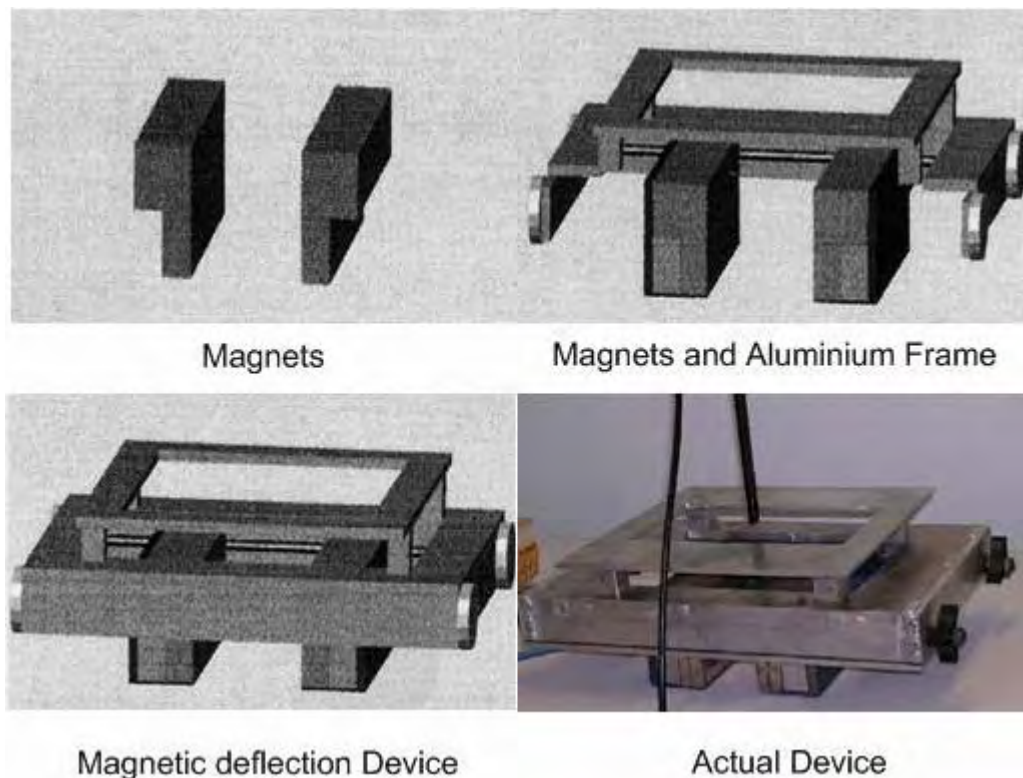


Figure 4.1. The magnetic deflector in location for simulated clinical measurements.

4.1.1 Magnetic deflector device

Neodymium Iron Boron (NdFeB) permanent magnets were chosen as the magnets in the magnetic deflection device due to their high magnetic field properties, namely, being approximately 16 times stronger magnets than iron ferromagnetic devices per unit mass. NdFeB magnets have a high magnetic flux and are light weight, making them suitable for placement in a simple Aluminium holding frame that can be inserted directly into an accessory mount or similar in a linear accelerator. The magnets in the device comprise of two large banks of 4 NdFeB magnets, each having dimensions of 5 x 5 x 5 cm and 16 smaller NdFeB magnets (5 x 5 x 1.25 cm) (AMF Magnetics). The smaller magnets have been added to form a second set of banks below the original larger set. The original set-up (Butson et al., 1996, 1997) used as the basis for our design only has two banks of NdFeB permanent magnets. We have made different sorts of improvements to the original set, including the addition of more NdFeB magnets and the removal of sections of the magnet-supporting frame to allow for larger x-ray fields to pass through. This design development has the effect of increasing the volume of the space that contains a strong magnetic field within the radiation field while increasing the distance for deflection of contamination electrons by 2 times. Figure 4.2 shows the device in greater detail.



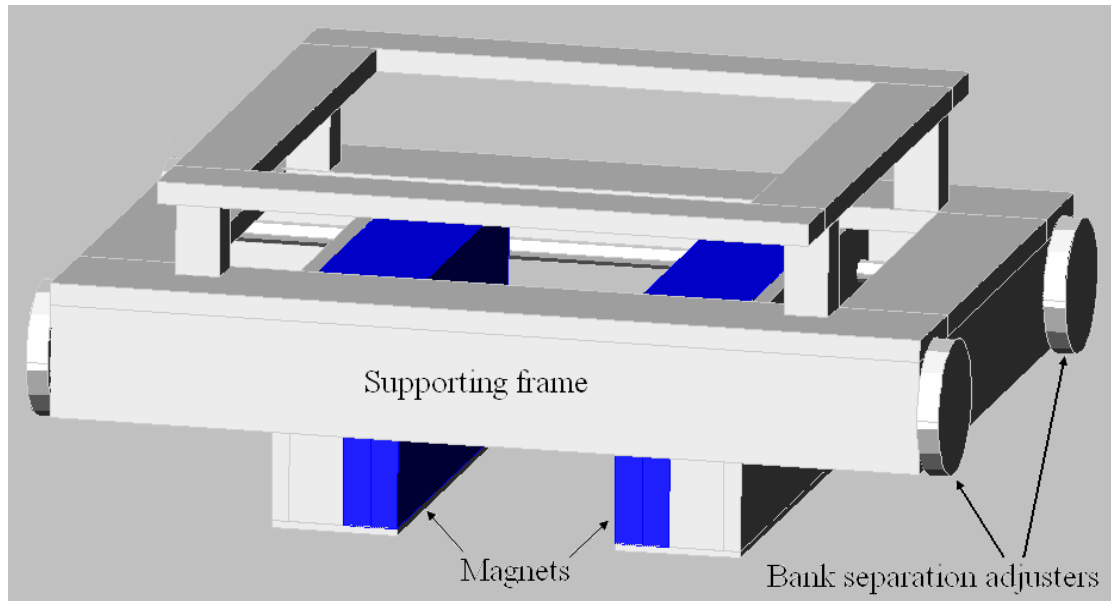


Figure 4.2. Schematic diagram of the details of the magnetic deflector device with a photograph of the actual device.

4.1.2 Simulation of magnetic fields around magnetic deflector device

The magnetic field generated by a permanent magnet is described by vector quantities. These vectors lie along closed loops running from the north pole (or face) of the magnets and back to the south pole. A computer generated (Vizimag 3.0) image of this can be found at <http://www.vizimag.com/vizimag> 3.0. As more magnets are added the magnetic field lines become more complex. This is because the field at any point is comprised of the superposition of the fields generated by all magnetic volume elements of each of the magnets. Figure 4.3(a) shows a 2-dimensional slice of the field lines through the central plane of our magnetic deflector as generated by Vizimag. Figure 4.3(b) shows how this particular arrangement of the magnets generates a large region of high magnetic field strength between the magnet banks. It is this region (or volume) of high magnetic field strength in the +Y-direction that sets up the deflection process. This high magnetic intensity region is perpendicular to the central axis of the radiation treatment field.

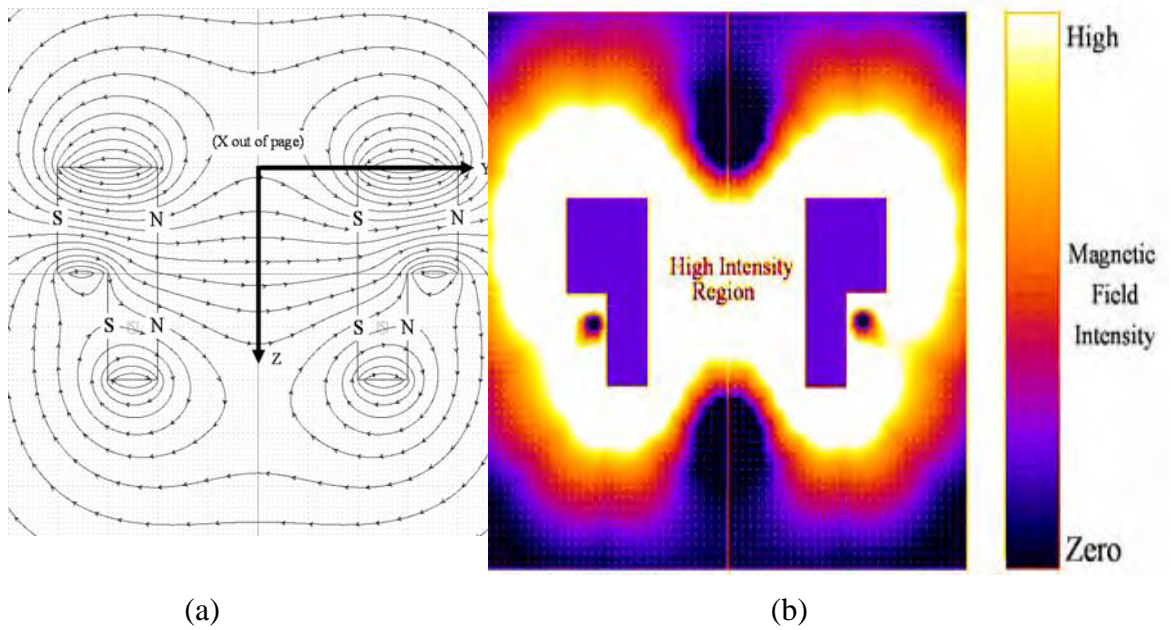


Figure 4.3. (a) Magnetic field lines through the central plane of our magnetic deflector as determined by Vizimag. (b) Colour-scale intensity image of the magnetic field intensity (magnitude) around the magnetic deflector. Note the extended high intensity region between the magnets.

The Vizimag simulation software also generates magnetic field strength values. It initially calculates relative values, which the user can then to assign a calibration point to give the relative values an absolute equivalent. This was performed in our case. Vizimag, however, does make an important assumption about the magnet shape that is simulated. Any permanent magnet drawn in the Vizimag workspace is represented graphically in 2D, while the modelling is done on a 3D cylinder that has the viewed 2D slice as the central slice of the 3D cylinder (Beetson, 2004). For example, a bar magnet with a square cross section is modelled as a bar magnet with circular cross section. In our case the magnet banks extend considerably beyond the actual depth that Vizimag assumes. This is shown in Figure 4.4.

Please see print copy for figure 4.4

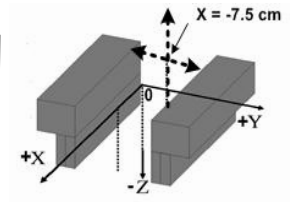
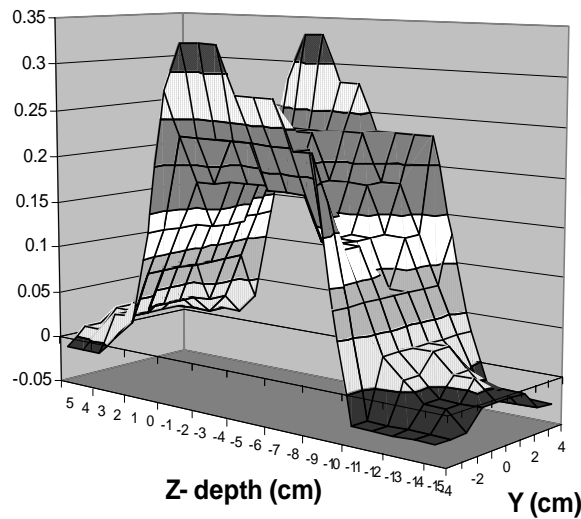
4.1.3 Measurement of magnetic fields around magnetic deflector device

Manual measurements of the magnetic field strength in the volume between the magnet banks were performed with a Digital Hall Effect Teslameter (DTM-132). The probe of the Teslameter is direction dependent, and so caution was taken to ensure that the field measured was comprised entirely of just the Y-direction component of the overall field at any given point. This is because the Y-component generates the desired deflection away from the treatment area. The other components are of no interest: the Z-component results in no deflection, while the X-component is very small in the strong deflection region. The DTM-132 Digital Teslameter offers accurate resolution measurements of magnetic flux densities with a precision of ± 0.005 T for mapping, or precise field control with an active area of 1.0×0.5 mm housed in a probe head size of $14 \times 5 \times 2$ mm. Our designed magnet was measured using this probe for magnetic field strength in the plane of the magnetic field direction at a distance from the Y-plane component in the central axis and along the Z-depth plane component. The reproducibility of spatial measurements for this configuration was found to be ± 0.2 cm. Figure 4.5 (a), (b) and (c) shows that the measurements were performed at distance of $x = 7.5$ cm away from the central plane ($x = 0$). The measured data show a magnetic field strength from 0.08 T to 0.36 T. Note that a negative magnetic field strength means positive field strength in the opposite spatial direction. There were limited explanations for the magnetic fields strength at the outer edges of the measured area. Because our designed magnet was measured for magnetic field strength in the plane of the magnetic field direction at some distances between the magnet banks and along the Z-depth plane component. The aluminium frame that holds the magnets in position and other covering

material on the magnetic device is inappropriate for the measurement magnetic field strength at the outer edges. However two-dimensional slice of the field lines through the central plane of our magnetic deflector as generated by Vizimag from Figure 4.3(b) shows how this particular arrangement of the magnets generates a large region of high magnetic field strength between the magnet banks and at the outer edge of magnet with colour-scale intensity image of the magnetic field magnitude around the magnetic deflector.

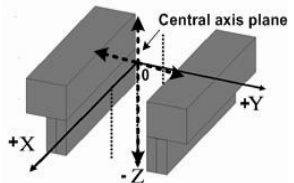
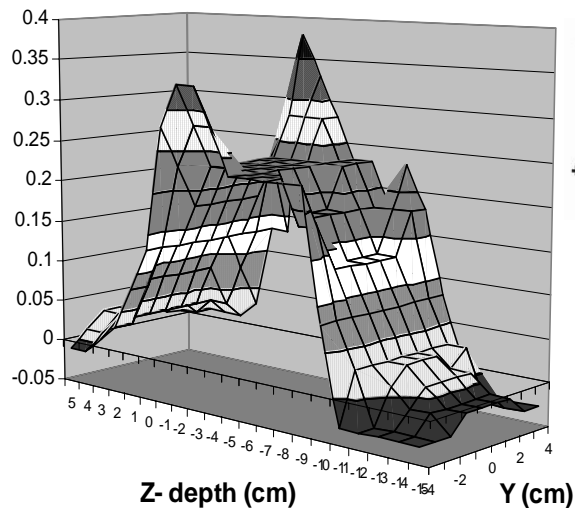
(a) Magnetic field strength at pole separation 10 cm at $X = -7.5$ cm

Magnetic field(T)



(b) Magnetic field strength at pole separation 10 cm at $X =$ Central plane

Magnetic field (T)



(c) Magnetic field strength at pole separation 10 cm at $X = 7.5$ cm

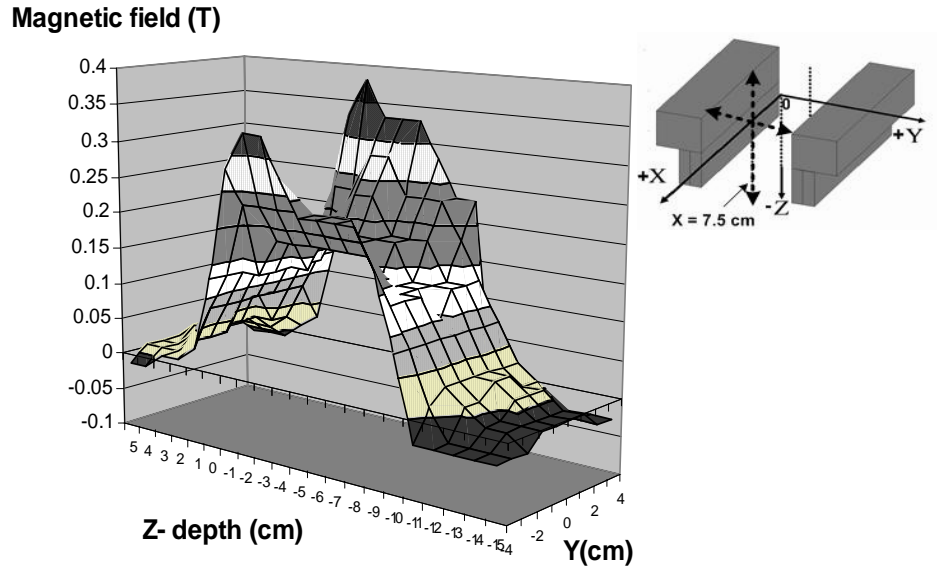


Figure 4.5. (a) The measurement performed at a distance of $x = -7.5$ cm, (b) at the central plane ($x = 0$), and (c) performed at distance of $x = 7.5$ cm away from the central plane.

4.1.4 Simulation and measurement of the magnetic field

The simulated and measured magnetic field strengths from our designed magnetic deflector are shown in Figures 4.6 and 4.7. The measured results show a magnetic field strength of 0.08 T to 0.36 T for the Y-direction component at the central plane and at various distances along the Z-depth axis for the 10 cm distance between the poles in the opposite banks. The measured data near the magnetic bank face have more variation than the measured data at the centre. However near the central region, the magnetic field strength has a smaller variation in the area that the radiation beam passes through as displayed in Figure 4.7.

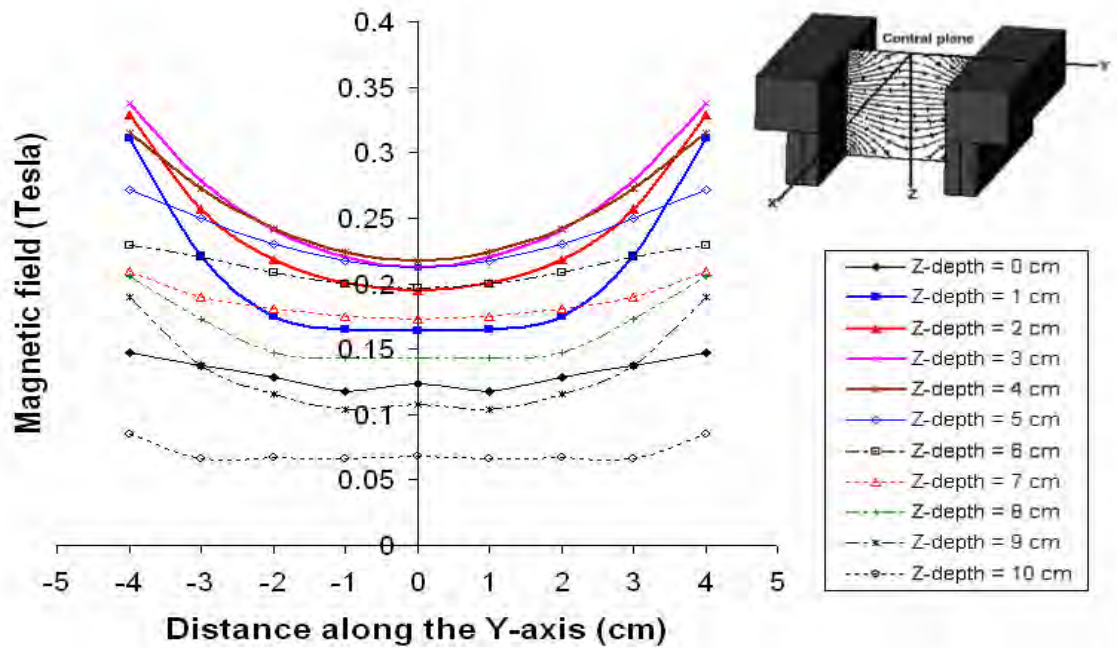


Figure 4.6. Simulation of Y-component magnetic field strength using Vizimag within the 10 cm pole separation along the y-axis on the magnetic deflector central plane. The individual curves show field variation at different depths along the z-axis, down to 10 cm.

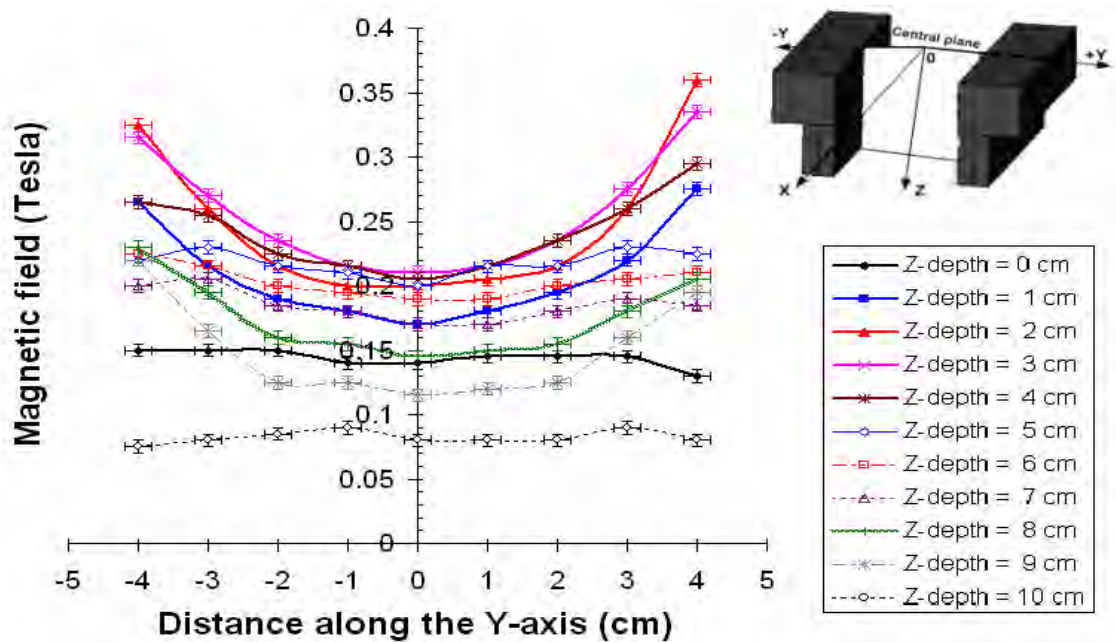


Figure 4.7. Measurement of magnetic field strength along the y-axis on the magnetic deflector central plane within the 10 cm pole separation. Curves represent data taken at different depths along the z-axis, down to 10 cm.

Figure 4.8 displays the Y-component of the magnetic field in the central Y-Z plane slice between the magnet banks as generated by Vizimag, where simulations and measurements were performed, and also a surface mesh plot of the measurements. Superimposed on this is the experimentally measured data for comparison. Errors have been omitted for clarity (with the manual measurement location ± 0.2 cm for the Y and Z-directions and the instrument error ± 0.005 T). Figure 4.9 shows the variation between the Vizimag and the experimentally measured Y-component data of the magnetic field values for the central slice shown in Figure 4.8. To reduce confusion the percentage difference is displayed, and errors have been omitted.

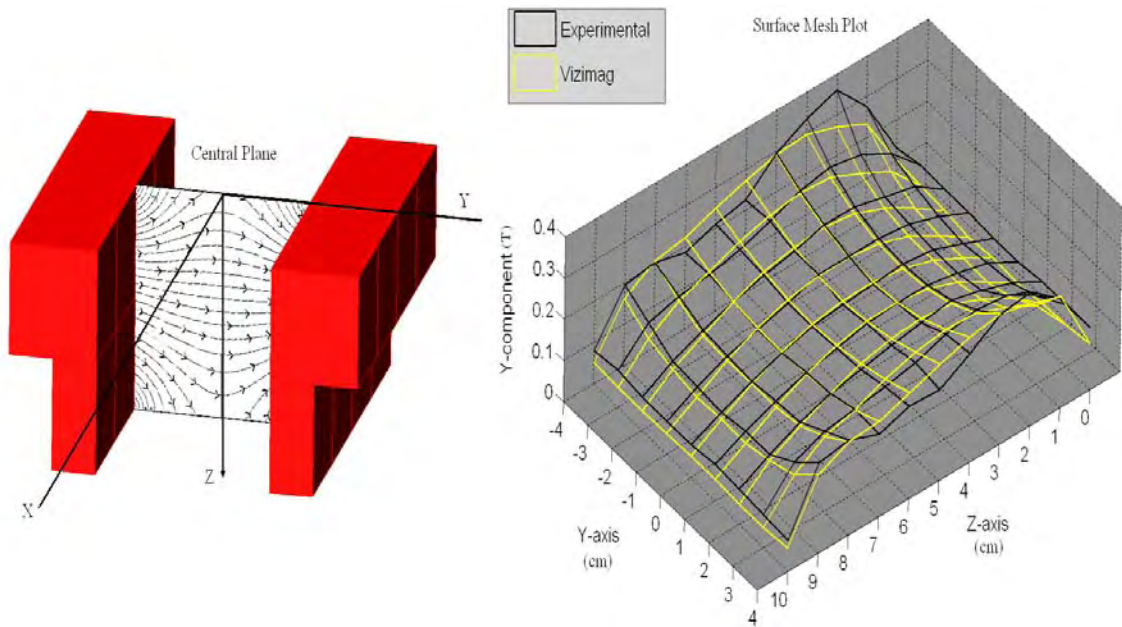


Figure 4.8. The central measurement and simulation plane and a 3D surface mesh plot of the Y-components.

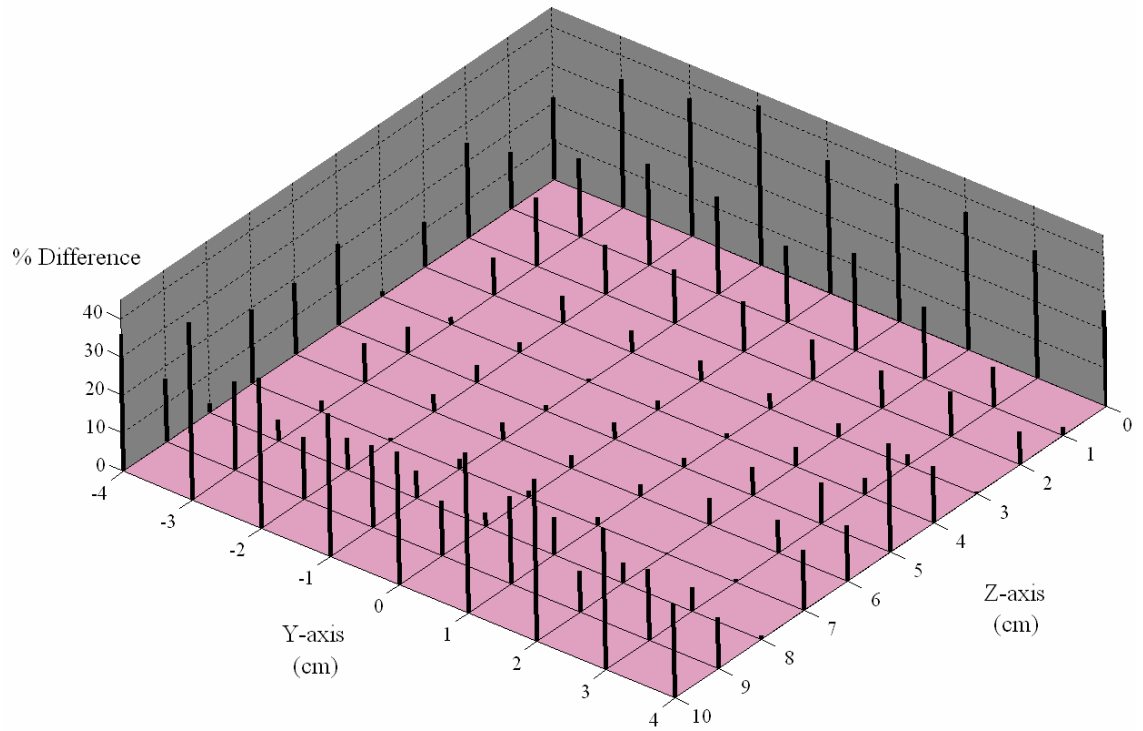


Figure 4.9. Variation between the experimental data and the Vizimag prediction in the central plane.

Good agreement is shown over most of the central region in the area of the radiation treatment field. We have noticed small differences in simulated and measured magnetic field results. The reasons for these small differences could be variations between the clinical magnetic deflector and the simplified simulated deflector. These variations include the aluminium frame to hold the magnets in position and other covering material on the magnetic device. The simulation is only of the magnets and does not include the frame. The difference becomes apparent within the regions above and below the banks of magnets.

The experimentally measured drop-off in field strength is much slower than in the Vizimag simulation. This can be accounted for primarily from the assumption Vizimag makes regarding the size of the magnets. In our case the magnet banks extend far beyond the depth in the simulation, which through the principle of superposition, gives rise to a slower drop-off as compared to a simple cylindrical magnet, such as that modelled in Vizimag. Vizimag is a two-dimensional program calibrated on the

assumption that all magnets have a circular cross section. The analysis is performed on the central section of the objects within 10 % accuracy (Beetson, 2004). However, Vizimag is useful for a visualisation of the magnetic field lines and flux density to identify magnetic field strength with its performance in the initial measurement. Figure 4.10 shows the Y-component of the field experimentally measured in planes other than the central plane, i.e. planes that Vizimag cannot simulate. This is the limitation of Vizimag software and means less accuracy when it is applied to a complex magnetic field. Figure 4.11 demonstrates that there is only about a 20 % reduction in Y-component magnetic field intensity at distances of $x = 7.5$ cm away from the central plane ($x = 0$). Hence a strong field is still achieved over the majority of the central $10 \times 10 \text{ cm}^3$ volume where most of the deflection should occur.

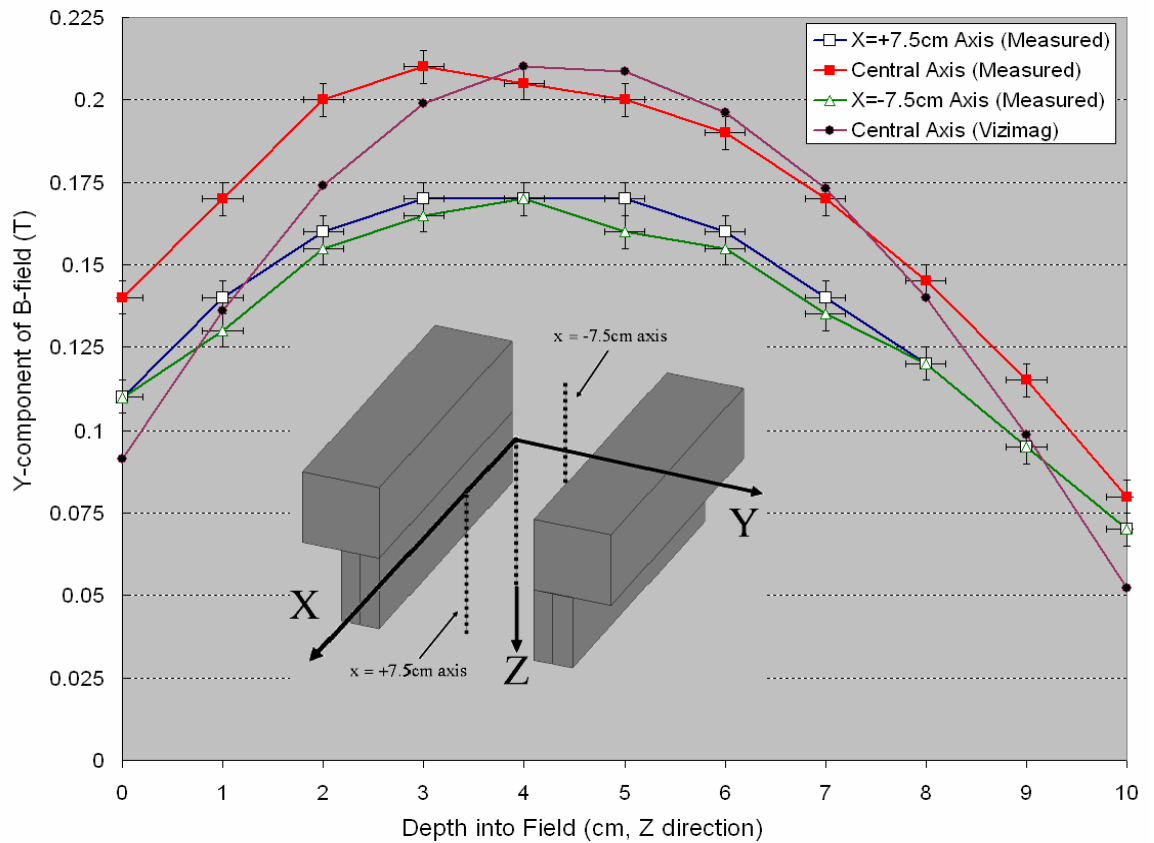


Figure 4.10. Y-direction magnetic field strength between the magnet banks on axes other than the central one.

4.1.5 Dose in the build up region with magnetic deflector device

Dose measurements were performed under the 6 MV x-ray beam of a Varian Clinac 2100C linear accelerator with the NdFeB magnetic deflector device placed in the block

tray position. Photon beam measurements were made using an Attix Model 449 parallel plate ionisation chamber in a solid water phantom (Constantinou et al., 1982) with dimensions of 30 x 30 x 30 cm³. Reproducibility of ionisation measurements for this configuration was found to be ± 0.5 %. The over-response of this type of chamber was calculated to be less than 1% (Rawlinson, 1992) as such no corrections were applied. For the build-up dose measurements at constant SSD 100 cm, thin solid water slabs were taken from below the chamber and placed on the top of varying thicknesses in front of the chamber to measure the build-up doses. In this way, the SSD would remain unchanged during experimental procedure which speeds up measurement process.

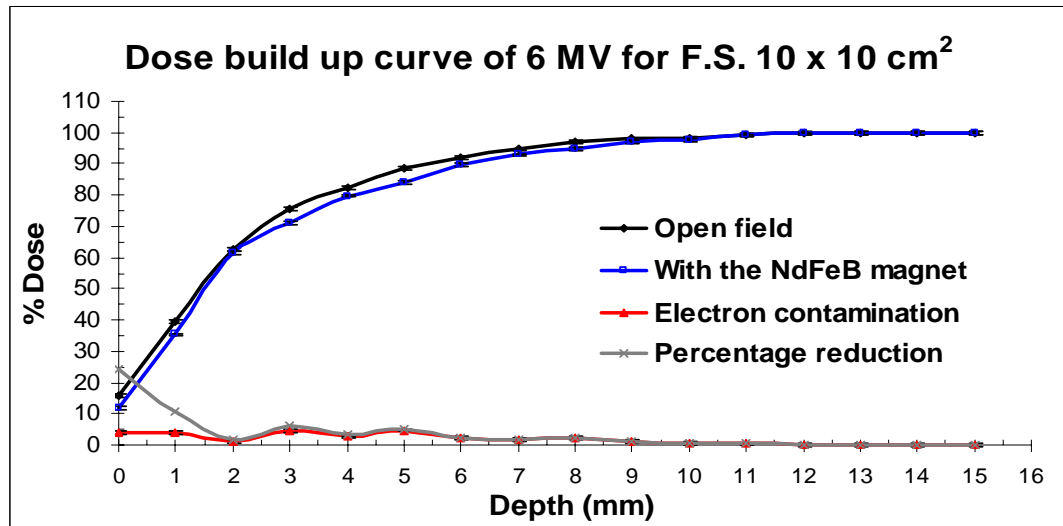
Percentage build up doses were measured on the central axis for 10 x 10 cm², 15 x 15 cm², and 20 x 20 cm² field sizes for open fields and with the NdFeB magnetic deflector device in place. The position of maximum dose for a 6 MV x-ray beam was measured at 15 mm in this configuration. It is known that the major source to contribute the absorbed dose at the surface and beyond this region comes from the electron contamination (Biggs and Ling, 1979). Results from using the magnetic field to reduce electron contamination from the radiation treatment field are presented in Figure 4.11. Electron contamination removed is also shown on the figure and was calculated by subtraction of the measured build-up dose curves of magnetic field results from open field results, with the magnetic deflector field in place, from the build-up dose without the deflector for a particular field size. Percentage surface dose reductions of up to 34 % (of their original values) are seen at the surface for the 20 x 20 cm² field, but it is expected that more reduction would be seen with larger field sizes.

In comparison with a previous work of Butson et al., where they had only the upper two banks of NdFeB permanent magnets at 5 cm distance apart, so that the magnetic field was less able to deflect electrons away from the radiation field, our optimal device with a greater area of effective magnetic field between the poles, is more than 2 times as likely to cause an electron to be deflected. Experimental results show significant decreases in the skin dose with a strong magnetic field still achieved over the larger volume where the most of the deflection takes place. An enhancement of dose is never seen in the irradiated area. Due to the high magnetic field strength in the Y-axis direction, which sets up the deflection process following the Lorentz force rule, the electron contamination is still present in the X-axis direction outside the treated area.

However, material such as a 1.5 cm thick layer of wax could be placed next to the field to absorb the electron contamination during the radiation process.

Although magnetic deflector device is portable and clinically usable for x-ray but the weight of this device after adding more magnets has made attachment inconvenient. If the device was used clinically it would be best suited now to have a specific table carry the magnetic device to the linear accelerator machine for easy insertion in the treatment head.

The definition of the surface dose is related to the depth at which the radiation sensitive layer begins and is at about 0.15 mm underneath the epidermis (Klevenhagen et al, 1991). Reducing the skin surface dose will be useful when a patient would otherwise receive an excessive dose to the skin through normal treatment and subcutaneous tissue, which is often not the site of treatment. Patients are treated with high-energy x-ray beams containing a large number of contaminant electrons from the linear accelerator head; the energy absorbed by the skin is greatly increased and may result in severe skin reactions. That is, the elimination of these doses due to contaminant electrons down to a depth of a few millimetres could be obtained with this magnetic deflector device.



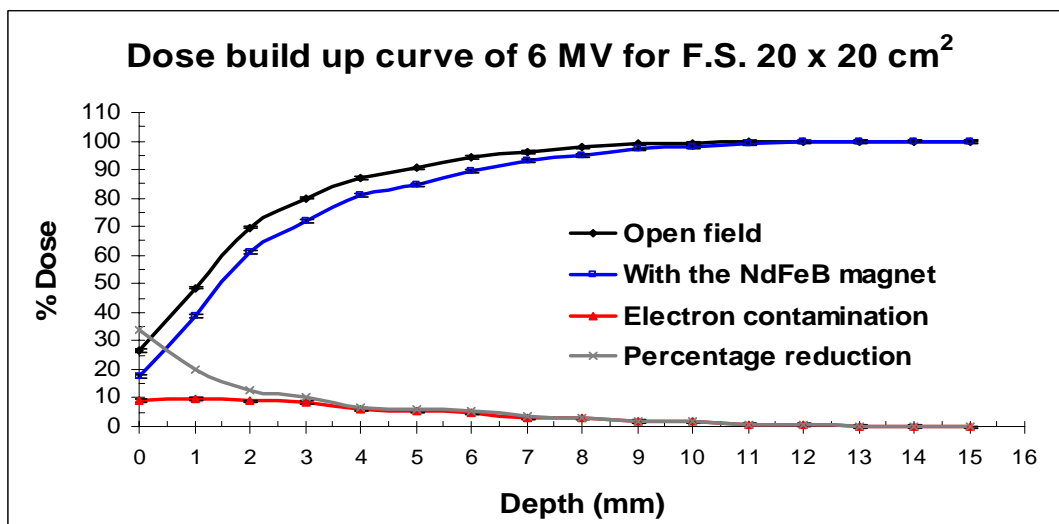
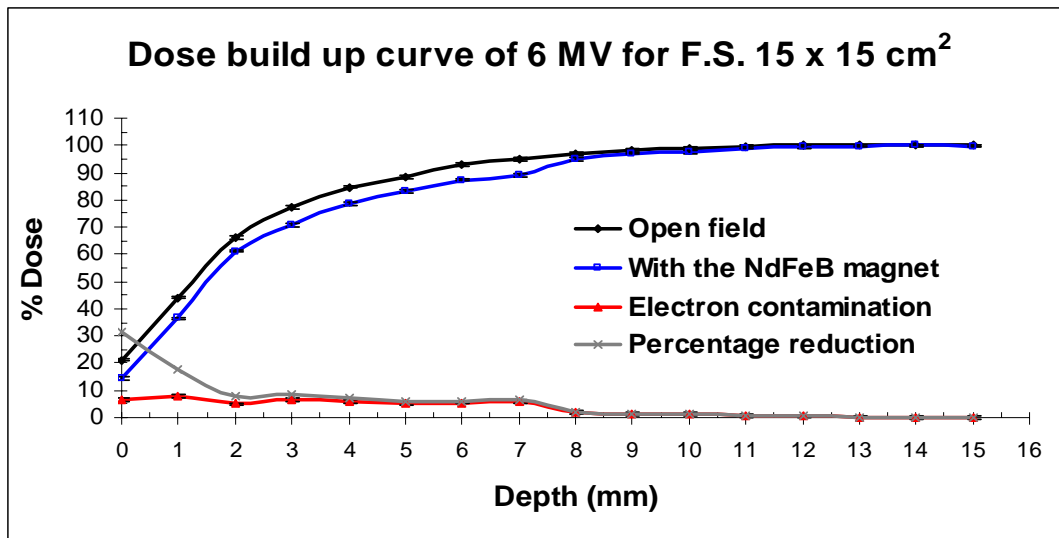


Figure 4.11. Measurements for open field (without deflector) and with the field when the magnetic deflector device in place for 6 MV x-ray beams in the build-up region. Electron contamination is shown for field sizes of 10 x 10 cm², 15 x 15 cm², and 20 x 20 cm².

4.1.6 Conclusions on magnetic fields produced by deflector device

The magnetic field strength generated by the magnetic deflector we have designed has been both measured and calculated using Vizimag 3.0. The two sets of results agree reasonably well in the important central region between the magnet banks where the majority of deflection should occur. The reasons for these differences are assumed to be mainly due to variations between the clinical magnetic deflector and the simplified simulated deflector. Specifically, the aluminium frame that holds the magnets in position and other covering material on the magnetic device is not included in the simulation. The difference becomes apparent within the regions above and below the

banks of magnets where the frame could have the most significant effect. The magnetic field strengths in this improved design mean more uniform magnetic flux densities in the area of interest in the measurement, with the prediction of a greater distance where the device is effective for removing electron contamination occurring in the linear accelerator treatment head. An enhancement of the dose is never observed in the irradiated area, and a percentage reduction of the skin and subcutaneous dose up to 34 % with the NdFeB magnetic device was seen for a 20 x 20 cm² field size. The magnetic field strengths obtained by the magnetic deflector will theoretically give rise to electron deflection radii that should cause the majority of electron contamination to exit the treatment field. The device can be located at any position between the target and the patient, depending on the deflector design, size, and purpose. In theory the ideal location tends to be closer to the patient surface than the x-ray source, as this potentially allows for removal of more contamination electrons, i.e. the only remaining contamination, which arises from the air column between the lowest part of the deflector and the patient surface. A simple magnetic field applied across the beam with its direction perpendicular to the beam axis will generate a sweeping action for any electrons passing through the region as described by the Lorentz Force rule. Such a magnetic field can be set up by a simple arrangement of permanent magnets that are mounted on either side of the x-ray beam. Further work is being performed in an attempt to experimentally confirm the theoretical amount of electron deflection by monitoring the paths of pure electron beams using radiographic film.

4.2 Electron deflection in magnetic field

The deflection and removal of electrons produced by a medical linear accelerator has been attained using a magnetic field device. These contaminants are produced by the interaction of x-rays with materials placed in the linear accelerators beam path during the radiating process. The amount of contamination affects the dose to the skin and subcutaneous tissue. To minimise these reactions and the dose delivered to the build-up region we wish to eliminate or at least minimise electron contamination from the entry beam whilst not affecting any other important beam qualities like depth dose profiles, beam symmetry and beam flatness in the process. Figure 4.12 shows a diagram of the locations of the component modules in the medical linear accelerator machine with the magnetic deflector device.

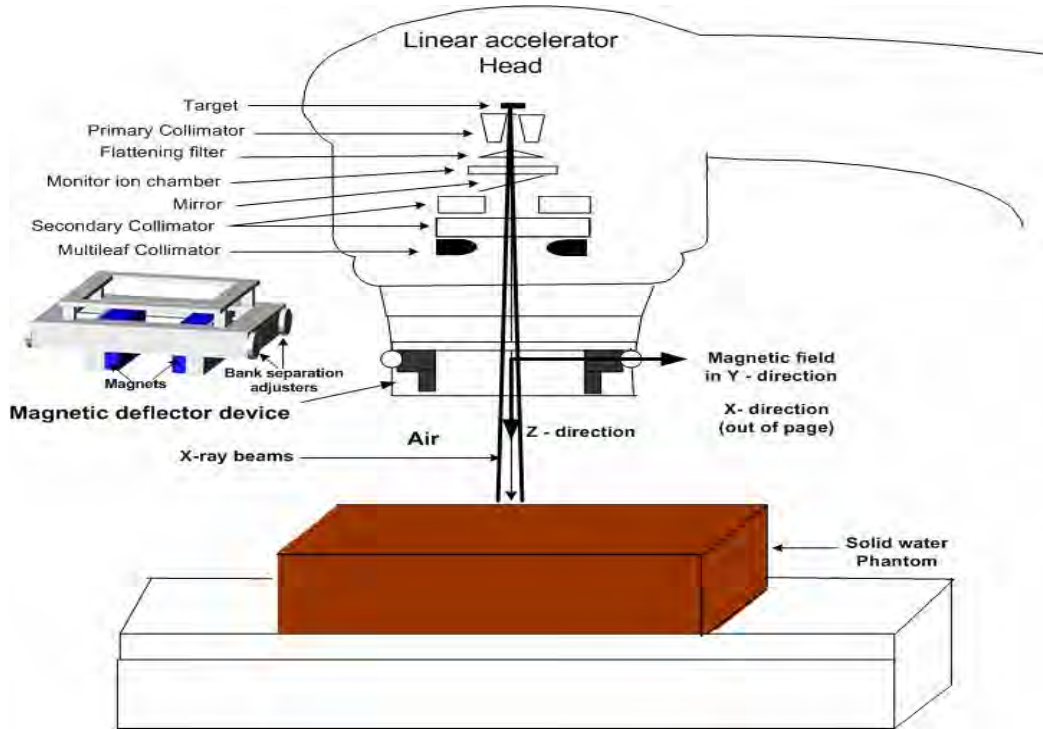


Figure 4.12. Diagram of the locations of the component modules in medical linear accelerator machine with magnetic deflector device.

One advantage of this magnetic deflection technique is that there is no need for a correction factor to account for the beam attenuation i.e. no extra material placed in the beams path to effect delivered dose at depth. The deflection of contaminants via a magnetic field following the Lorentz force rule is explained below.

4.2.1 Analytical Theory

In theory, if an electron has charge (q) and velocity (\vec{v}) moving in a magnetic field (\vec{B}), there is a magnetic force (\vec{F}) on it that is proportional to the magnitudes of (q) and (v). The magnetic force provides the centripetal force necessary for the centripetal acceleration (v^2/r) in circular motion where (r) is the orbital radius. Newton's second law is used to relate the radius of the circle to the magnetic field and the speed of the particle. When (\vec{v}) and (\vec{B}) are perpendicular.

Newton's second law implies $r = \frac{mv_{\perp}}{qB}$.

In our newly designed magnetic deflector device, the magnetic field (\vec{B}) is parallel to the y-axis and in the positive direction (Figure 4.13).

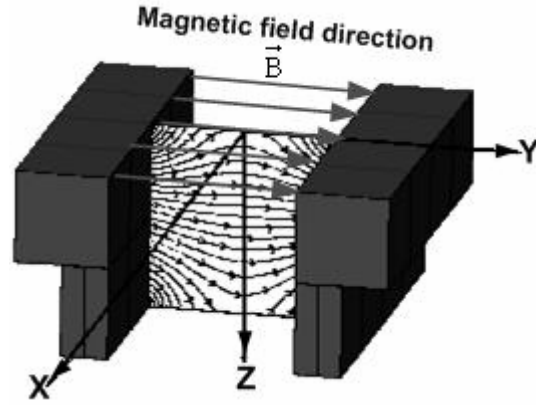


Figure 4.13. Magnetic deflector device with the magnetic field (\vec{B}) parallel to the y-axis.

Then the \vec{B} field can be expressed in terms of

$$\begin{aligned}\vec{B} &= 0\hat{x} + B\hat{y} + 0\hat{z} \\ \vec{B} &= B\hat{y}\end{aligned}\quad (4.1)$$

The equation of motion is

$$\begin{aligned}\vec{F} &= m\vec{a} = q(\vec{v} \times \vec{B}) = q(\dot{x}\hat{x} + \dot{y}\hat{y} + \dot{z}\hat{z} \times 0\hat{x} + B\hat{y} + 0\hat{z}) \\ \vec{F} &= q \begin{vmatrix} \hat{x} & \hat{y} & \hat{z} \\ \dot{x} & \dot{y} & \dot{z} \\ 0 & B & 0 \end{vmatrix} = q((\dot{y} \times 0 - \dot{z} \times B)\hat{x}, (\dot{z} \times 0 - \dot{x} \times 0)\hat{y}, (\dot{x} \times B - \dot{y} \times 0)\hat{z}) \\ \vec{F} &= q((- \dot{z}B)\hat{x}, (0)\hat{y}, (\dot{x}B)\hat{z}) \\ \vec{F} &= qB(-\dot{z}\hat{x}, \dot{x}\hat{z})\end{aligned}\quad (4.2)$$

$$\begin{aligned}\vec{F} &= m\vec{a} = m\left(\frac{d^2r_x}{dt^2}\hat{x}, \frac{d^2r_y}{dt^2}\hat{y}, \frac{d^2r_z}{dt^2}\hat{z}\right) \\ \vec{F} &= q((- \dot{z}B)\hat{x}, (0)\hat{y}, (\dot{x}B)\hat{z})\end{aligned}\quad (4.3)$$

It can be divided into three components

$$m\frac{d^2r_x}{dt^2} = -qB\dot{z}, \quad m\frac{d^2r_y}{dt^2} = 0, \quad m\frac{d^2r_z}{dt^2} = qB\dot{x}\quad (4.4)$$

Integrating these three components

$$\int m \frac{d^2 r_x}{dt^2} = \int -qB\dot{z}, \text{ and } m \frac{dr_x}{dt} = -qBz + C_1 \quad (4.5)$$

$$\int m \frac{d^2 r_y}{dt^2} = \int 0, \text{ and } m \frac{dr_y}{dt} = C_2 \quad (4.6)$$

$$\int m \frac{d^2 r_z}{dt^2} = \int qB\dot{x}, \text{ and } m \frac{dr_z}{dt} = qBx + C_3 \quad (4.7)$$

When $\omega = \frac{qB}{m}$ and solving the equations for velocity components in the x , y , z -directions

$$\frac{dr_x}{dt} = \dot{x} = -\omega z + A_1 \quad (4.8)$$

$$\frac{dr_y}{dt} = \dot{y} = \dot{y}_0 \quad (4.9)$$

$$\frac{dr_z}{dt} = \dot{z} = \omega x + A_2 \quad (4.10)$$

The velocity component in the y -direction along the magnetic field is unaffected. ω is the Larmor angular velocity or the cyclic frequency and the solutions are rearranged in terms of

$$\begin{aligned} m \frac{d^2 r_x}{dt^2} &= m\ddot{x} = -qB(\omega x + A_2) \\ \ddot{x} &= -\frac{qB}{m}(\omega x + A_2) \\ \ddot{x} &= -\omega^2 x + \omega A_2 \\ \ddot{x} &= -\omega^2 x + \omega^2 \left(\frac{A_2}{\omega} \right) \\ \ddot{x} &= -\omega^2 x + \omega^2 a \end{aligned} \quad (4.11)$$

where $a = \frac{A_2}{\omega}$, and therefore the solutions are

$$\ddot{x} + \omega^2 x = \omega^2 a.$$

If $x = a + r \cos(\omega t + \theta)$ where r and θ are constant then,

$$\dot{x} = -r\omega \sin(\omega t + \theta) \quad (4.12)$$

Substituting $\dot{x} = -\omega z + A_1$ gives

$$\begin{aligned}
\dot{x} &= -\omega z + A_1 = -r\omega \sin(\omega t + \theta) \\
z &= \frac{A_1}{\omega} + \frac{r\omega \sin(\omega t + \theta)}{\omega} \\
z &= b + r \sin(\omega t + \theta)
\end{aligned} \tag{4.13}$$

Where $b = \frac{A_1}{\omega}$. This equation describes the charged particle motion in the z -direction.

From $x = a + r \cos(\omega t + \theta)$ and $z = b + r \sin(\omega t + \theta)$, we then combine the two motions to give

$$\begin{aligned}
(x-a) &= r \cos(\omega t + \theta), \text{ so } \frac{(x-a)^2}{r^2} = \cos^2(\omega t + \theta) \\
(z-b) &= r \sin(\omega t + \theta), \text{ so } \frac{(z-b)^2}{r^2} = \sin^2(\omega t + \theta) \\
\frac{(x-a)^2}{r^2} + \frac{(z-b)^2}{r^2} &= \cos^2(\omega t + \theta) + \sin^2(\omega t + \theta) = 1
\end{aligned} \tag{4.14}$$

This equation describes the path of a charged particle projected onto the x - z plane at the centre (a,b) with a radius (r) . When a charged particle moves in a magnetic field, it travels in a spiral around the magnetic field. This means it is radiating a sine-wave field polarised perpendicularly to the magnetic field lines. The radius $r = \frac{mv}{qB}$ and the

angular velocity $\omega = \frac{qB}{m}$, so then $r = \frac{v}{\omega}$. Since an electron moves in a uniform

magnetic field, the equation $\frac{(x-a)^2}{r^2} + \frac{(z-b)^2}{r^2} = \cos^2(\omega t + \theta) + \sin^2(\omega t + \theta) = 1$ represents the electron path of radius r projected onto the x - z plane at point (a,b) , and then the frequency with an electron orbit (ω_g) in the magnetic field is given by

$$\omega_g = \frac{1}{\gamma} \omega_{cycl}^e |B|.$$

Generally, the motion of an electron in a uniform magnetic field in a perpendicular direction to the direction of the magnetic field is always circular movement. Thus contamination electrons produced by the clinical linear accelerator can be considered as relativistic particles with energy (E) and with kinetic energy (KE) so that

$\tan\theta = \frac{t}{b} = \frac{c}{m}$ hence $c = \frac{tm}{b}$. The deflection distance (d) is given by

$$\begin{aligned}
 d &= r - \sqrt{r^2 - t^2} + \frac{tm}{\sqrt{r^2 - t^2}} \\
 &= \frac{\sqrt{E^2 - E_0^2}}{qBc} - \sqrt{\left(\frac{\sqrt{E^2 - E_0^2}}{qBc}\right)^2 - t^2} + \frac{tm}{\sqrt{\left(\frac{\sqrt{E^2 - E_0^2}}{qBc}\right)^2 - t^2}} \\
 &= \frac{\sqrt{E^2 - E_0^2}}{qBc} - \left(\left(\frac{\sqrt{E^2 - E_0^2}}{qBc}\right)^2 - t^2\right)^{1/2} + tm \left(\left(\frac{\sqrt{E^2 - E_0^2}}{qBc}\right)^2 - t^2\right)^{-1/2}
 \end{aligned} \tag{4.18}$$

The deflection distance depends on the thickness (t) of the magnetic field and the radius (r), which comes from the energy of the electron. The deflection angle (θ) is the correlation of the longitudinal distance out of the magnetic field (m) and the lateral distance (d) of an electron beam deflected from the central axis of the beam. It can be calculated by

$$\theta = \tan^{-1} \frac{d}{m}. \tag{4.19}$$

This assumption can produce a first approximation of our clinical situation because the magnetic field strength of our device is not uniform throughout the magnetic field region. It is stronger near the magnetic poles than in the centre of the magnetic field, and the magnetic field strength is not zero outside the magnetic field region. Thus the deflection distance and angle of the electron trajectory that results from using the magnetic field to sweep the electron away from the radiation treatment field could be expected from the measurement results and be in reasonable agreement with the calculation from the above equations. These are important because the magnetic field produces surface dose reductions in the treatment region of a patient under irradiation by photon beam. Thus, experiments to determine the effect of magnetic field from this magnetic deflector device to deflect electrons were carried out.

4.2.2 Electron deflection using magnetic deflection device

Measurements were performed under electron beams of a Varian 2100C linear accelerator with the NdFeB magnetic deflector device put under the block tray location. Experiments were performed with monoenergetic high-energy electron beams from 6 MeV up to 20 MeV that passed through the magnetic deflector device to determine

deflection distances and angles. With a field size of $2 \times 2 \text{ cm}^2$ a monoenergetic electron beam was directed through the magnetic deflector with a pole separation of 20 cm. This field size was achieved by using the collimator jaws of the linear accelerator. No electron cut-out or applicator devices were used during the experiment. The applicator interlocks were overridden. The deflection angle is calculated from trigonometry by the relationship between the longitudinal and lateral distances of the electron beam deflected from the central axis. For the lateral distance, the electron beam deflection from the central axis was measured using Kodak X-Omat V radiographic film placed perpendicular to the beam axis on the surface of a solid water phantom at 100 cm SSD. In the calculation, we used a magnet thickness of 10 cm for a magnetic field strength of 0.15 T and placed the radiographic film 18 cm away from the magnetic deflector (Figure 4.15). The deflection distance was measured as the distance from the central axis of the irradiated field to the centre of an image of the deflected beam. The errors quoted are the deviations in size of the image compared to original $2 \times 2 \text{ cm}^2$ field (Figure 4.17).

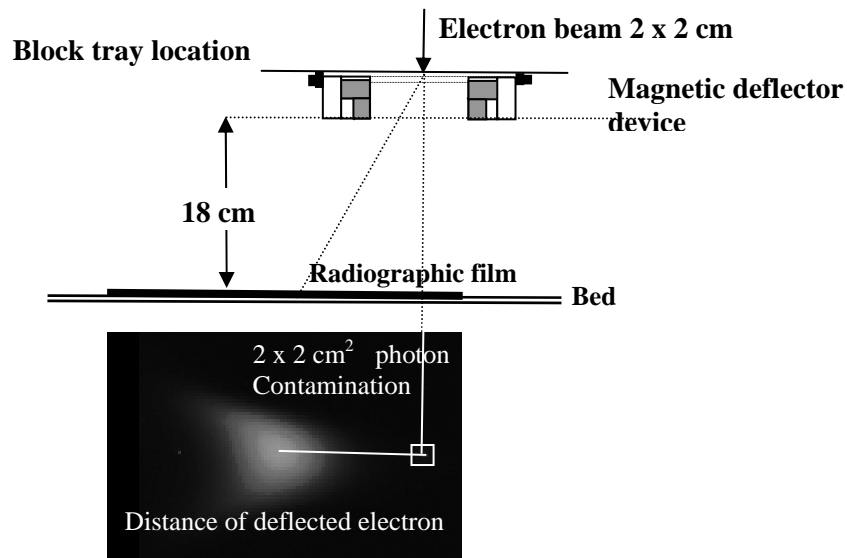
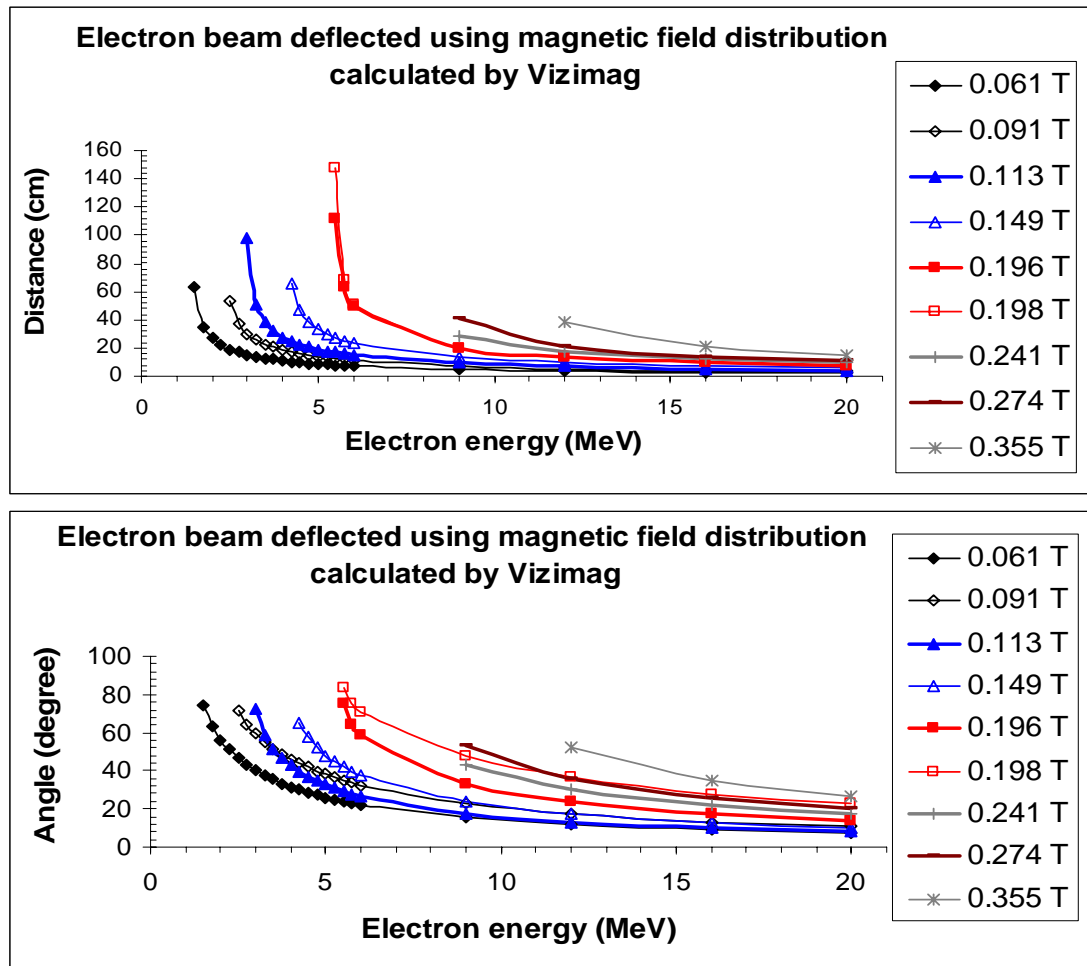


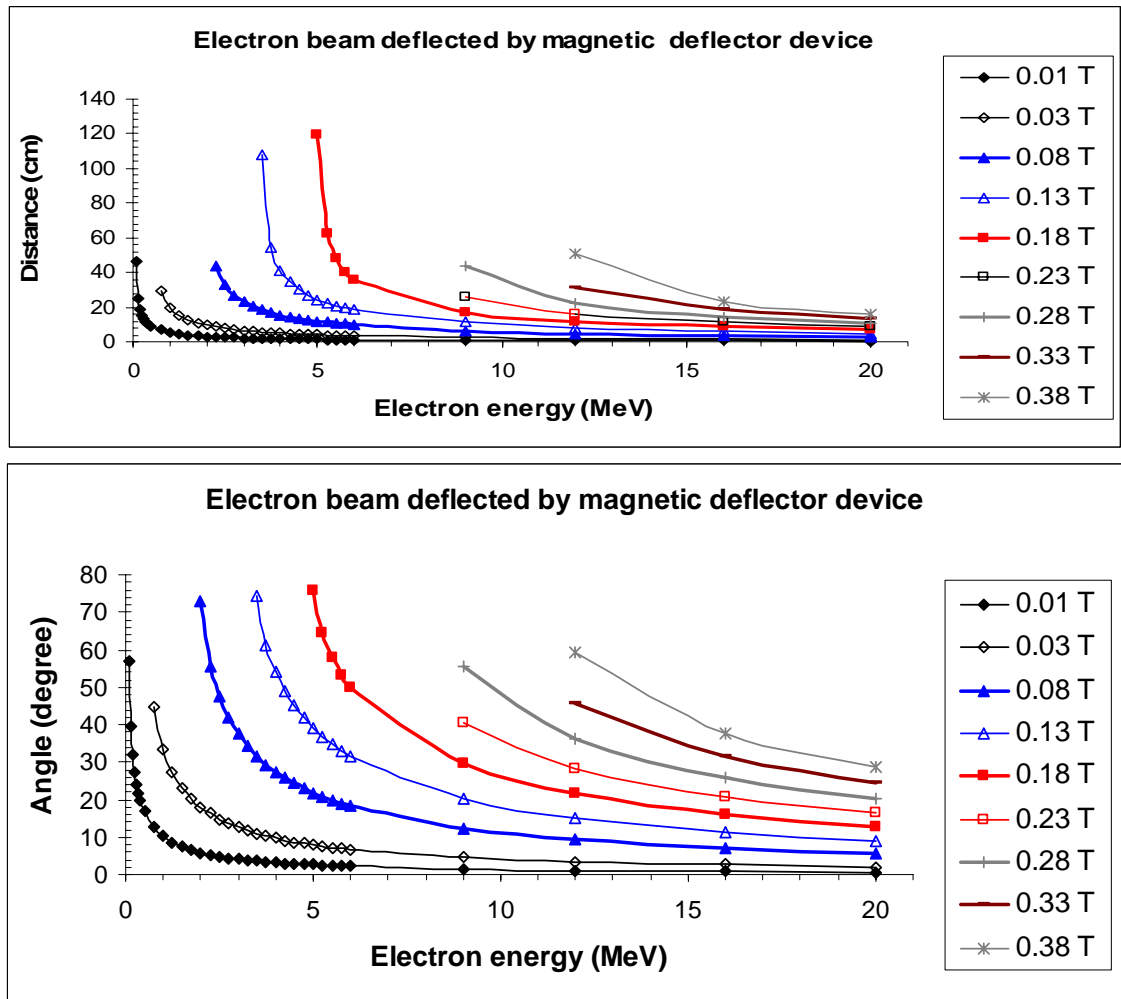
Figure 4.15. The experimental set-up, with the magnetic device attached to the treatment head of the linear accelerator by placement under the block tray location and with the radiographic film placed perpendicular to the beam axis.

The electron energy during measurements of the trajectories in magnetic field was varied from 0.5 to 6 MeV, in the relativistic range. For higher energy, the radius of this

path is larger for constant magnetic field strength. This causes the electrons to be deposited along a straight path not far from the radiated field site. Lower energy electrons and a stronger magnetic field strength allow the majority of electrons to be removed from the beam within a smaller radius. The deflection distance and the angle of the electron beam with energy from 0.5 to 20 MeV in several magnetic field strengths were calculated from the theory with the equation (4.17) and (4.18), and the results are shown in Figure 4.16. (a) and (b). Figure 4.16 (a) shows calculations of the deflect distance and angles using simplified model of uniform magnetic field distribution calculated by Vizimag. Figure 4.16 (b) shows calculations of the deflection distance and angles use a simplified model of uniform magnetic field represented measured data of the magnetic field strength in the volume between the magnet banks of magnetic deflector device.



(a) The deflection distance and angle of electrons as a function of electron energy from 0.5 to 20 MeV in different magnetic field strengths using simplified model of uniform magnetic field distribution calculated by Vizimag.



(b) The deflection distance and angle of electrons as a function of electron energy from 0.5 to 20 MeV in different magnetic field strengths measured data of the magnetic field strength of magnetic deflector device.

Figure 4.16. The deflection distance and angle of electrons as a function of electron energy from 0.5 to 20 MeV in different magnetic field strengths by Vizimag (a), and measured data of the magnetic field strength of magnetic deflector device (b).

Applying this relationship in the magnetic field produced by our magnetic deflector, we can see that electrons entering the magnetic field from directly above the deflector will undergo a deflection. For example, an electron energy of 6 MeV results in a smaller radius of the electron path as the magnetic field strength increases; it means that electron is deflected away from the beam path by a larger distance with a larger deflection angle. If the deflection radius is small enough, then the contamination electrons can be swept totally away from the treatment site. An approximation of our

clinical situation the magnetic field strength of our device is not uniform throughout the magnetic field region. The magnetic field strength is not zero outside the magnetic field region. Thus the deflection distance and angle of the electron trajectory that results from using the magnetic field to sweep the electron away from the radiation treatment field could be expected from the measurement results and be in reasonable agreement with the calculation from the equation (4.17) and (4.18).

Figure 4.17 shows a radiographic image of deflection distances of electrons as a function of the energy of electron beams passing through the magnetic deflector device, with a fixed pole separation to keep the magnetic field strength fixed. The images indicate the spatial trajectories of electron beams from 6 to 20 MeV, with the electrons directed along the central axis perpendicular to the magnetic field which can be seen by the light mark with square x-ray contamination field on lower part of each film. All electron beams have bremsstrahlung contamination in a field size of $2 \times 2 \text{ cm}^2$ that results from interactions between the electrons and materials in the scattering foils, collimators, and air on the way to the radiographic films.

The electrons are swept out of the beam path through the magnetic field, which is much stronger at the magnetic poles than in the centre. Deflection distances were measured directly on the radiographic films as shown in Figure 4.17. The measured and calculated values for deflection distances and angles due to the magnetic field are shown in Table 4.1. As can be seen, electrons were bunched together and swept away from the radiation field by a smaller distance when the electrons were of higher energy. The angle of deflection is decreased when the deflection distances become smaller for higher energy of electrons, such as 12, 16, and 20 MeV at a particular magnetic field strength (Table 4.1). From the experiments, these magnetic field strengths of our magnetic deflector can produce surface dose reductions in treatment regions of a patient under irradiation by photon beams. The results also allow us to predict that all electron contamination with energy up to 6 MeV can be removed over an $18 \pm 6 \text{ cm}$ distance away from the central axis of the treatment field of a 6 MV photon beam with the radiation field size up to $10 \times 10 \text{ cm}^2$. However, in the case of a $15 \times 15 \text{ cm}^2$ field size, this electron contamination is not totally removed from the beam, because the deflection distance is less than the radiation field size. For example, with a 9 MV x-ray beam of $10 \times 10 \text{ cm}^2$ field size, if all electron contamination has less than 9 MeV energy, the smallest deflection angle would

be approximately 33.7° with the deflection distance 12 ± 5 cm, resulting in partial removal of the electron contamination produced above the deflector.

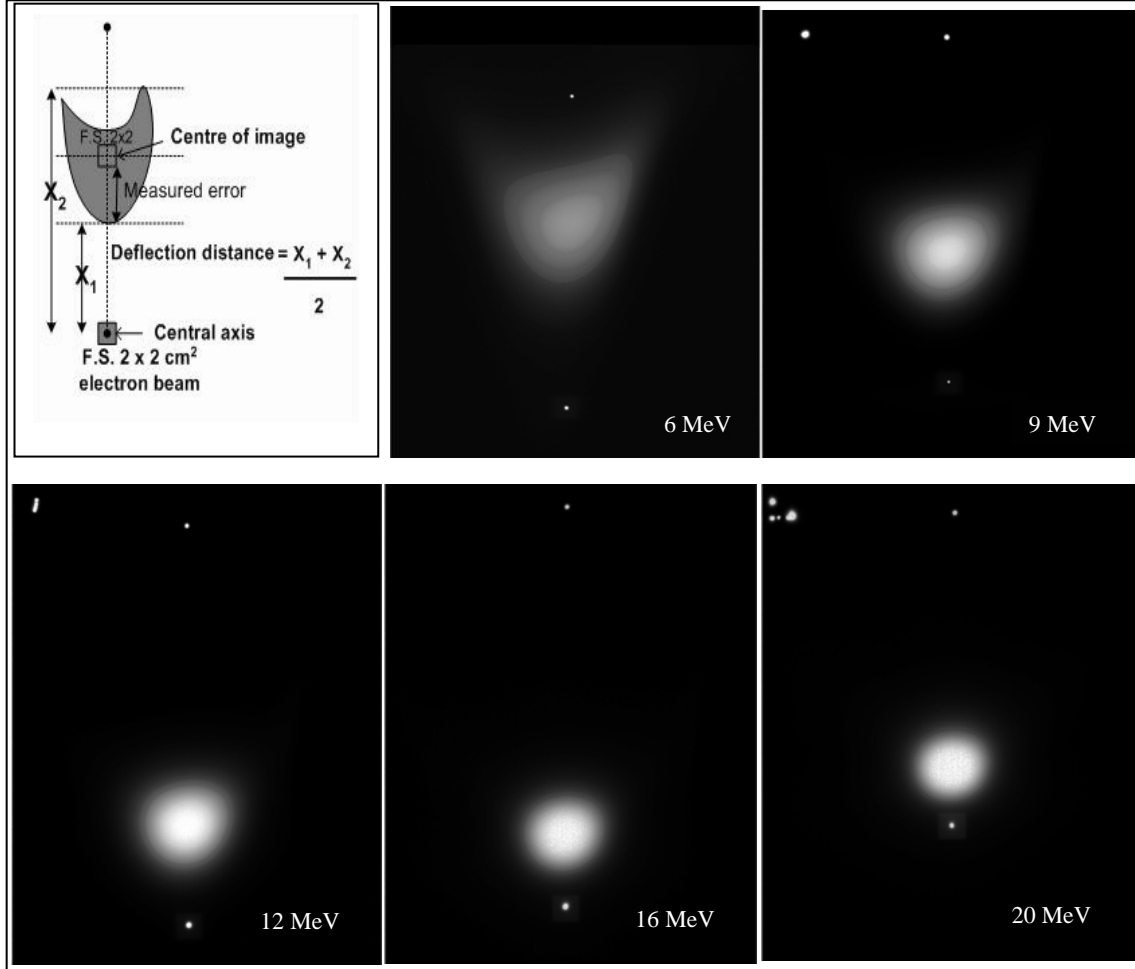


Figure 4.17. Radiographic images used to determine deflection distances of electron beams from 6 MeV up to 20 MeV after passing through the magnetic deflector device.

From Table 4.1, all electrons with energy higher than 12 MeV thus can not escape from the treatment field within these limits of the magnetic field strength for field sizes larger than $5 \times 5 \text{ cm}^2$. It was demonstrated that for the current set-up with the magnetic deflector we were able to remove all scattered electrons from the radiation field in case of photons with energy less than 6 MV and radiation fields less than $10 \times 10 \text{ cm}^2$. However, for radiation fields of $15 \times 15 \text{ cm}^2$ and more, part of the scattered electrons still stay in the irradiation area.

When compared to the calculated assumption for deflection distance, there are small variations between the measurements and calculations in deflection distances of electrons with higher energy. When distances are measured from the film with electron energies of 6 and 9 MeV, the errors are in the form of larger deviations in the size of the image. It is also difficult to accurately determine the spatial displacement from the measured distance on film. The theoretical calculations came from the computation of one point on the central axis of electron beam with a uniform magnetic field strength. Variation between measurement and calculation for higher energy is less than 1 %. Thus the deflection distances and angles of electrons with higher energy can be extrapolated from this in relation to the model and calculations. Assuming that the magnetic field is perpendicular to the direction of the electron velocity then the electron travels in a circular path with the radius depending on the magnetic field strength. However, in reality, our magnetic deflector produced a magnetic field strength that was not uniform throughout the magnetic field region, the magnetic field was weak initially, and the kinetic energy of the electrons was high, so that the electrons only experienced slight deviation.

As the electrons slow down, they also enter into a region of the magnetic deflector that has a strong transverse magnetic field and are therefore diverted into a small radius. This means a large deflection distance away from the radiation beam. In fact, the electron beams that are incident upon the surface are not monoenergetic. If we take into account the multiple scattering of the beam and the fluctuations in the energy, the calculation becomes more complicated. In addition, electron contamination produced by x-ray interactions is lower than the photon nominal energy. If the deflection radius of the electron contamination is small enough then the contamination electrons can be swept totally away from the treatment site and hence not contribute to any skin dose within the treatment zone. Another assumption with simple model is that all electrons are travelling straight down to begin with. In reality this is not true and some electrons will be travelling in a direction against the magnetic deflection direction and will thus receive larger deflection angles to be remained.

Table 4.1. The electron deflection in magnetic field for electron energies ranging from 6 MeV up to 20 MeV.

Electron (MeV)	Deflection Distance (cm)			Deflection angle (°)		
	Measurement	Calculation	Variation between Measurement and Calculation	Measurement	Calculation	Variation between Measurement and Calculation
6	18 ± 6	21.3	3.3	45.0	49.9	4.9
9	12 ± 5	12.2	0.2	33.7	34.1	0.4
12	9 ± 4	8.8	0.2	26.6	26.1	0.5
16	6.8 ± 3	6.5	0.3	20.7	19.8	0.9
20	5 ± 2	5.1	0.1	15.5	16.0	0.5

4.2.3 Conclusion on magnetic deflection

We have proved that a new design of magnetic deflector attached to the accelerator head under an accessory tray holder is sufficient to remove the contamination of scattered electrons from the photon field. The reduction of the skin dose by using magnetic fields is practicable in clinical radiotherapy treatment. These field strengths are enough to deflect all electron contamination with electron energies less than 6 MeV over 12 cm distances from a 10 x 10 cm² treatment area. This technology and the new magnetic deflector that we have developed are of great value for improvement of the clinical outcome of cancer treatment when a patient would otherwise receive an excessive dose to the skin, which is often not even the site of treatment.

4.3 Surface dose measurement in magnetic field

The production of electron contamination from the interaction of x-rays in linear accelerators during the radiation process affects the dose to the skin and subcutaneous tissue, which can be both inside and outside the site of treatment. Because electrons deposit their dose primarily in the skin, due to their low penetration ability, these electrons may then contribute unwanted dose to the patient. Skin dose can vary significantly within the first few millimetres of depth due to the build-up region of high-energy x-ray beams. In this part of the work we study the ability to measure surface dose in two dimensions for open fields without deflection and with a magnetic deflector, which are calculated by an extrapolation technique using radiographic film.

4.3.1 Film dosimetry and calibration method

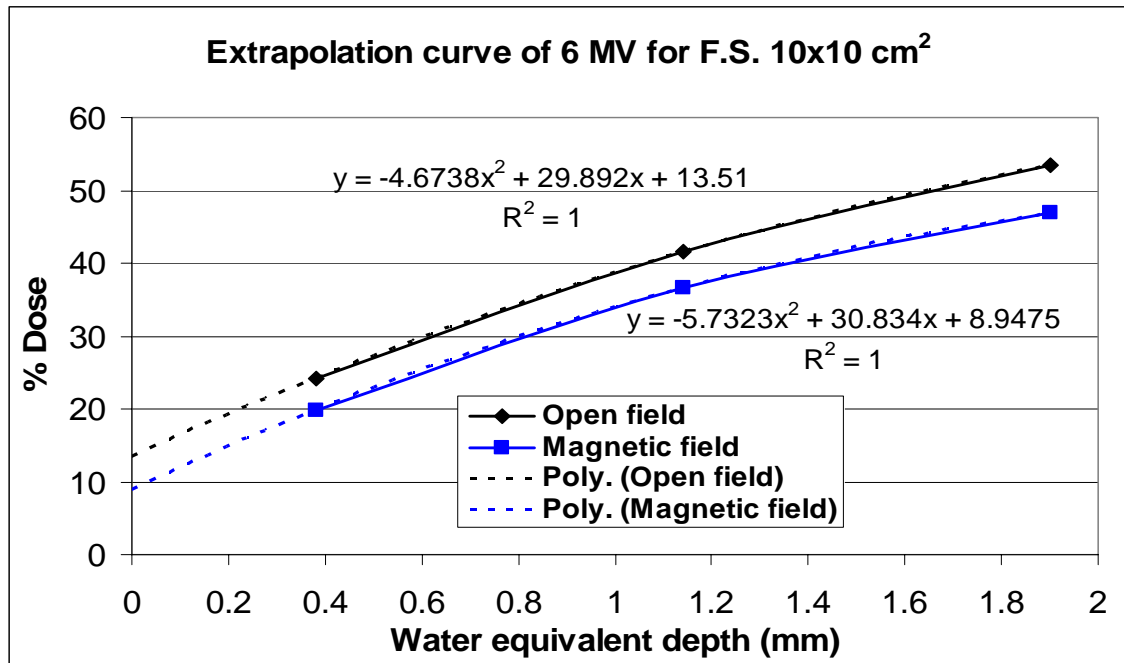
Measurements were performed with a Varian 2100C linear accelerator with the NdFeB magnetic deflector device inserted under the block tray location. Kodak X-Omat V radiographic film was used for the assessment of surface dose. All radiographic films were from the same batch, avoiding confounding effects by inter-batch differences (Bos et al., 2002). A simple extrapolation technique was employed to estimate surface dose by irradiating a stack of radiographic films, which were placed on top of a solid water phantom (Constantinou et al., 1982) at 100 cm SSD. The films were in ready-pack form. The stack of three films were exposed to a 6 MV x-ray beam in field sizes of 10 x 10 cm², 15 x 15 cm², and 20 x 20 cm².

For dose calibration, the calibration films were positioned in a solid water phantom of dimensions 30 cm x 30 cm x 30 cm. The film was positioned at a depth of $D_{\max} = 1.5$ cm for 6 MV x-rays, and doses of 0, 5, 10, 20, 30, 40, 60, 80 and 100 MU were given with the film perpendicular to the central axis of the beam. Field size dose calibration was performed at 10 x 10 cm², 15 x 15 cm², and 20 x 20 cm² to account for effects caused by variations in photon spectrum produced at different field sizes. The effective depth of measurement for our radiographic film ready pack was calculated as 0.38 mm \pm 0.03 mm water equivalent (Butson et al., 2004). The films were processed in an automatic X-Omat processor. Optical density to dose conversions was performed on the experimental films using results supplied from the calibration curve. In each case, the optical density was measured at the centre of each film piece to minimise the effects of variations in measured dose near the edge of the film. Using the optical density calibration function of the Vidar VXR-12 visible light densitometer and Scion imaging software scanner results from H and D curves produced a calibration curve, which was adequately fitted over the range from 5 to 100 MU by a third order polynomial.

4.3.2 Extrapolation Technique

Results from the calibration curves using a third order polynomial function over the dose range of 0 to 100 cGy show an adequate match to delivered dose for each of the three radiographic films. The effective depth of measurement for our radiographic film ready-pack was calculated as 0.38 mm \pm 0.03 mm water equivalent (Butson et al., 2004). The effective point of measurement was assumed to be at the centre of each film, and thus results for each film layer are quoted at half the water equivalent thickness of 0.38 mm with the relative depths of measurement being 0.38 mm on film sheet 1, 1.14

mm on film sheet 2, and 1.9 mm on film sheet 3. Surface dose assessment was performed using an extrapolated dose, whereby dose is extrapolated to 0 cm effective depth with a second order polynomial to perform the optimal calculation, due to the nonlinear nature of photon build-up characteristics (Butson et al., 1999). The extrapolation technique used is illustrated in Figure 4.18. Measurements were performed with radiation field sizes of 10 x 10 cm², 15 x 15 cm² and 20 x 20 cm² with the NdFeB magnetic deflector device of 1.8 T at the centre of the magnetic field of a 20 cm pole separation. These results for open field extrapolated surface dose match well with Attix chamber results. Dose profiles were measured in-plane and cross-plane for open (no deflector) and magnetic field situations. For a field size of 10 x 10 cm² at the surface and at 0.38, 1.14, and 1.9 mm depths, results are shown in Figures 4.19, 4.20, 4.21 and 4.22. For a field size of 20 x 20 cm² at the same depths, results are shown in Figures 4.23, 4.24, 4.25 and 4.26.



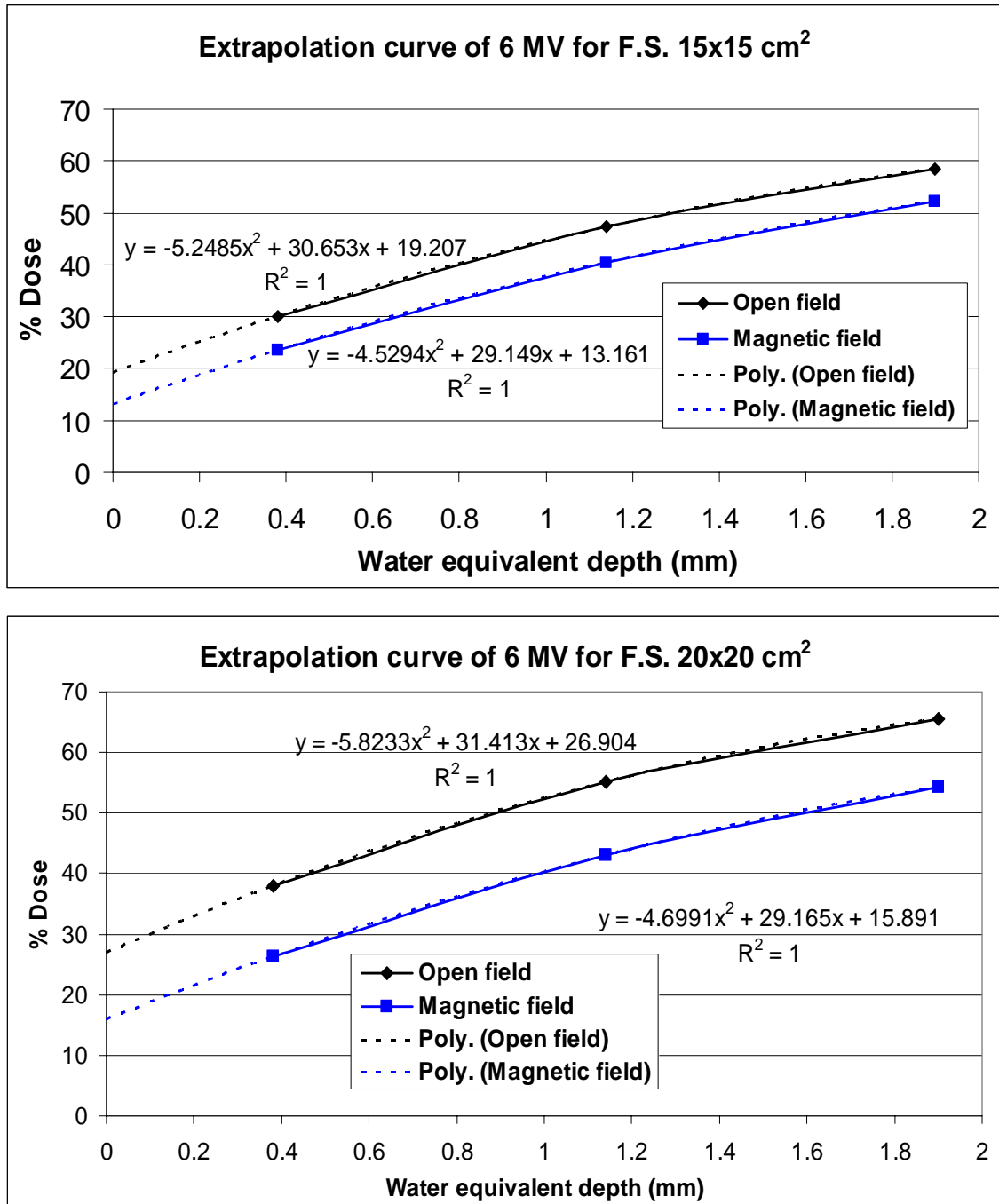


Figure 4.18. Surface dose can be obtained from a second order polynomial extrapolation from radiographic film. Three films are placed in a stack to measure depth dose at water equivalent depth of 0.38, 1.14 and 1.9 mm for field size 10 x 10 cm², 15 x 15 cm² and 20 x 20 cm² with magnetic field and without (indicated by open field symbols).

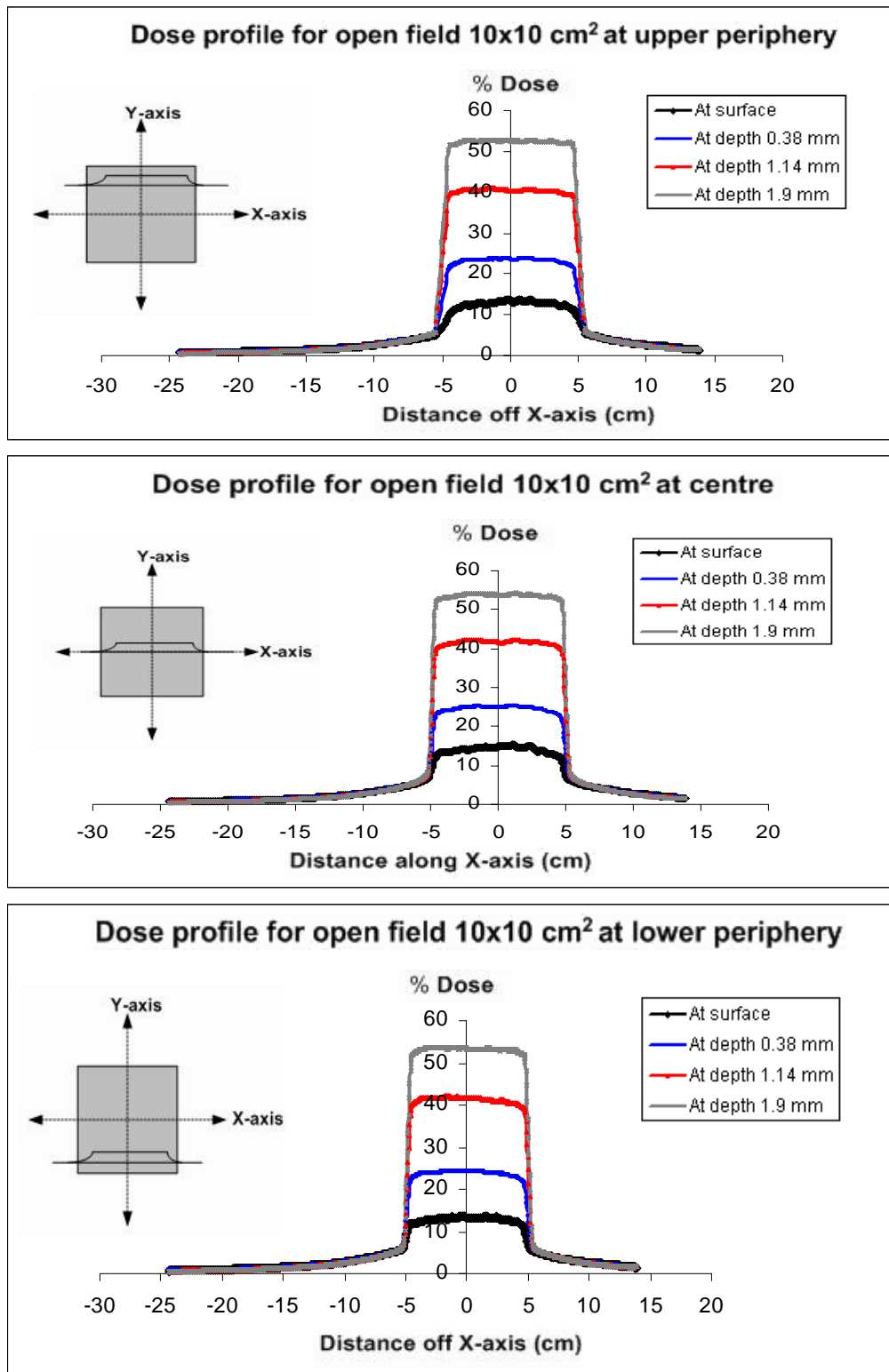


Figure 4.19. Dose profiles measured cross-plane without (open field) magnetic deflection for a field size of 10 x 10 cm² at the surface and at 0.38, 1.14, and 1.9 mm depths.

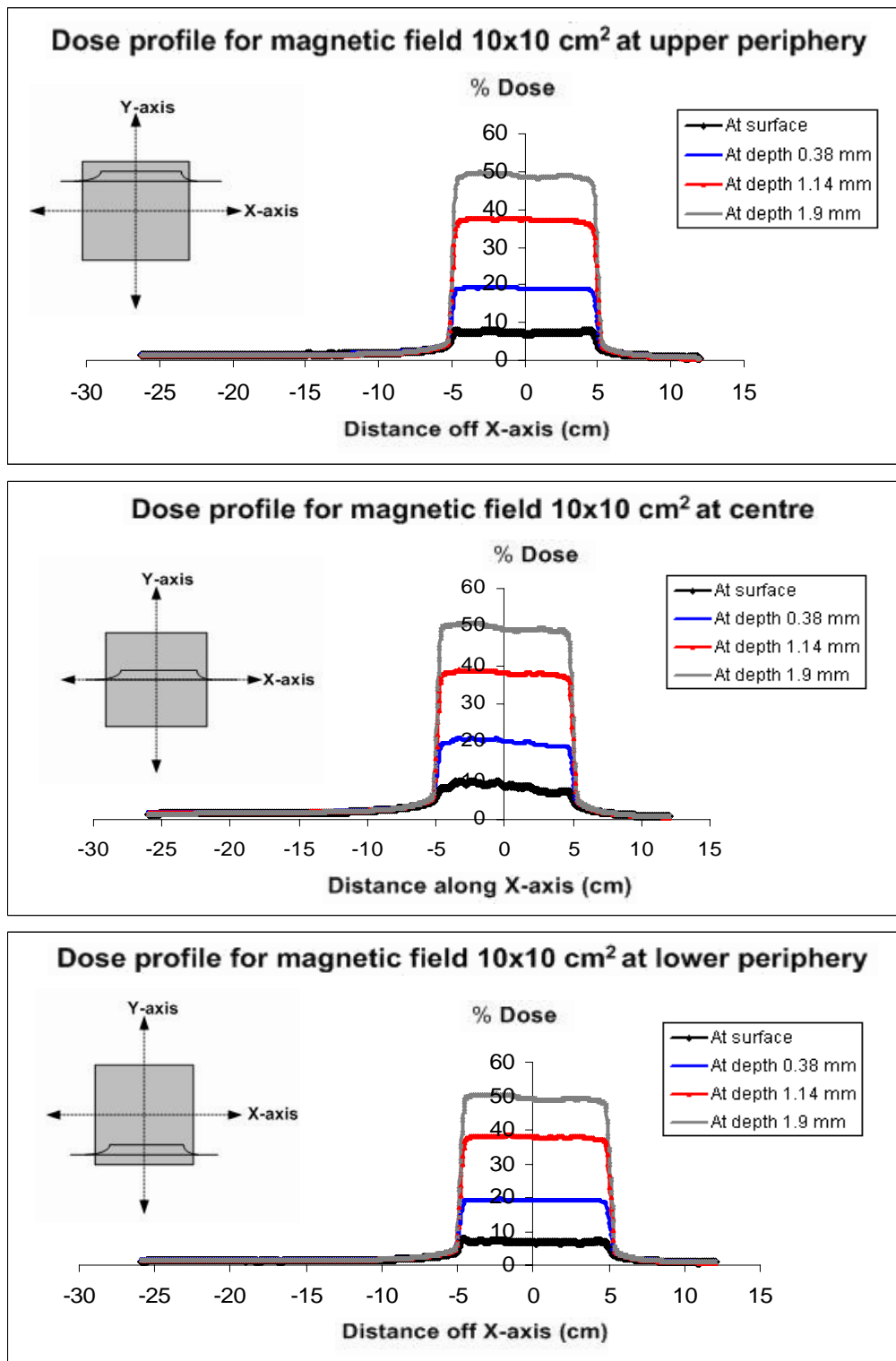


Figure 4.20. Dose profiles measured cross-plane with magnetic deflection for a field size of 10 x 10 cm² at the surface and at 0.38, 1.14, and 1.9 mm depths.

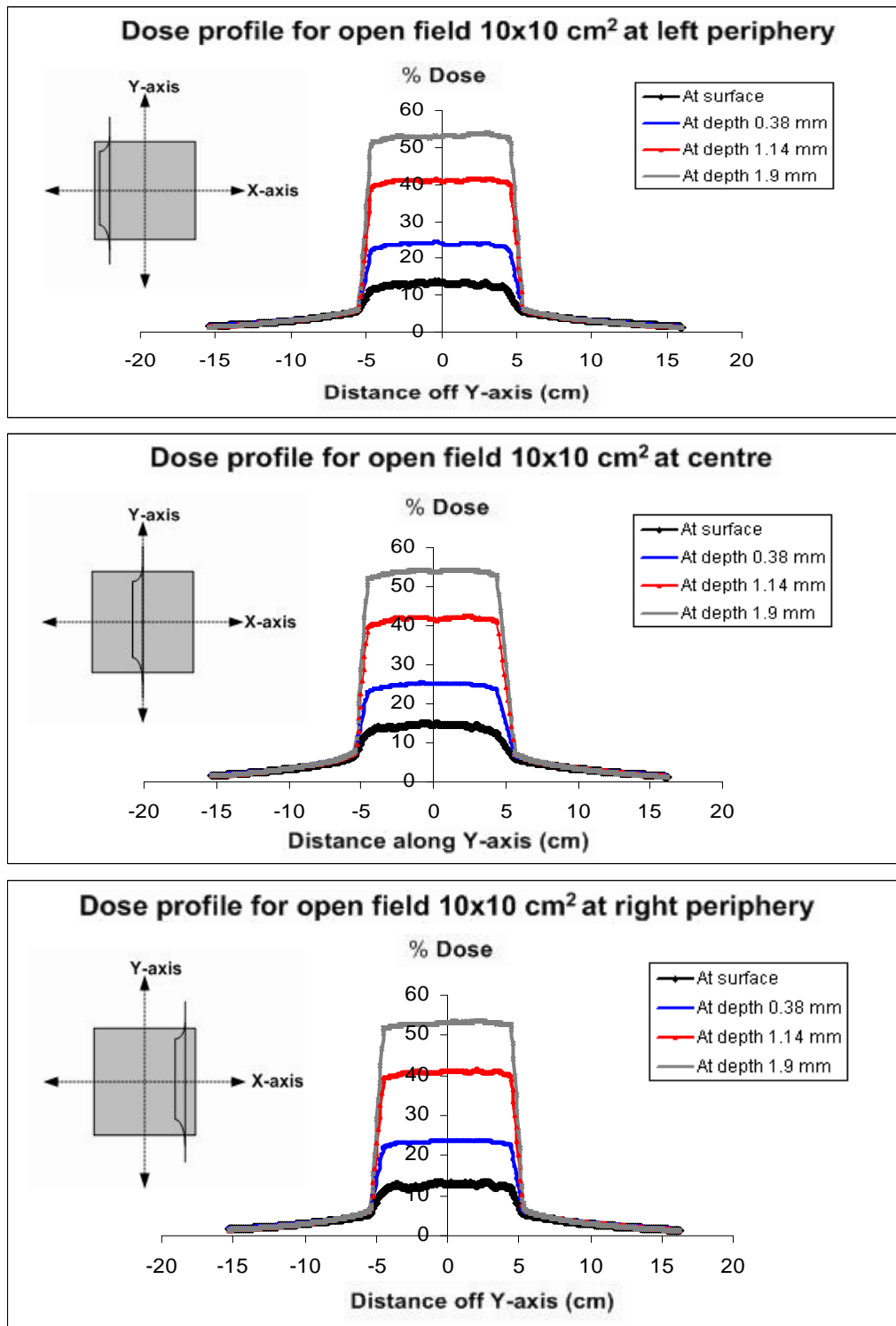


Figure 4.21. Dose profiles measured in-plane without (open field) magnetic deflection for a field size of 10 x 10 cm² at the surface and at 0.38, 1.14, and 1.9 mm depths.

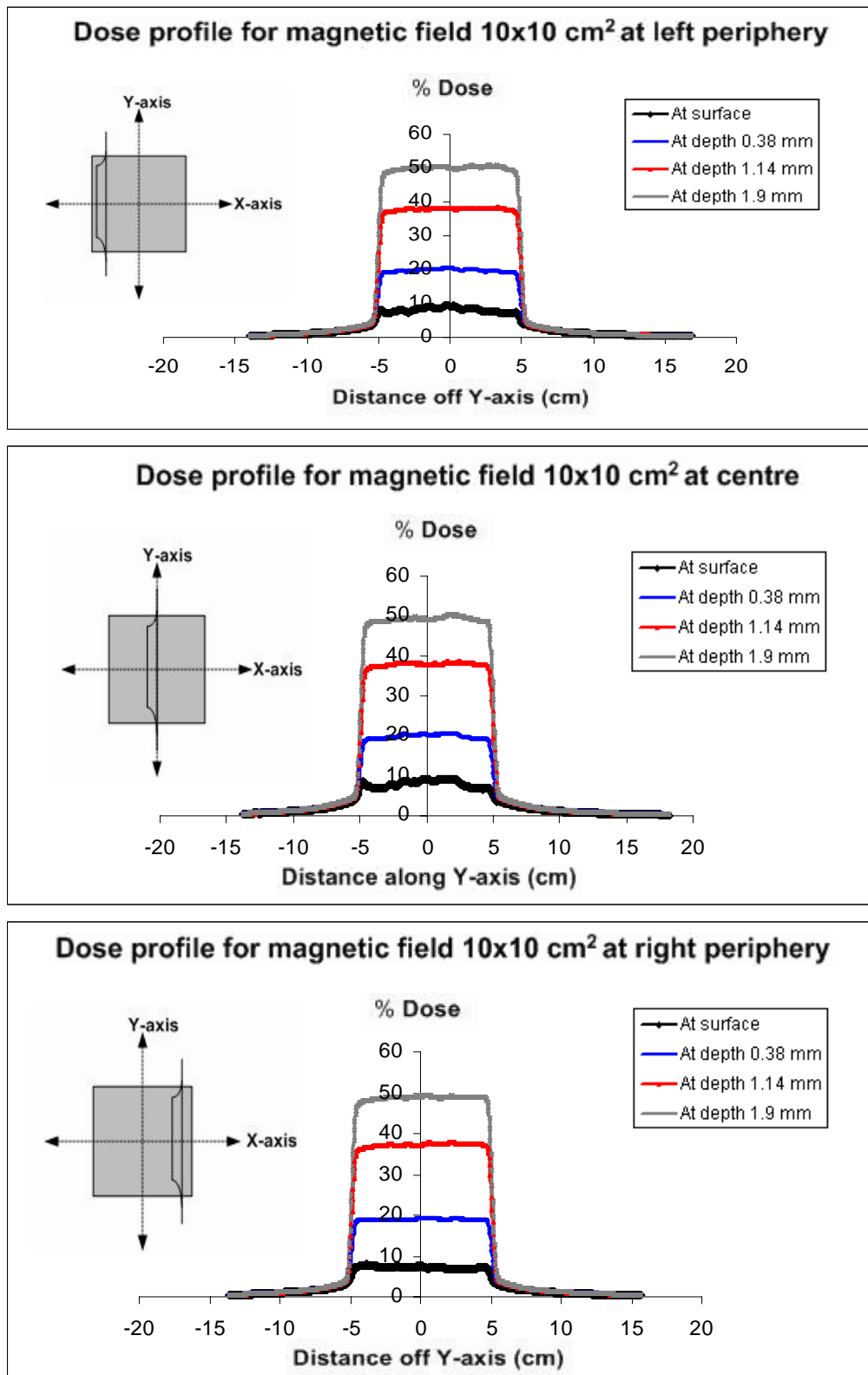


Figure 4.22. Dose profiles measured in-plane with magnetic deflection for a field size of 10 x 10 cm² at the surface and at 0.38, 1.14, and 1.9 mm depths.

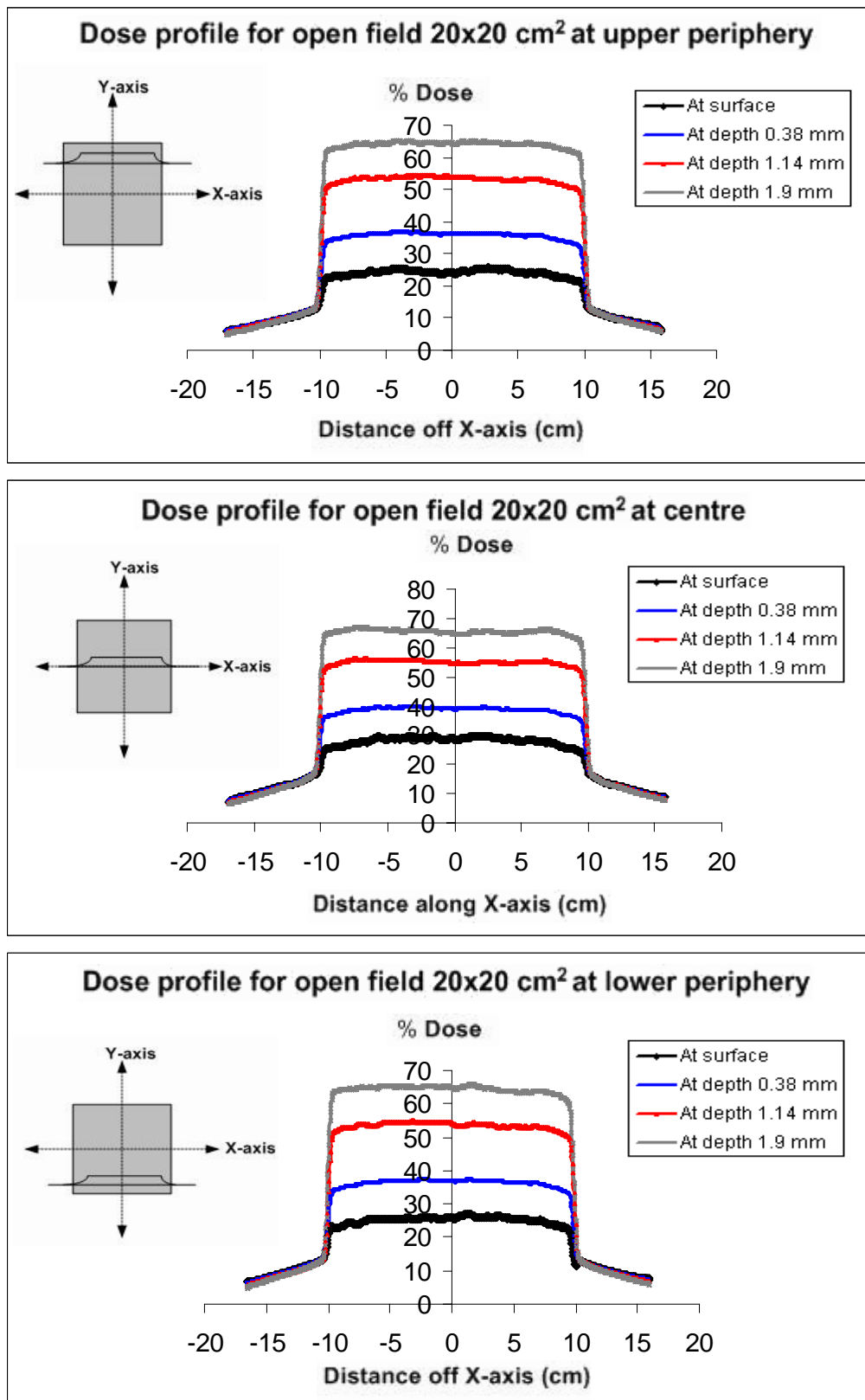


Figure 4.23. Dose profiles measured cross-plane without (open field) magnetic deflection for a field size of 20 x 20 cm² at the surface and at 0.38, 1.14, and 1.9 mm depths.

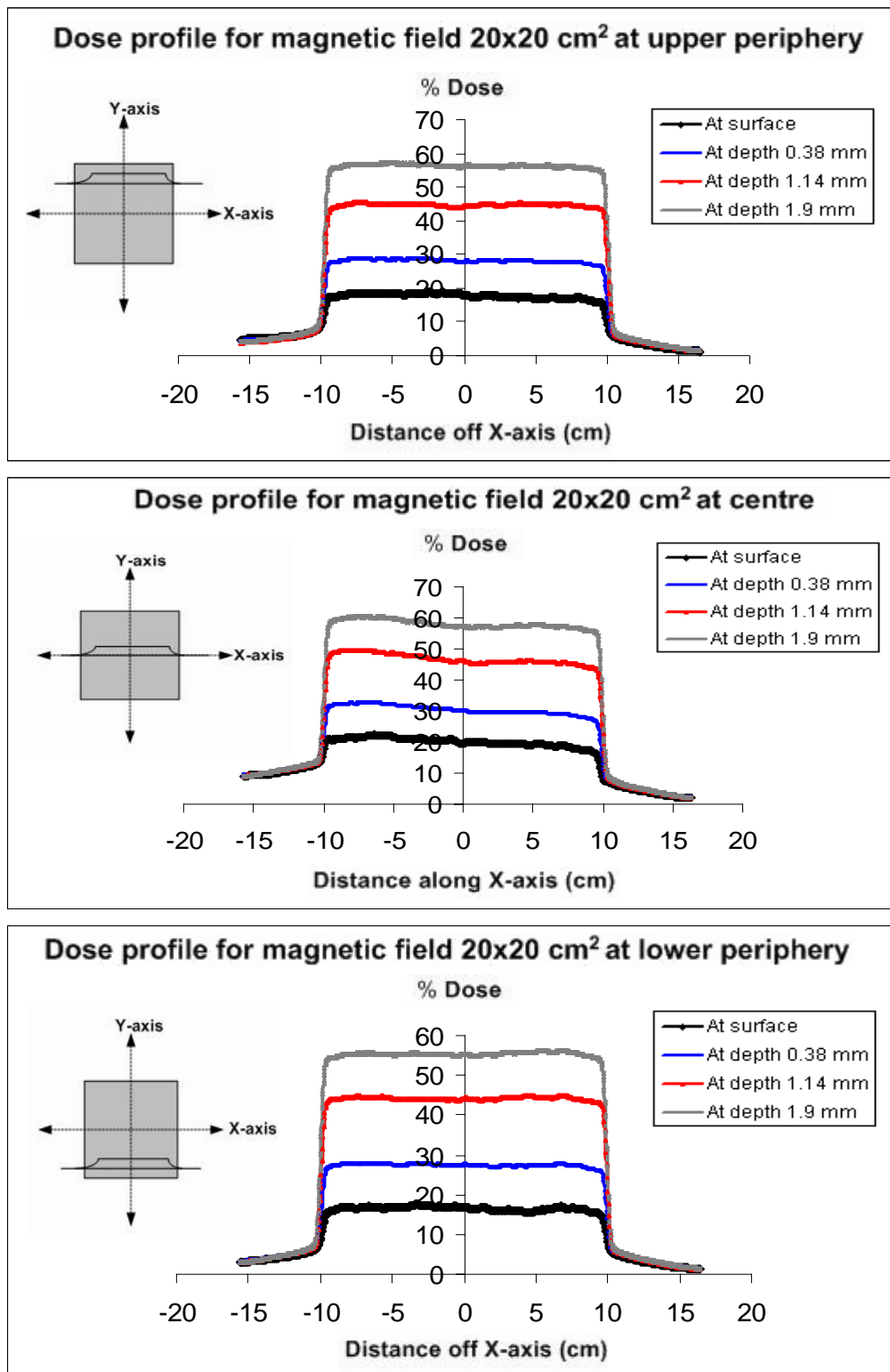


Figure 4.24. Dose profiles measured cross-plane with magnetic deflection for a field size of 20 x 20 cm² at the surface and at 0.38, 1.14, and 1.9 mm depths.

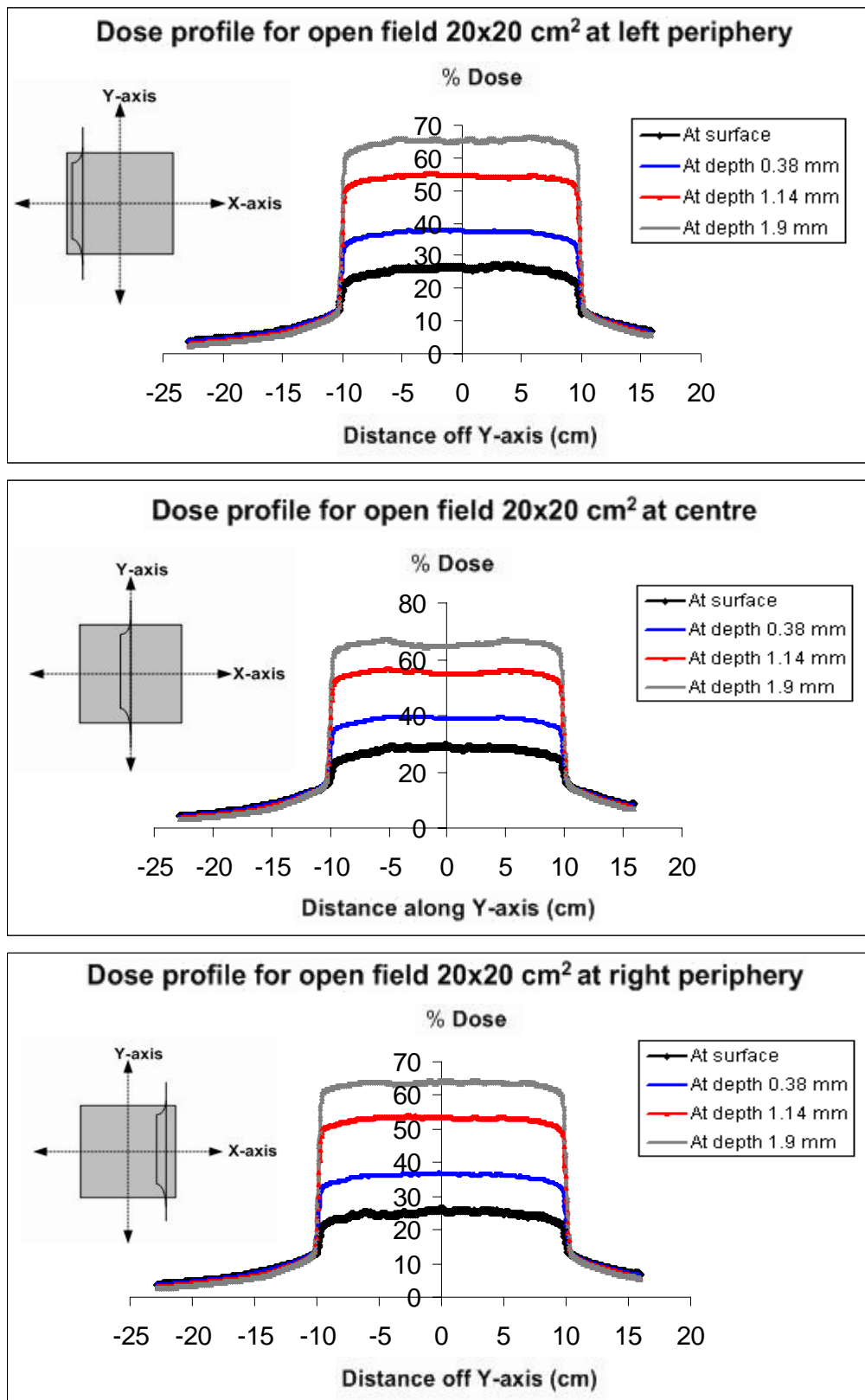


Figure 4.25. Dose profiles measured in-plane without (open field) magnetic deflection for a field size of 20 x 20 cm² at the surface and at 0.38, 1.14, and 1.9 mm depths.

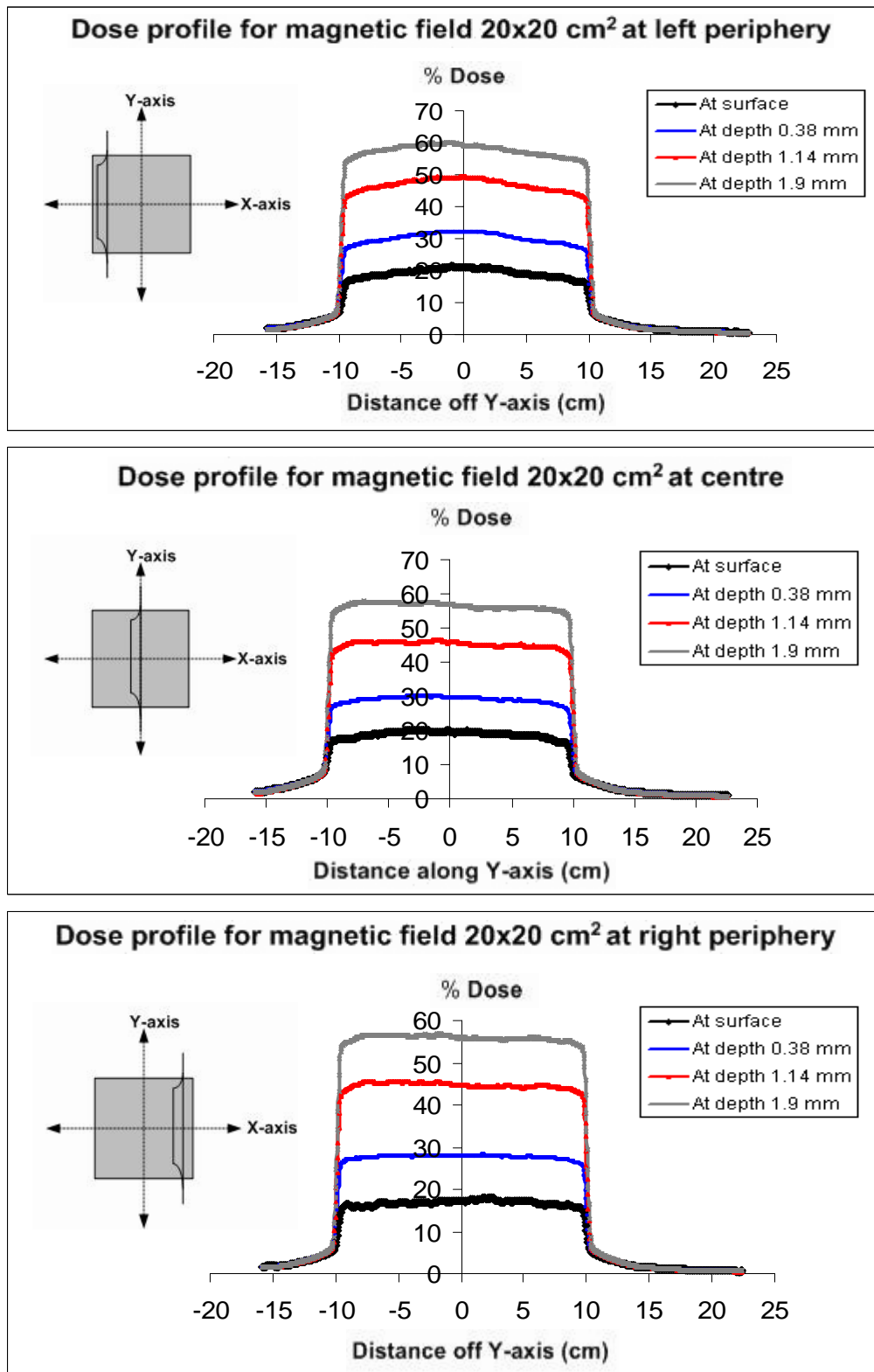


Figure 4.26. Dose profiles measured in-plane with magnetic deflection for a field size of 20 x 20 cm² at the surface and at 0.38, 1.14, and 1.9 mm depths.

4.3.3 Extrapolated surface dose of 6 MV x-rays with magnetic device

Radiographic images from 6 MV x-ray beams with the magnetic deflector are shown in Figure 4.27. Note the presence of ring-shaped electron contamination around the irradiated field size from 10 x 10 cm² to 20 x 20 cm² and that the path of the electron contamination has been swept to the left hand side of the fields at all depths. The magnitudes of these doses are shown in Figure 4.29.

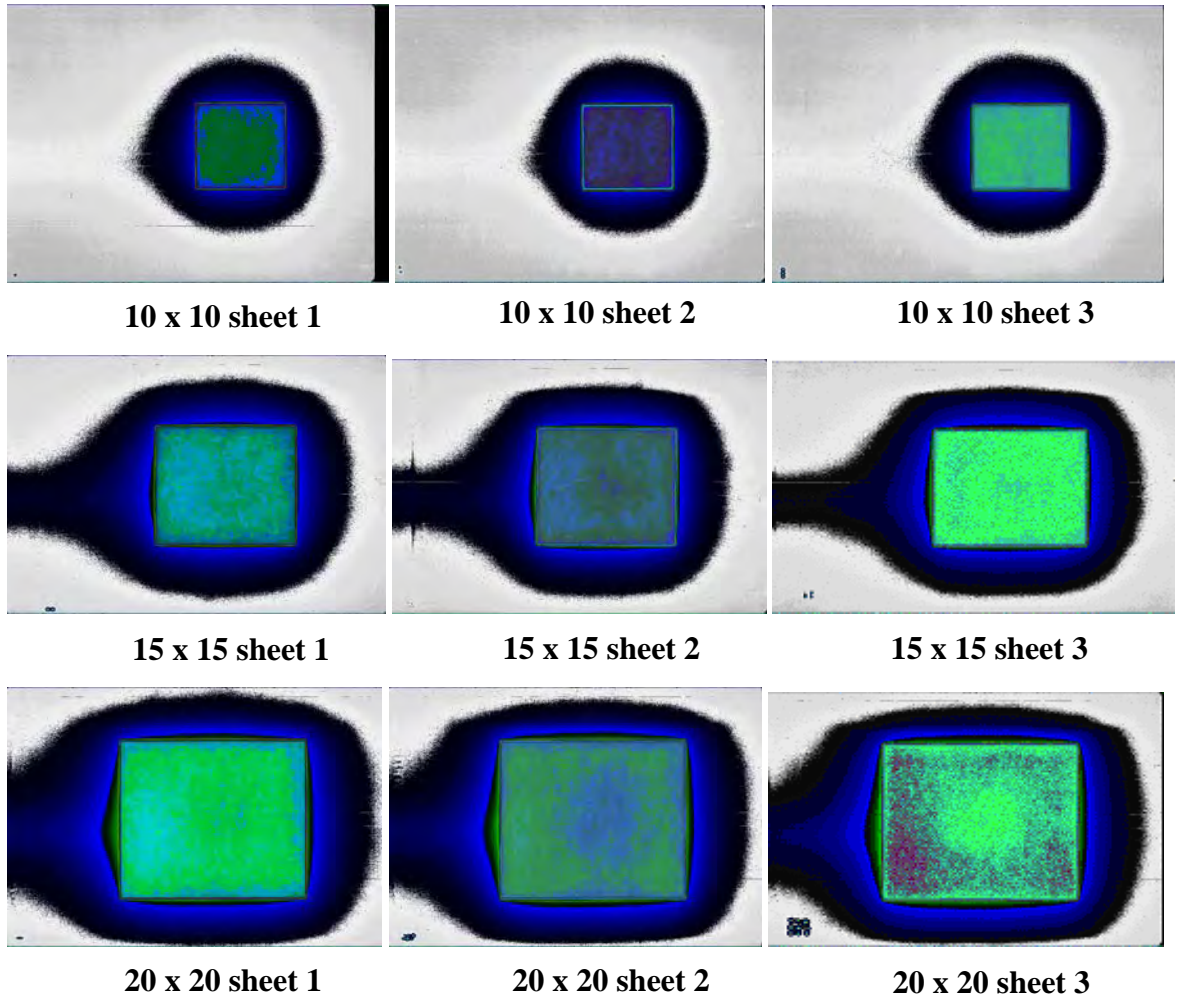


Figure 4.27. Radiographic images of 6 MV beams of the three layers of film for field sizes of 10 x 10 cm², 15 x 15 cm², and 20 x 20 cm² illustrate that the electron contamination is swept away by the magnetic field.

Surface dose analysis is obtained from an extrapolation curve with a second order polynomial to perform the optimal calculation due to the nonlinear nature of the photon build-up characteristics (Butson et al., 1999). Figure 4.28 shows the extrapolation

technique used where layers of films are employed to produce a central axis percentage depth dose measurement, which is normalised to 100 % at $D_{\max} = 1.5$ cm. As can be seen, there is an increase in dose through the three layers of film due to the photon build-up characteristics of x-ray beams and also dose contributed by electron contamination in this region. The accuracy of our measurements with radiographic film are from ± 3 % to ± 7 %, obtained from a combination of errors correlated with the film calibration method, variations in the data set, and non-linearity in the depth dependence of the build-up dose (Butson et al., 2004). A series of extrapolated surface doses for 10×10 cm², 15×15 cm², and 20×20 cm² of 6 MV x-ray field sizes at the central axis with magnetic field are 9 ± 7 %, 13 ± 3 %, and 16 ± 4 %, respectively.

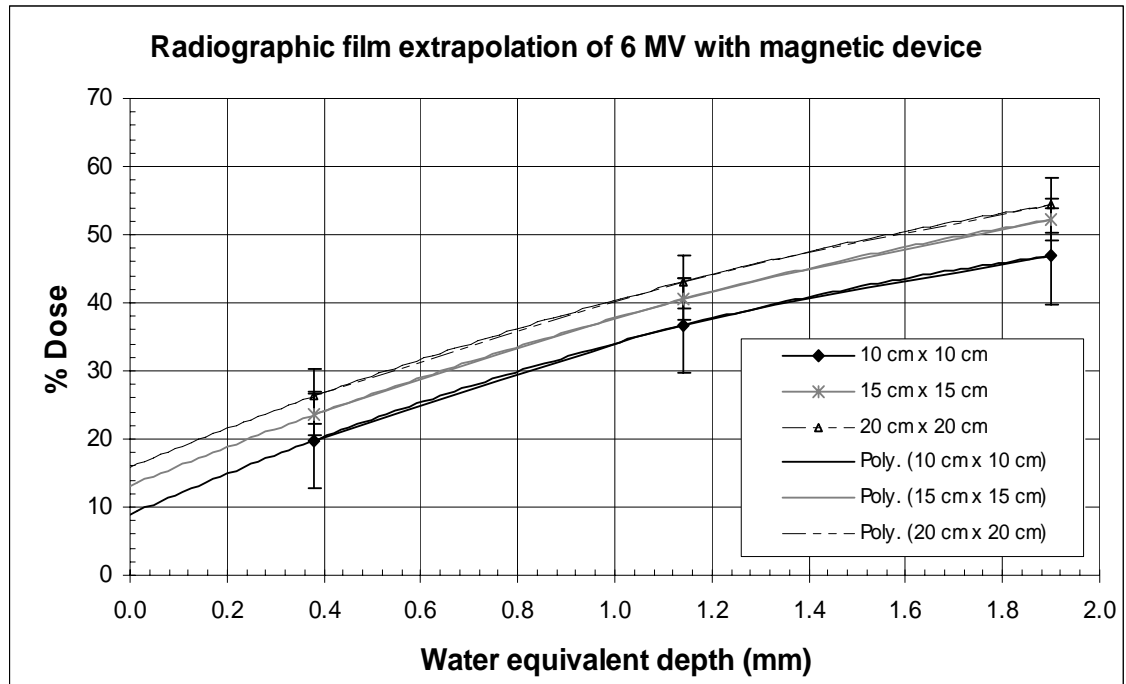


Figure 4.28. Surface dose can be obtained from a second order polynomial extrapolation from radiographic film. Three films are placed in a stack to measure depth dose at water equivalent depths of 0.38, 1.14, and 1.9 mm for field sizes of 10×10 cm² (± 7 %), 15×15 cm² (± 3 %), and 20×20 cm² (± 4 %). Results were obtained with the magnetic deflector in use of a 20 cm pole separation for the magnetic field strength of 1.8 T at the centre of the magnetic field.

Figures 4.29, 4.30 and 4.31 show dose profiles for the extrapolated surface dose with $10 \times 10 \text{ cm}^2$, $15 \times 15 \text{ cm}^2$, and $20 \text{ cm} \times 20 \text{ cm}^2$ field sizes, respectively with and without the magnetic field. Scans were performed along the x-axis (cross-plane) of the beam from the central axis. Results showed a reduction in surface dose along the x-axis in the presence of magnetic field, with a different magnitude of dose from the central axis when compared to the open field situation. As can be seen, the surface dose in the regions on the negative side of the x-axis is higher than on the positive side. This is due to the high magnetic field strength in the +y-axis direction that sets up the deflection process via a magnetic field following the Lorentz force rule, hence the strong deflection path occurs for negative distances along the x-axis. This reduction is increased for larger field sizes, but the field strength attainable is not large enough to remove all contamination from the treatment field. However, an enhancement of dose is never seen in this treatment area. The electron contamination is still on the negative side of the x-axis outside the treated area, so material such as a thin sheet of lead or a 1.5 cm thick layer of wax could be placed next to the treatment field to absorb the electron contamination during irradiation.

Figures 4.29, 4.30 and 4.31 also show the results on surface dose along the y-axis (in-plane) for open fields (no deflector) and magnetic fields, using the same irradiation field sizes. Results showed that a surface dose along the y-axis was still reduced in the presence of our magnetic deflector. For our magnetic deflector to set up the deflection process in our design there is a high magnetic field strength in +y-axis direction, with a very small force to deflect electron contamination in this direction. When electron contamination moves parallel to the magnetic field direction, no deflection of electrons occurs. As can be seen, the shape of the surface dose profile is quite symmetrical along this y-axis distance, especially for field sizes of $15 \times 15 \text{ cm}^2$ and $20 \times 20 \text{ cm}^2$.

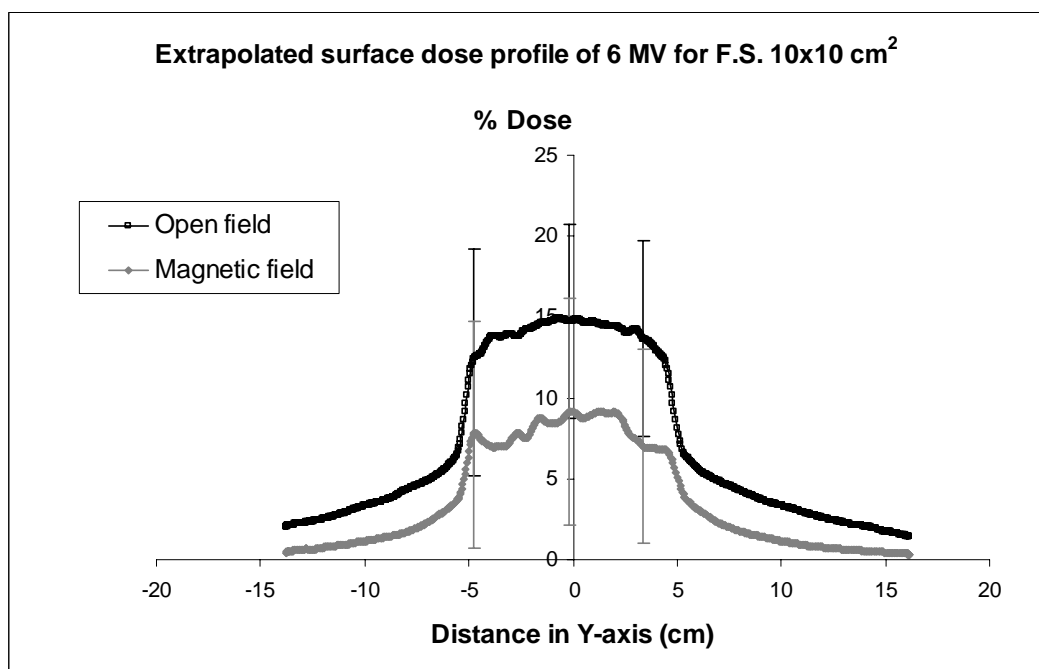
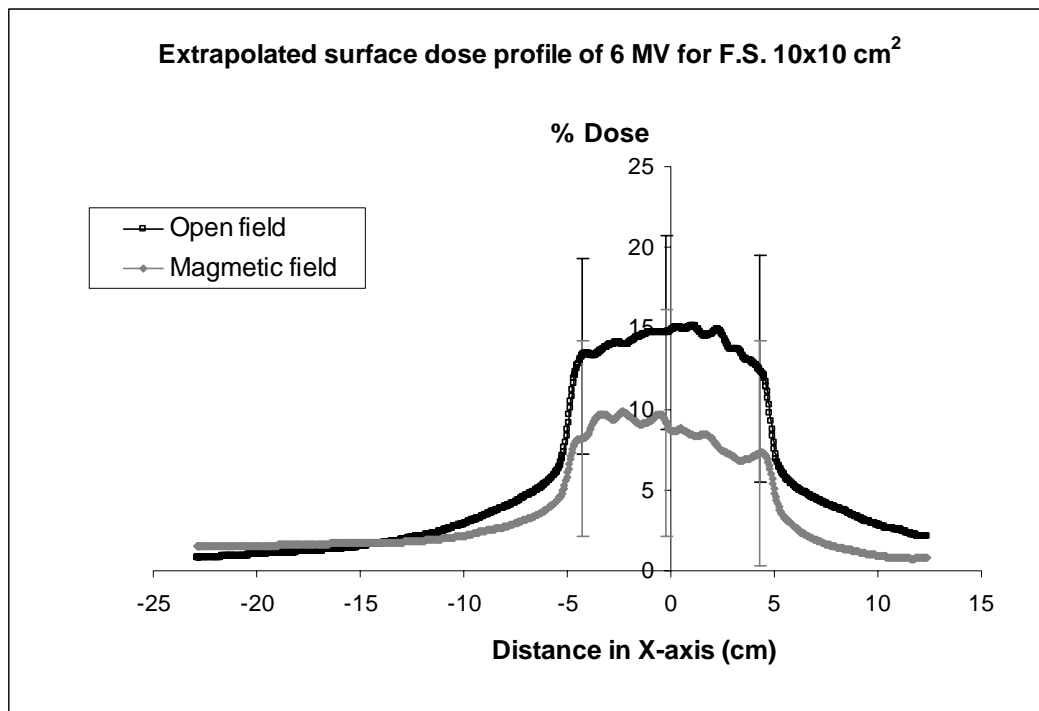


Figure 4.29. Extrapolated surface dose profile at central axis for 6 MV, measured cross-plane and in-plane with and without (open field) magnetic field from the deflector for a radiation field size of 10 x 10 cm².

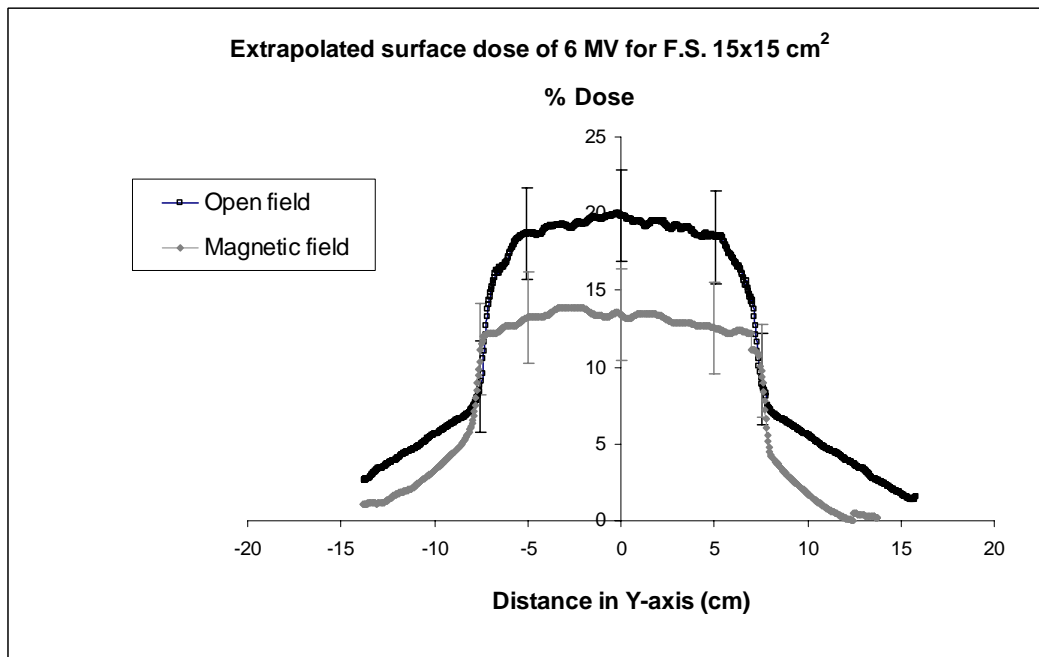
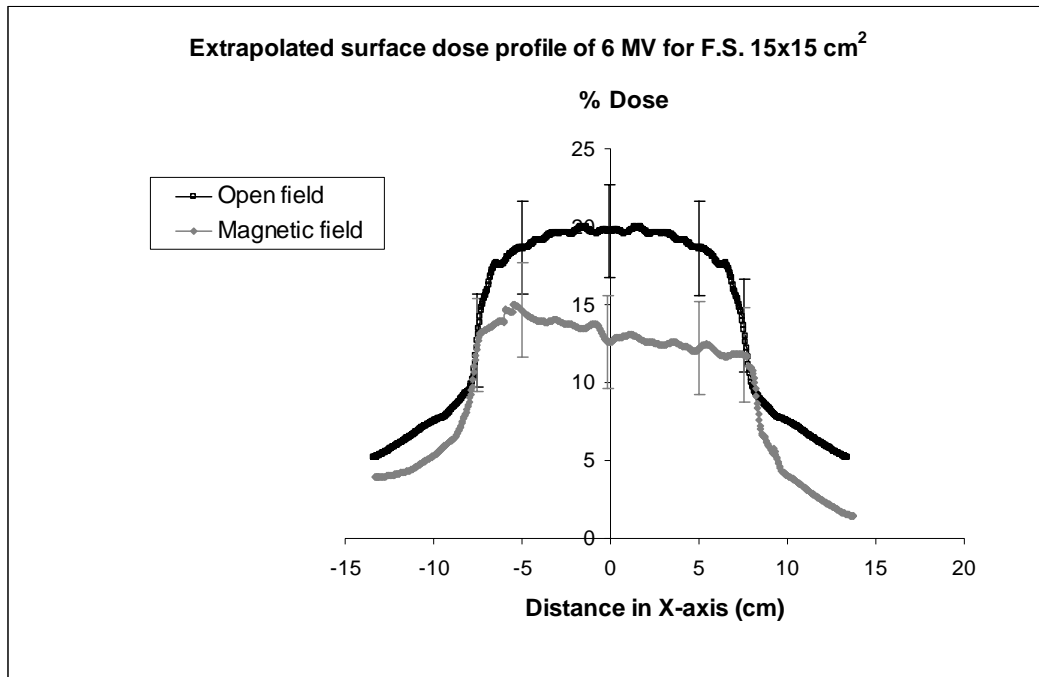


Figure 4.30. Extrapolated surface dose profile at central axis for 6 MV, measured cross-plane and in-plane with and without (open field) magnetic field from the deflector for a radiation field size of 15 x 15 cm².

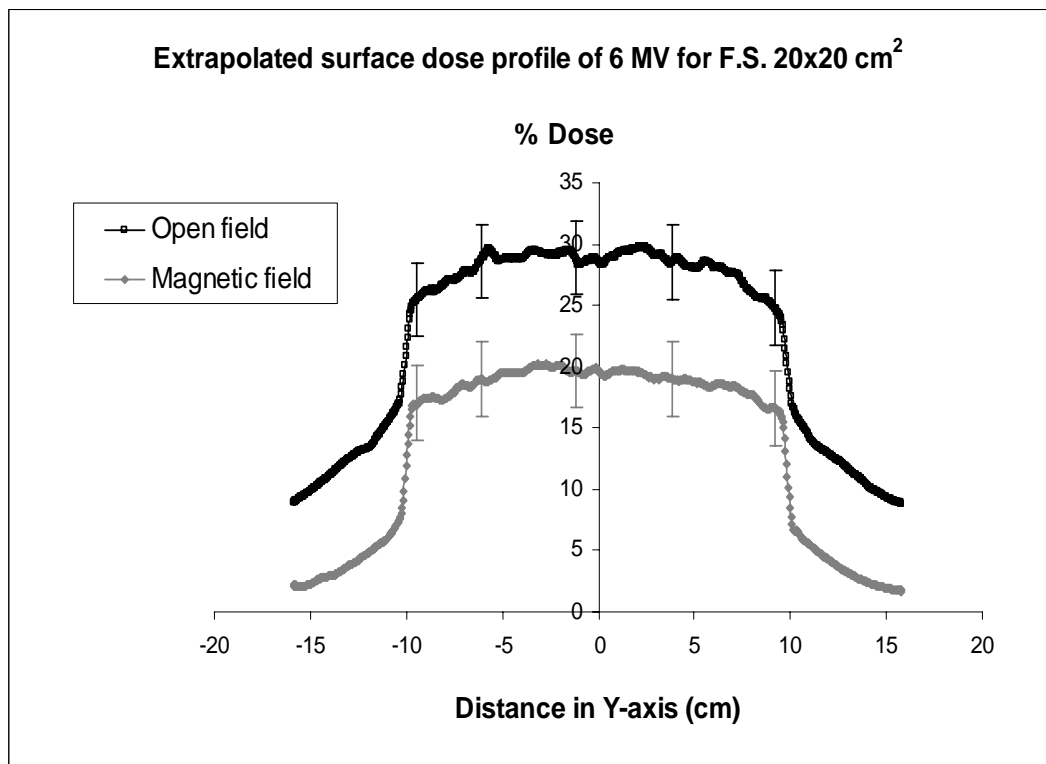
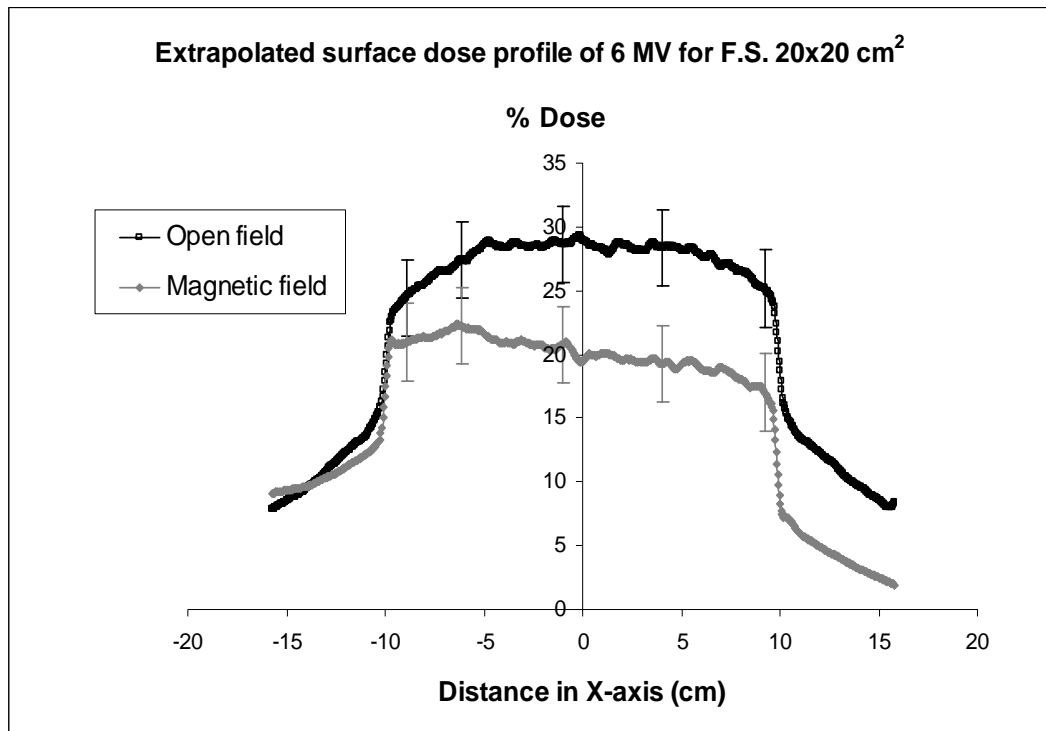


Figure 4.31. Extrapolated surface dose profile at central axis for 6 MV, measured cross-plane and in-plane with and without (open field) magnetic field from the deflector for a radiation field size of 20 x 20 cm².

Surface doses extrapolated from radiographic film and Attix chamber measurements are compared in Table 4.2. This 6 MV data is measured for open field versus magnetic field, surface dose results are for the Attix chamber compared to the radiographic film extrapolation technique matched to within 3 % for a field size of 10 x 10 cm², 2 % for a field size of 15 x 15 cm², and 2 % for a field size of 20 x 20 cm². The accuracy of our measurements from radiographic film was from ± 3 to ± 7 % for field sizes ranging from 10 x 10 cm² to 20 x 20 cm². This is due to the extrapolation technique and was obtained from the combination of errors correlated with the film calibration method. So an error in the surface dose from the extrapolation method is higher when compared with the dose directly measured from film. However, this technique still provides essential information for surface dose measurement.

Table 4.2. Surface dose measurements by the extrapolation technique from radiographic film compared to the Attix chamber results for 6 MV x-rays with and without (open field) magnetic field from the deflector.

% Surface dose measurement				
F.S. (cm ²)	Attix chamber		Radiographic film	
	Open field	Magnetic field	Open field	Magnetic field
10 x 10	16 \pm 1	12 \pm 1	14 \pm 7	9 \pm 7
15 x 15	21 \pm 1	15 \pm 1	19 \pm 3	13 \pm 3
20 x 20	27 \pm 1	18 \pm 1	27 \pm 4	16 \pm 4

4.3.4 Conclusion on surface dose measurement

Surface doses can be measured using radiographic film with an extrapolation technique for 6 MV x-rays, showing the effects of the magnetic deflector. The advantage of the film extrapolation technique is that a 2D map of the surface dose can be calculated with minimal measurements required. This technique calculated surface dose values that match well with Attix chamber results. The dose profiles are able to present information from outside the treatment field using a single exposure to a radiographic film.

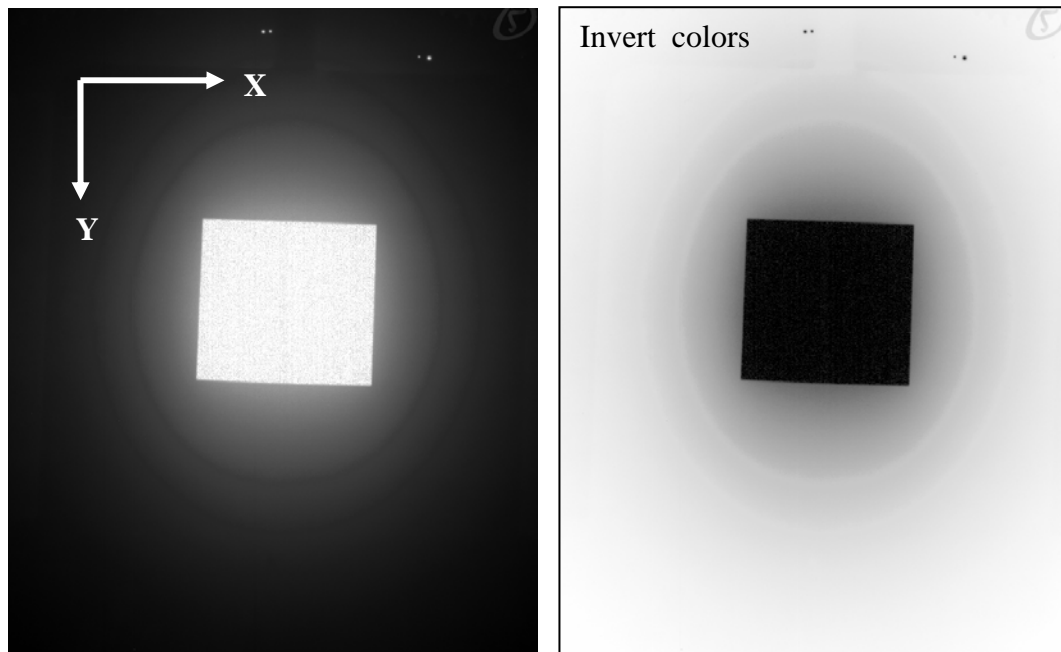
CHAPTER 5

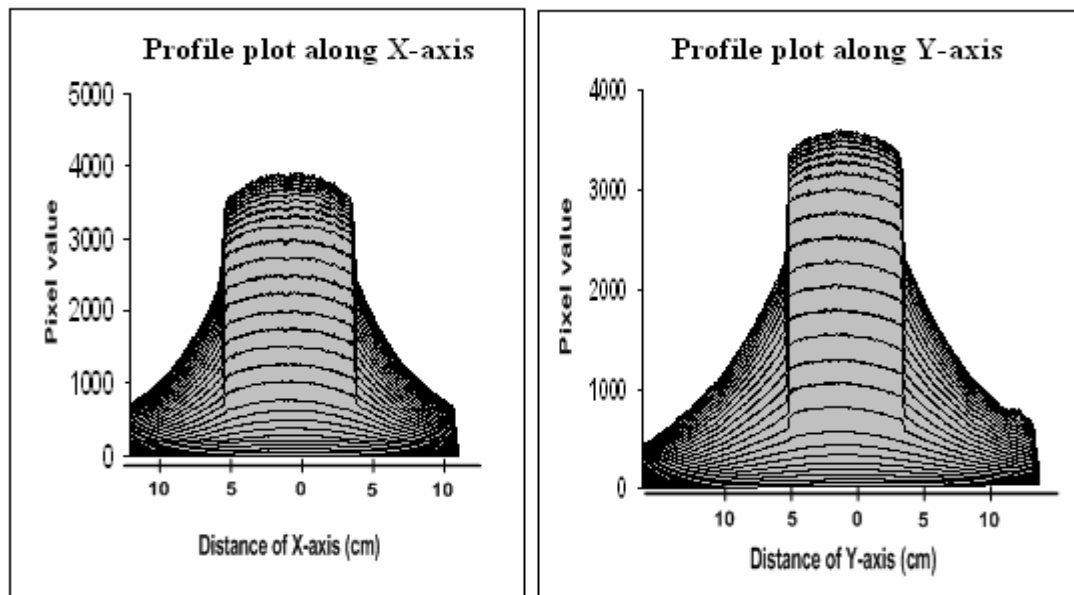
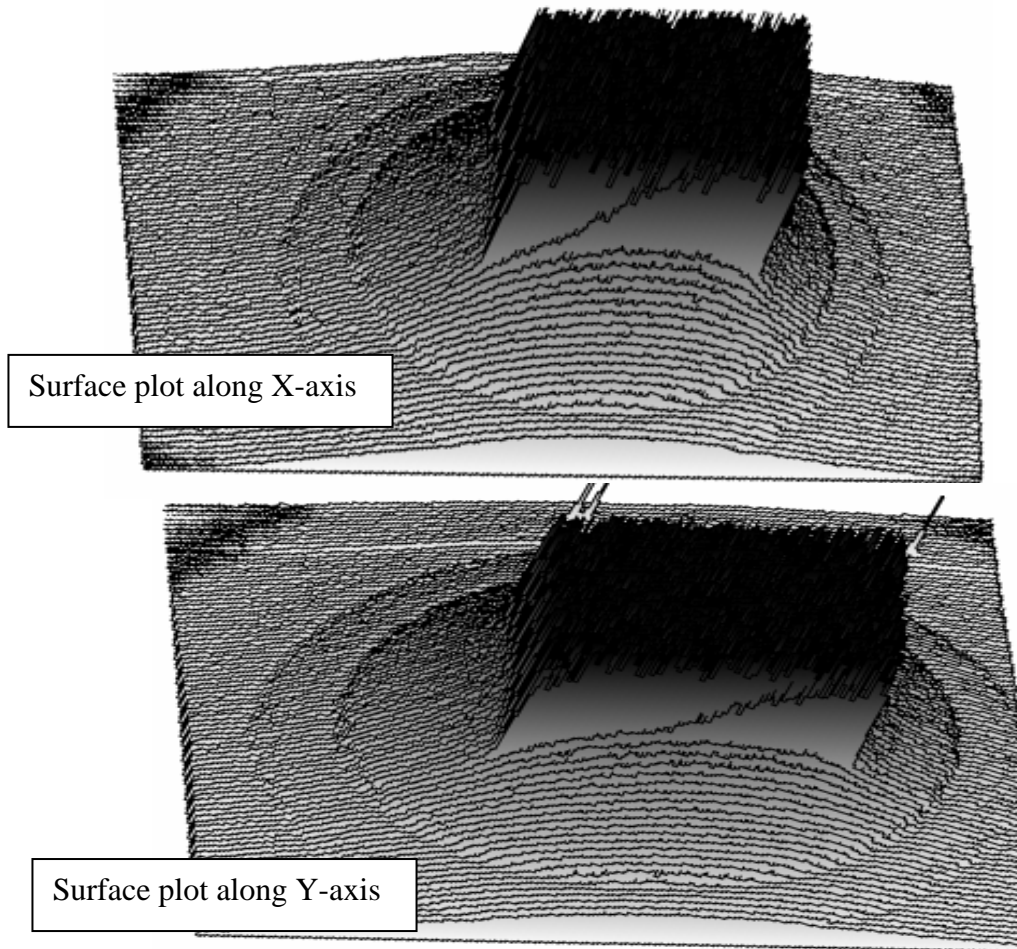
LEPTON CONTAMINATION IN 6 MV X-RAYS

Leptons are by-product particles, such as electrons and positrons that have no strong interactions. These particles, in this context called lepton contamination, are usually produced by interactions of a high-energy x-ray beam from a medical linear accelerator. Lepton contamination accumulated in the skin surface is generated from the scattering interactions of the high-energy x-rays with many components in the medical linear accelerator head and in the air volume between the linear accelerator machine and the patient surface. There is variation in contaminant doses, which is caused by parameters such as the field size and the use of beam modifying devices (Ling and Biggs, 1979, Nilsson, 1985, Purdy, 1986, Sjogren and Karlsson, 1996). Images of lepton contamination from the linear accelerator treatment head and the effect of the magnetic field are shown using radiographic films in Figure 5.1 (a) and (b). These radiographic films give a picture of the presence of lepton contamination in an elliptical ring around the radiation treatment field and the effect of the magnetic field in sweeping away these particles. Halo on radiographic film images may not totally represent the contaminations but may be caused by scattered x-rays and partial x-ray penetration through a beam collimator. Application of magnetic field distorted the halo but did not completely eliminate it. The presence of contaminations on both sides of x-ray field image is explained by presence of both electrons and positrons in the beam. A Monte Carlo calculation of contamination in high energy x-ray beam will maintain for the further proof and investigation.

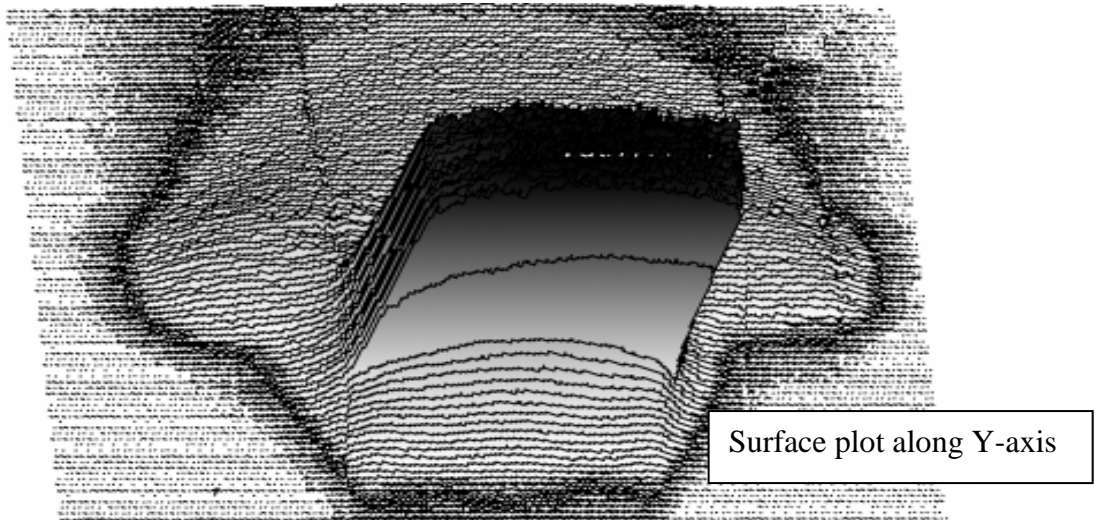
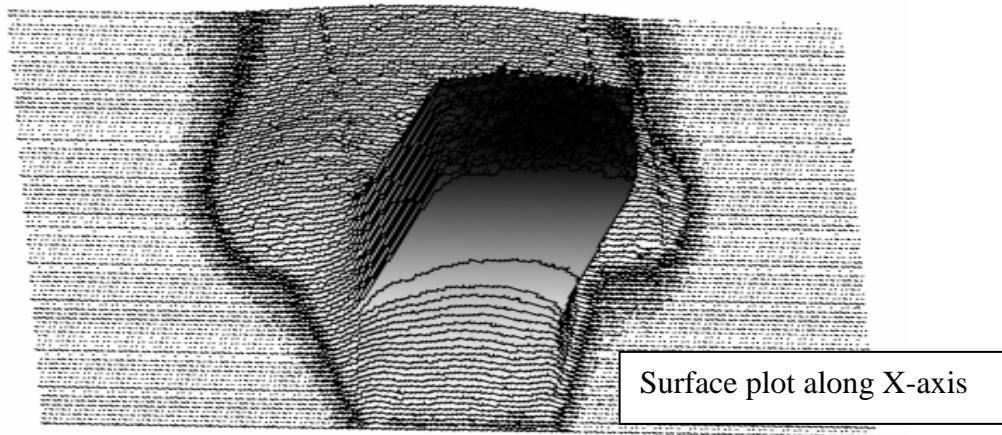
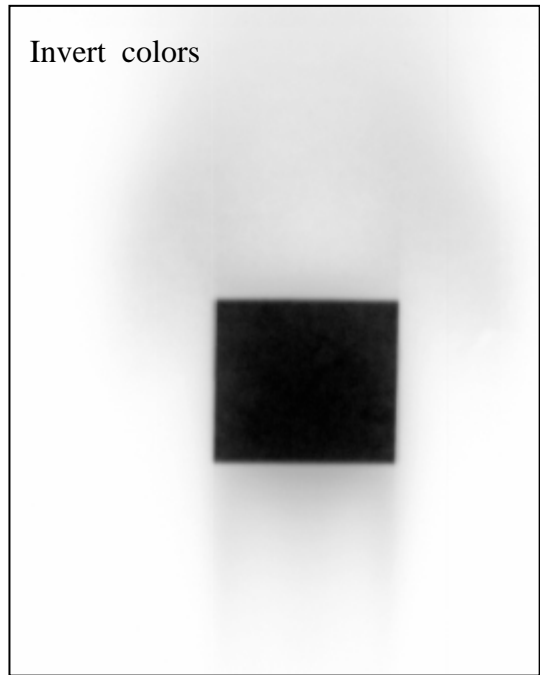
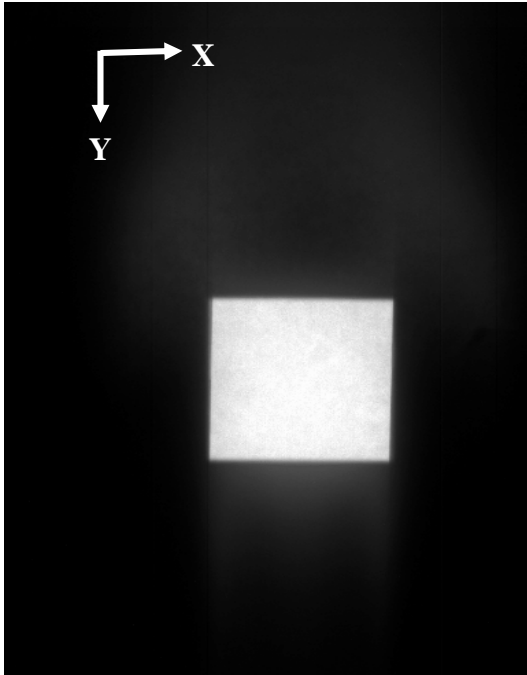
Surface and Profile plots also show lepton contamination occurring in-plane and cross-plane of radiation treatment field. A number of the contaminant particles produced by an interaction of high-energy x-ray beams come from the Compton scattering and pair production processes. Profile plots obviously demonstrate electrons and positrons swept in opposite direction following the Lorentz force rule in a magnetic field. A large amount of electrons originate from Compton scattering and pair production, whereas a low percentage of positrons are generated from the pair production process. Thus, electron particles are the most important kind of contamination in this study. The various treatment parameters, such as the field size, wedges, tray, and blocks in the

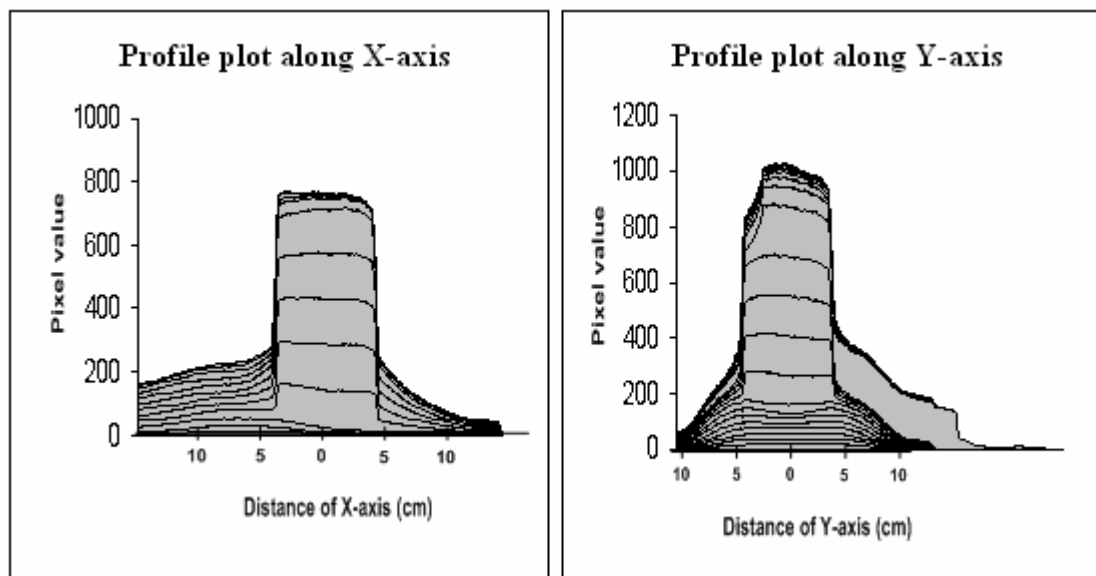
treatment set-up, also affect the lepton contamination to the skin. The skin surface dose can be changed when different treatment set-up parameters are used in clinical applications. Thus, the purpose of this study is to investigate the surface dose for various field sizes with a Perspex tray and wedge filter in the linear accelerator for 6 MV x-rays combined with the magnetic deflector device. Measurements of the skin surface dose in this study used radiographic film. Although radiographic film has a composition that differs from tissue it is still widely used for measurements of electron and photon beam dosimetry because it can be used to obtain the dose distribution of a radiation field with high spatial resolution and low cost. Radiographic film offers a convenient medium for easily generating profiles and two-dimensional distributions.





(a) Radiographic image with Surface and Profile plots present the lepton contamination of an open field (without deflection or beam-modifying devices) of $10 \times 10 \text{ cm}^2$.





(b) Radiographic image with Surface and Profile plots present the lepton contamination with magnetic field. Electrons and positrons are swept in opposite directions following the Lorentz force rule.

Figure 5.1. Radiographic image with Surface and Profile plots present the ring around the radiation field size (a), and the effect when the magnetic field sweeps contamination occurring around the radiation field away from the radiation treatment field (b).

5.1 Electron contamination from high-energy x-ray beams

One of the most advantageous features of high-energy x-ray beams is the skin sparing effect, but in some situations, this effect may be reduced or even lost if the beam is excessively contaminated with secondary electrons. When the patient is treated with a radiation beam, various skin reactions are often noticed. Electrons are the major contaminants produced from Compton scattering and the pair production process. Thus, doses delivered in the skin surface are often dominated by electron contamination and can vary quite considerably within the first few millimetres of depth due to the build-up characteristics of x-ray beams. These electrons arise from photon interactions with the collimating system and with any other scattering medium in the beam path. This is important, especially in the isocentric method of treatment in which these absorbers are brought close to the skin. Normally, a patient is treated either supine or prone. If anterior and posterior beams are used, usually one of the beams must traverse through the treatment couch. The introduction of material into the beam path will increase the

dose delivered to the patient's skin during treatment. In addition, patient support devices such as an Alpha Cradle and the graphite of the table can increase the surface dose (Klein and Purdy, 1993). Thus the pattern of behaviour of the skin dose can be attributed to variations in electron contamination caused by using accessory devices in radiotherapy treatment.

5.2 Source of electron contamination

It is known that for megavoltage photon beams using static fields sources of contamination at different distances from the target are clinically relevant. Several of studies have focused on the source of dose build-up for high-energy x-ray beams and found that the surface dose is highly dependent on electrons scattered from accelerator structures and from the air above the measurement surface. Treatment head materials such as the target, flattening filter, beam monitor chambers, and collimator jaws (Petti et al., 1983, Nilsson and Brahme, 1986) are sources of contamination electrons because these contamination electrons are produced from x-ray beam interactions with the air, collimator jaws, or any other materials.

Treatment set-up parameters involving the field size, wedges, tray, blocks, and source-to-surface distance (SSD) (Klein, 1997, Mellenberg, 1995) are sources of electron contamination affecting the surface dose (Mackie and Scrimger, 1982). It is known that for a clinical treatment, it is not practical to alter the effect of treatment head materials, except for the surface dose, which can be modified by using special set-up parameters in clinical applications.

Yang et al. (2004) studied contaminant electrons from a planar source to explain the source, size, and location of electron contamination. They assumed that the source plane (electron contamination) is located on the surface of the upper jaws because most contaminant electrons come from the components above the upper jaws. The source size is represented by the projection of the field size on the source plane. Thus, the planar source size is dependent on the treatment field size, which is determined by the secondary collimator (Figure 5.2).

Please see print copy for figure 5.2

5.3 Experimental set up

Measurements were performed with an Attix Model 449 parallel plate ionisation chamber in a solid water stack phantom. Percentage dose build up curves were measured on the central axis for various beam configurations from the surface to 16 mm depth in 1 mm increments, with radiation field sizes of $10 \times 10 \text{ cm}^2$, $15 \times 15 \text{ cm}^2$, and $20 \times 20 \text{ cm}^2$ with the NdFeB magnetic deflector device inserted under the block tray location. The Attix chamber provides surface ionisation accuracy within 1 % (Rawlinson, 1992). The films used for this study were Kodak X-Omat V films $33 \times 41 \text{ cm}$ in size. In order to minimise variations in the emulsion, all films used for one particular experiment were always from the same box. All measurements were performed at a 100 cm source to surface distance with the magnetic deflector device inserted below the block tray location in the linear accelerator treatment head (Figure 5.3). An extrapolation technique was used to derive the surface dose from the radiographic film traces for field sizes ranging from $5 \times 5 \text{ cm}^2$ up to $30 \times 25 \text{ cm}^2$ for open field and a 6 mm Perspex tray. For the physical wedge field, the field size is $20 \times 20 \text{ cm}^2$, with wedge angles of 15° , 30° , 45° , and $15 \times 15 \text{ cm}^2$ with a wedge angle of 60° .

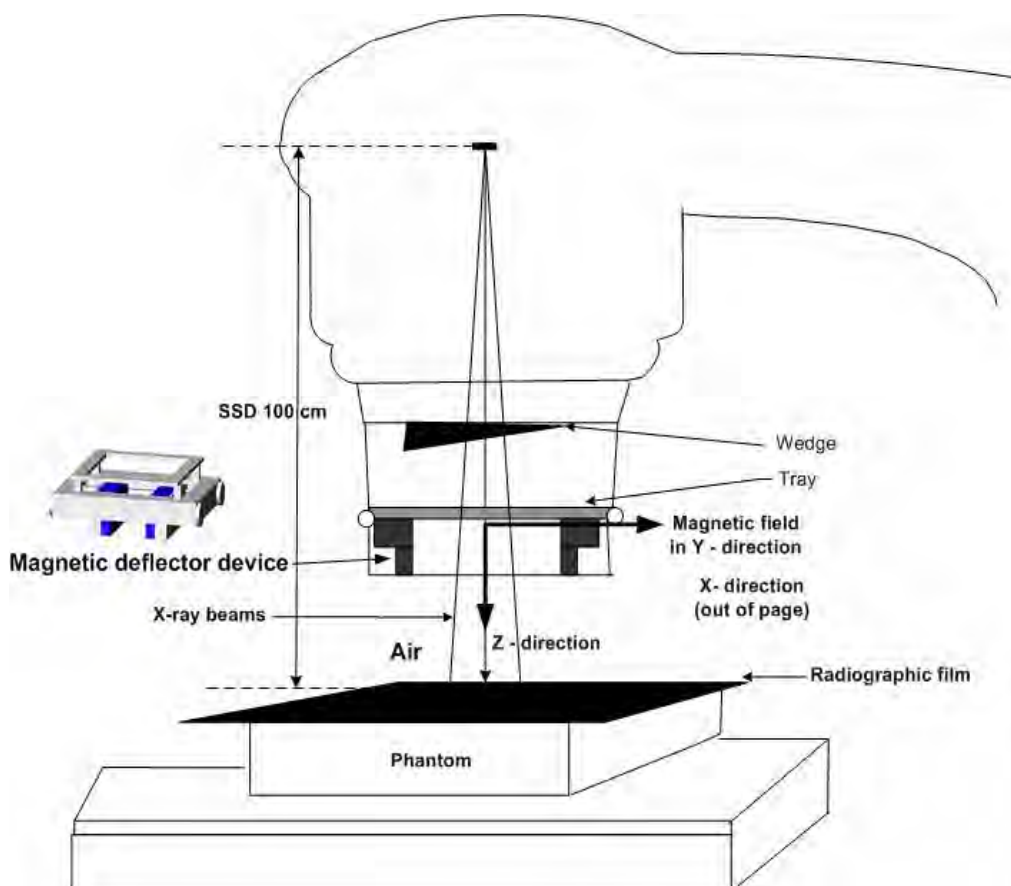


Figure 5.3. Diagram of the linear accelerator with magnetic deflector device and radiographic film as used in the experiments.

Measurements were performed using a Varian 2100C linear accelerator with a 0.36 T magnetic field strength from a NdFeB magnetic deflector device inserted below the block tray location. Kodak X-Omat V radiographic film was used for the assessment of surface dose. An extrapolation technique was employed to estimate surface dose by irradiating a stack of radiographic films, which were placed on top of a solid water phantom at 100 cm SSD. The films were in ready pack form. The stack of three films was exposed to a 6 MV x-ray beam for field sizes of $5 \times 5 \text{ cm}^2$ to $30 \times 25 \text{ cm}^2$. The effects of field size and of beam modifying devices on the dose response shown on the films were investigated for field sizes ranging from $5 \times 5 \text{ cm}^2$ to $30 \times 25 \text{ cm}^2$. For dose calibration, the calibration films were positioned in a solid water phantom of dimensions $30 \text{ cm} \times 30 \text{ cm} \times 30 \text{ cm}$ (Constantinou et al., 1982). The film was positioned at a depth of $D_{\text{max}} = 1.5 \text{ cm}$ for 6 MV x-rays, and doses of 0, 5, 10, 20, 30, 40, 60 and 80 MU were given with the film perpendicular to the central axis of the beam.

Field size dose calibration was performed for fields ranging from 5 x 5 cm² up to 30 x 25 cm² to account for effects caused by variations in the photon spectrum at different field sizes. The films were processed in an automatic X-Omat processor. Optical density to dose conversions was performed on the experimental films using results supplied from the calibration curve. In each case, the optical density was measured at the centre of each film piece to minimise the effects of variations in the measured dose near the edge of the film. Using the optical density calibration function of the Vidar VXR-12 Plus visible light densitometer and Scion imaging software scanner, results from the H and D curves produced calibration curves that were adequately fitted over the range from 5 to 100 MU by a third order polynomial, which was used to fit results. Surface dose assessment was performed using a dose extrapolation technique (Butson et al., 1999) whereby dose is extrapolated to 0 cm effective depth. The effective depth of measurement for the radiographic film ready-pack was calculated as 0.38 mm \pm 0.03 mm water equivalent (Butson et al., 2004).

5.4 Results and discussion of measurement

The Attix chamber provides surface ionisation accuracy within ± 1 % for radiation field sizes of 10 x 10 cm², 15 x 15 cm², and 20 x 20 cm². For the build-up dose measurements at a constant SSD of 100 cm, thin solid water slabs were taken from below the chamber and placed on the top of varying thicknesses in front of the chamber to measure the build-up doses.

5.4.1 Dose build up region

Results were measured with an Attix chamber at 100 cm SSD with and without magnetic field. Figure 5.4 illustrates dose build-up curves for 6 MV x-ray beams (open field) for 10 x 10 cm², 15 x 15 cm², and 20 x 20 cm² field sizes, and surface doses of 16 %, 21 %, and 27 %, respectively.

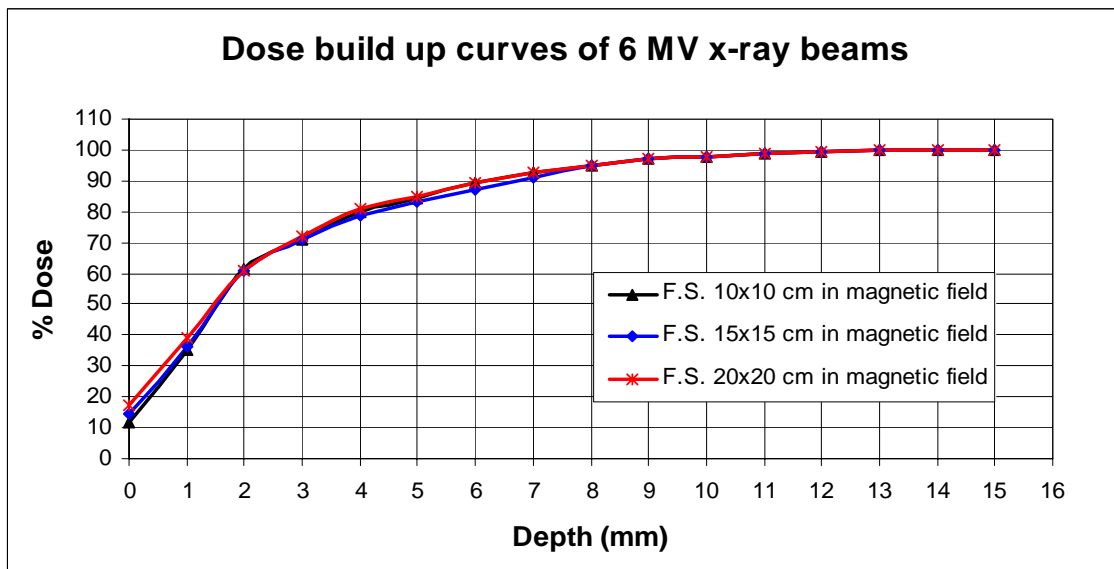
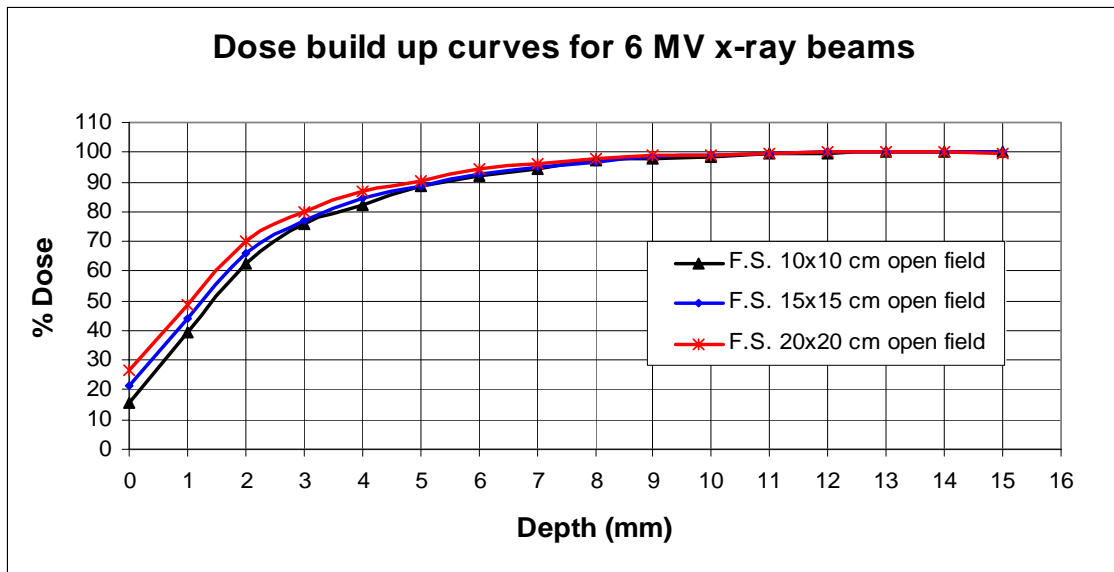


Figure 5.4. Percentage dose build up for 6 MV x-rays from an Attix chamber (open field) and in magnetic field for field sizes of 10 x 10 cm², 15 x 15 cm², and 20 x 20 cm².

For the same field size in magnetic field, surface doses are 12 %, 15 %, and 18 %, respectively. The dose in the build-up region rapidly increases within the first few millimetres and gradually reaches the maximum dose at 13 mm depth. It is known that dose is determined by the x-ray energy for depths greater than a few centimetres, but for an electron, the deposited energy is limited to within a depth of a few centimetres. Thus, the contribution to the dose in this region comprises the primary photons beam, backscattered radiation, and lepton contamination.

Contamination produced from the material in the treatment head will occur in each beam from the smaller field sizes to the larger, but most of the contamination produced above the jaws will be stopped by the jaws when they are in a small field size configuration. However, as the field size is increased, an enhanced effect occurs because the upper surface of the jaws allows more contamination produced in the areas of the flattening filter, ionisation chambers, mirror and Mylar to pass through, and a greater surface area of the sides of the jaws is exposed to the beam. Extra focal photons in particular may interact with these surfaces, causing lepton contamination; the air volume exposed to x-rays also increases the probability of contamination. Consequently, as field size is increased the near surface dose increases. Dose build-up characteristic curves change with field size. This is due to the effect of scattered photons, as well as contamination produced in the treatment head of the machine and within the air column above the phantom. Results from measurements with magnetic field display a decreasing dose in the build-up region compared with open fields. By subtracting the percentage dose open field results from magnetic field results, the differences that represent contamination swept off the central axis of the beam can be calculated and are shown in Figure 5.5. The dose in the build-up region is 9 % and the percentage reduction is 34 % (of their original values) with the addition of the magnetic field for a field size of 20 x 20 cm².

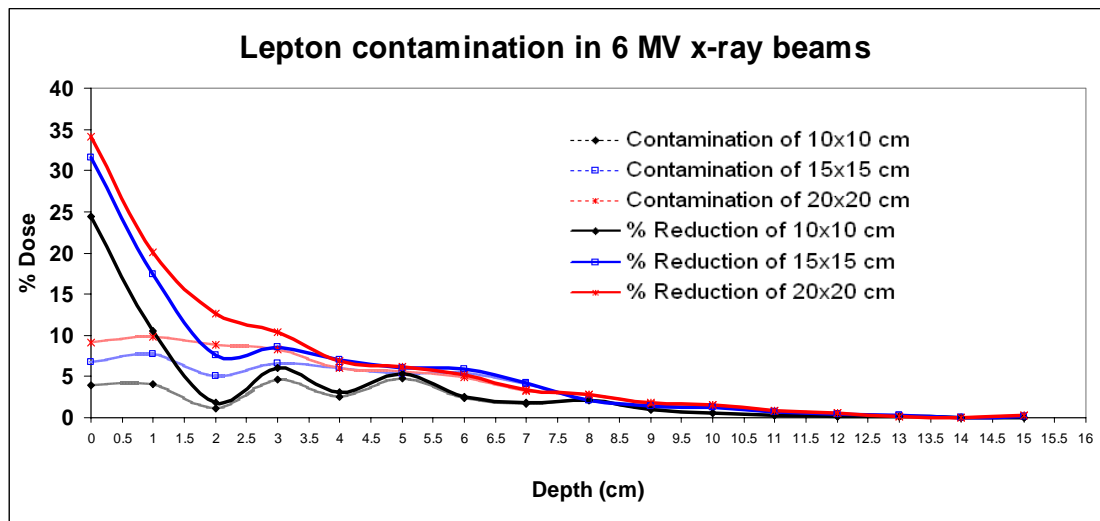


Figure 5.5. Percentage contamination dose reduction for 6 MV x-rays from an Attix chamber with a magnetic field applied to a linear accelerator treatment head for 10 x 10 cm², 15 x 15 cm², and 20 x 20 cm² field sizes.

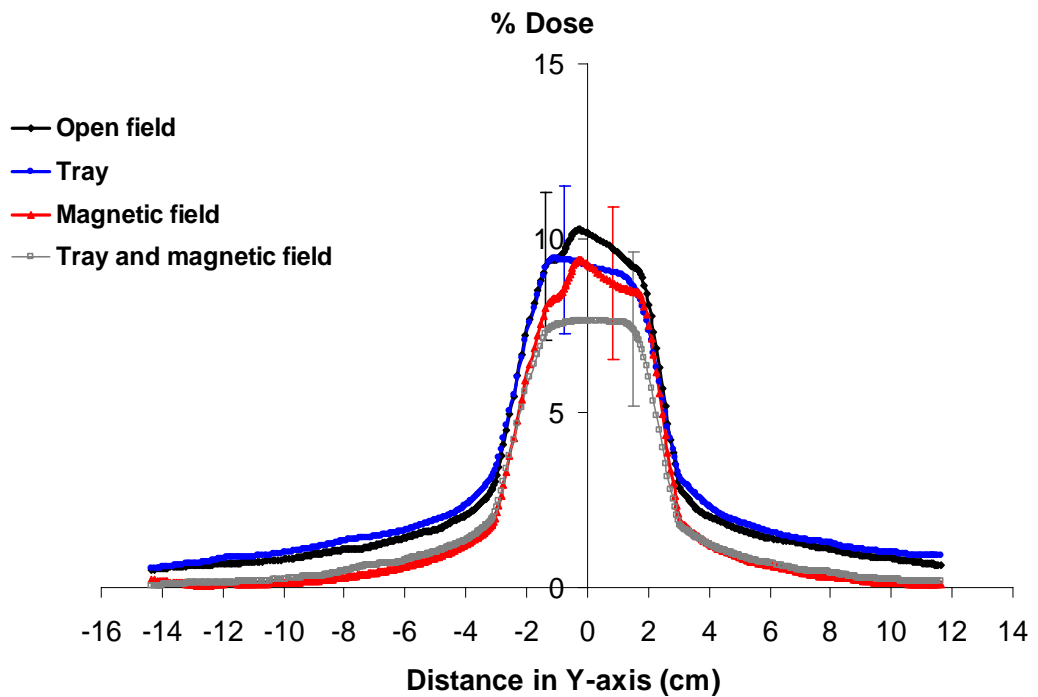
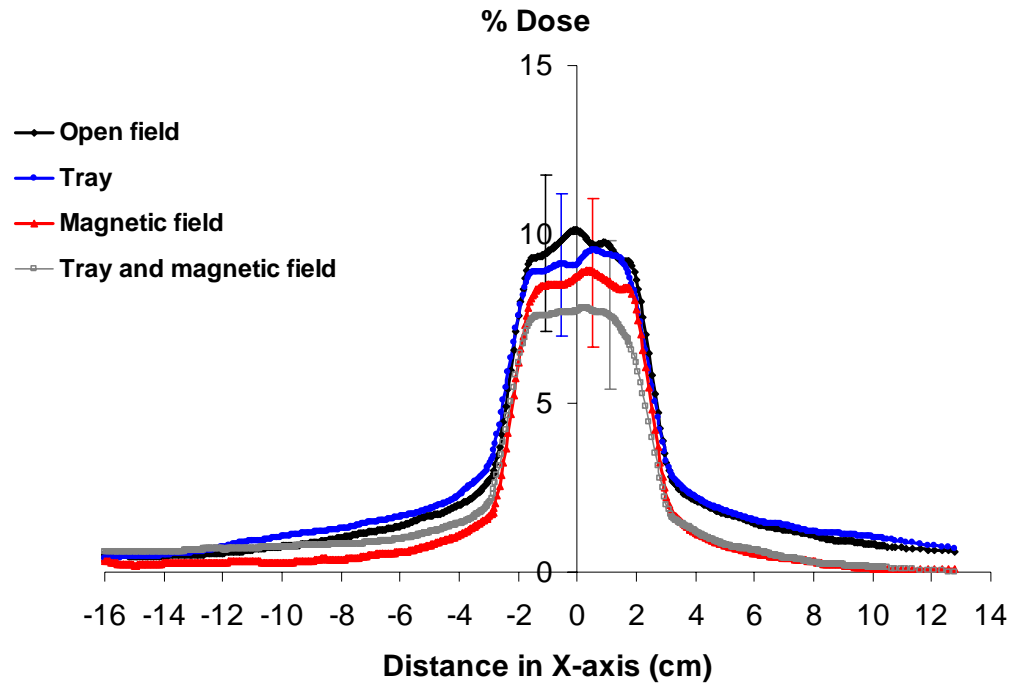
This means that the magnetic field eradicates the contamination in the beam path. Applying a magnetic field in a linear accelerator treatment head results in a big contamination dose reduction in the region within the first few millimetres of the surface. It is well known that it is the dose delivered to the surface and within a 1 mm depth that is important in terms of skin reactions within the basal cell and dermal layers. The high skin surface dose, which is completely unwanted in many clinical situations, might even induce so much damage to the skin as to cause the treatment to be interrupted. Thus, the data on the dose build-up characteristics of a patient is important for appropriate treatment decisions. As the magnetic field assists in sweeping lower energy electrons or positrons more effectively than higher energy electrons or positrons, some contamination is still present beyond the magnetic deflector position and thus passes through the phantom. This is in addition to any contamination produced in the air column above the phantom.

5.4.2 Field size

Surface dose analysis is obtained from an extrapolation curve, with a second order polynomial to perform the optimal calculation due to the nonlinear nature of photon build up characteristics (Butson et al., 1999). The extrapolation technique is used where layers of films are employed to produce a central axis percentage depth dose measurement, which is normalised to 100 % at $D_{\max} = 1.5$ cm. The effective point of measurement was assumed to be at the centre of each film, and thus results for each film layer are quoted at half its water equivalent thickness, i.e. 0.38 mm with the relative depths of measurement being 0.38 mm on film sheet 1, 1.14 mm on film sheet 2 and 1.9 mm on film sheet 3. We estimate that the accuracy of our surface dose measurements that were extrapolated from radiographic film ranges from ± 3 to ± 7 % for field sizes ranging from $5 \times 5 \text{ cm}^2$ to $30 \times 25 \text{ cm}^2$. This estimate is obtained from a combination of errors correlated with film calibration method. Therefore, the error in the surface dose from the extrapolation method is higher when compared with a dose directly measured from film. Extrapolated surface doses from radiographic films for profiles measured cross-plane and in-plane at the central axis of 6 MV x-ray beams, both for open field and for the tray combined with magnetic field for field sizes from $5 \times 5 \text{ cm}^2$ to $30 \times 25 \text{ cm}^2$, are shown in Figure 5.6. The surface dose increases with the use of a 6 mm Perspex tray, but this effect is minimal when combined with magnetic deflector device.

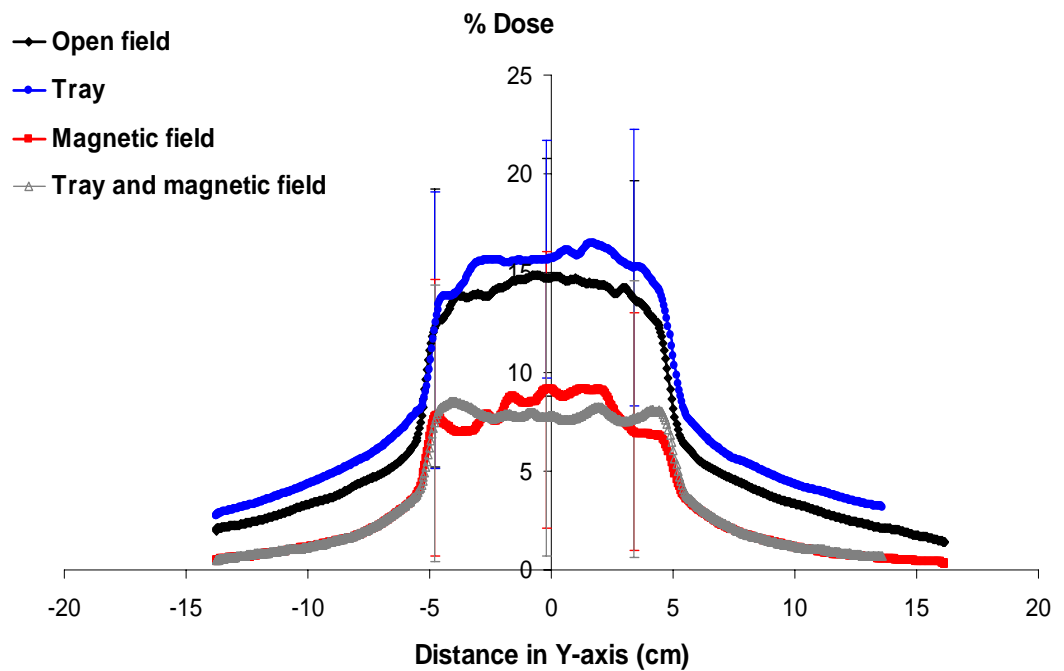
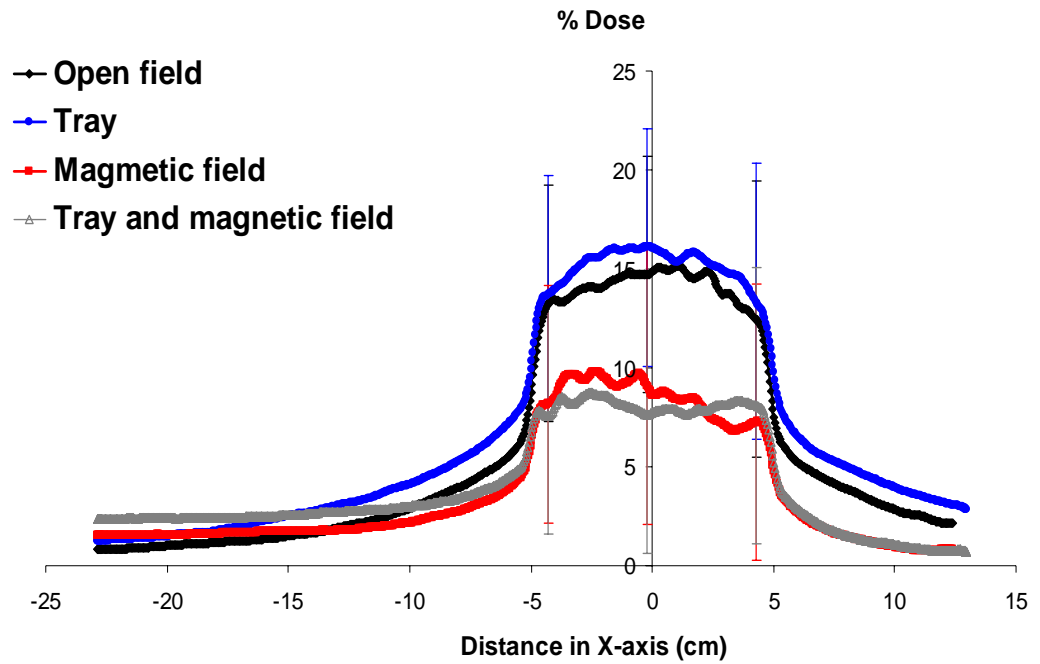
As can be seen, when the open field size is increased from $5 \times 5 \text{ cm}^2$ to $30 \times 25 \text{ cm}^2$, the surface dose increases from $10 \pm 3 \%$ to $35 \pm 6 \%$.

Extrapolated surface dose profile of 6 MV for F.S. $5 \times 5 \text{ cm}^2$



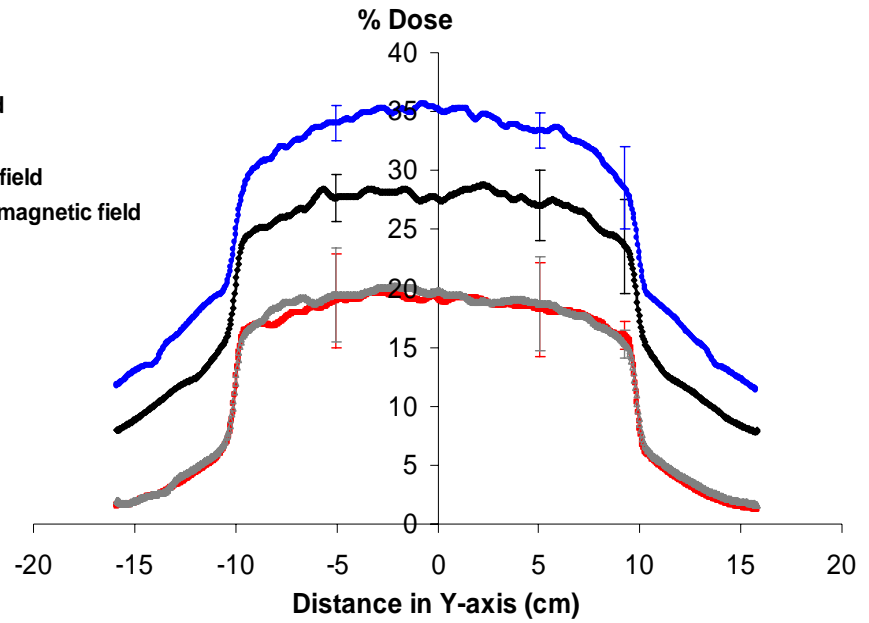
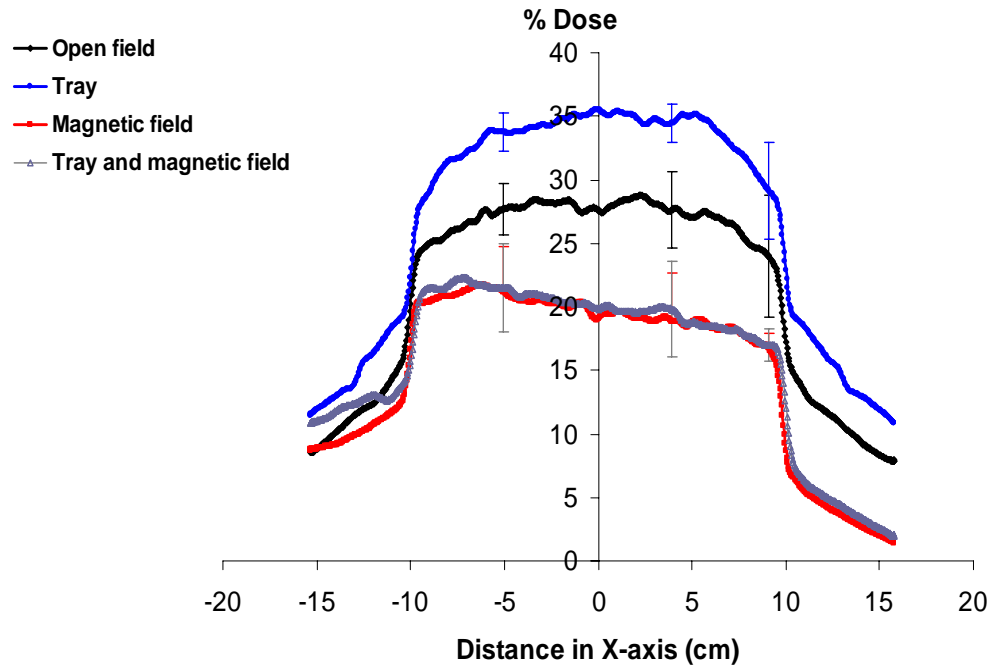
(a) Profiles measured in-plane and cross-plane of 6 MV x-ray beam for open field, tray in place, and magnetic field and tray in place with magnetic field for a field size of $5 \times 5 \text{ cm}^2$.

Extrapolated surface dose profile of 6 MV for F.S. 10x10 cm²



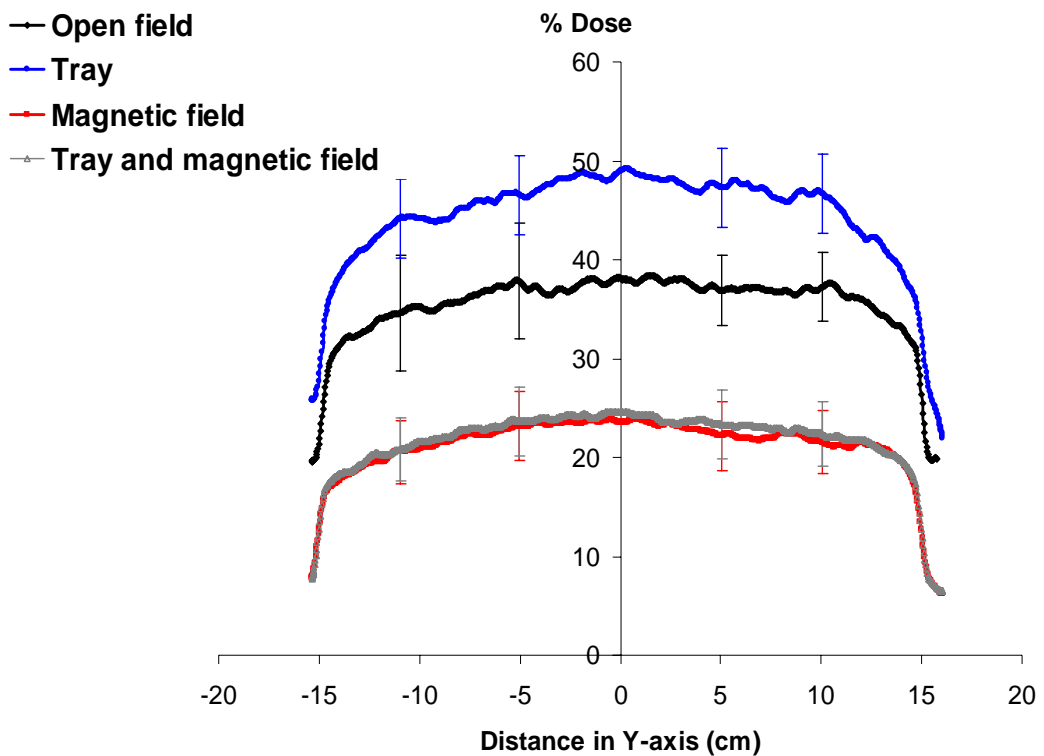
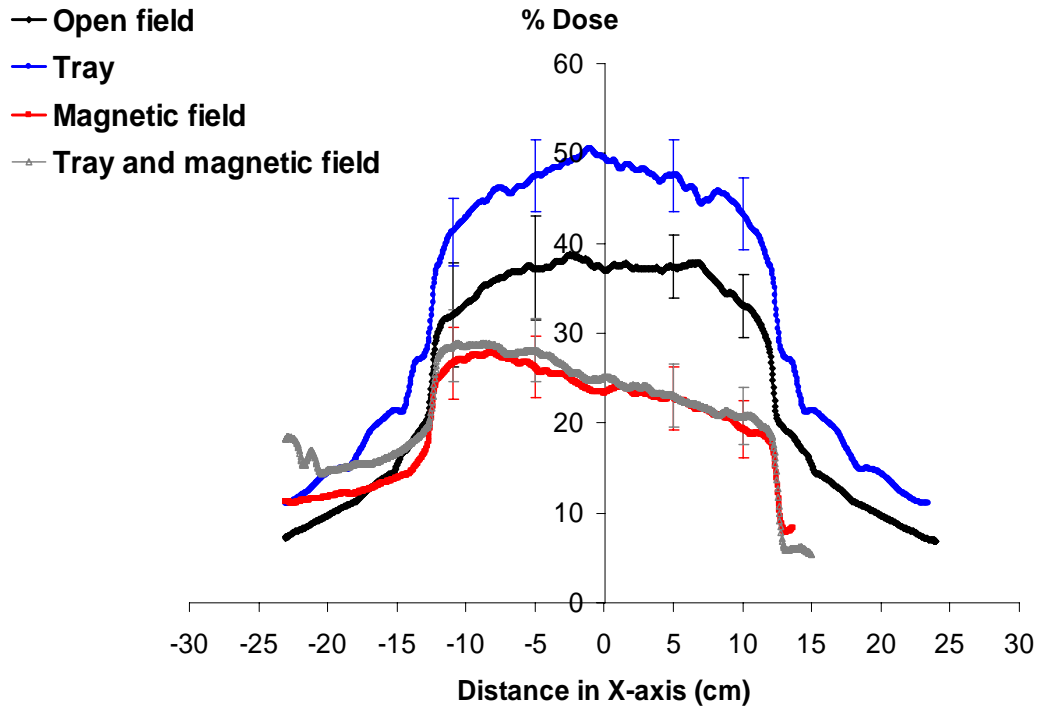
(b) Profiles measured in-plane and cross-plane of 6 MV x-ray beam for open field, tray in place, and magnetic field and tray in place with magnetic field for a field size of 10 x 10 cm².

Extrapolated surface dose profile of 6 MV for F.S. 20x20 cm²



(c) Profiles measured in-plane and cross-plane of 6 MV x-ray beam for open field, tray in place, and magnetic field and tray in place with magnetic field for a field size of 20 x 20 cm².

Extrapolated surface dose profile of 6 MV for F.S. 30x25 cm²



(d) Profiles measured in-plane and cross-plane of 6 MV x-ray beam for open field, tray in place, and magnetic field and tray in place with magnetic field for a field size of 30 x 25 cm².

Figure 5.6. Extrapolated surface doses from radiographic films are shown for profiles measured in-plane and cross-plane of 6 MV x-ray beam for open field, tray in place, and magnetic field and tray in place with magnetic field for field sizes of (a) $5 \times 5 \text{ cm}^2$, (b) $10 \times 10 \text{ cm}^2$, (c) $20 \times 20 \text{ cm}^2$, and (d) $30 \times 25 \text{ cm}^2$.

When using with a 6 mm Perspex tray, the surface dose is higher than for open field for field sizes larger than $5 \times 5 \text{ cm}^2$. This increased surface dose may come from the scattered radiation produced from the material in the treatment head, which occurs in each beam from the smaller to the larger field sizes. The contamination is mainly produced in the areas of the flattening filter, mirror, and ionisation chambers as the beam passes through the jaws, which allows more contamination to be produced when the field size is increased.

These 6 MV data are also measured for open field combined with magnetic field and tray with magnetic field. The measured percentage surface doses for open field (no tray) and magnet range from $9 \pm 3 \%$ to $22 \pm 6 \%$ for field sizes from $5 \times 5 \text{ cm}^2$ to $30 \times 25 \text{ cm}^2$, while percentage surface doses with a 6 mm Perspex tray and magnet range from $8 \pm 3 \%$ to $23 \pm 6 \%$ for the same field sizes. As can be seen, surface dose profiles are reduced in all sites within the radiation field when a magnetic field is present. Results showed a reduction in the surface dose along the x-axis distance in the presence of a magnetic field with different magnitudes of dose from the central axis when compared to open field. The surface dose in the region on the negative side of the x-axis is higher than that at a positive distance along the x-axis. This is due to the high magnetic field strength in the positive y-axis direction that sets up the deflection process via a magnetic field according to the Lorentz force. Thus, the strong deflection path occurs in on the negative side of the x-axis. This reduction is increased for larger field sizes, but the magnetic field strength attainable is not large enough to remove all contamination from the treatment field. The electron contamination is still in a negative x-axis position outside the treated area, so material such as a 1.5 cm thick layer of wax or a thin sheet of lead could be placed next to the field to absorb the electron contamination during the radiation process.

The surface dose profile along the y-axis is still reduced in a presence of magnetic deflection device. For our newly designed magnetic deflector to set up the deflection process, there is a high magnetic field strength in the +y-axis direction with a very small

force to deflect electron contamination in this direction. When electron contamination moves parallel to the magnetic field direction, no deflection of electrons can occur. As can be seen, the shape of the surface dose profile is quite symmetrical along the y-axis, especially for field sizes larger than $10 \times 10 \text{ cm}^2$.

These results demonstrate that contamination originating from the treatment head is partially responsible for the dose enhancement in the surface region, even when the magnetic field strength is sufficient to deflect the contaminations away from the x-ray beams. The field size dependence that remains in the presence of the magnetic field may be due to either radiation components that are not affected by the magnetic field, such as secondary photons from the flattening filter and collimator jaws, or by components that are not completely deflected away from the area of measurement, such as electrons and positrons produced in the air volume near the phantom surface where the magnetic field is weak or nonexistent. It has been confirmed in this study for 6 MV x-rays that the observed enhancement at the surface with increasing field size is due to scattered electrons emerging from the device upstream in the linear accelerator treatment head.

5.4.3 Beam modifying devices

Beam modifying devices such as the Perspex tray and wedges inherently change the surface dose due to changes in the scattered photons and in contamination production. Figure 5.7 demonstrates the percentage relative dose on the surface for 6 MV x-rays with and without magnetic field in the beam for a $5 \times 5 \text{ cm}^2$ to $30 \times 25 \text{ cm}^2$ field sizes with open field and with a 6 mm Perspex tray. Relative surface doses for field sizes from $5 \times 5 \text{ cm}^2$ to $30 \times 25 \text{ cm}^2$ normalised to the surface dose for an open field size of $10 \times 10 \text{ cm}^2$ show an increase in surface dose of more than 2-3 times for field sizes larger than $10 \times 10 \text{ cm}^2$ in the case of open field with a Perspex tray.

An important feature is that the Perspex tray has more effect on the dose to the surface. The Perspex tray absorbs and produces contamination when exposed to x-rays. Contamination produced within the linear accelerator head must pass through the tray before reaching and interacting with the phantom. Such low energy electrons will be absorbed and higher energy electrons will be attenuated to varying degrees. They are also generated and scattered towards the phantom by the interactions with the x-rays. Thus, the Perspex tray can significantly increase the surface dose due to the production

of lepton contamination. The magnetic deflector effect results in reduced surface doses for the case where there is a Perspex tray.

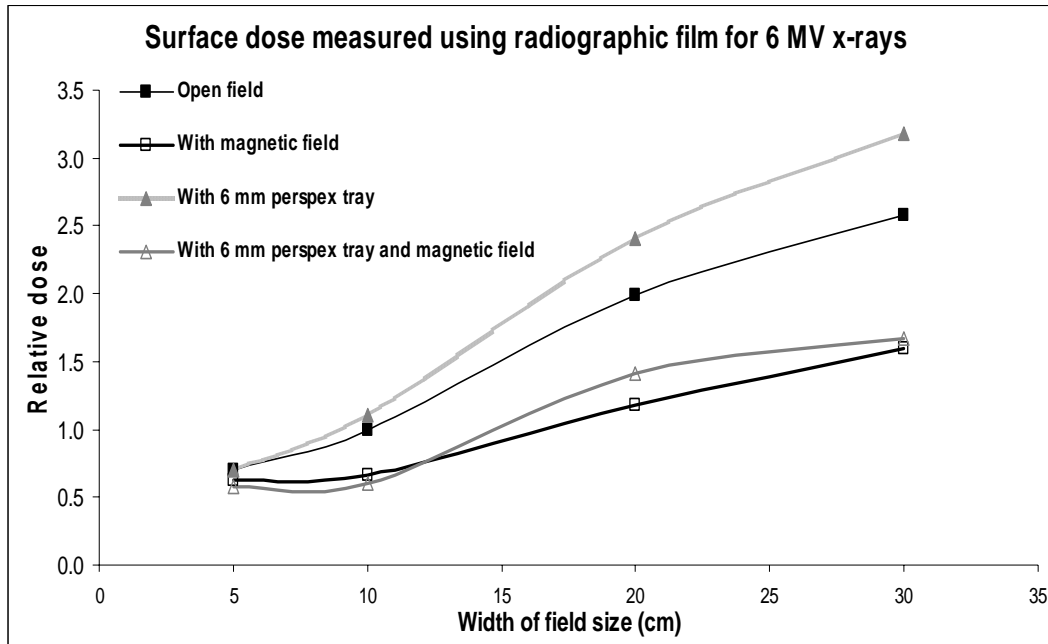
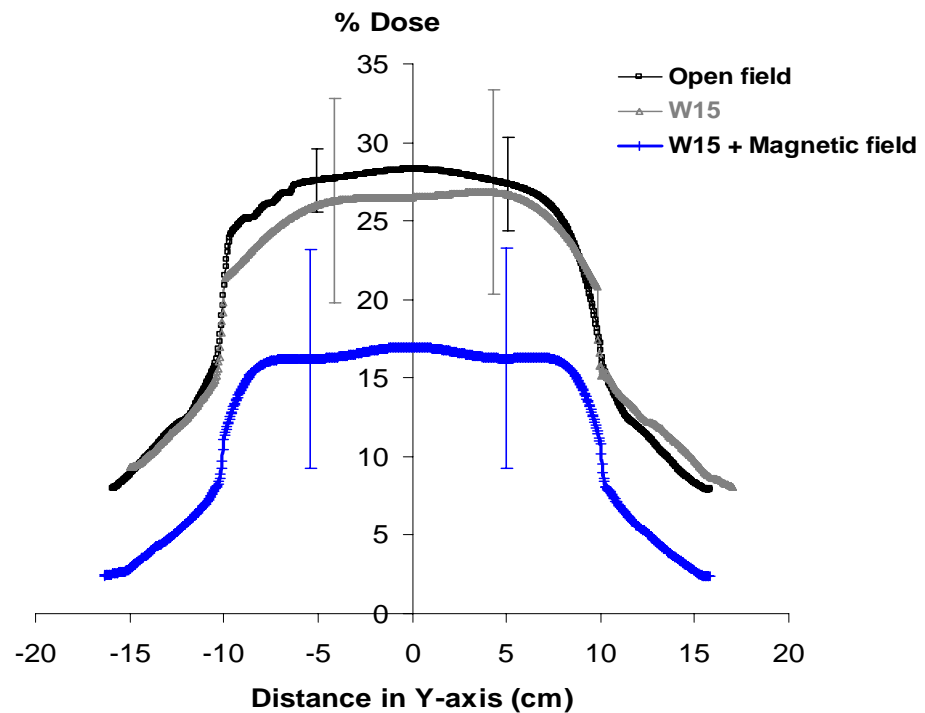
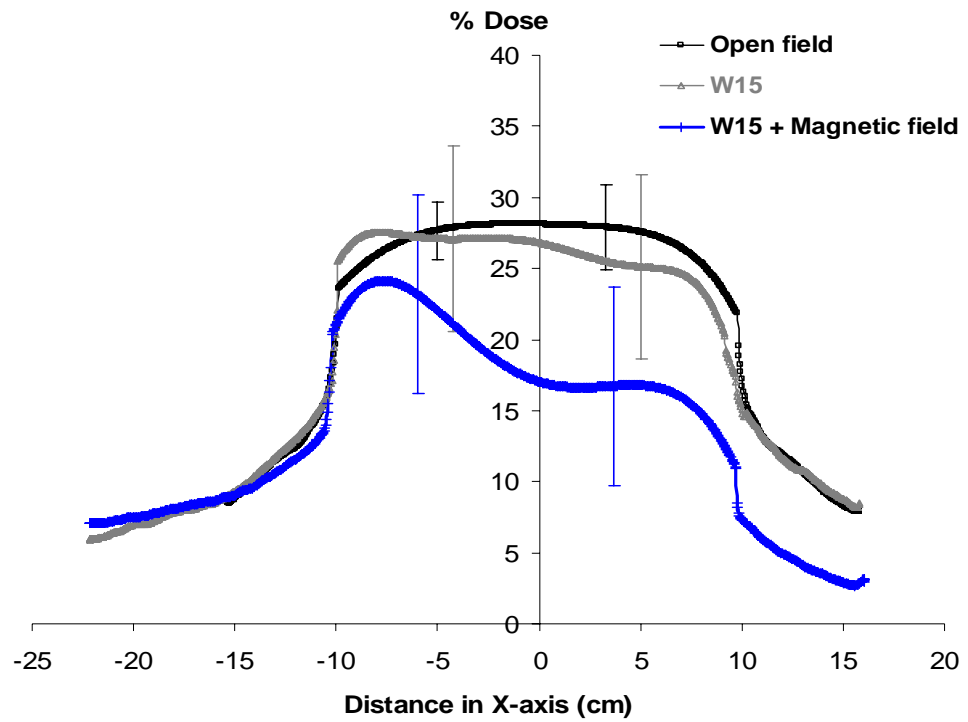


Figure 5.7. Relative surface dose from radiographic film of 6 MV x-rays for open field and 6 mm Perspex tray with and without magnetic field for 5 x 5 cm², 10 x 10 cm², 20 x 20 cm², and 30 x 25 cm² field sizes.

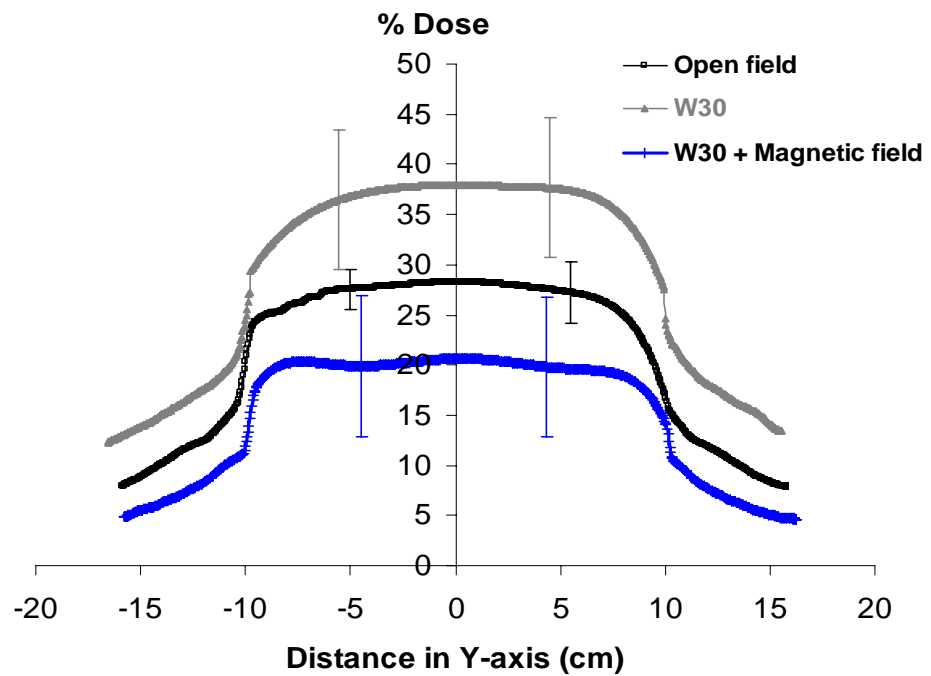
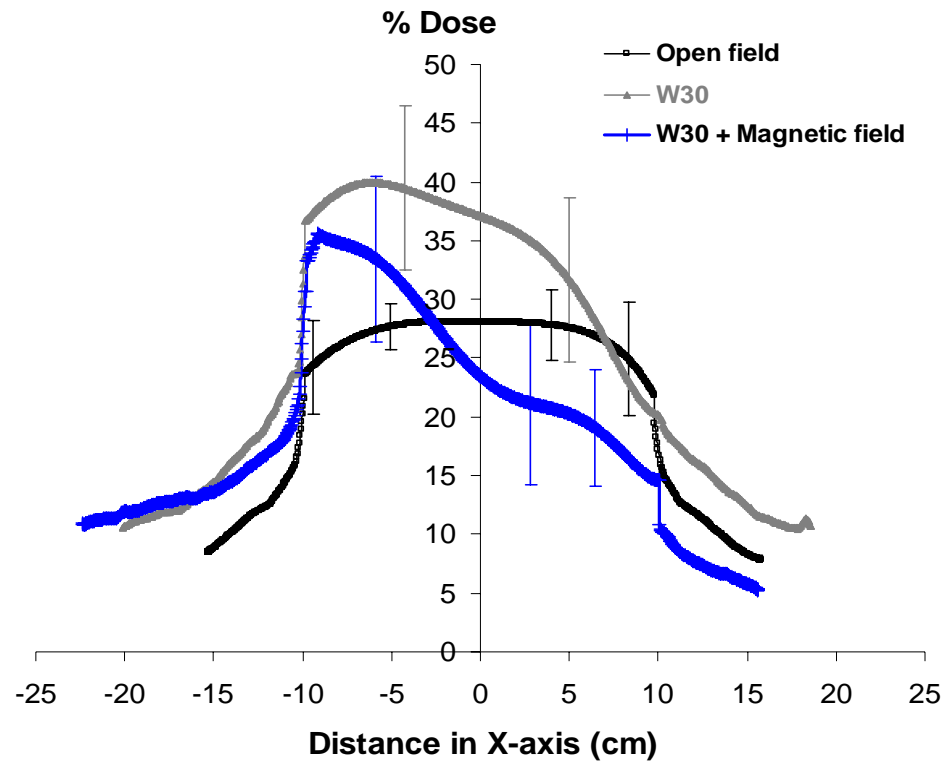
Effectively, the magnetic deflector can remove the effects of increased surface dose produced by the use of a Perspex tray. Results shows that the surface dose increases with field size and with the use of a Perspex tray, but this effect is minimal when it is used with the magnetic deflection device. Another commonly used beam-modifying device is a physical wedge. This design changes the isodose curves of an x-ray beam and is used to compensate for the patient's sloping external contour or to compensate for angled wedge pairs. Extrapolated surface doses of radiographic films for profiles measured cross-plane and in-plane at the central axis of a 6 MV x-ray beam with magnetic field for a wedge-shaped field with a wedge angle of (a) W15°, (b) W30°, (c) W45°, and (d) W60° compared with open field are shown in Figure 5.8.

Extrapolated surface dose profile for 6 MV



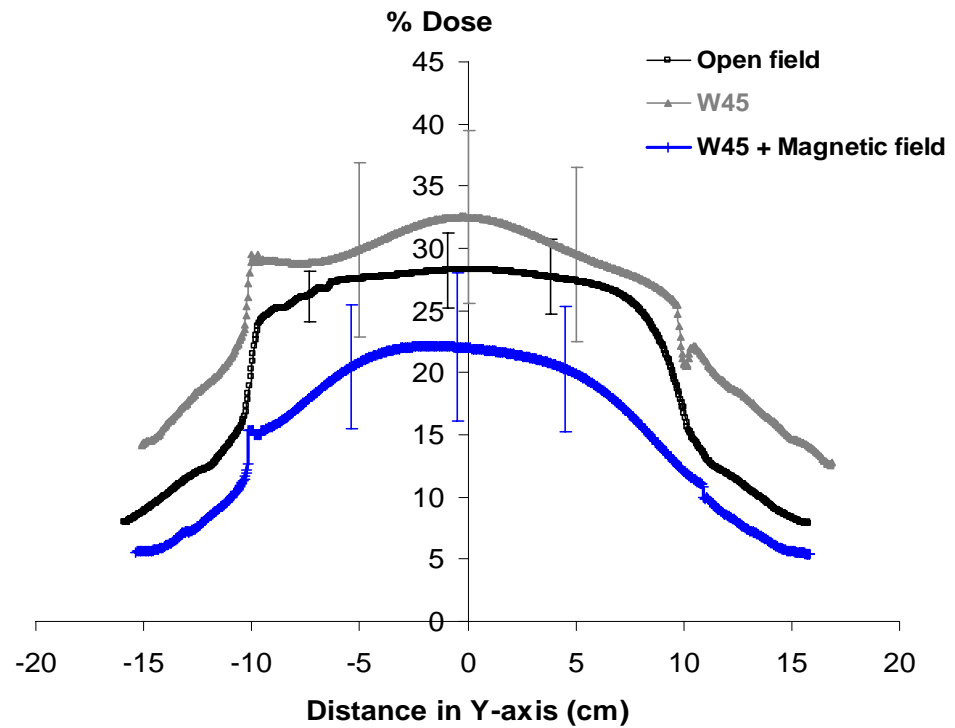
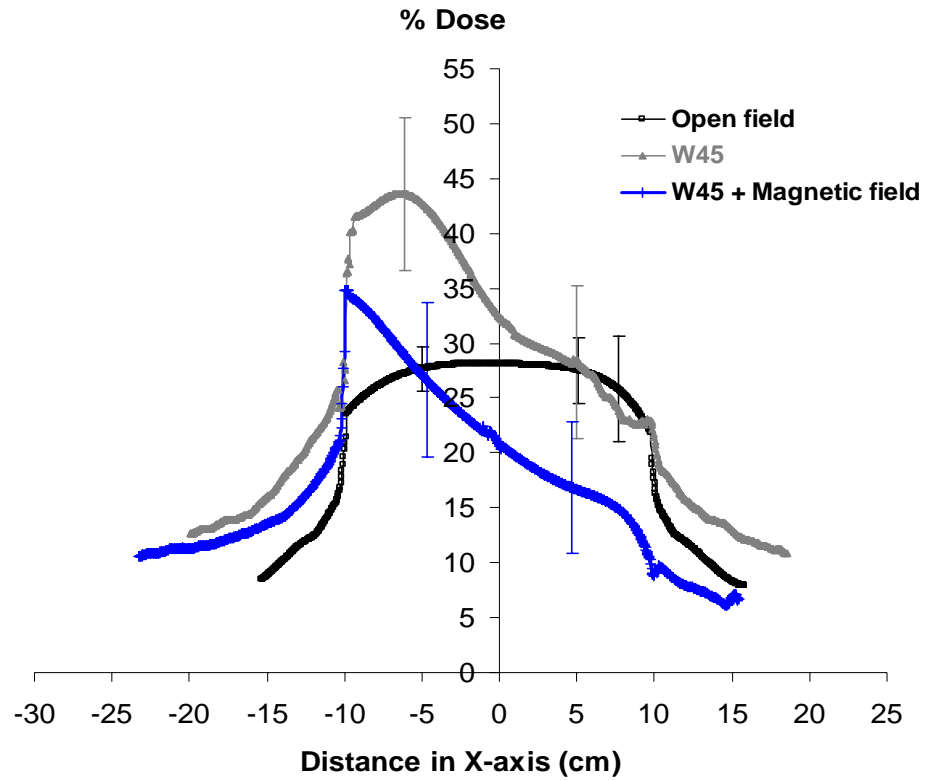
(a) Profiles measured in-plane and cross-plane for 6 MV x-ray beam with magnetic field for wedge field with a wedge angle of W15° compared with open field.

Extrapolated surface dose profile for 6 MV

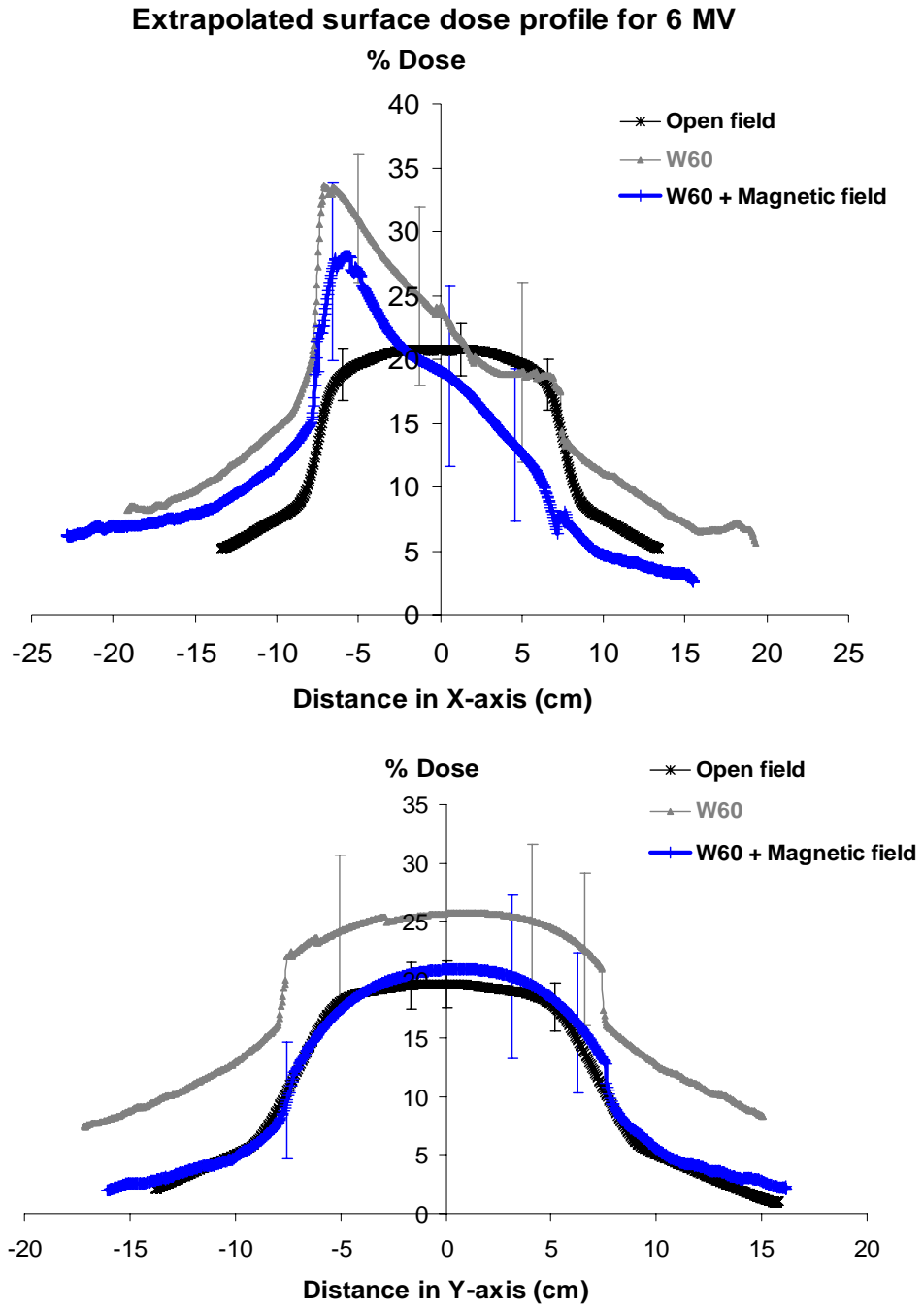


(b) Profiles measured in-plane and cross-plane for 6 MV x-ray beam with magnetic field for wedge field with a wedge angle of W30° compared with open field.

Extrapolated surface dose profile for 6 MV



(c) Profiles measured in-plane and cross-plane for 6 MV x-ray beam with magnetic field for wedge field with a wedge angle of W45° compared with open field.



(d) Profiles measured in-plane and cross-plane for 6 MV x-ray beam with magnetic field for wedge field with a wedge angle of $W60^\circ$ compared with open field.

Figure 5.8. Extrapolated surface doses are shown for profiles measured in-plane and cross-plane for 6 MV x-ray beam with magnetic field for wedge field with a wedge angle of (a) $W15^\circ$, (b) $W30^\circ$, (c) $W45^\circ$, and (d) $W60^\circ$ compared with open field.

The surface dose profile measured cross-plane differs from the surface dose profile measured in-plane when the magnetic field is used. Results have shown that the surface dose is reduced at all sites within the radiation field size with larger reductions seen on one side of the field due to the nature of the Lorentz force rule. The effects of 15°, 30°, 45°, and 60° wedges on the surface dose for a 6 MV x-rays is displayed in Table 5.1. Percentage surface doses are shown for field sizes of 15 x 15 cm² to 20 x 20 cm². These results were measured using radiographic film. The surface dose for a 15° wedge field was lower than the dose for an open field for the same field size, but the surface dose is higher than that of the open field in the case of the higher degree wedges.

Table 5.1. Surface doses for field sizes of 15 x 15 cm² and 20 x 20 cm² for 6 MV x-rays using radiographic film combined with a wedge and magnetic field.

% Surface dose from radiographic film									
F.S. (cm ²)	Open field	W15°	W15°+ magnet	W30°	W30°+ magnet	W45°	W45°+ magnet	W60°	W60°+ magnet
15 x 15	19.3							23.38	17.31
20 x 20	26.9	25.29	17.64	37.58	23.09	32.41	20.05		

These effects come from the elimination of contamination by the wedge and production of contamination by the secondary x-rays produced in the wedge. A small wedge angle such 15° produces a decontamination effect or effectively reduces the percentage dose at the surface compared to open field. The effects come from the hardening of the x-ray beam where lower energy photons are absorbed, increasing the electron range, and the wedge absorbs electron contamination produced inside the treatment head. However, higher wedge angles, such as 30°, 45°, and 60°, produce more contamination at the surface compared to open field. Table 5.2 illustrates an extrapolated surface dose for a field size of 20 x 20 cm² with a Perspex tray and with a wedge, with and without magnetic field. Results from Table 5.2 show that the percentage surface dose is higher with a beam modifier such as a Perspex tray or wedge.

Table 5.2. Surface dose for field size of 20 x 20 cm² with a Perspex tray and with different wedges used with and without magnetic field.

Percentage of surface dose of 6 MV x-rays for radiographic film		
	F.S. 20 x 20 cm ²	With magnetic field
Open field	27 ± 4 %	16 ± 4 %
With 6 mm Perspex tray	33 ± 4 %	19 ± 4 %
15° Wedge	25 ± 7 %	18 ± 7 %
30° Wedge	38 ± 7 %	23 ± 7 %
45° Wedge	32 ± 7 %	20 ± 7 %

In practice, a tray has to be designed to have a small amount of scattered radiation and transmit almost all of the incident photons, whereas a wedge is designed to have an intermediate amount of scattered radiation and transmit most of the incident radiation. As can be seen, surface doses are reduced in all cases when a magnetic field is used as well. With the use of a 6 mm Perspex tray in magnetic field, the surface dose is decreased because the magnetic field removes the particles such as electrons, while the tray both eliminates and generates the particles. A wedge also both eliminates the particles from upstream and generates new particles. It should be noted that the number of particles eliminated in the wedge is less than the number of particles produced by the wedge. According to the results, these effects increase the surface dose in case of the larger wedge angles. As can be seen, the surface dose is increased with the use of physical wedges, but the surface dose can diminish when a physical wedge is used in combination with a magnetic deflector device. As can be seen, surface doses also change significantly with different treatment set-up parameters. However, the contamination can be reduced in the treatment head by using a magnetic deflector device within the clinical treatment set-up.

5.4.4 Surface dose from Attix chamber and radiographic film

Results on the surface dose measured using an Attix chamber and radiographic film in the case of open field and magnetic field for field sizes of 10 x 10 cm², 15 x 15 cm², and 20 x 20 cm² are illustrated in Table 5.3. These 6 MV x-ray beam data from the Attix

chamber and radiographic film show that where there was a magnetic deflector, surface doses are matched well within 3 %. Surface doses in the case where the NdFeB deflector was used were reduced by 29-33 % \pm 1 % from the Attix chamber, and surface doses with the deflector were reduced by 32-41 % \pm 7 % from the surface dose extrapolated from the radiographic film. The reduction of the skin dose by using magnetic field is practicable in clinical radiotherapy treatment. This technology of the newly developed magnetic deflector is of great value for improvement in clinical outcomes of cancer treatment related to skin overdosing. We have proved that the new design of magnetic deflector attached to the accelerator head using an accessory tray is sufficient to remove the contamination-scattered electrons from the x-ray field.

Table 5.3. Surface dose measurements by an Attix chamber and extrapolated from radiographic film for field sizes of 10 x 10 cm², 15 x 15 cm², and 20 x 20 cm².

% Surface dose measurement						
Attix chamber				Radiographic film		
F.S. (cm ²)	Open field	Magnetic field	% Reduction	Open field	Magnetic field	% Reduction
10 x 10	16 \pm 1	12 \pm 1	33	14 \pm 7	9 \pm 7	36
15 x 15	21 \pm 1	15 \pm 1	29	19 \pm 3	13 \pm 3	32
20 x 20	27 \pm 1	18 \pm 1	33	27 \pm 4	16 \pm 4	41

5.5 Conclusion

Lepton contamination, which is usually produced by interactions of a high-energy x-ray beam from a medical linear accelerator, comes from Compton scattering and pair production process. A large amount of electrons originate from Compton scattering and pair production, whereas a small percentage of positrons is generated from the pair production process. Thus, electron particles are most important contaminants to study. These sources of contamination are ultimately responsible for the variation in contaminant doses caused by parameters such as the field size or the use of beam modifying devices. The secondary electrons that are set in motion and can accumulate

in the skin surface are generated from the scattering interactions of the high-energy x-rays with many of the components in a medical linear accelerator head and in the air volume between the linear accelerator machine and the patient or phantom. Thus, doses delivered in the skin surface are often dominated by electron contamination and can vary quite considerably within the first few millimetres of depth due to the build-up characteristics of x-ray beams.

Sources of electron contamination come from treatment head materials and treatment set-up parameters. An effective way to reduce this unwanted dose is by using a magnetic deflector mounted into the lower part of the linear accelerator treatment head. Measurements of the skin surface dose carried out using an Attix chamber and radiographic film are matched well within 3 %. Although radiographic film has a composition that differs from that of tissue, it still is commonly used for radiation dosimetry because it can be used to obtain a dose distribution of the radiation field with high spatial resolution. Radiographic film offers a convenient medium for easily generating profiles and two-dimensional distributions. These 6 MV x-ray beam data with and without the magnetic deflector show that a significant reduction of the skin dose by using magnetic field is practicable in clinical radiotherapy treatment. We have proved that our new design of magnetic deflector attached to the accelerator head is sufficient to remove the contamination-scattered electrons from the photon field.

CHAPTER 6

MONTE CARLO CALCULATIONS

6.1 Introduction

The energy and dose distributions of photons and contaminant charged particles such as electrons and positrons from medical accelerators are important information for radiotherapy using high-energy x-ray beams. Knowledge of clinical beams is essential for dosimetry and the development of a new accurate treatment planning system. Experimentally, it is difficult to obtain detailed information because of various limitations in the clinical environment and detectors. Monte Carlo simulation can be used to obtain the information that cannot be measured experimentally. One of the major advantages of the Monte Carlo technique is that it allows detailed information about each particle's history to be known. Originally, Mohan et al. (1985) calculated a photon's energy spectra and angular distributions using the EGS3 Monte Carlo code. The charged particles in the photon beams were not studied. Using the BEAM code, van der Zee and Welleweerd (1999) investigated some characteristics of a 10 MV photon beam from an ELEKTA SL Linac. Deng et al. (2000) also studied photon beam characterisation and modelling for treatment planning of 4 to 15 MV beams from Varian Clinac 2100C and 2300CD accelerators. Our study aims to provide more information on radiotherapy photon beams, including incident photons as well as contaminating electrons and positrons in a radiotherapy beam for different field sizes. This information enhances our knowledge of radiotherapy photon beams. It also serves as a benchmark to demonstrate the accuracy of the Monte Carlo technique in simulating the radiotherapy photon beams. In addition, it provides detailed information on the Monte Carlo computing speed required to simulate an incident beam and to calculate a dose distribution on current computers.

6.2 Monte Carlo approach to electron contamination sources in Varian Clinac 2100C

Monte Carlo methods are capable of determining doses accurately for the entire range of situations encountered in the treatment of cancer by modelling linear accelerators. These methods are able to correctly characterise beams of photons or electrons

emerging from medical linear accelerators. Calculated information on beam characteristics can be very useful for a variety of radiation dosimetry problems, such as studies of electron contamination in photon beams and accurate estimation of quantities difficult or impossible to measure in clinical physics. This is because the Monte Carlo method uses basic physics and interaction probabilities to determine the behaviour of particles. The interactions between each particle and the surrounding media are simulated. The particles reaching the patient are generated in parts of the accelerator head, such as in the collimating jaws or multileaf collimators, and in the air column between the accelerator and the patient.

In contrast to the other common techniques, the Monte Carlo method tracks individual particle histories and is used to calculate the trajectories of particles, including the secondary particles that they may generate from the accelerator head to the patient. All of the energy is introduced into the system from the initial particle. These particles must be absorbed by or escape from the system. Then a map of the energy deposition throughout the system is created and iterated for a very large number of particles. The result is an estimate of the average energy deposited in the system per particle due to the radiation source. The obtained data for each simulated particle at any location in the system consists of the dose deposited per particle, the dose deposited per electron or per photon, the particle fluence, the energy spectrum, and the electron and photon spectra. Moreover, the Monte Carlo technique used for dose calculations produces accurate results and provides an accurate method for the simulation of patient treatment doses. One problem with the method is the long computing time needed to get statistically acceptable dose results.

Although Monte Carlo code has been suitable for patient dose calculations in radiotherapy, its achievements have been limited by the lack of a general and accurate model of the accelerator radiation source. Recently, advances in Monte Carlo dose calculation algorithms, combined with increasing computer-processing speed, have made the Monte Carlo dose calculation procedure acceptable for radiotherapy clinics. Thus, Monte Carlo techniques to calculate the behaviour of radiotherapy beams have been studied in various groups. The user code BEAMnrc is a general purpose EGSnrc user code for the simulation of radiotherapy beams from treatment units (Rogers et al., 2002). The code has been used in various beam simulations and shows very good

agreement between measurements and calculations. The user code BEAMnrc was used in this study for a photon beam of 6 MV generated by a Varian Clinac 2100 C linear accelerator.

It is recognised that the various components of the accelerator treatment head present as sources of contaminating electrons. The interaction of the x-rays beam with the mechanical parts of the linear accelerator and the air below the machine head produces a continuous spectrum. High-energy photon beams have the advantage of the skin-sparing effect while the presence of contaminating electrons reduces this advantage. Investigation of the electron contamination sources offers important knowledge for developing methods for detection of electron contamination. Experimentally, it is difficult to find the origin of these electrons.

The influence of electron contamination on the dose distribution in a phantom has been investigated by the number of authors (Biggs and Ling, 1979, Biggs and Russel, 1983, Sixel and Podgorsak, 1994, Rogers et al., 1985, Attix et al., 1983, Jursinic and Makie, 1996, Zhu and Palta, 1998, Sjogren and Karlsson, 1996). They performed experiments to measure the increase in surface dose and the shift of the depth of the maximum dose to near the surface from increasing the field size or decreasing the source-to-surface distance (SSD). In some experimental studies a magnet was used below the treatment head to sweep away the electrons that were also coming from the linear accelerator head (Biggs and Russel, 1983, Jursinic and Mackie, 1996, Sjogren and Karlsson, 1996). Attix et al. (1983), LaRiviere (1983), and Sjogren and Karlsson (1996) measured the contamination in the therapeutic beams.

The Monte Carlo technique can separate the contamination components from the beam so that its contribution to the dose distribution can be studied. In this study, a Monte Carlo simulation of components of the Varian Clinac 2100C has been performed in order to locate the main sources of contamination of the x-ray beams and the contribution to the dose at the surface and the build-up region. Deterministic radiation fields are divided into two regions that correspond to the linear accelerator head region and the phantom volume of interest. Each region contains a number of component modules of uniform composition. In the linear accelerator head region, the component modules represent such components as the target, primary collimator, flattening filter,

vacuum window, ion monitor chamber, mirror and secondary collimators as well as the multileaf collimators, Mylar plate, or air column. In the phantom region, the component modules usually correspond to rectangular voxel elements describing the phantom geometry.

6.3 Methods and materials

6.3.1 Monte Carlo method

Simulating a photon beam from a medical linear accelerator by BEAMnrc has the aim of obtaining a better understanding of the radiation transport in a linear accelerator's radiation head with regards to the influence of field size, spectral and fluence distribution of photons and electrons, and the contaminant particles. Simulations in phantoms have been done using DOSXYZnrc code to determine the build-up depth dose curves and beam profiles. All these data have been compared with measurements in identical geometries. The geometrical description for Monte Carlo simulations of dose depositions in phantoms, including a full linear accelerator description such as of the particle transport through target and flattening filter, ion monitor chamber, and mirror, will enter the calculations in all simulations, while the only varying parts can be found in the jaw setting and the phantom. Therefore, the simulated geometry has been separated into a phantom and a linear accelerator section, which describes the treatment head of a Varian Clinac 2100C. The latter section again was subdivided in two subsections. For each part the component module (CM) from EGSnrc user-code BEAMnrc that is used is shown between parentheses as describe below:

First section (Figure 6.1) containing

1. X-ray target consisting of Tungsten and Copper material (SLABS)
2. Primary collimator consisting of Tungsten material (CONS3R)
3. Vacuum window consisting of Beryllium material (SLABS)
4. Flattening filter consisting of Aluminium material (FLATFILT)
5. Ion monitor chamber consisting of Kapton material(CHAMBER)
6. Mirror consisting of Mylar (MIRROR)

Second section (Figure 6.1) containing

1. Secondary collimator consisting of Tungsten material including Y (upper) jaws and X (lower) jaws (JAWS)
2. Multileaf collimator consisting of Tungsten material (VARMLS)

3. Sheet of Mylar at the underside of the radiation head consisting of Mylar (SLABS)
4. Air (SLABS)

The details of the construction and materials were taken from original drawings made available for this application by the manufacturer, Varian Oncology Systems, using the files generated by the EGSnrc user-code BEAMnrc at the lower end of each section. All particles were scored and stored in a phase space file (a file containing all parameters of a particle crossing a plane of interest). This file can be used as an input file for the lower part of the linear accelerator head. Simulations in phantoms were done using the EGSnrc user-code DOSXYZnrc to determine the build-up depth dose curves and cross beam profiles for the calculation of beam characteristics.

The configuration of BEAMnrc during these simulations allowed tracking of each particle through the geometry. Therefore, it was possible to find out where each particle interaction occurred. The phase-space files that were produced contained all scored particles at a plane of 100 cm from the target of the linear accelerator. A total of 5.0×10^8 and 9.0×10^8 electron histories were simulated for the $10 \times 10 \text{ cm}^2$ and $20 \times 20 \text{ cm}^2$ fields, respectively. The parameters for EGSnrc controlling the particle transport are: AE = 0.521, 0.700 MeV, ECUT = 0.521, 0.700 MeV, AP = 0.010 MeV, and PCUT = 0.010 MeV; Rayleigh scattering OFF; boundary crossing algorithm EXACT; electron-step algorithm PRESTA-II; bound Compton scattering, photoelectron angular sampling, atomic relaxations and spin effects ON; and pair angular sampling as well as bremsstrahlung angular sampling KM (Koch and Motz).

To increase the efficiency of our BEAMnrc code simulations, a variance reduction technique called selective bremsstrahlung splitting was used. In two sections of phase-space file data, selective bremsstrahlung splitting (SBS) was used for 150 photons for each event. The Russian roulette option was also turned on. The simulation speed depended on the number of electron histories and field sizes as well as the incident electron beam characteristics. The size of a phase space file varied from 1.0 to 2.0 Gbytes. To investigate the BEAMnrc phase-space data to calculate the spectral and fluence distributions we used BEAMDP. BEAMDP (BEAM Data Processor) is a program to analyse the BEAMnrc phase-space data and to derive the following data:

1. Spectral distributions from phase-space data

Spectra have been generated by sampling the energy of all particles inside the area of interest in equally spaced energy bins. For fluence profiles, sampling is done using equally spaced rings around the beam axis. The contribution of each ring is normalised using its surface relative to the surface of the central area.

2. Fluence versus position from phase-space data

When this option is chosen BEAMDP will process the phase-space data and generate fluence versus position data file for xvgr plots. The field types, field dimensions, particle type, LATCH options, and the names of the phase space file will be selected to process the data file for outputs. The graph type allows fluence to be plotted as a function of position. Each data point in the data file represents the total number of particles scored within a given spatial bin for the particle types and LATCH options.

3. Mean energy distributions from phase-space data

When this option is chosen BEAMDP will process the phase-space data and generate a mean energy data file for xvgr plots. Each data point in the data file represents the mean energy of the particles scored within a given spatial bin for the particle types and LATCH options.

The following parameters are used to analyse the BEAMnrc phase-space data. The number of energy bins (N_{bin}) for the spectrum is 100.

1. Energy of particle (kinetic energy) in MeV
2. IQ, charge of particle (-1 for electron, 0 for photon, 1 for positron)
3. X and Y -coordinates in cm
4. U, V, W, the direction cosines with respect to the x-, y-, and z-axes
5. WEIGHT, weight of particle
6. LATCH, a tag to record the history of a particle. (Only bits 0 - 28 will be chosen.)

For dose calculation, the stored phase-space files were used repeatedly as source inputs for the calculation in a water phantom of Cartesian voxel geometry using the EGSnrc user-code DOSXYZnrc. Simulations in phantoms were done using DOSXYZnrc code to determine the build-up depth dose curves and cross profiles. For the calculation of beam characteristics, two different media have been used:

1. A full-scatter simulation of a water phantom used for direct measurements of the dose build-up curves and cross profiles, for calculations in full scatter geometries.
2. A radiographic film for calculations of the surface dose in a water phantom so that dose build-up curves could be calculated.

All voxels in the phantom as well in the full scatter phantom have a $0.2 \times 0.2 \times 0.01 \text{ cm}^3$ size, being a compromise between accuracy and available calculation power. The voxel size ranged in volume from 0.01 to 1.0 cm^3 . These divisions were not equal in size in order to minimise the total number of voxels while maintaining good resolution where needed. Usually, a smaller voxel size was chosen for the build-up depth dose region. Central axis depth dose curves were calculate in the $1 \times 1 \text{ cm}^2$ region around the central axis for $10 \times 10 \text{ cm}^2$ fields. Moreover, the depth of 10 cm was chosen because of the dose profile's insensitivity to the effect of contamination electrons. The calculation speed was about 5.0×10^8 histories for field size $10 \times 10 \text{ cm}^2$ and $20 \times 20 \text{ cm}^2$.

During the DOSXYZnrc simulation, the phase space sources were recycled many times in most cases to obtain acceptable statistical uncertainty. Walters et al. (2002) recommended that the recycling of phase space sources be accurately reflected in the uncertainty estimation of the photon beam simulation. Therefore, when the phase space source was restarted, the DOSXYZnrc simulation was repeated after adjusting a parameter, NRCYCL, by taking into account the number of missing and rejected particles during the previous run, to avoid an underestimation of the uncertainty. The statistical uncertainties of the simulated dose values were generally 1 %. The full scatter phantom has been configured in DOSXYZnrc. This user code is specially designed for the calculation of dose distributions in arbitrary geometries at SSD 100 cm for each square field in the range from $5 \times 5 \text{ cm}^2$ to $20 \times 20 \text{ cm}^2$. For each field size, the following data have been sampled:

1. Dose build-up curves on the central axis of all particles and electrons.
2. Cross profiles for four depths: at the surface and at 1.5 , 5 and 10 cm distance along the X and Y-axes for all particles and electrons.

6. 3.2 Linear accelerators

The study was carried out on a Varian Clinac 2100C linear accelerator with a nominal energy of 6 MV . A detailed description of the geometry that is required for the most accurate simulation was provided by the manufacturer (Figure 6.2 and Table 6.1).

6.3.2.1. Target

The target in the linear accelerator machine is made of tungsten and copper. The electron beam strikes a target button composed of two layers. The first layer is made of tungsten with a thickness of 0.0889 cm . (Most of the bremsstrahlung photon production

occurs here.) The second is made of copper with a thickness of 0.15748 cm (for fast heat dissipation).

6.3.2.2 Primary collimator

The primary collimator is made of tungsten with a thickness of 6.0 cm. It has a conical opening with a 14° angle from the isocentre line.

6.3.2.3 Vacuum window

The vacuum window is downstream of the primary collimator by 1.2 cm. It is 0.254 mm thick and made of beryllium material.

6.3.2.4 Flattening filter

The flattening filter, which is made of aluminum, lies below the primary collimator. The filter is designed to be thicker in the centre than on the outer edges in order to produce a flat radiation field at depth. The x-rays spectra are harder at the centre and become soft away from the centre.

6.3.2.5 Ion monitor chamber

The ion monitor chamber is made of Kapton. It can be modelled as several equidistant parallel plates with 3 windows and 4 signal plates.

6.3.2.6 Mirror

The mirror is made of Mylar with an angle of 35° .

6.3.2.7 Secondary collimator

The secondary collimator jaws are made of tungsten. The upper jaws rotate in towards each other about a radius. The lower jaws pivot in towards each other about a line.

6.3.2.8 Multileaf collimator

The multileaf collimator is 120 Millennium MLC Varian 2100C. The thickness of a leaf is 6.5 cm. There are 40 leaves with a tongue and groove.

6.3.2.9 Light field

The light field is made of Mylar with a thickness of 0.01016 cm it is 2 cm below the multileaf collimator.

6.3.2.10 Air

The air column is between the accelerator and the patient.

A feature of the EGSnrc Code system is that the radiation transport of photons or electrons can be simulated in any element, compound, or mixture. The data package PEGS4 creates data to be used by EGSnrc Code. The cross-section data for BEAMnrc is created by PEGS4 code. Data are based on the density effect corrections in ICRU

Report 37 of two large data files where the energy range is from the AE values of 0.521 or 0.700 MeV up to 55 MeV in both cases. The parameter AE is the low-energy threshold for electron productions, and AP is the low-energy thresholds for the production of secondary bremsstrahlung photons. The parameters PCUT and ECUT are required to be greater than or equal to AP and AE. Both photons and charged particles are transported in steps of random length. The physics processes in this code are bremsstrahlung production, positron annihilation, multiple scattering of charged particles, Moller ($e^- e^-$) and Bhabha ($e^+ e^-$) scattering, pair production, Compton scattering, Rayleigh scattering, the photoelectric effect, and the relaxation of excited atoms after photoelectric or Compton scattering events.

Table 6.1. The description of the accelerator geometry is provided by the manufacturer.

Component	Distance from Target to isocentre	Material
X-ray Target 6 MV	0	Tungsten (W) 0.0889 cm Copper (Cu) 0.15748 cm
Primary collimator	1.6 cm	Tungsten (W) 6 cm thick
Vacuum window	9 cm	Beryllium (Be) 0.0254 cm
Flattening filter	10.45 cm	Copper (Cu) with 19 layers
Ion monitor chamber (3 windows, 4 signal plates)	14.835 cm	Kapton
Mirror	17.985 cm	Mylar 0.00508 cm
Secondary collimator jaws Upper (Y) -jaws Lower (X) -jaws	28 cm 36.7 cm	Tungsten (W) 7.8 cm Tungsten (W) 7.8 cm
Multi-leaf collimator 120 Millennium Varian 2100C	47.8 cm	Tungsten (W) 6.5 cm thick 40 leaves (width = 0.25525 cm)
Mylar plate	57 cm	Mylar 0.01016 cm

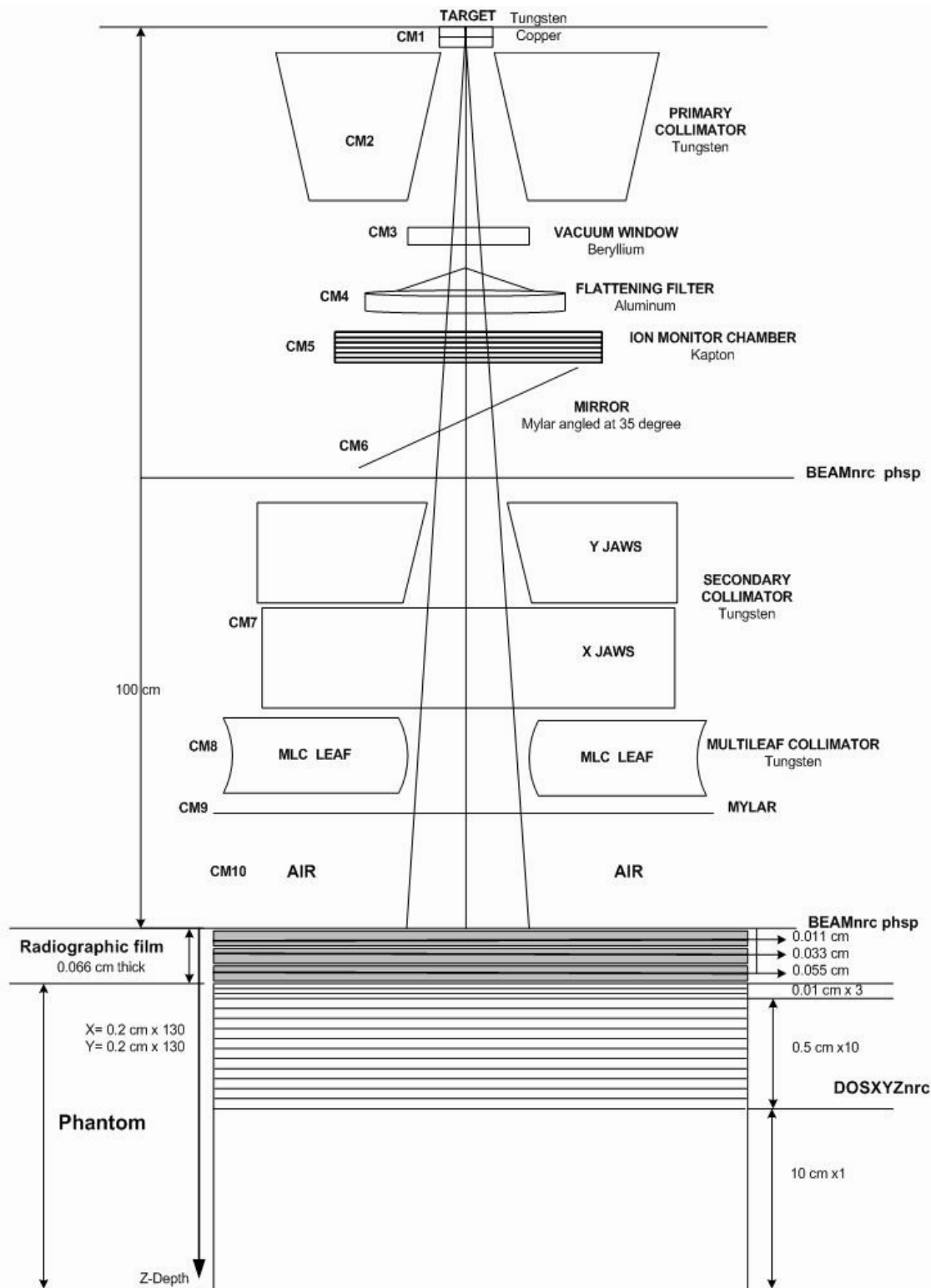


Figure 6.1. Schematic drawing of linear accelerator components modelled in Monte Carlo simulations.

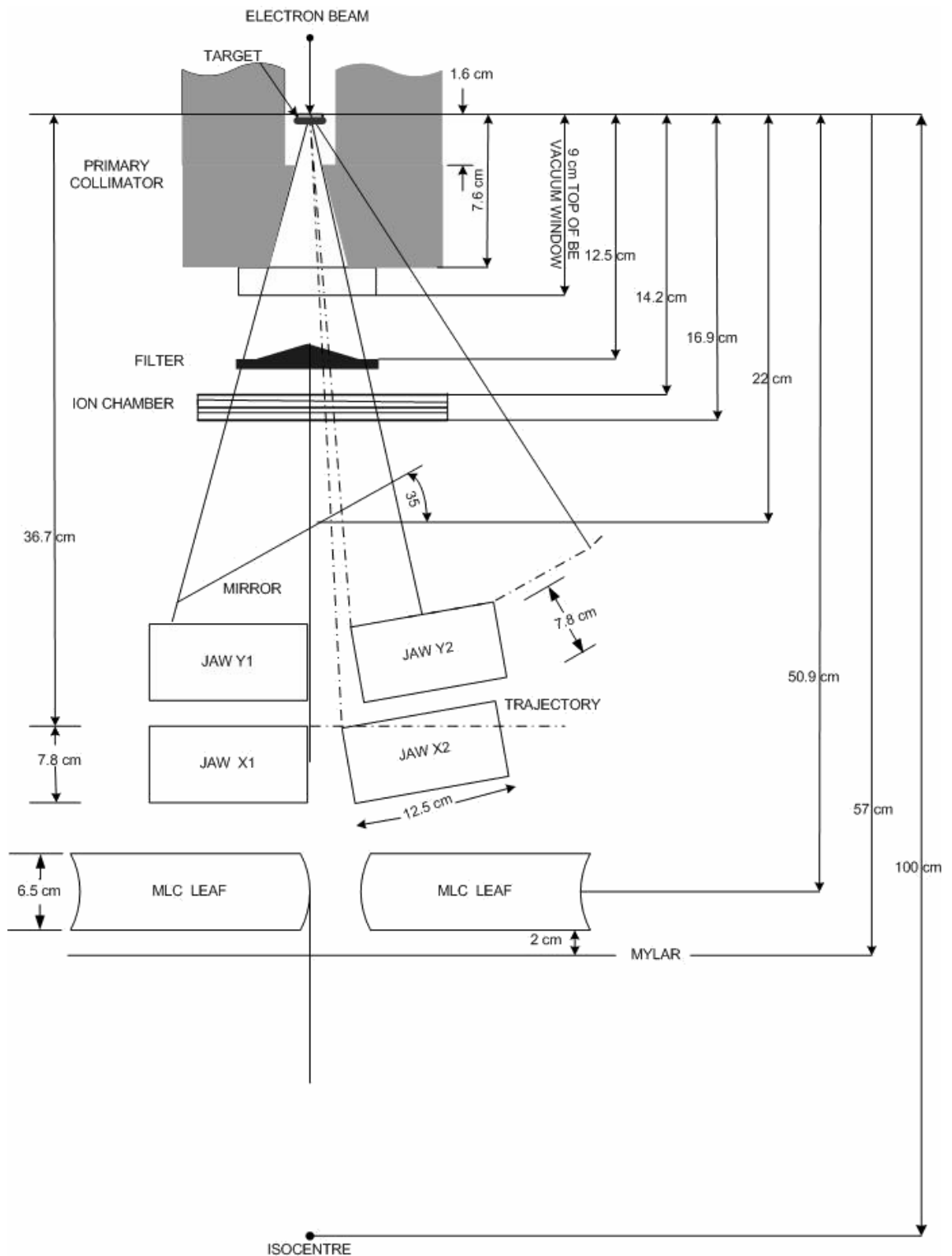


Figure 6.2. Schematics of the geometry illustrating the accelerator head components. The distance from the source to the isocentre is 100 cm.

6.3.3 Monte Carlo simulation

The simulation was performed using the code BEAMnrc (Rogers et al., 2002) running in Linux. The BEAMnrc is a code based on the EGSnrc Monte Carlo code system for the simulation of radiotherapy beams from a linear accelerator. EGSnrc Monte Carlo codes in these studies were BEAMnrc and DOSXYZnrc. BEAMnrc was used for transport through the accelerator treatment head and DOSXYZnrc was used for tallying dose in a water phantom.

6.3.3.1 Beam model

Figure 6.1 shows a schematic layout of the treatment head configuration used in this study. The model consists of several units, such as the target, primary collimator, vacuum window, flattening filter, ion monitor chamber, mirror, jaws, MLC leaves, Mylar plate, and phantom. The phase space files specify the energy, position, and direction of photons and electrons on a plane situated between the mirror and jaws as well as on a plane in air after passing through linear treatment head at 100 cm SSD. All radiation transport through the linear accelerator head was modelled using the BEAMnrc code. Details of the geometric modelling of the all the component modules are described below.

Transport from the phase space definition plane, through the beam defining jaws, and following the jaws to and through the phantom was accomplished using EGSnrc with the user codes BEAMnrc and DOSXYZnrc. To create phase-space data for calculation, Monte Carlo simulations of the radiation transport for both photons and electrons of a 6 MV beam from a Varian Clinac 2100C was performed using BEAMnrc. The treatment head geometry and materials used for input were based on data supplied by the accelerator's manufacturer. Simulations were initiated with electrons striking the target. Primary and secondary particles were transported through the linear accelerator head, which contains the target, primary collimator, vacuum window, flattening filter, monitor chamber, mirror, secondary collimator, multileaf collimator, light field, and intervening air volume. The appropriate transport parameters and variance reduction techniques were used. In the simulation of the full linear accelerator head, we split the calculation into three steps for the scoring plane in order to save time.

6.3.3.1.1 Scoring plane at mirror

In the first step for the scoring plane, which takes the most computing time, photons are initiated uniformly throughout the material region within which particles are transported directly to the flattening filter through the ion monitor chamber and mirror, where coordinates are saved in a phase-space data file. The target, primary collimator, and vacuum window are also included in this scoring plane. The output of this scoring plane is a phase space file containing the data on position, energy, direction, charge, and history variables for each particle exiting downstream from the primary collimator. The phase-space scoring plane is perpendicular to the beam axis. Since the target and primary collimator do not move during the adjusting of the outer collimator for different openings, it is possible to use this phase space data for the simulation of all field sizes. Thus this set of particles is used repeatedly as the input to the next step of the simulation.

6.3.3.1.2 Scoring plane in air volume at SSD 100 cm

The second step of the scoring plane simulates the passage of the particles through the secondary collimator, multileaf collimator, light field, and air volume to the SSD plane. We simulate different openings of the outer collimator to get field sizes from $5 \times 5 \text{ cm}^2$ to $30 \times 30 \text{ cm}^2$ at an SSD equal to 100 cm. We use the variable LATCH, which allows us to store each particle's history during the first and second steps of the beam simulation. Therefore, we are able to determine if a particle is scattered in the target, primary collimator, adjustable collimator, or air slab before reaching the scoring plane. This information will be used in the next step to calculate the fluence and energy spectra of the particles scattered by different regions.

6.3.3.1.3 Scoring plane in the water phantom

In the third step of the simulation, the phase space files for field sizes of $5 \times 5 \text{ cm}^2$ up to $30 \times 30 \text{ cm}^2$ at an SSD of 100 cm are used from the BEAMnrc code as an input to dose calculations in a water phantom using DOSXYZnrc code. In these cases we transport the particles through a phantom of 30 cm diameter by 13 cm thick.

6.4 Results and discussion

6.4.1 Linear accelerator head

6.4.1.1 Spectral distribution

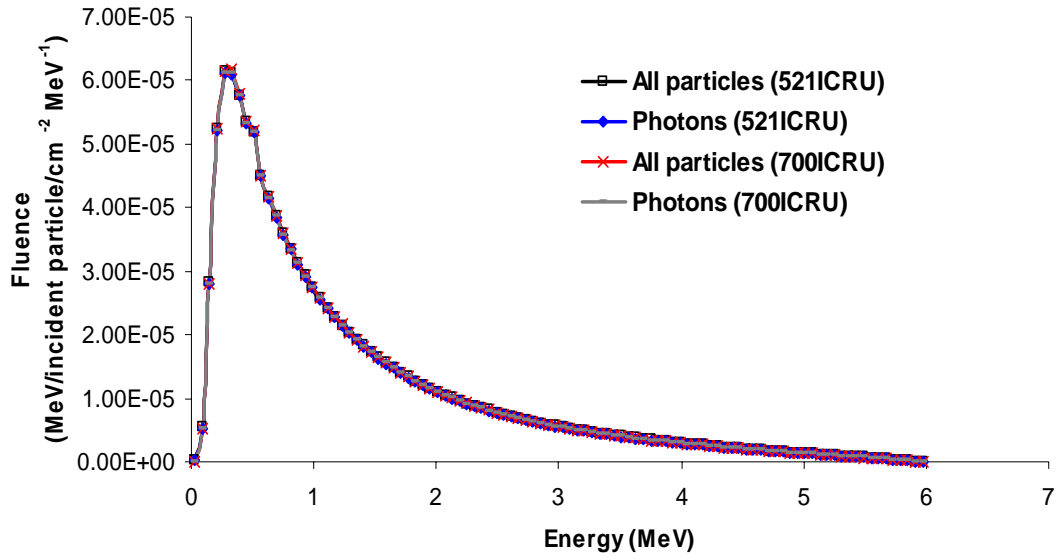
Results are shown in Figures 6.3 and 6.4 for the 6 MeV beam from a Clinac 2100C. Interactions that produce secondary electrons with energy greater than AE and photons with energy greater than AP are explicitly simulated. The spectra calculated with AE = 0.521 and AE = 0.700 MeV for all particles and photon spectral shapes are the same; only the electron spectra are different. However, the electron spectral shapes are similar to the photon spectrum. The cross sections and number of particles to be transported are increased by using a lower AE value. AE is the low energy threshold for the secondary electron production, while AP is the low energy threshold for bremsstrahlung production. The more incident electrons, the more photons are produced, therefore most of the photon fluence is directly contributed by photons that have interacted in the target, before reaching the scoring plane at 100 cm. Secondary photons and electrons produced within the accelerator head are also generated from the Compton process. The photon spectrum increases from zero at 0 MeV to a maximum at a modal energy of 0.51 MeV, and then decreases from this modal energy to zero at the maximum energy of 5.97 MeV for AE = 0.521 and 0.700 MeV at the scoring plane at 100 cm. Whilst the photon spectrum increases from zero at 0 MeV to a maximum at a modal energy of 0.27 MeV, it then decreases to zero at the maximum energy of 5.97 MeV for AE = 0.521 and 0.700 MeV at the scoring plane after passing through the mirror material.

The selection of AE is more complex since there is some computing time associated with lower values of AE. This is because the lower values lead to more accurate simulations and the value of AE controls the statistical fluctuations in the energy loss that can affect the electron step sizes. The spectrum calculated with AE = 0.521 MeV is clearly more practical than that calculated with AE = 0.700 MeV for an explanation of the details of electron behaviour. The values of the electron spectrum for lower energy components are increased by using AE = 0.521 MeV as compared to AE = 0.700 MeV. These effects are caused exclusively by the contribution to the lower energy component of electron production by using the lower AE value.

From the phase space files for different cross-section data – PEGS4 (521ICRU and 700ICRU), cross-section data for BEAMnrc is created by the code PEGS4 with two large data files. The energy range is from the AE values of 521 or 700 keV up to 55 MeV in both cases. These data are based on the density effect corrections in ICRU Report 37. The parameters AP and AE are the low-energy thresholds for the production of secondary bremsstrahlung photons and knock-on electrons, respectively. The parameters are required for $PCUT \geq AP$ and $ECUT \geq AE$. The technique to increase calculation speed is to set photon and electron transport cut-off energies. The values quoted for the photon transport cut-off values are from 0.005 to 0.1 MeV, while for the electron transport cut-off in linear accelerator materials they are from 0.1 to 1.0 MeV (Verhaegen and Seuntjens, 2003). For analysing, we used $AE = 0.521$ and 0.700 MeV and $ECUT = 0.521$ MeV, $AP = 0.01$ MeV and $PCUT = 0.01$ MeV, respectively. The electron (AE) and photon (AP) production thresholds were set to kinetic energies of 10 keV. The phase space files for the different cross-section data after passing from the target through the air at SSD 100 cm from the linear accelerator head have the same results, as the investigation focuses on the spectral distribution to visualise all the particle, photon, and electron distributions from the first section of linear accelerator (after leaving the mirror material).

According to our model, influence of $AE = 0.521$ MeV on the spectrum for a 6 MV beam for all particles and photons after passing through mirror as well as electrons after passing through mirror with estimated accuracy 1% in Figure 6.3 is better because the spectrum calculated with 521ICRU is clearly more practical than that calculated with 700ICRU for an explanation of the details of electron behaviour. Influence of AE on the spectrum for a 6 MV beam for all particles and photons and electrons at SSD5100 cm with estimated accuracy 1% also choose the phase space files for different cross-section data 521ICRU in Figure 6.4. The resultant electron energy spectrum using 521ICRU in a clinical photon beam will be similar to that in a clinical photon energy spectrum. As demonstrated by Ma et al (1997), the electron energy spectrum is an important component of any dose calculation code used for electron beam radiotherapy. The electron energy spectrum has a dominant effect on the central axis depth dose curves. Thus in this study using electron energy with 521ICRU is clearly more practical for an explanation of the details of electron behaviour.

a) Spectral distribution of 6 MV beam from Target to Mirror



b) Spectral distribution of 6 MV beam from Target to Mirror

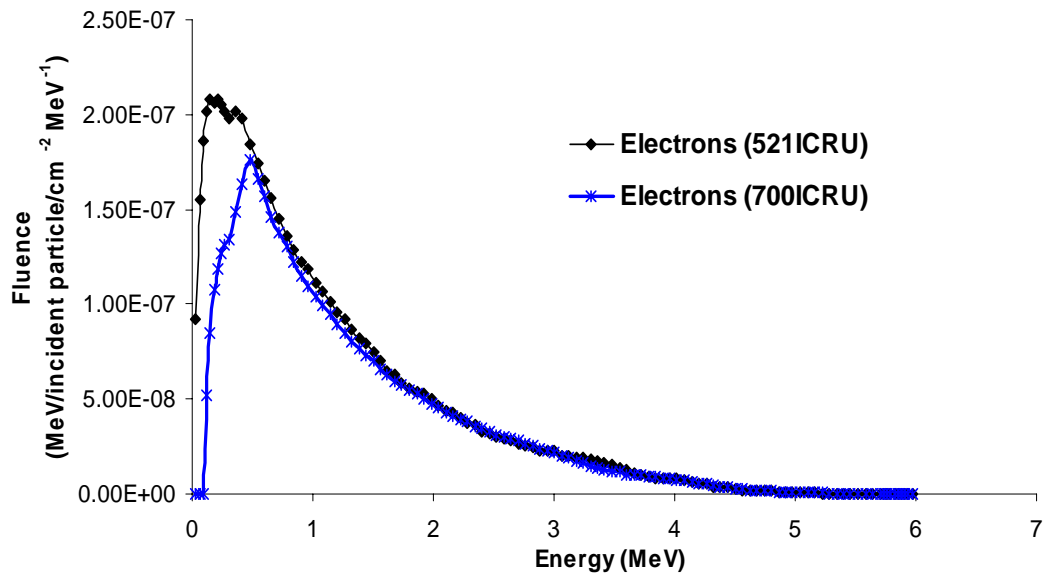
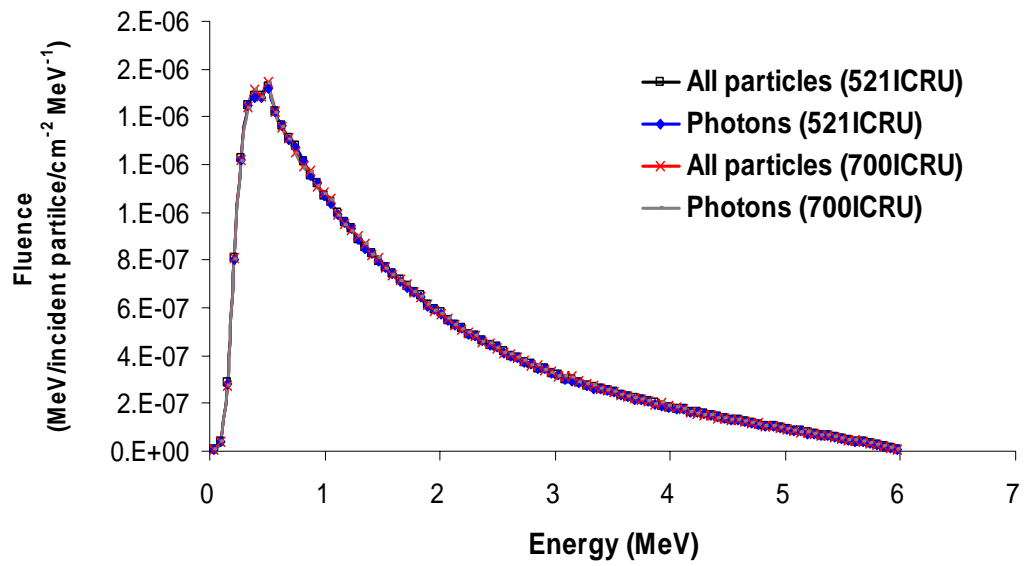


Figure 6.3. Influence of AE on the spectrum for a 6 MV beam for a) all particles and photons after passing through mirror, b) electrons after passing through mirror; estimated accuracy 1%.

a) Spectral distribution of 6 MV beam for F.S. 10x10 cm² at 100 cm SSD



b) Spectral distribution of 6 MV beam for F.S.10x10 cm² at 100 cm SSD

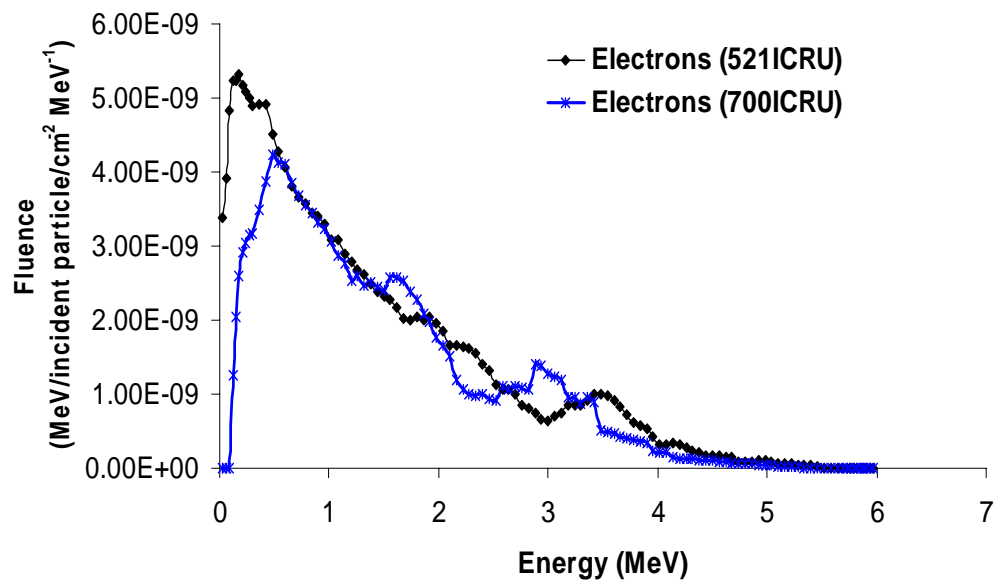


Figure 6.4. Influence of AE on the spectrum for a 6 MV beam for a) all particles and photons, b) electrons at SSD5100 cm; estimated accuracy 1%.

6.4.1.2 Fluence distribution

Results from Figures 6.5 and 6.6 show the fluence distribution of photon and electrons at the scoring plane after passing through the mirror material in the linear accelerator head and at 100 cm from the target material. For all particles and photons the fluence distributions are the same except that the electron fluence distributions are different when compared with different AE values. A lower AE means a broader electron fluence distribution, because the lower threshold is for the production of low energy knock-on electrons that are important for the study of electron contamination. Bremsstrahlung production would be the dominant interaction.

The photon beams produced in clinical linear accelerators are modified by a series of attenuating devices, including the target itself and the-beam flattening filter. These devices attenuate some of the photons in the un-attenuated beam before they reach the scoring plane, changing the spectral distribution. This is because the flattening filter is the primary modifier of the beam spectrum. The flattening filter is radially symmetric, and removes more low-energy photons from the centre of the beam than from the edge, which differentially hardens the beam in the radial direction by attenuating many of the low energy photons in the beam. The photon fluence distributions vary as a function of distance from the central ray. When the x-ray photons and particles are transported from the target and through the flattening filter, the ion monitor chamber, and the mirror, the secondary jaw setting defines the area for the fluence at the distance of 100 cm from the target material. These photon fluences are more uniform when compared to the fluences at the scoring plane after the mirror material.

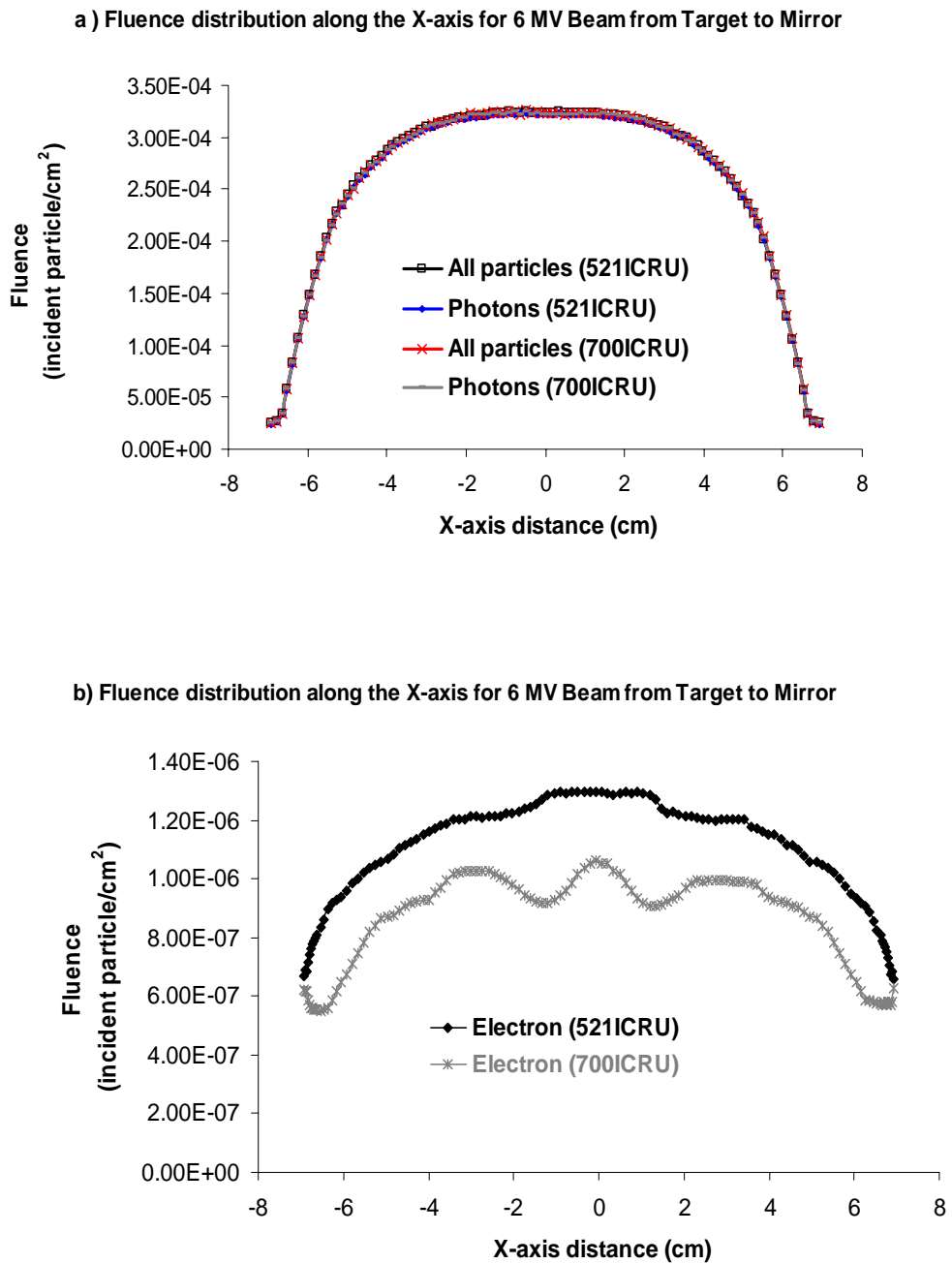
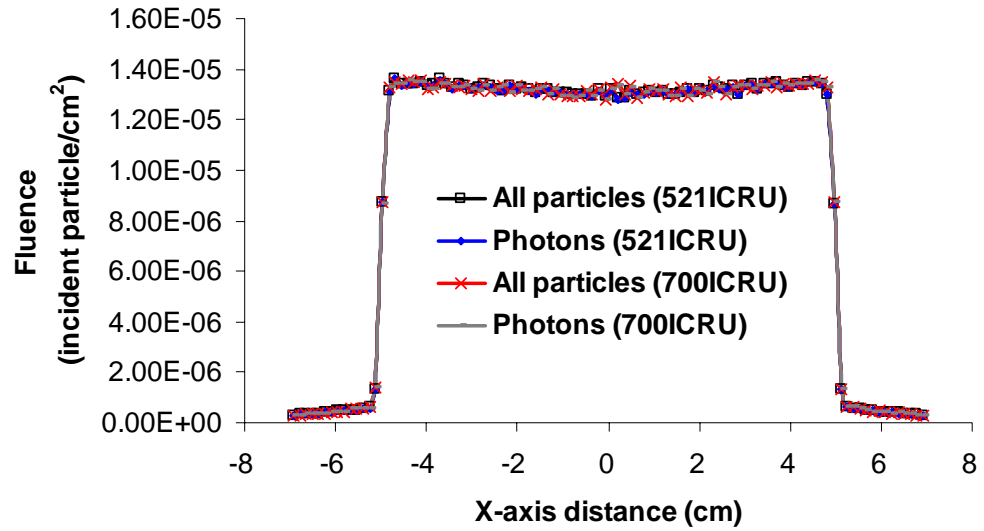


Figure 6.5. Influence of AE on the fluence along the X-axis for a 6 MV beam for a) all particles and photons after passing through the mirror, b) electrons after passing through mirror; estimated accuracy 1%.

**a) Fluence distribution along the X-axis of 6 MV Beam
for F.S. 10x10 cm² at 100 cm SSD**



**b) Fluence distribution along the x-axis of 6 MV Beam
for F.S. 10x10 cm² at 100 cm SSD**

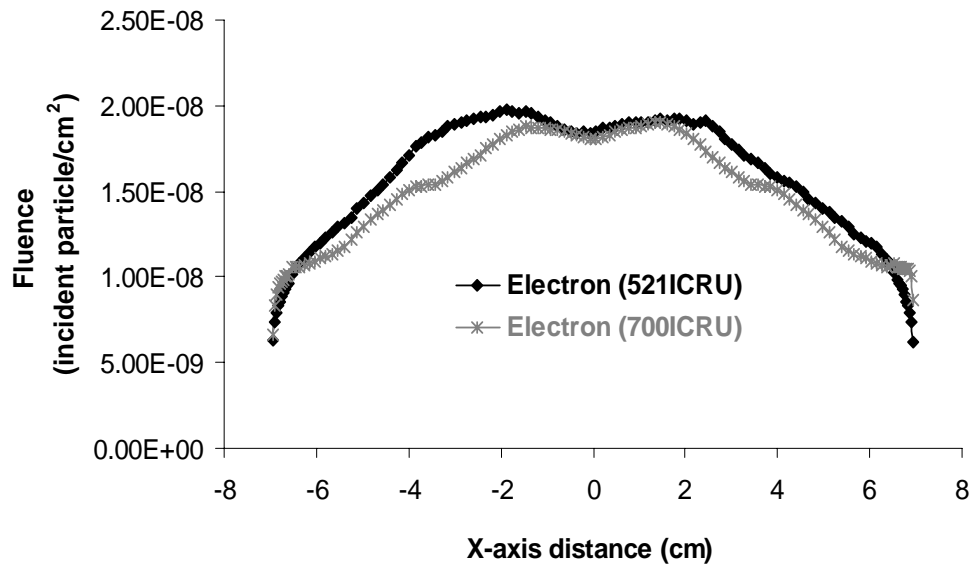


Figure 6.6. Influence of AE on the fluence along the X-axis for a 6 MV beam for a) all particles and photons after passing through air at 100 cm, b) electrons after passing through air at 100 cm; estimated accuracy 1%.

6.4.1.3 Mean energy of particles

Results from Figure 6.7 illustrate the mean energy of photons and electrons for different AE values. A 6 MeV electron beam strikes a thin, high-Z target. The primary collimator collimates the bremsstrahlung radiation so produced. The forward-peaked bremsstrahlung energy fluence distribution is flattened by a conical piece of metal and then passes through the aperture defined by the secondary jaws. Photons escaping the bottom of the linear accelerator and heading for the $10 \times 10 \text{ cm}^2$ field size are shown. The mean energy for photons is 1.68 MeV at distance of 100 cm for both AE = 0.521 and 0.700 MeV, whereas the mean energies of the electrons are 1.47 and 1.53 MeV for AE = 0.521 and 0.700 MeV, respectively.

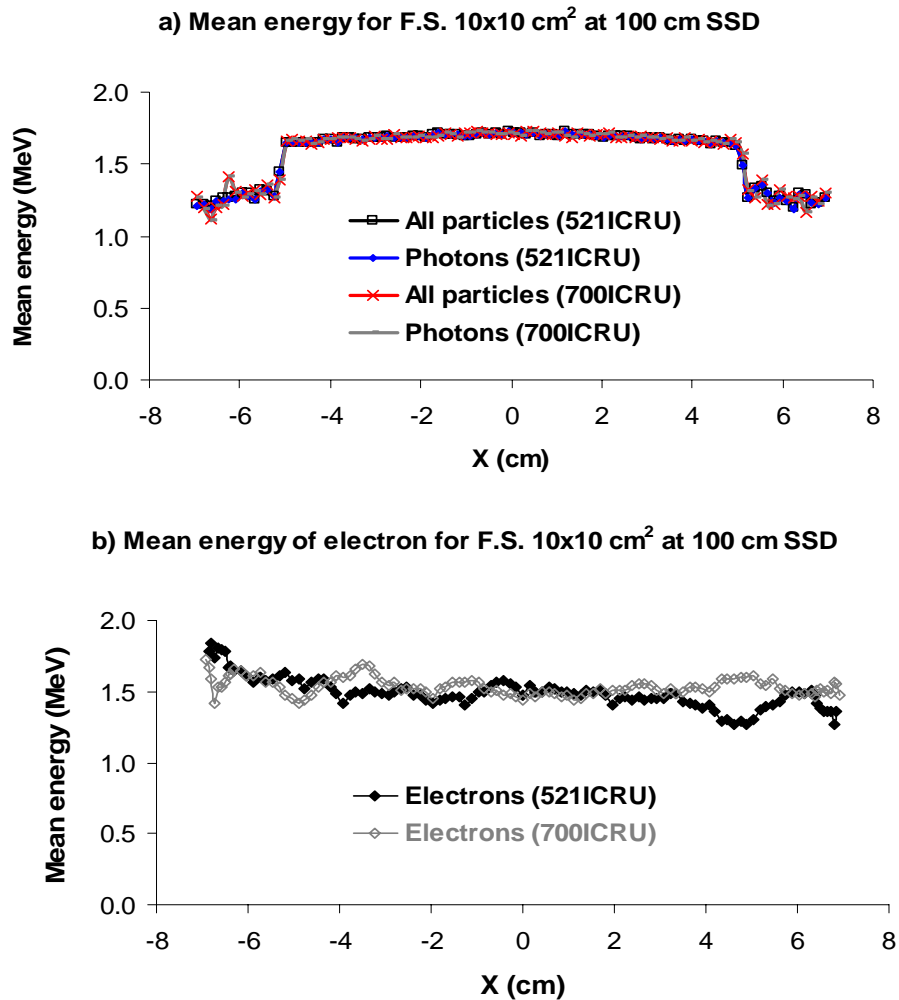


Figure 6.7. Mean energy distribution of a $10 \times 10 \text{ cm}^2$ 6 MV photon beam simulated along the x-axis after passing through the linear accelerator treatment head at 100 cm for a) all particles and photons, b) electrons; estimated accuracy 1%.

6.4.2 Contaminant particles

Results from the simulations show the spectra of contaminants (electrons and positrons) and the particle fluences of contamination compared with electron contamination using $AE = 0.521$ and 0.700 MeV in Figure 6.8. To employ a lower AE means more particle contamination. As can be seen, electron contamination is the major part of the particles produced in the linear accelerator head. They nearly have equal values to all of the contaminant particles put together. Previous investigators have used the Monte Carlo method to determine the source of electron contamination from the linear accelerator treatment head and to demonstrate the increase in build-up dose from electron contamination. Thus, the number of contaminant particles in the photon beam (electrons and positrons) has been determined in order to check if the total amount of contaminant particles is small enough to allow modifications in the linear accelerator geometry. From our results on the contamination at the scoring plane between the mirror and the secondary jaws, values are higher than that of the value from the scoring plane at 100 cm downstream from the target. Photon interactions within the linear accelerator head material generate secondary electrons that are less able to contribute dose to a scoring plane at a distance of 100 cm in air than at the scoring plane between the mirror and the secondary jaws in the target section. This is because some secondary electrons may be absorbed in air while passing through the scoring plane. For a field size of $10 \times 10 \text{ cm}^2$, over 99 % of the particles are photons, and less than 10 % of the contaminant particles are positrons. Therefore, their number was insufficient for further analysis. The fraction of electrons shows the largest variation with PEGS4 cross-section data in Figure 6.9. Because electrons usually have larger scattering angles than photons, they will escape more easily from smaller fields.

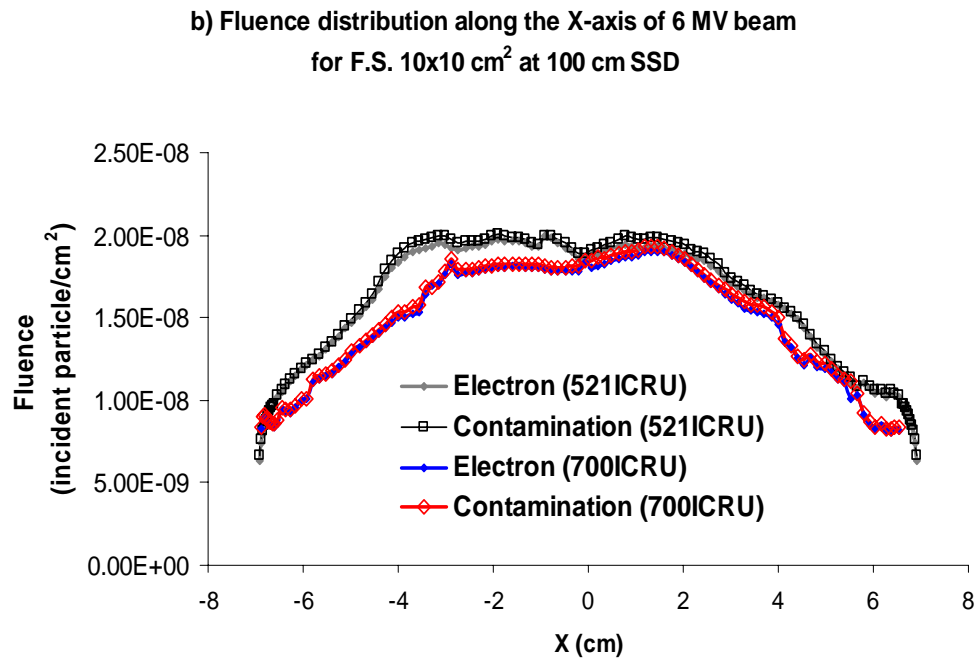
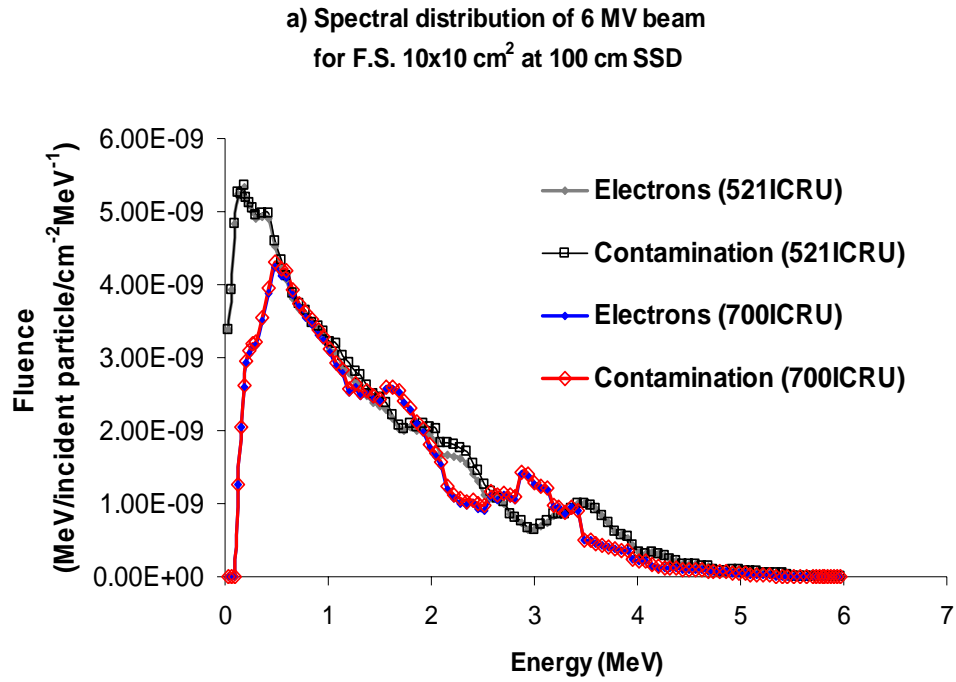


Figure 6.8. Influence of AE values on spectral distribution and fluence of particle and electron contamination along the X-axis of 6 MV beam at 100 cm SSD for 10 x 10 cm² field size: a) spectral distribution of particle and electron contamination, b) fluence of particle and electron contamination; estimated accuracy 1%.

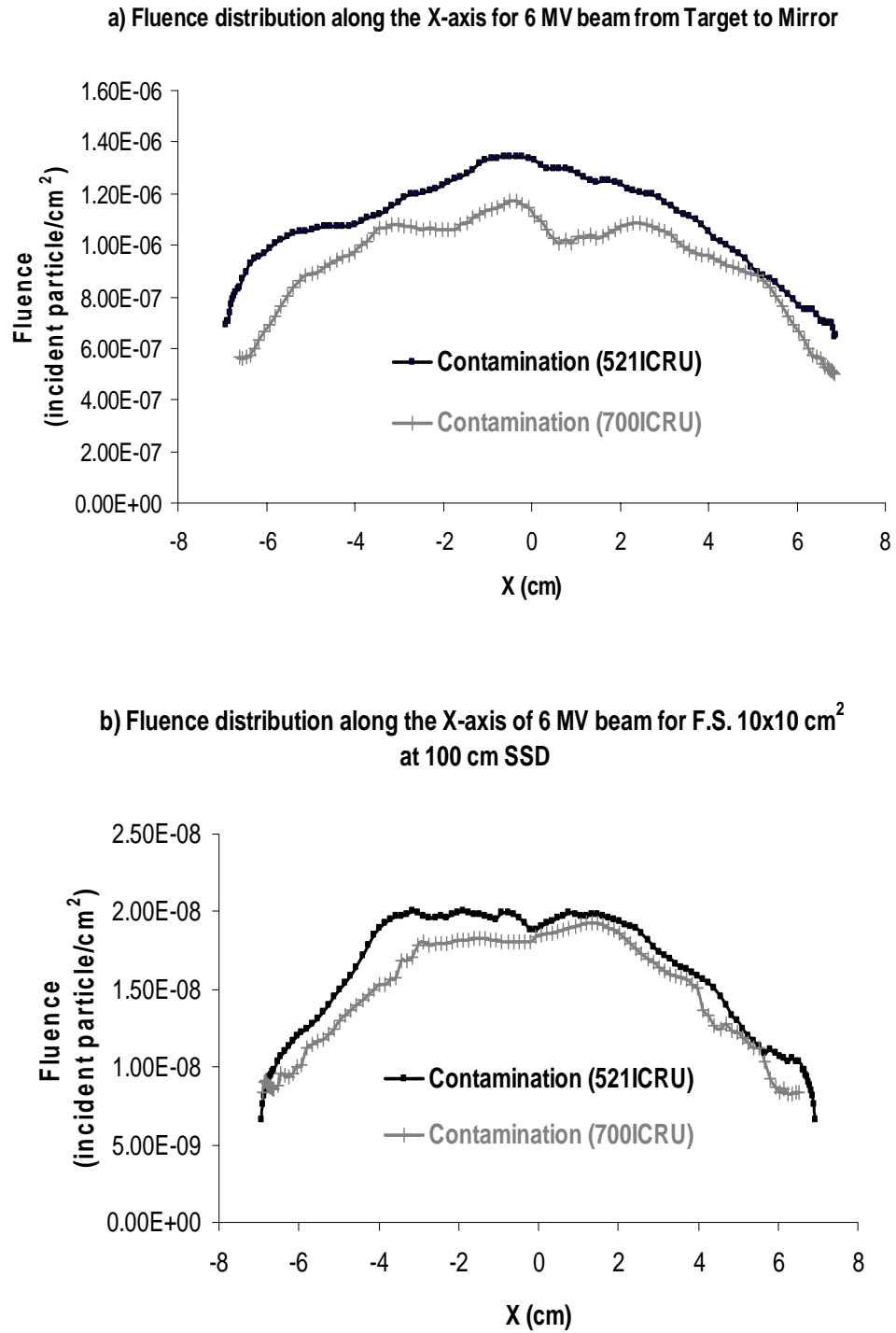


Figure 6.9. Influence of AE values on fluence of contaminant particles along the X-axis of 6 MV beam at a) scoring plane after mirror material, b) 100 cm SSD for 10 x 10 cm² field size; estimated accuracy 1%.

6.5 Characteristics of radiation from a linear accelerator head

Monte Carlo methods are able to characterise beams of electrons and photons emerging from a linear accelerator. In this work, we describe the x-ray beam produced in a

medical linear accelerator to determine the characteristics of the photon and contamination radiation emanating from the linear accelerator head (Figure 6.10). In this study, we separate out each component module (CM) to score the phase-space information for Monte Carlo calculations on the accelerator treatment head. A schematic of the modelling process is shown in Figure 6.11. A kinetic electron beam strikes a target at the top of the accelerator head. The primary collimator collimates the beam, generating bremsstrahlung photons. The photon beam and secondary photons as well as electrons produced within the accelerator head pass through a primary collimator, flattening filter, ion monitor chamber, mirror, jaws, Mylar plate, and air in the accelerator head. Thus, the combined radiation fields can make up several distributions of particles that arrive at the isocentre plane according to the various distributions of bremsstrahlung and scattered radiation.

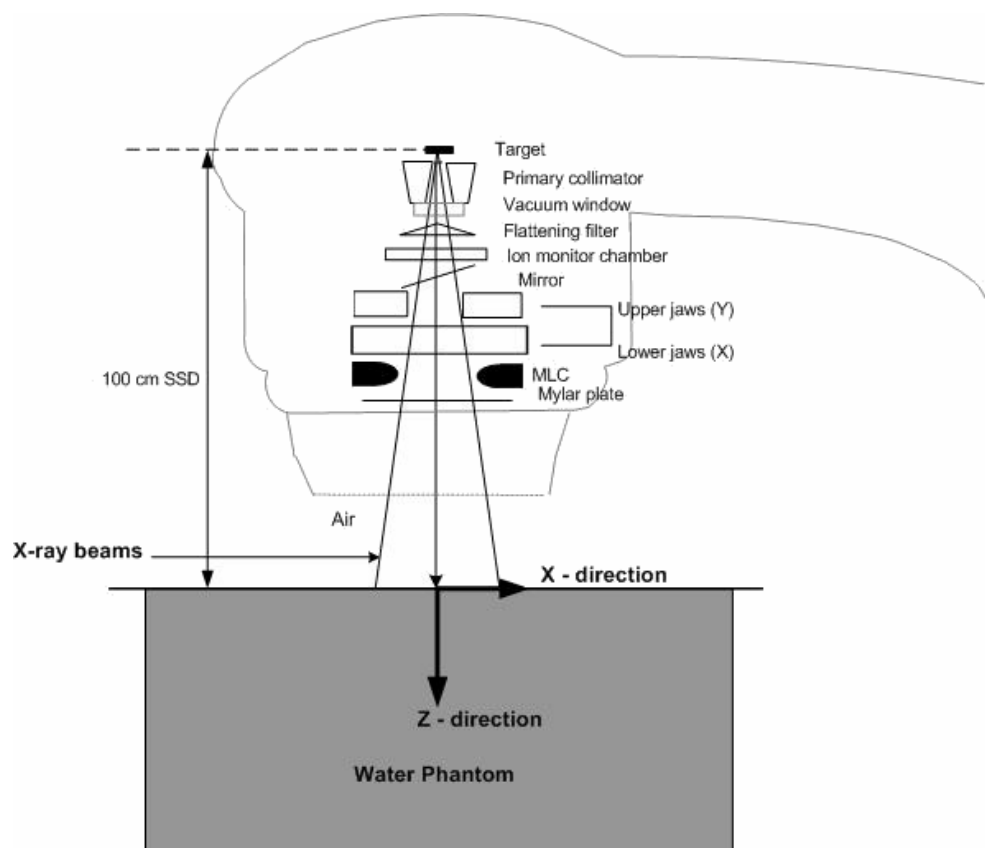


Figure 6.10. Schematic representation of a linear accelerator with the photon radiation originating from the accelerator head, passing through the air, and propagating this radiation down to the phantom.

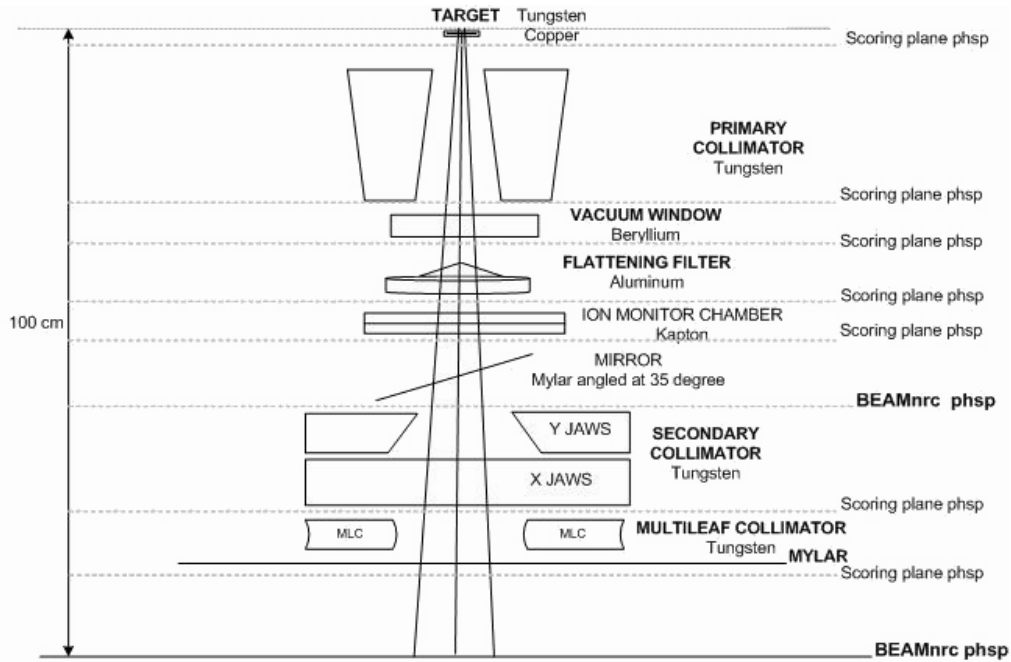


Figure 6.11. A schematic of the modelling process for each scoring plane for the phase-space information for Monte Carlo calculations of radiation from a linear accelerator treatment head.

6.5.1 Methods and materials

Our simulations are performed using the EGSnrc Monte Carlo BEAMnrc GUI code based on machine drawings and material data supplied by the accelerator manufacturers. The accelerator is modelled on a Varian Clinac 2100C for a 6MV data set simulated with EGSnrc BEAMnrc GUI code. The maximum number of histories to run is 1.0×10^7 . Source parameters for initial particles are parallel electron beams with 2-D Gaussian X-Y distribution on the front face at $Z = 0.0000$ cm, Beam Sigma = 0.0425 cm (FWHM = 0.1000 cm), X, Y, Z direction cosines = (0.00000 0.00000 1.00000), and kinetic energy of source = 6.0 MeV. Phase space files will be output at each scoring plane. Range rejection is switched ON, and it runs on i1586_pc_Windows_NT (gnu_win32) on a Dell Optiplex GX 280 Intel (R) Pentium 4 computer with a CPU running at 3.40 GHz. In all simulations, the energy cut-offs for particle transport were set to $AE = ECUT = 0.521$ MeV and $AP = PCUT = 0.01$ MeV. The variable ESAVE was set to 0.500 MeV, and the variance reduction technique, Selective Bremsstrahlung Splitting (SBS) was applied with $N_{max} = 250$. The option of photon interaction forcing was not used. A history-by-history method of estimating uncertainties was used in the

statistics for BEAMnrc. The history-by-history method (Walters et al., 2002) involves grouping scored quantities such as fluence and energy deposited according to primary history during a run, and determining the root mean square standard deviation on the mean of the groupings.

6.5.2 Results and discussion

Results from Table 6.2 show that photons originate from the target and also come from the primary collimator with some reduction in number. They tend to come from the ion monitor chamber and the flattening filter as well. Unlike the primary collimator, however, where the photons originate in only a small fraction of the collimator, photons are created in the total volume of the flattening filter. The energy fluence distributions at the scoring plane are shown in Table 6.3 and Figure 6.12. Most of the fluence comes directly from the target, with contributions at the several percent levels from the flattening filter, ion chamber, vacuum window, and mirror, respectively. These parts are the components that the radiation beam directly passes through and give a quantitative description of the relative importance of the treatment head components. Electrons and contamination spectra are also displayed in the scoring plane of the target, primary collimator and vacuum window. Other regions of the scoring plane cannot be displayed graphically because the fluence was too small.

The contamination comes from the subtraction of all particle and photon fluences. The number and energy fractions coming from each treatment head component and the physics mechanisms involved are given in Tables 6.2 and 6.3. As can be seen bremsstrahlung is the dominant production mechanism of target photons and a few particles generate the electron production. The problem is still that Monte Carlo simulations of a medical accelerator head require a long time to perform, as can be seen in Table 6.3.

CPU time per history was about 20-23 hours for the running process when applied with $AE = 0.521$ MeV because we are concentrating on a detailed spectrum of a secondary electron emerging from an accelerator head. The combined radiation can be characterised by several distributions of bremsstrahlung and scattered radiation. The angles of particles between the x-ray target surface and the Z-axis are shown in Table

6.4. The energy distributions and angular distributions of the photons at the bottom of the accelerator head are determined from this information. Thus, all of these distributions must be known in order to develop a useful source algorithm for input into any Monte Carlo dose calculation code.

In this study, we separate out each component module to produce the phase-space information for Monte Carlo calculations of beams from the accelerator treatment head. Errors in the fluence distribution of photons, electrons, and positrons in each region of the simulation are also shown in Tables 6.2 and 6.4. As can be seen, for most of the beams, the photons originate directly from the target. The scattered photons are scattered from the primary collimator, the flattening filter or the field defining jaws. Most of the scattered photons appear to originate from the flattening filter, the primary collimator and other structures, which the beam passes through and may interact with. The scatter from those additional structures is generally much less than 1% in total, and is not explicitly depicted. In Figure 6.12, the spectral shapes of particles from many component modules are generally similar. The calculated fluence spectra for contaminant electrons show a sudden drop in the fluence of very low-energy electrons, which is due to the cut-off kinetic energy of 10 keV for the transport of electrons.

Table 6.2 Fluence-averaged quantities for first-time crossing of the scoring plane normalised per incident particles (1×10^7 histories).

CM	Photon Fluence (/cm ²)	Electron Fluence (/cm ²)	Positron Fluence (/cm ²)
Target	$1.004 \times 10^{-1} \pm 0.0\%$	$1.952 \times 10^{-3} \pm 0.3\%$	$1.532 \times 10^{-5} \pm 3.4\%$
Primary collimator	$6.427 \times 10^{-5} \pm 0.1\%$	$1.952 \times 10^{-3} \pm 0.3\%$	$3.229 \times 10^{-8} \pm 6.5\%$
Vacuum window	$6.440 \times 10^{-5} \pm 0.1\%$	$1.492 \times 10^{-6} \pm 0.9\%$	$2.596 \times 10^{-8} \pm 7.1\%$
Flattening filter	$1.510 \times 10^{-3} \pm 0.1\%$	$1.029 \times 10^{-5} \pm 2.2\%$	$4.183 \times 10^{-7} \pm 12.0\%$
Ion chamber	$1.977 \times 10^{-4} \pm 0.1\%$	$1.467 \times 10^{-6} \pm 1.9\%$	$5.487 \times 10^{-8} \pm 9.0\%$
Mirror	$3.192 \times 10^{-4} \pm 0.1\%$	$1.149 \times 10^{-6} \pm 2.8\%$	$3.104 \times 10^{-8} \pm 17.2\%$
Jaws	$1.651 \times 10^{-6} \pm 0.1\%$	$8.580 \times 10^{-9} \pm 12.9\%$	
Mylar	$6.349 \times 10^{-6} \pm 0.1\%$	$3.276 \times 10^{-8} \pm 12.0\%$	
Air	$3.599 \times 10^{-7} \pm 0.4\%$	$2.926 \times 10^{-9} \pm 18.3\%$	

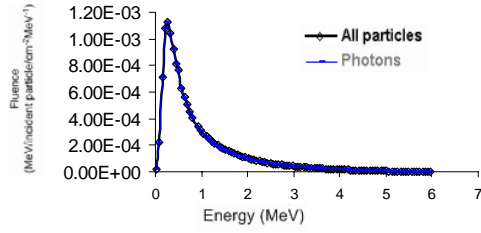
Table 6.3. Number and energy fluence distributions of 6 MeV electron beams from Varian Clinac 2100 C linear accelerator.

Scoring plane Component Module	Position (cm)	# Fluence output of Photons (for initial 1×10^7 electron histories)	Max. KE of Particles (MeV)	Min. KE of Electrons (MeV)	CPU Time per history (seconds)
Target	0.25	1,258,350,771	5.9997	0.0100	0.00751
Primary collimator	7.60	130,791,991	5.9993	0.0100	0.00838
Vacuum window	9.03	116,505,720	5.9999	0.0099	0.00844
Flattening filter	12.82	62,181,234	5.9986	0.0108	0.00828
Ion chamber	16.95	49,902,439	5.9991	0.0103	0.00822
Mirror	26.01	30,325,915	5.9993	0.0104	0.00800
Jaws	44.50	1,829,061	5.9973	0.0517	0.00824
Mylar	57.01	1,605,166	5.9980	0.0286	0.00821
Air	100	259,837	5.9964	0.0684	0.00833

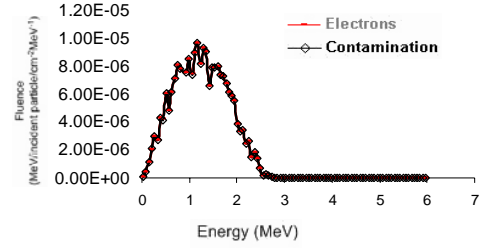
Table 6.4. Angular distributions of photons and particles. The averaged angle is taken as the weighted sum of $1 / \cos\theta$ where θ is the angle of the particle with respect to the Z-axis. (Quantities for first-time crossing of the scoring plane normalised per incident particles).

CM	Angle wrt Z- axis of Photons (degrees)	Angle wrt Z- axis of Electrons (degrees)	Angle wrt Z- axis of Positrons (degrees)
Target	$41.065 \pm 0.0\%$	$40.080 \pm 0.1\%$	$40.686 \pm 1.3\%$
Primary collimator	$9.481 \pm 0.0\%$	$17.257 \pm 0.7\%$	$26.140 \pm 4.0\%$
Vacuum window	$9.569 \pm 0.0\%$	$22.395 \pm 0.6\%$	$27.605 \pm 4.1\%$
Flattening filter	$16.848 \pm 0.0\%$	$36.964 \pm 0.9\%$	$33.422 \pm 4.7\%$
Ion chamber	$15.268 \pm 0.0\%$	$33.689 \pm 0.9\%$	$30.932 \pm 4.7\%$
Mirror	$10.369 \pm 0.0\%$	$23.821 \pm 1.5\%$	$20.710 \pm 10.0\%$
Jaws	$3.989 \pm 0.3\%$	$29.103 \pm 7.6\%$	
Mylar	$3.010 \pm 0.2\%$	$25.579 \pm 7.0\%$	
Air	$24.301 \pm 0.3\%$	$26.558 \pm 9.9\%$	

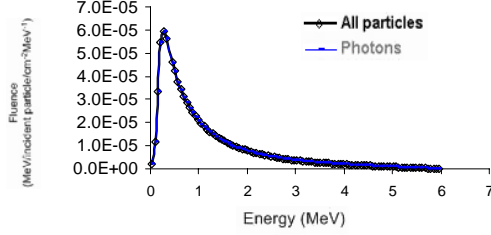
(a) Spectral distribution of 6 MV beam from Target



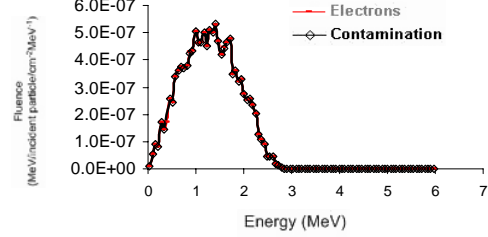
(b) Spectral distribution of 6 MV beam from Target



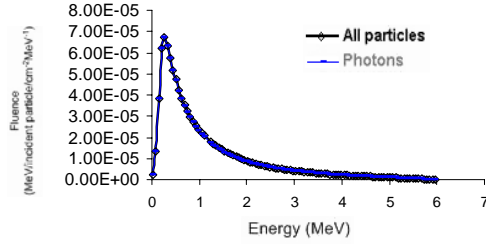
(c) Spectral distribution of 6 MV beam from Primary collimator



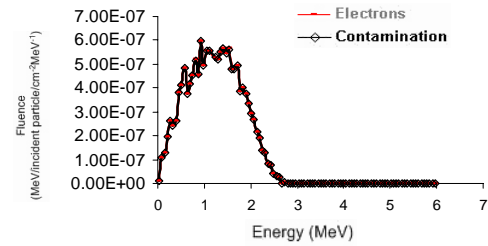
(d) Spectral distribution of 6 MV beam from Primary collimator



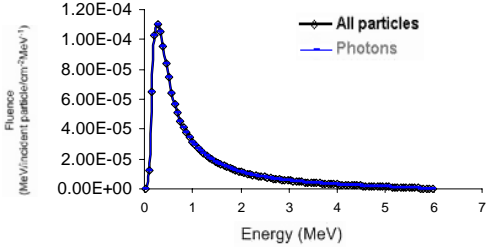
(e) Spectral distribution of 6 MV beam from Vacuum window



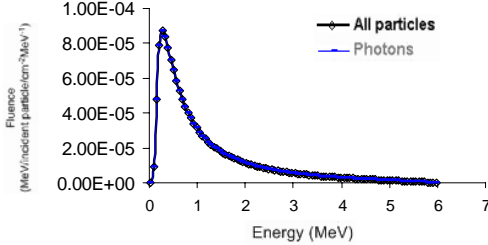
(f) Spectral distribution of 6 MV beam from Vacuum window



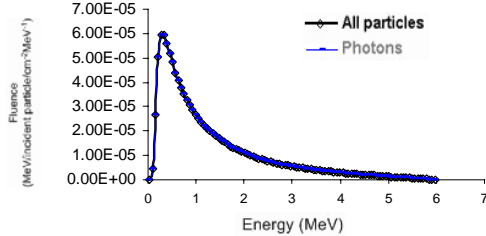
(g) Spectral distribution of 6 MV beam from Flattening filter



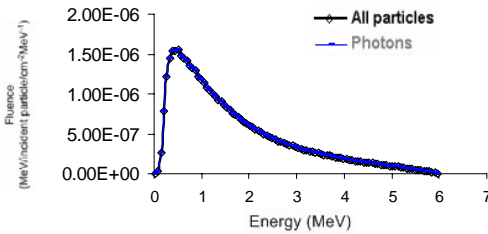
(h) Spectral distribution of 6 MV beam from Ion chamber



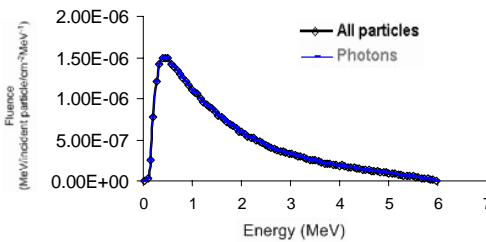
(i) Spectral distribution of 6 MV beam from Mirror



(j) Spectral distribution of 6 MV beam from Secondary collimator



(k) Spectral distribution of 6 MV beam from Mylar



(l) Spectral distribution of 6 MV beam in Air at SSD 100 cm

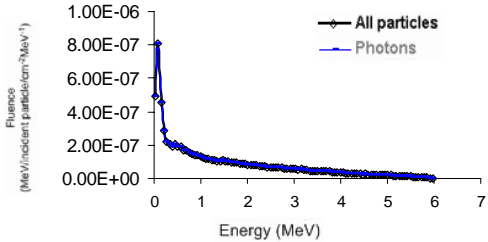


Figure 6.12. Spectral distribution of all particles and photons in (a), (c), (e), (g), (h), (i), (j), (k), electrons and contamination in (b), (d), (f) from a Varian Clinac 2100 C with a 6 MV beam.

6.6 Monte Carlo Depth dose distribution

6.6.1 Methods and Materials

Depth build-up curves for the dose calculations in this study used the Monte Carlo method. Monte Carlo results were obtained using the transport parameters of the DOSXYZnrc code. DOSXYZnrc is an EGSnrc-based Monte Carlo simulation code for calculating dose distributions in a rectilinear voxel phantom. The geometry is a rectilinear volume with the X-Y plane on the page, X to the right, Y down the page, and the Z-axis into the page. Voxel dimensions are completely variable in all three directions. Every volume element can have different materials and/or varying densities. As for the source parameter in this study, the source type is a phase-space source incident from any direction in which particles are incident on the front face. The phase space files from the BEAMnrc calculation data (Figures 6.13 and 6.14) on the linear accelerator head were used as input data for the DOSXYZnrc calculations. After phase space data were obtained, depth dose data and beam profiles in water for the field sizes from $5 \times 5 \text{ cm}^2$ to $30 \times 30 \text{ cm}^2$ at a 100 cm source-to-surface distance (SSD) were calculated using the DOSXYZnrc code for the dose build-up region. In-water beam profiles were compared at surface and at depths of 1.5, 5, and 10 cm.

The Monte Carlo calculations were done on a processor machine equipped with Mandrake Linux 9.2, KDE 3.1, and 2.2 GB. The electron and photon cut-off energies were: AE, ECUT = 0.521 and 0.700 MeV, AP, and PCUT = 0.01 MeV (AE = ECUT, AP = PCUT), and ESAVE = 0.5 MeV. Other parameters: Rayleigh scattering turned off, boundary crossing algorithm EXACT, electron-step algorithm PRESTA-II, pair angular sampling and bremsstrahlung angular sampling KM (Koch and Motz). Photoelectron angular sampling, spin effects and atomic relaxation were turned on. The Russian roulette was also turned on. The size of the scoring voxels during the DOSXYZnrc simulation varied between $1.0 \times 1.0 \times 0.01 \text{ cm}^3$ and $0.2 \times 0.2 \times 0.01 \text{ cm}^3$, depending on the spatial resolution required (Figure 6.13). Usually, a smaller voxel size was chosen for the depth dose build-up region. The size of the water phantom for the DOSXYZnrc

simulation was $35 \times 35 \times 15 \text{ cm}^3$. The total number of histories for the Monte Carlo calculations varied depending on each situation. For example, the numbers of histories for generating a phase space file and depth dose data were approximately 5.0×10^8 and 9.0×10^8 , respectively. During the DOSXYZnrc simulation, the phase space sources were recycled many times for most cases to obtain acceptable statistical uncertainty. The statistical analysis is based on a history-by-history method. According to Walters et al. (2002), the recycling of phase space sources is accurately reflected in the uncertainty estimation of photon beam simulation.

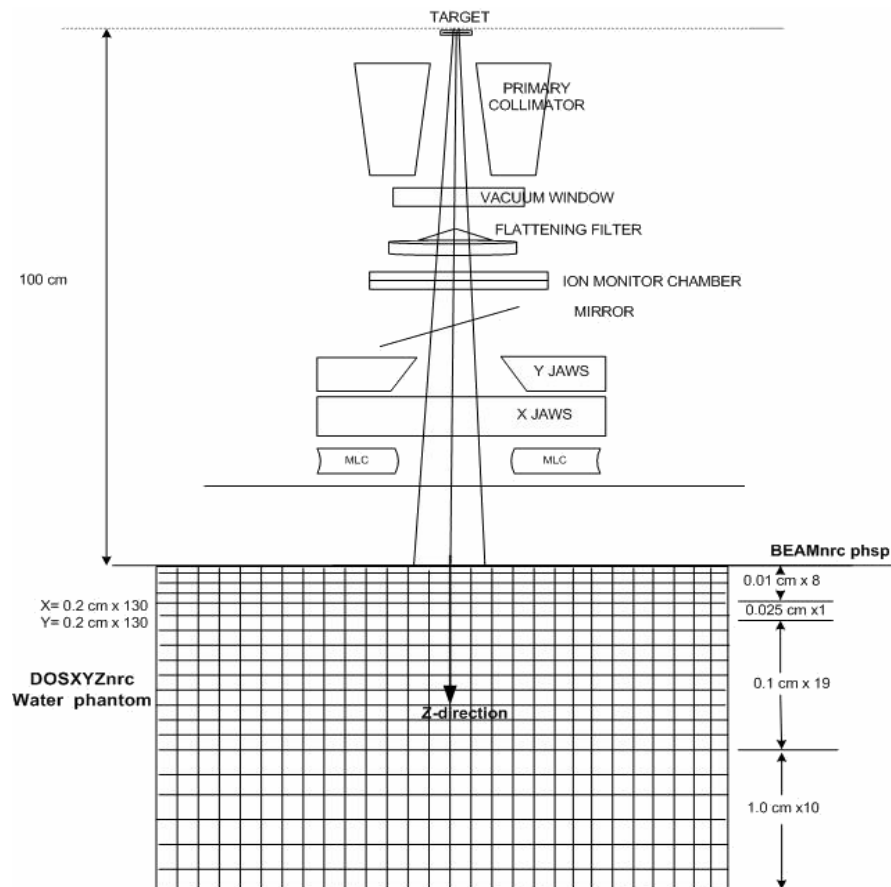


Figure 6.13. Schematic drawing of linear accelerator for the DOSXYZnrc simulation.

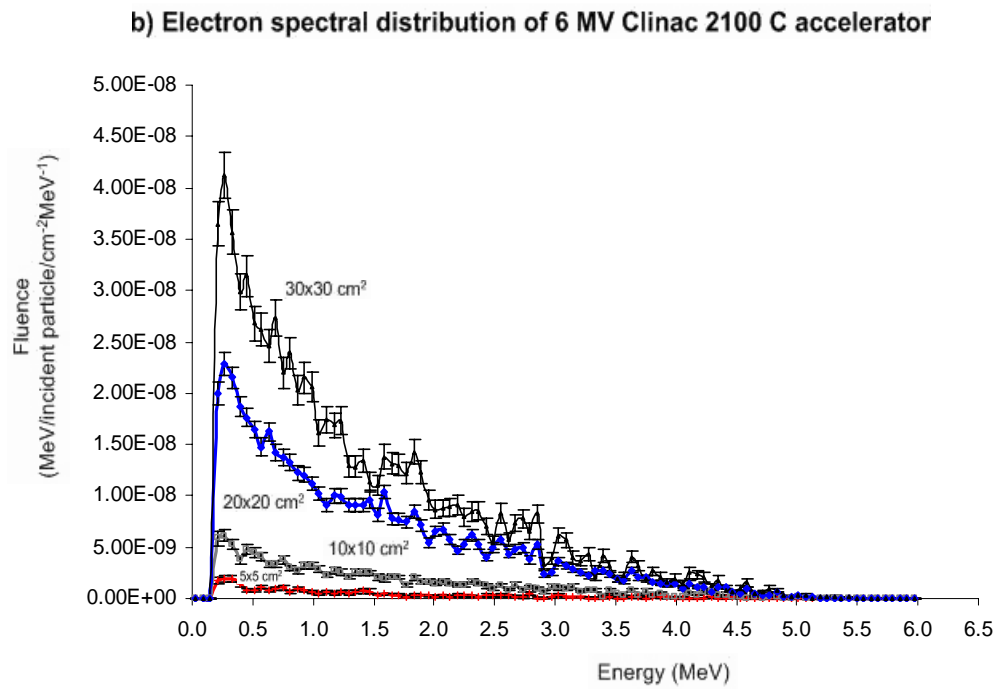
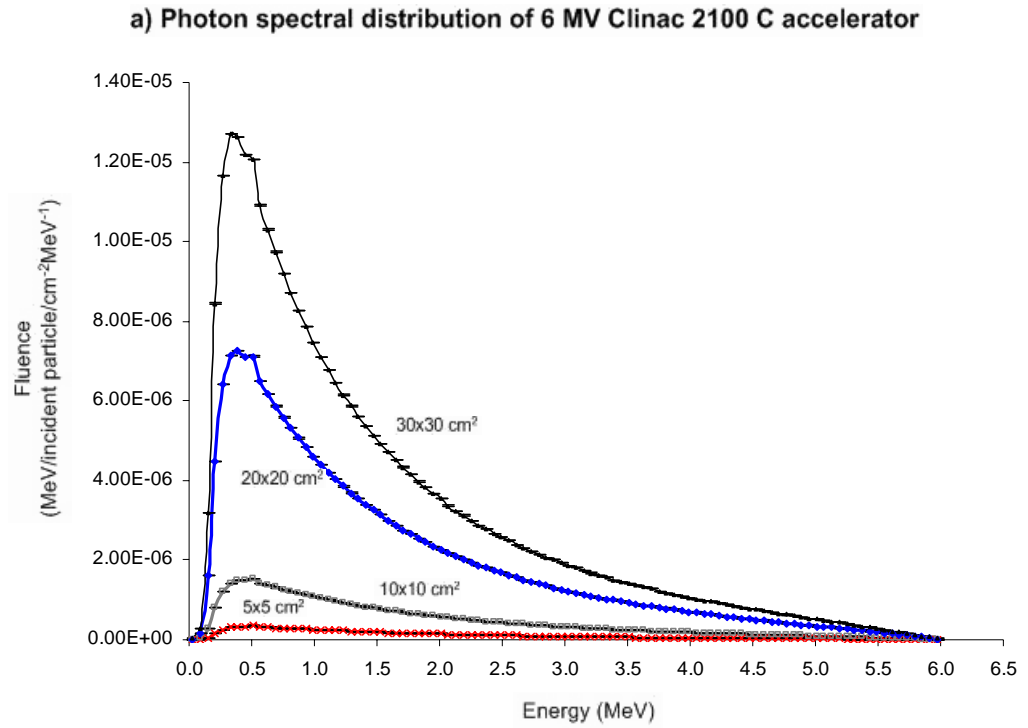


Figure 6.14. Spectral distribution from BEAMnrc phase-space data ($\Delta E = 0.700$ MeV) of linear accelerator head at 100 cm from the target using BEAMDP calculations of field sizes 5×5 cm², 10×10 cm², 20×20 cm², and 30×30 cm² for a) photon fluence, b) electron fluence.

6.6.2 Results and Discussion

6.6.2.1 Dose build-up region

The dose build-up curve data from the Monte Carlo calculations using $AE = 0.700$ MeV for various field sizes are presented in Figure 6.15. This shows a region near the incident surface where the dose rapidly increases within the first few millimetres and gradually attains its maximum dose value at the depth of 1.4-1.5 cm. The simulations have all the data normalised to the value of the dose at the depth of the maximum dose (d_{max}) for field sizes of 5×5 cm², 10×10 cm², 20×20 cm², and 30×30 cm². In Figure 6.16, the build-up dose data from Monte Carlo calculations are compared with the different field sizes. The data are normalised at the depth of the maximum dose for all field sizes, so the greater the field size, the higher the dose contribution in this region.

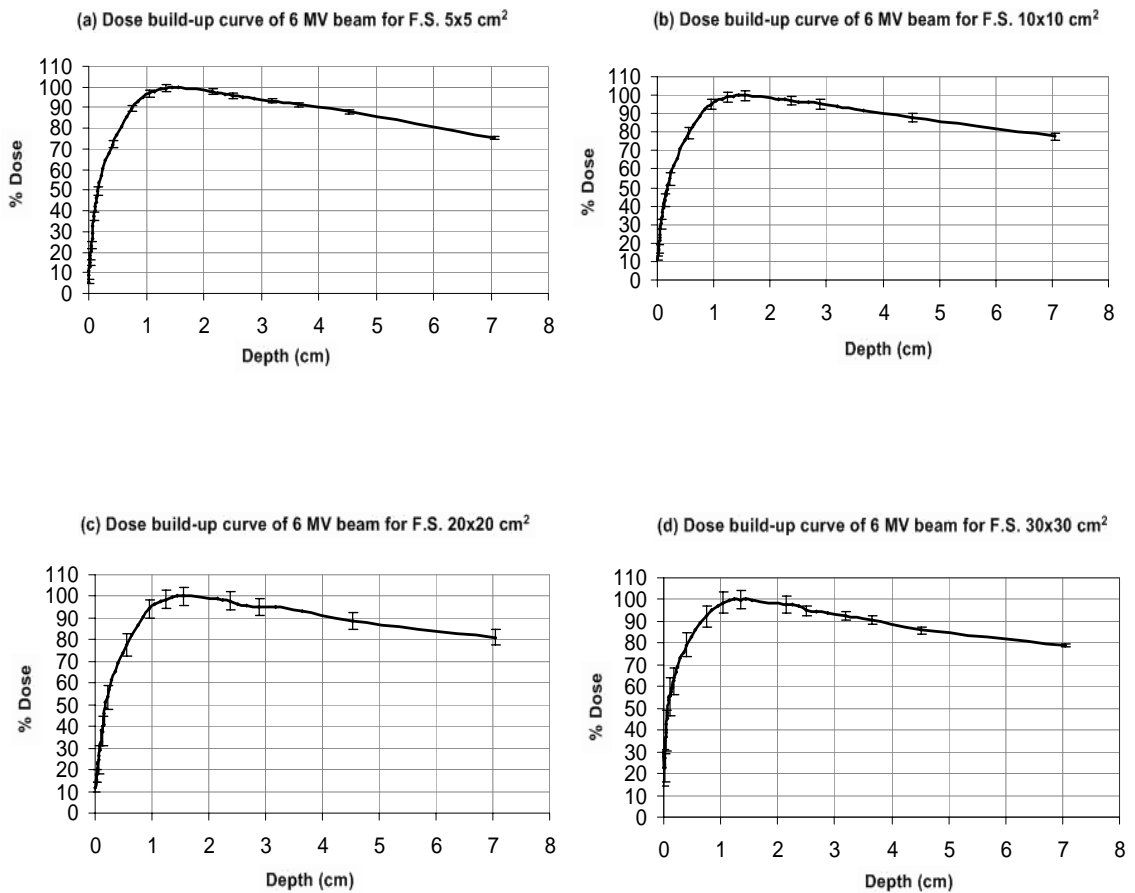


Figure 6.15. Monte Carlo calculations using $AE = 0.700$ MeV to calculate the percent dose build-up distribution for 6 MV Clinac 2100 C for field sizes: a) 5×5 cm², b) 10×10 cm², c) 20×20 cm², d) 30×30 cm².

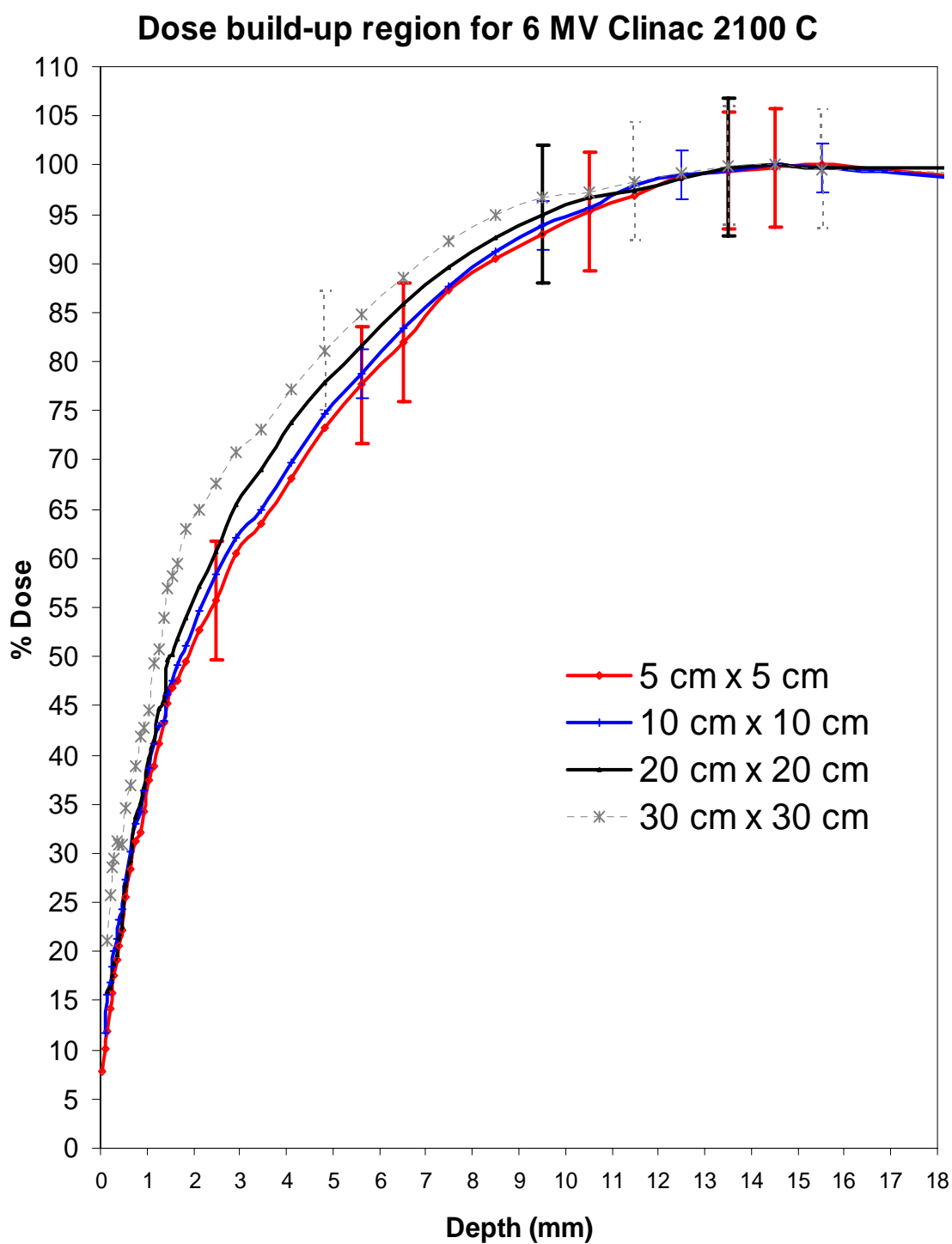


Figure 6.16. Monte Carlo calculation ($AE = 0.700$ MeV) in the build-up region for 6 MV Clinac 2100 C for field sizes of $5 \times 5 \text{ cm}^2$, $10 \times 10 \text{ cm}^2$, $20 \times 20 \text{ cm}^2$, and $30 \times 30 \text{ cm}^2$.

6.6.2.2 Surface dose

Figure 6.17 illustrates the surface dose profiles from Monte Carlo calculated results with the data normalised at the depth of the maximum dose for all field sizes in a water phantom with field sizes of 5 x 5, 10 x 10, and 20 x 20 cm² in for distances along the X and Y-axes. As can be seen, the surface doses for a larger field size such as 15 x 15 or 20 x 20 cm² show large differences as compared to the smaller field size e.g., 5 x 5 or 10 x 10 cm². This is due to the lack of electronic equilibrium in this region and because the larger the field size, the more scattered radiation is present. Surface dose profiles for various field sizes using AE = 0.700 MeV in the build-up region for a 6 MV beam along the X and Y-axis for only 5 x 5 cm², 10 x 10 cm², and 20 x 20 cm² with the percent variations at the surface $\pm 0.9\%$ for 5 x 5 cm², $\pm 1.8\%$ for 10 x 10 cm², and $\pm 4.8\%$ for 20 x 20 cm². For field size 30 x 30 cm², surface dose profile has a percent variation more than 5 % and is not presented in the Figure 6.17. The calculated surface doses from Monte Carlo simulation start at depth 1×10^{-12} cm, while the surface measured doses from Attix chamber with the correction for effective point of measurement from the Attix chamber start at zero depth. There are high contributed dose variations in the build-up region because the results of Monte Carlo calculated contributed dose data have more different doses for the following depth. Thus the difference between the calculated and measured dose is more significant for the larger field sizes. For this explanation Monte Carlo calculated surface dose presented in Figure 6.17 are less than half of the measured doses from the Figure 5.8 only at a zero depth. Then the depth after this depth the difference between the calculated and measured contributed dose is not more significant even for the larger field sizes.

6.6.2.3 Dose calculation in a different medium with cross-section data

The dose distribution of a 6 MV Clinac 2100 C for a field size of 10 x 10 cm² in a water phantom is shown in Figure 6.18 for AE = 0.521 MeV, with the threshold for secondary electron production 10 keV and AE = 0.700 MeV with the threshold of 189 keV kinetic energy. For the several millimetres in the build-up region, the doses are different. This is because this build-up region involves scattered and contamination doses that have lower energy. AE = 0.521 MeV is the lower energy threshold for production of electron interaction as compared to AE = 0.700 MeV. Figure 6.19 shows the electron dose distribution for AE = 0.521 and 0.700 MeV in the build-up region. The doses of

electrons that occur in this region are higher for the lower AE value. Table 6.5 illustrates a comparison of dose distribution on the central axis for a 6 MV Clinac 2100 C with a field size of $10 \times 10 \text{ cm}^2$ for AE = 0.521 and 0.700 MeV at the same depth in a water phantom in terms of the all the particle and electron doses.

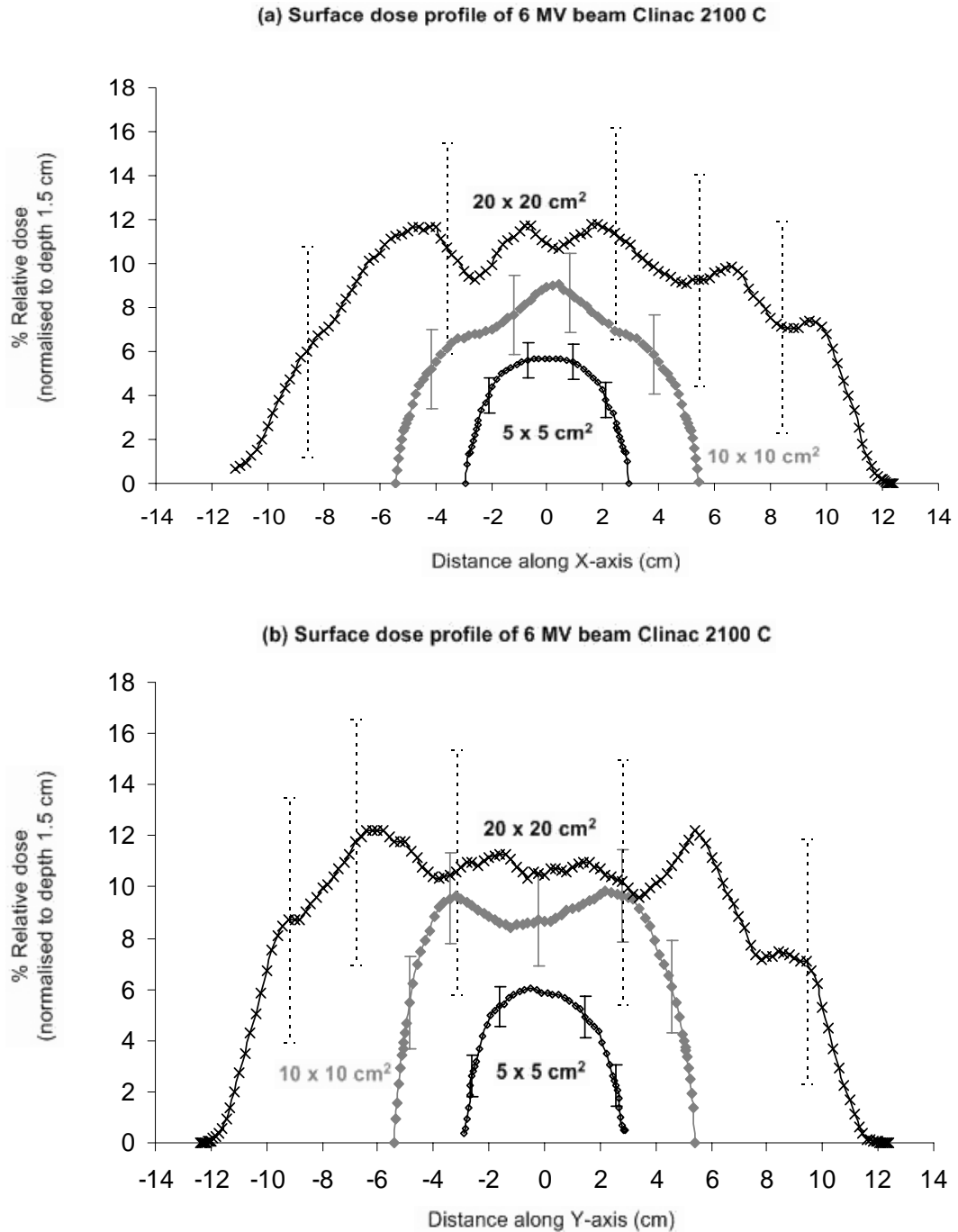
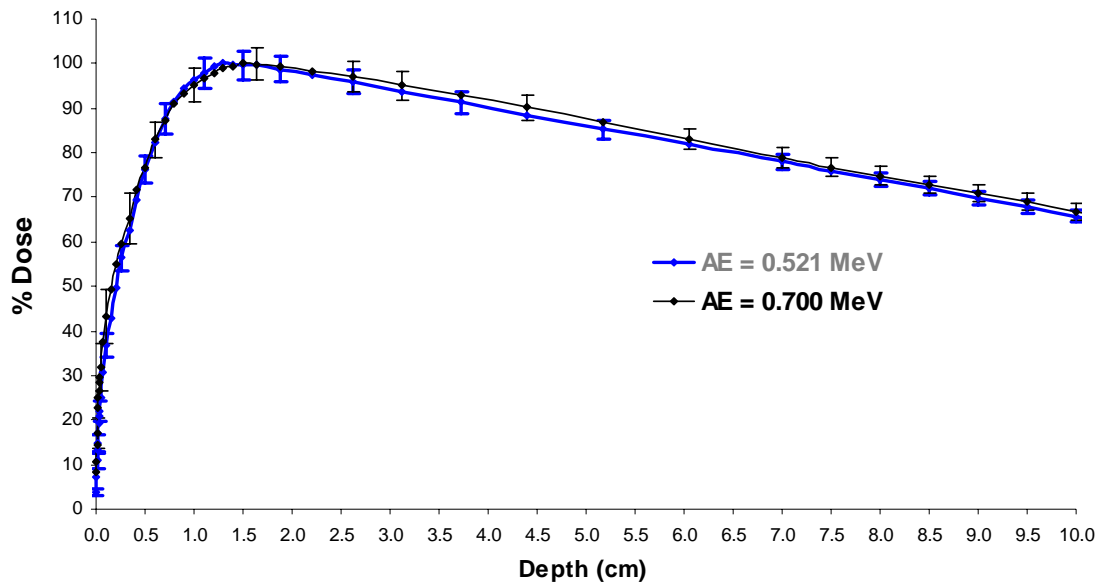


Figure 6.17. Surface dose profile plot calculated from Monte Carlo (AE = 0.700 MeV) results with field sizes $5 \times 5 \text{ cm}^2$, $10 \times 10 \text{ cm}^2$, and $20 \times 20 \text{ cm}^2$ in: (a) distance along the X-axis, and (b) distance along the Y-axis.

a) Depth dose distribution of 6 MV beam for F.S. $10 \times 10 \text{ cm}^2$



b) Dose build-up curves of 6 MV beam for F.S. $10 \times 10 \text{ cm}^2$

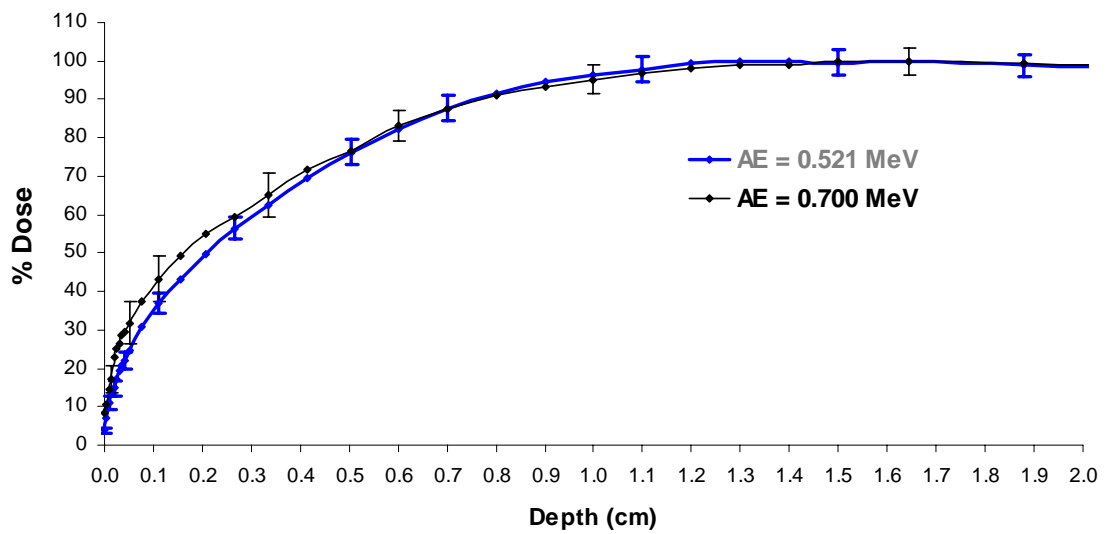
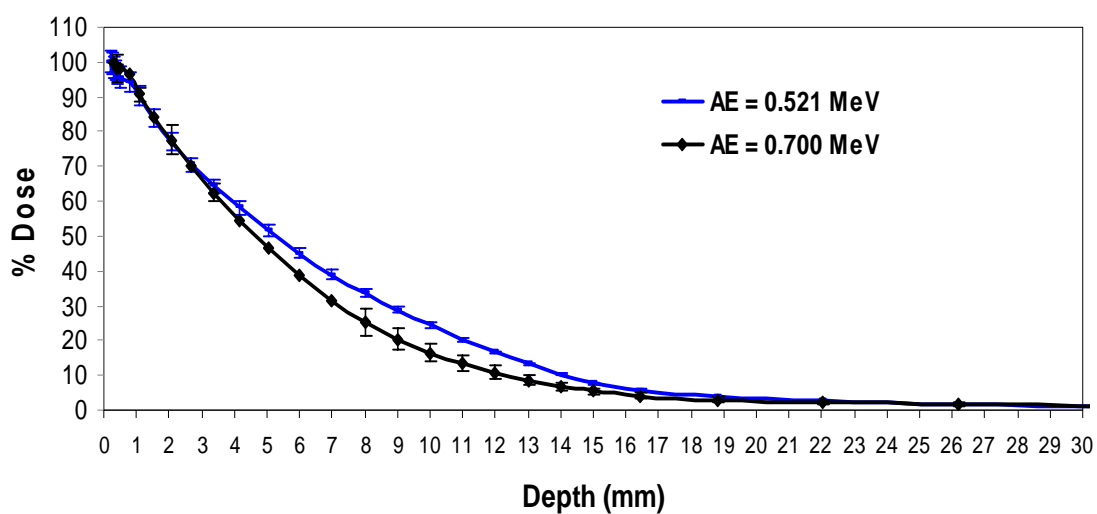


Figure 6.18. Dose distribution on central axis of 6 MV Clinac 2100 C for field size of $10 \times 10 \text{ cm}^2$ at AE = 0.521 and 0.700 MeV in a water phantom: a) depth dose distribution, b) dose in the build-up region.

a) Electron dose in build up region of 6 MV beam for F.S. $10 \times 10 \text{ cm}^2$



b) Electron dose distribution of 6 MV beam for F.S. $10 \times 10 \text{ cm}^2$

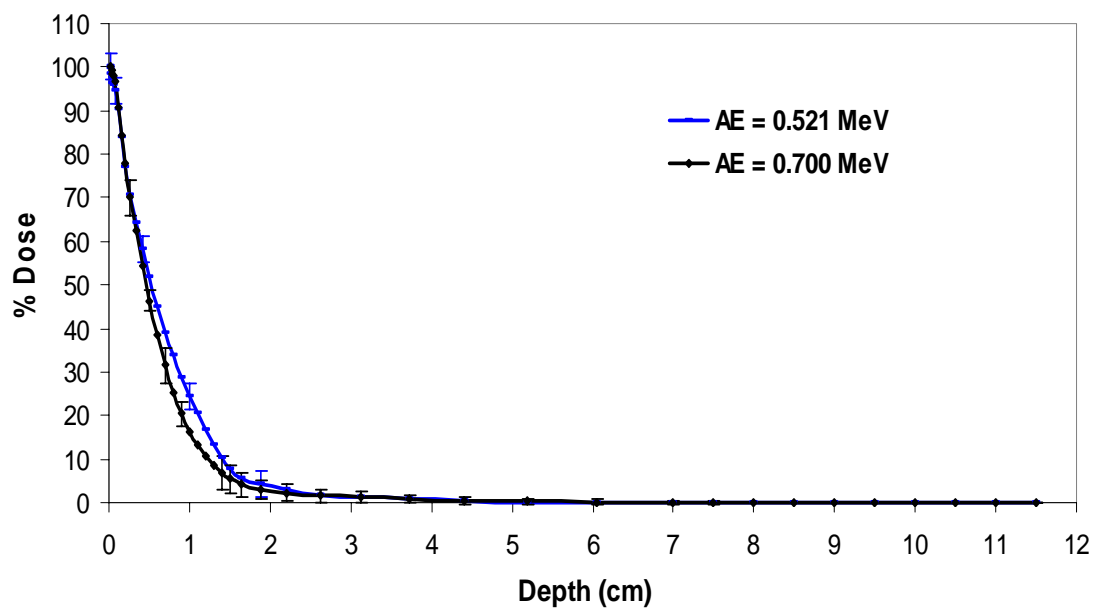


Figure 6.19. Electron dose distribution on central axis of 6 MV Clinac 2100 C for field size of $10 \times 10 \text{ cm}^2$ for AE = 0.521 and AE = 0.700 MeV in a water phantom: a) electron distribution in the build-up region, b) electron depth dose distribution.

Table 6.5. The depth dose distribution on the central axis of 6 MV Clinac 2100 C for field size of $10 \times 10 \text{ cm}^2$ using AE = 0.521 and 0.700 MeV at the same depth in a water phantom.

Dose distribution	AE = 0.521 MeV	AE = 0.700 MeV
All particles	lower	higher
Electrons	higher	lower

Figure 6.20 illustrates the profile comparison between AE = 0.521 MeV and AE = 0.700 MeV in a water phantom for a field size of $10 \times 10 \text{ cm}^2$ along the X and Y-axes. As can be seen, there is a variation in dose along the beam axis in the X and Y-directions at the surface and at a depth of 1.5 cm where the electron contamination has a more important influence on the dose. Electron dose profiles at different depths for AE = 0.521 and 0.700 MeV in a water phantom of the same field size along in the X and Y-axis directions are shown in Figure 6.21. The electron dose along the X-axis is higher for the lower AE where the electron contamination has more dose to deposit in this region. Table 6.6 shows the dose profile distribution of a 6 MV Clinac 2100 C for a field size of $10 \times 10 \text{ cm}^2$ for AE = 0.521 and 0.700 MeV at the same depth in a water phantom along the X and Y-axes. From Tables 6.5 and 6.6, this means that the photon doses have a higher dose distribution for AE = 0.700 MeV whilst the electron doses have a higher dose distribution for AE = 0.521 MeV.

We used a lower AE (value of AE = ECUT) to study the contamination in a high-energy x-ray beam. This is because the value of AE is used for the energy threshold of the production of secondary electrons and the value of ECUT is used for the global cut-off energy for electron transport, below which the electron history terminates and the energy is deposited in the current region. Thus the threshold of the ECUT was selected to discard low-energy electrons with kinetic energy below 0.010 MeV in the simulation because these are the major concern in the electron contamination study and further operations on them were not deemed worthwhile.

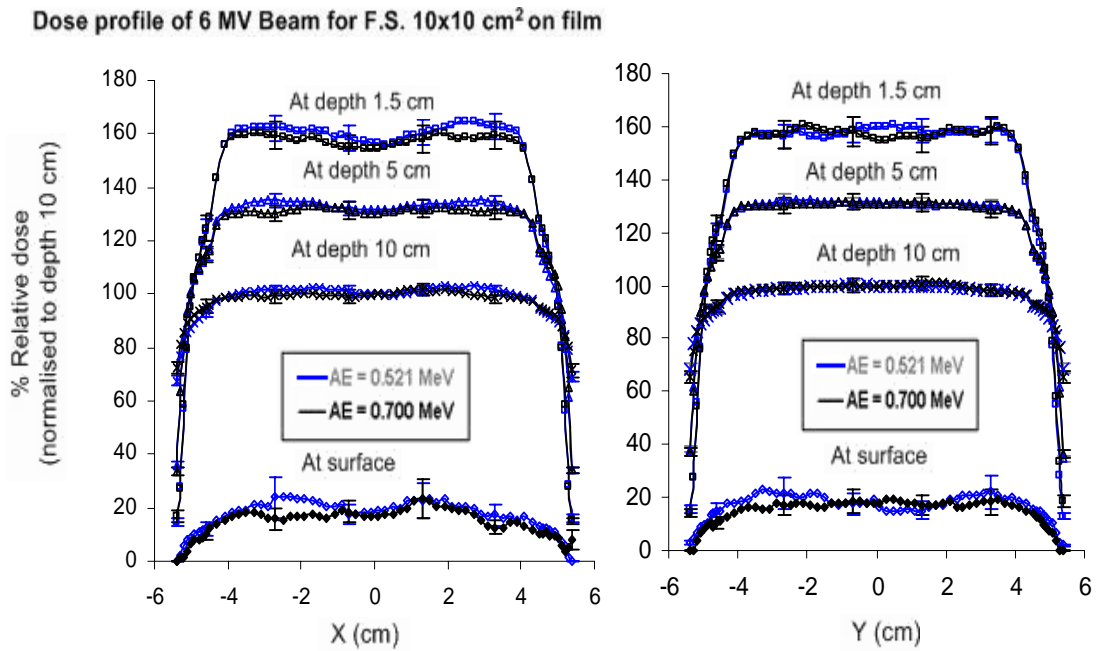


Figure 6.20. Total dose profile plot at different depths in a water phantom for AE = 0.521 and 0.700 MeV from 6 MV Clinac 2100 C for field size of 10 x 10 cm² along the X and Y-axes.

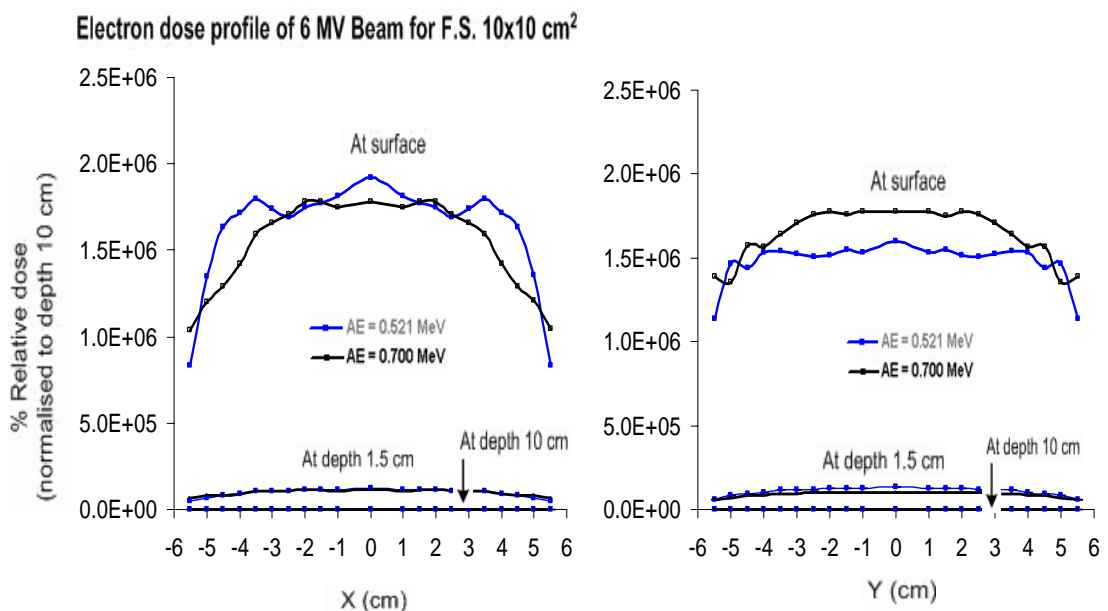


Figure 6.21. Electron dose profile plot at different depths for AE = 0.521 and 0.700 MeV for 6 MV beam in a water phantom along the X and Y-axes.

Table 6.6. The dose profile distribution of 6 MV Clinac 2100 C for field size of 10 x 10 cm² using AE = 0.521 and 0.700 MeV at the same depth in a water phantom along the X and Y-axes.

Dose distribution	AE = 0.521 MeV		AE = 0.700 MeV	
	Surface	Depth = 1.5cm	Surface	Depth =1.5 cm
Distance along X-axis				
All particles	lower	higher	higher	lower
Electrons	higher	higher	lower	lower
Distance along Y-axis				
All particles	lower	same	higher	same
Electrons	lower	higher	higher	lower

6.7 Conclusions

The Monte Carlo method for simulation and analysis of the linear accelerator treatment head used the EGSnrc Monte Carlo codes BEAMnrc and DOSXYZnrc. BEAMnrc was used for transport through the accelerator treatment head and DOSXYZnrc was used for tallying dose in a water phantom. The user code BEAMnrc was used in this study for a photon beam of 6 MV that was generated by a Varian Clinac 2100 C linear accelerator. It is accepted that the various components of the accelerator treatment head present as sources of contaminating electrons. The interaction of the x-ray beam with the mechanical part of the linear accelerator and the air below the machine head produces a continuous spectrum.

Investigation of the electron contamination sources offers important knowledge for developing methods for detection of electron contamination. Most of the photon beam originates directly from the target. The scattered photons are scattered from the primary collimator, the flattening filter or the field defining jaws. Most of the scattered photons appear to originate from the flattening filter, the primary collimator and other structures, which the beam passes through and may interact with. The spectral shapes of particles from many component modules are generally similar. The calculated fluence spectra for

contaminant electrons show a sudden drop in the fluence of very low-energy electrons, which is due to the cut-off kinetic energy of 0.010 MeV for the transport of electrons. The photon doses have a higher dose distribution for $AE = 0.700$ MeV, whilst the electron doses have a higher dose distribution for $AE = 0.521$ MeV. A lower AE (value of $AE = ECUT$) was used to study the contamination in the high-energy x-ray beam. This is because the value of AE is used for the energy threshold of the production of the secondary electrons and the value of ECUT is used for the global cut-off energy for electron transport, below which the electron history terminates and energy is deposited in the current region. So the threshold of ECUT was selected to discard low-energy electrons with kinetic energy below 10 keV in the simulation in the electron contamination study.

The depth dose and profile comparison between $AE = 0.521$ MeV and $AE = 0.700$ MeV in a water phantom for field size $10 \times 10 \text{ cm}^2$ found a variation in doses along the beam axis in the X and Y-axis directions at the surface and at a depth of 1.5 cm, where the electron contamination has a more important influence on the dose in this region. Electron dose profiles in a water phantom of the same field size along the X and Y-axis directions have the electron dose higher when the lower AE is used. The threshold of the cut-off energy for electron transport was selected to discard low energy electrons with kinetic energy below 10 keV as they were of primary concern in the clinical photon beam.

CHAPTER 7

EXPERIMENTS AND MONTE CARLO CALCULATION

Monte Carlo dose calculation algorithms combined with increasing computer-processing speed have made the Monte Carlo dose calculation procedure acceptable for radiotherapy clinics. Thus, Monte Carlo techniques to simulate radiotherapy beams have been studied in several groups. The user codes BEAMnrc and DOSXYZnrc are general-purpose EGSnrc user code for the simulation of radiotherapy beams from treatment units (Rogers et al., 2002). The codes have been used in various beam simulations, and there is very good agreement between measurements and calculations.

The simulation of a linear accelerator is carried out using two steps. The first step involves a detailed simulation of the components of the linear treatment head to score the bremsstrahlung energy spectra and fluence distribution as a function of radial position from the central axis of the beam. In the second step, the fluence distributions are reconstructed to create a source description that is used for subsequent simulations to calculate information related to the beam, such as the depth dose and profile characteristics from the machine to the phantom. It is well known that the high-energy photon beams have the advantage of a skin-sparing effect while the presence of contaminating electrons reduces this advantage. Investigation of the electron contamination sources offers essential knowledge for developing methods for detection of electron contamination.

A number of authors, i.e., Biggs and Ling (1979), Biggs and Russel (1983), Rogers et al. (1985), Sixel and Podgorsak (1994), Jursinic and Makie (1996), Sjogren and Karlsson (1996), Zhu and Palta (1998), and Sheikh-Bagheri et al. (2000), have investigated the influence of electron contamination on the dose distribution in a phantom. They performed experiments to measure the increase in the surface dose and the shift of the depth of the maximum dose to near the surface by increasing the field size or decreasing the source-to-surface distance (SSD). This chapter illustrates some benefits and challenges associated with the use of Monte Carlo simulation of a high-energy x-ray beam. As described in the previous Chapter, Monte Carlo simulations

combined with actual measurements have verified that the effects are observed due to scattered contamination of the primary beam from the linear accelerator head.

In the present study, a comparison between experiments and the Monte Carlo calculation makes it possible to estimate the contribution of contaminating electrons to the dose and to investigate the dose contribution due to secondary electrons. Ionisation measurements were made in a solid water phantom by means of an Attix chamber. Another dosimeter used in the study is radiographic film for the measurement of the surface dose. Megavoltage photon beams interactions with any object on their path give rise to secondary photons and electrons. These secondary particles produce an unwanted dose contribution both on the beam path and outside the geometrical edges of the irradiation field. The details of this are particularly important in radiotherapy. Several different methods have been developed for solving this problem. Thus, it is useful for the treatment planning to know the characteristics of the dose distribution in the build-up region from the complex system involving the linear accelerator components and the phantom geometry.

7.1 Experimental setup

7.1.1 Dose build-up region

Dose build-up region measurements were carried out using an Attix parallel-plate ion chamber in the solid water phantom for various field sizes ranging from $10 \times 10 \text{ cm}^2$ to $20 \times 20 \text{ cm}^2$. The measurements were performed using a Varian Clinac 2100 C generating 6 MV x-rays with a magnetic deflector inserted under the block tray location. For the normalisation depth at the depth of the maximum dose, 1.5 cm was chosen for the 6 MV x-ray beams. The Attix chamber was embedded in a solid water phantom and 20 cm of backscatter thickness were used to ensure phantom scatter equilibrium. Solid water phantom sheets of 1 mm thickness were placed, one by one, on the chamber. A SSD of 100 cm was chosen for measurements. The percentage build-up region depth dose data were measured for each set-up. For the build-up dose measurements at a constant SSD of 100 cm, thin solid water slabs were taken from below the chamber and placed on the top of varying thicknesses in front of the chamber for measurements of the build-up doses. Percentage build up doses were measured on the central axis for 10

x 10 cm², 15 x 15 cm², and 20 x 20 cm² field sizes for open fields and with the NdFeB magnetic deflector device.

7.1.2 Radiographic film with magnetic deflection device

Measurements were performed under a Varian 2100C linear accelerator with the NdFeB magnetic deflector device inserted under the block tray location. Kodak X-Omat V radiographic film was used for the assessment of surface dose measurements. All radiographic films were from the same batch, avoiding confounding effects due to inter-batch differences (Bos et al. 2002). A simple extrapolation technique was employed to estimate surface dose by irradiating a stack of radiographic films, which were placed on top of a solid water phantom (Constantinou et al., 1982) at 100 cm SSD. The films were in ready-pack form. The stack of three films were exposed to a 6 MV x-ray beam for field sizes of 10 x 10 cm², 15 x 15 cm², and 20 x 20 cm². For dose calibration, the calibration films were positioned in a solid water phantom of dimensions 30 cm x 30 cm x 30 cm. The film was positioned at a depth of D_{max} , 1.5 cm for 6 MV x-rays, and doses of 0, 5, 10, 20, 30, 40, 60, 80, and 100 MU were given with the film perpendicular to the central axis of the beam. Field size dose calibration was performed at 10 x 10 cm², 15 x 15 cm², and 20 x 20 cm² to account for effects caused by variations in the photon spectra that were produced at different field sizes. The effective depth of measurement for our radiographic film ready pack was calculated as 0.38 mm \pm 0.03 mm water equivalent (Butson et al., 2004). The films were processed in an automatic X-Omat processor. Optical density to dose conversions was performed on the experimental films, using results supplied from the calibration curve. In each case, the optical density was measured at the centre of each film piece to minimise the effects of variations in measured dose near the edge of the film. Using the optical density calibration function of the Vidar VXR-12 Plus visible light densitometer and Scion imaging software scanner, results from H and D curves produced a calibration curve adequately fitted over the range from 5 to 100 MU by a third order polynomial, which was used to fit results. Surface dose assessment was performed using a dose extrapolation technique (Butson et al., 1999) whereby the dose is extrapolated to 0 cm effective depth to compare results for surface dose and investigate the characteristics of the build-up dose. Measurements were performed with radiation field sizes of 10 x 10 cm², 15 x 15 cm², and 20 x 20 cm² with the NdFeB magnetic deflector device inserted

under the block tray location. All measurements were performed at a 100 cm source to surface distance.

7.2 Monte Carlo method

Simulations in phantoms were done using EGSnrc user-code DOSXYZnrc to determine the build-up depth dose curves and cross profiles for the calculation of beam characteristics. A total of 5.0×10^8 and 9.0×10^8 electron histories were simulated for the $5 \times 5 \text{ cm}^2$ and $30 \times 30 \text{ cm}^2$ fields, respectively. The parameters for EGSnrc to control the particle transport are: AE = 0.521, 0.700 MeV, ECUT = 0.521, 0.700 MeV, AP = 0.010 MeV, and PCUT = 0.010 MeV; Rayleigh scattering OFF; boundary crossing algorithm EXACT; electron-step algorithm PRESTA-II; bound Compton scattering, photoelectron angular sampling, atomic relaxations and spin effects ON; and pair angular sampling as well as the bremsstrahlung angular sampling KM (Koch and Motz).

Central axis depth dose curves were calculated in the $1 \times 1 \text{ cm}^2$ region around the central axis for $10 \times 10 \text{ cm}^2$ fields. For each field size, the following data were sampled for doses of all particles and electrons in the build-up region on the central axis of beams, and a cross profile was derived for four depths: at the surface, and 1.5, 5, and 10 cm distance in the X and Y-axis directions. In-water beam profiles were compared at the surface and at these depths of 1.5, 5, and 10 cm. The Monte Carlo calculations were done on a processor machine equipped with Mandrake Linux 9.2, KDE 3.1, and 2.2 GB.

The total number of histories for the Monte Carlo calculations varied depending on each situation. For example, the numbers of histories for generating a phase space file and depth dose data was approximately 5.0×10^8 . During the DOSXYZnrc simulation, the phase space sources were recycled many times for most cases to obtain acceptable statistical uncertainty. The statistical analysis is based on a history-by-history method. According to Walters et al. (2002), the recycling of phase space sources is accurately reflected in the uncertainty estimation of photon beam simulation. The user code DOXYZnrc in EGSnrc simulates the passage of the photon beam in a finite geometry and samples the absorbed dose in specified regions. Their compositions and shapes define the water phantom and the radiographic film. The effects of energy cut-offs for

particles were also investigated for the different conditions. The dose distributions can be analysed using a program called STATDOSE (McGowan et al., 1995) for the 3D dose distribution and plotting dose distributions along the X, Y and Z- axes.

7.2.1 Water phantom

The size of the scoring voxels during the DOSXYZnrc simulation varied between $0.2 \times 0.2 \times 0.01 \text{ cm}^3$ and $1.0 \times 1.0 \times 0.01 \text{ cm}^3$, depending on the spatial resolution required. The thickness in the depth of the water phantom is shown in Figure 7.1 and Table 7.1.

7.2.2 Radiographic film

DOSXYZnrc presents absorbed dose at the radiographic film on a water phantom. The film is modelled as described in Figure 7.2. The total thickness of the film is 0.066 cm. The X-Omat V film is simulated based upon information from Palm et al. (2004) for the elemental composition of the emulsion, in terms of the fraction by weight: H: 0.023948, C: 0.222374, N: 0.099407, O: 0.473944, Br: 0.076736 and Ag: 0.103592, with the density: 1.731 g/cm^3 . In the Monte Carlo simulation, the film is modelled as a 0.022 cm thickness per film as shown in the Figure 7.2 and Table 7.1. The cross-section data for the materials used are available in a pre-processed PEGS4 cross-section data file. The density effect corrections for the stopping powers of the material are included in the PEGS4 data file for 521ICRU and 700ICRU.

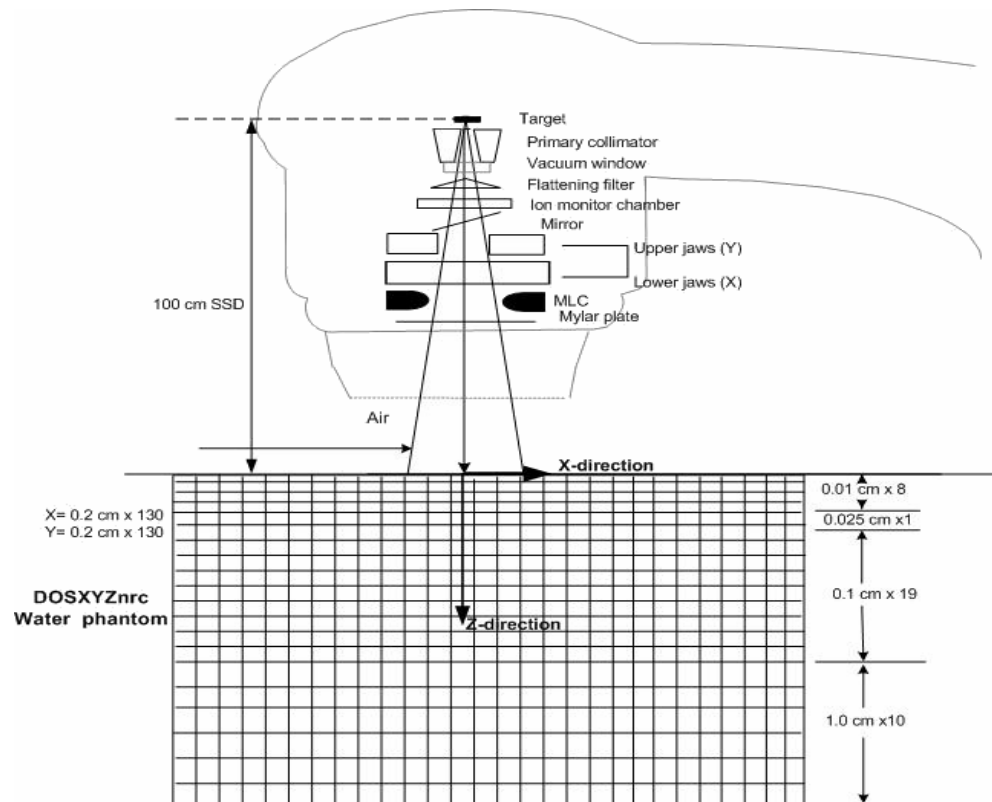


Figure 7.1. Schematic drawing of linear accelerator for the DOSXYZnrc simulation in a water phantom.

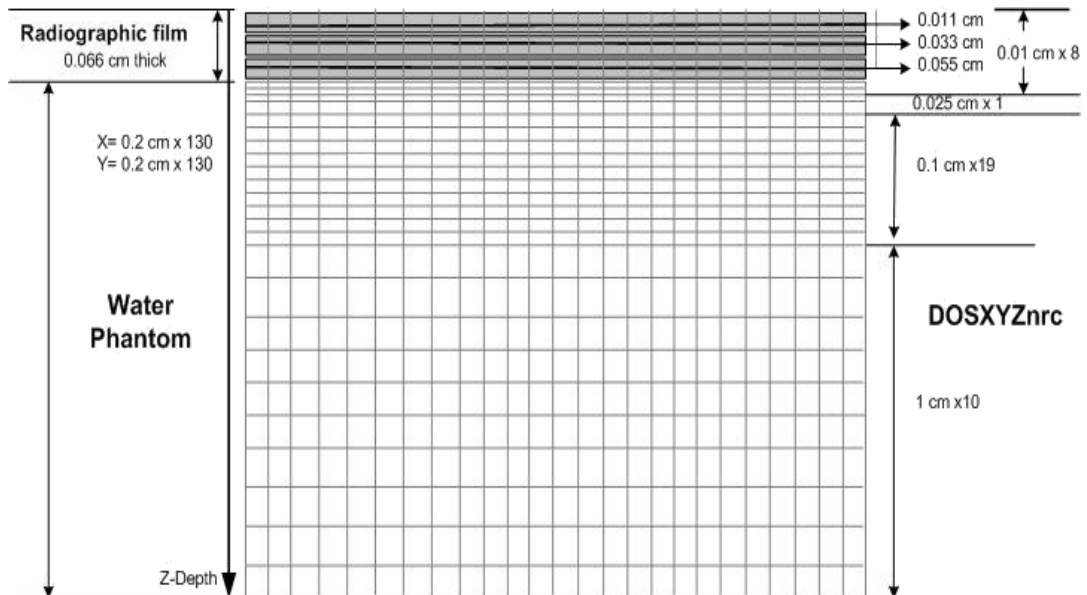


Figure 7.2. Schematic drawing of the size of scoring voxels for the DOSXYZnrc simulation in the radiographic film on a water phantom.

Table 7.1. DOSXYZnrc simulation parameters.

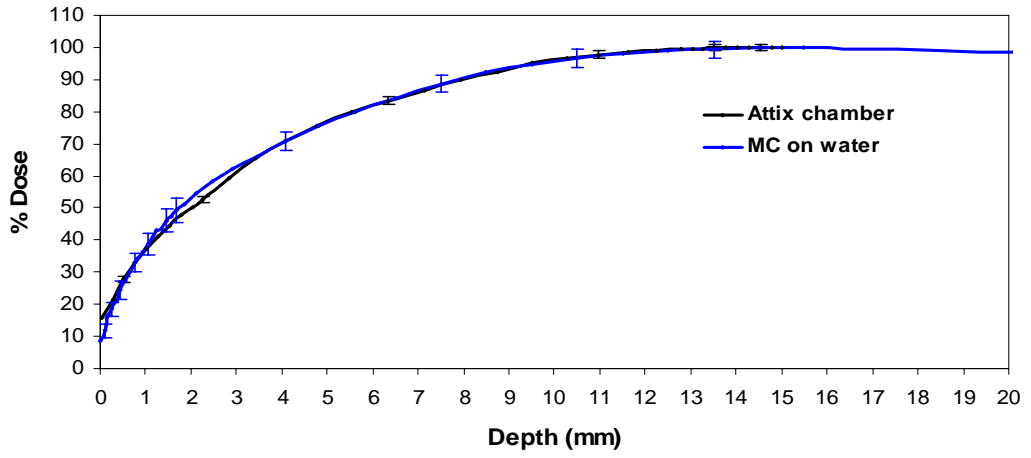
Media	Slab (cm ³)	Thickness (cm)	ECUT (MeV)	PCUT (MeV)	Field size (cm ²)
Water	0.2 x 0.2 x 0.01	0.08	0.521,0.700	0.01	10 x 10
	0.2 x 0.2 x 0.025	0.025			15 x 15
	0.2 x 0.2 x 0.1	19			20 x 20
	0.2 x 0.2 x 1	10			
Radiographic film	0.2 x 0.2 x 0.01	0.08	0.521,0.700	0.01	10 x 10
					15 x 15
					20 x 20

7.3 Results and Discussion

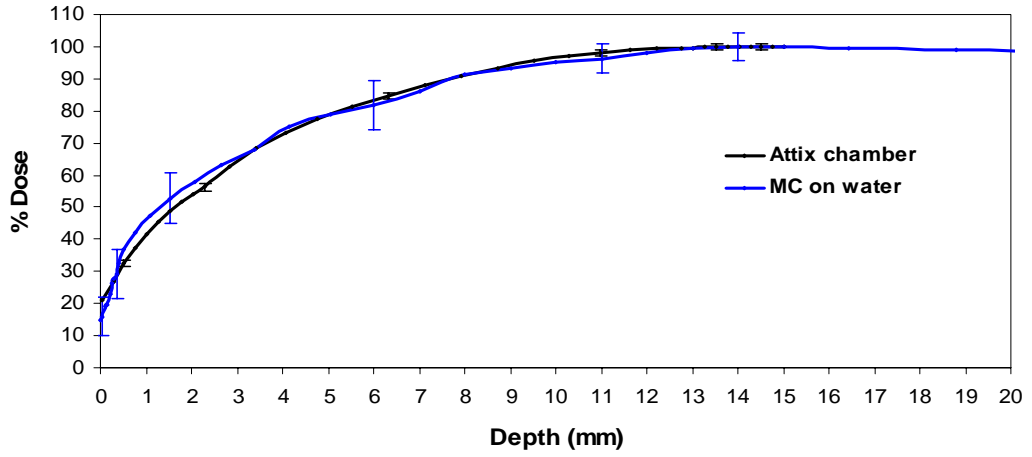
7.3.1 Dose in the build-up region

In Figure 7.3, the build-up dose curves from Monte Carlo calculations are compared with the data from Attix chamber measurements. Measurements and calculations were separately normalised to their respective depth of the maximum dose for all field sizes. Figure 7.3 a), b) and c) present a detailed comparison between Monte Carlo and measured data with the correction for effective point of measurement from the Attix chamber, showing good agreement within the dose build-up region for a field size of 10 x 10 cm². At a zero depth, Monte Carlo calculations present lower dose than those obtained with the measurement. While the depth below surface until 10 millimetres depth, Monte Carlo calculations present higher dose than those obtained with the Attix. Away from a depth of 10 millimetres, Monte Carlo calculations present again lower dose than those obtained with the Attix depended on field size; for the larger the field size the lower the contributed dose. This means that good agreement was achieved between the Monte Carlo simulations and measurements in the dose distributions in a water phantom after a few millimetre depths from the surface in the build-up region. The components of primary photons, scattered photons and contaminant electrons are the multiple sources caused to contribute the surface dose and the dose at shallow depths. As expected, because of a well-known problem in the dose build-up region for larger field sizes such as 15 x 15 cm² and 20 x 20 cm², the agreement for these field sizes was relatively poor as compared to that for the smaller field sizes (e.g., 10 x 10 cm²) as illustrated in Figure 7.3. As can be seen the discrepancy between Monte Carlo calculated build-up dose and measurement data appears in a first few millimeters depth in the build-up region for the larger field size.

a) Dose build-up curves of 6 MV beam for F.S. 10x10 cm²



b) Dose build-up curves of 6 MV beam for F.S. 15x15 cm²



c) Dose build-up curves of 6 MV beam for F.S. 20x20 cm²

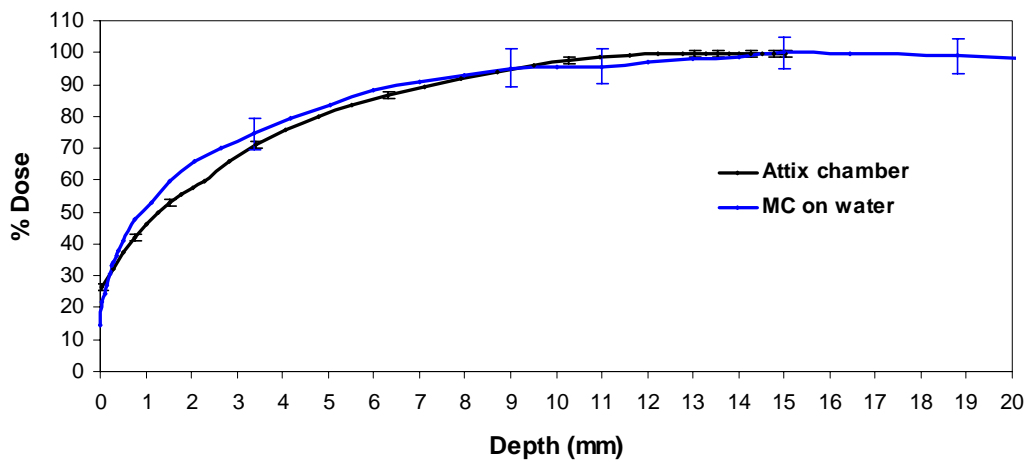


Figure 7.3. Match between experimental data and Monte Carlo calculation in the build-up region for a 6 MV beam in a water phantom for AE and ECUT = 0.700 MeV for field sizes of: a) 10 x 10 cm², b) 15 x 15 cm², c) 20 x 20 cm².

Table 7.2 (a) presents the percentage of the dose between the experimental data and the Monte Carlo calculation in the build-up region in a water phantom and radiographic film for a 6 MV beam in a water phantom using the energy-cut-offs for particle transport and $AE = 0.700$ MeV for field sizes of $10 \times 10 \text{ cm}^2$ and $20 \times 20 \text{ cm}^2$. The modelling of the simulation data contributes to the deviations in the build-up region by presenting a higher dose than those obtained with the Attix measurements except for the zero depth. At a zero depth, Monte Carlo calculations present lower contributed dose than those obtained with the measurement. Monte Carlo calculations present higher dose than those obtained with the Attix chamber at a depth beyond zero. It is known that photons are indirectly ionizing particles and do not deposit significant energy themselves. For contributed dose in the build-up region, radiations from the treatment head or the incident photons transfer their energy to electrons and positrons that ionize and excite atoms along particle tracks until their energy is lost. Through the interaction history, one can make definitions of the various dose categories relevant to dose modelling. Thus there are noticeable discrepancies between Monte Carlo calculated surface dose data and the Attix measurements presented in Table 7.2 at the zero depth. Monte Carlo calculated surface doses in Table 7.2 (a), (b) are still lower than the measured surface doses with Attix chamber, additionally the calculated doses from Monte Carlo simulation start at depth $1 \times 10^{-12} \text{ cm}$, while the surface measured doses from Attix chamber start at zero depth. Surface doses achieved from the Monte Carlo calculations derive from an extrapolated surface dose method to a modified exponential curve beyond the first two millimetres, where uncertainty is difficult to estimate in Table 7.2 (b), surface doses are still lower than the measured surface doses with Attix chamber and then the doses increase rapidly about two times after this depth showing good agreement within the surface dose between extrapolated surface dose with Monte Carlo calculations. The dose contributions in the first two millimetres are very sensitive to expect the dose profile. Figure 6.17 in the previous chapter presents the calculated surface doses without extrapolated surface dose method at the zero depth. The difference between the calculated and measured dose is more significant for the larger field sizes. For this explanation Monte Carlo calculated surface dose presented in Figure 6.17 are less than half of the measured doses.

Radiographic film is known to have an energy-dependent response because of the high atomic number of silver and has a greater cross section for low-energy photons causing the high ratio of mass-energy absorption coefficients for radiographic film to water for

photon energies below 100 keV. As can be seen the percentage of the dose in the build-up region from Monte Carlo calculations in a water phantom were lower than those achieved on radiographic film in a water phantom (Table 7.2 (a)).

Table 7.2. (a) Percentage of the dose in the build-up region between experimental data and Monte Carlo calculations for 6 MV beam in a water phantom and radiographic film for AE = 0.700 MeV of field size 10 x 10 cm² and 20 x 20 cm².

Depth (cm)	F.S. 10 x 10 cm ²			F.S. 20 x 20 cm ²		
	Attix chamber	MC: Water	MC: Film	Attix chamber	MC: Water	MC: Film
0	15.84	9.65	13.77	26.65	13.78	19.47
0.025	21.73	25.17	25.35	32.14	32.99	38.86
0.05	27.57	31.50	31.81	37.55	40.49	48.70
0.075	32.77	36.98	37.81	42.23	47.20	53.36
0.1	37.24	41.43	41.98	46.27	51.24	57.40
0.125	41.16	45.32	45.63	49.74	55.11	60.89
0.15	44.60	48.85	48.99	52.77	58.99	64.00
0.175	47.63	51.72	51.95	55.44	62.06	66.54
0.2	50.34	54.48	54.84	57.80	64.98	68.98
0.34	65.58	65.40	68.61	71.24	74.75	80.20
0.55	79.73	79.71	82.63	83.36	85.62	87.77
0.95	95.00	94.28	96.51	96.23	95.33	98.18
1.16	98.54	96.94	98.85	99.02	96.44	99.80
1.3	99.54	98.83	99.54	99.69	97.92	99.80
1.4	99.91	99.22	100.00	99.85	98.75	99.80
1.5	100.00	100.00	99.54	99.73	99.68	99.86

Table 7.2. (b) Percentage of the dose in the build-up region between experimental data and Extrapolated surface dose of Monte Carlo calculations for 6 MV beam in a water phantom for AE = 0.700 MeV of field size 10 x 10 cm² and 20 x 20 cm².

Depth (cm)	F.S. 10 x 10 cm ²			F.S. 20 x 20 cm ²		
	Attix chamber	MC: Water	Extrapolated MC: Water	Attix chamber	MC: Water	Extrapolated MC: Water
0	15.84	9.65	11.76	26.65	13.78	24.82
0.025	21.73	25.17	25.17	32.14	32.99	32.99
0.05	27.57	31.50	31.50	37.55	40.49	40.49
0.075	32.77	36.98	36.98	42.23	47.20	47.20
0.1	37.24	41.43	41.43	46.27	51.24	51.24
0.125	41.16	45.32	45.32	49.74	55.11	55.11
0.15	44.60	48.85	48.85	52.77	58.99	58.99
0.175	47.63	51.72	51.72	55.44	62.06	62.06
0.2	50.34	54.48	54.48	57.80	64.98	64.98
0.34	65.58	65.40	65.40	71.24	74.75	74.75
0.55	79.73	79.71	79.71	83.36	85.62	85.62
0.95	95.00	94.28	94.28	96.23	95.33	95.33
1.16	98.54	96.94	96.94	99.02	96.44	96.44
1.3	99.54	98.83	98.83	99.69	97.92	97.92
1.4	99.91	99.22	99.22	99.85	98.75	98.75
1.5	100.00	100.00	100.00	99.73	99.68	99.68

Figure 7.4 shows dose distributions in the build-up region for $AE = 0.521$ MeV and 0.700 MeV compared with results from an Attix chamber for a field size of 10×10 cm². The results of calculated data must achieve agreement for the 6 MV photon beam with the Attix chamber, as the Attix chamber is an appropriate dosimeter to measure dose in the build-up region. As can be seen, the experimental data and the Monte Carlo calculation in a water phantom are matched well in terms of the percentage dose values, but the Monte Carlo results have relatively higher statistical uncertainties in this region. Note that the large differences in dose between experimental data and Monte Carlo calculated data relate to small difference in spatial terms of about 1 mm. This is due to the steep dose gradient and the lack of electronic equilibrium.

There have been many reports on the build-up region dose. The largest contribution to the dose in the build-up region near the surface is from electron contamination from the accelerator head. Electron contamination contributes to the dose at the surface but decreases rapidly with depth. Dose build-up characteristic curves also change with field size. Experimentally it is difficult to obtain detailed information because of various limitations in the clinical environment and detectors. The modelling of the simulation data contributes to the deviations in the build-up region by presenting an uncertainty of more than 10 %. Being a high dose gradient region, these deviations could occur where electronic disequilibrium is significant. This is because the physics of photon interactions is relatively easy to track, while a more complex investigation is needed for the electron distributions. It is especially important to investigate the dose in the build-up region. This is because this region is impacted on by the effects of contamination produced in the treatment head of the machine and within the air column above the phantom. Monte Carlo simulation can be used to obtain information that can predict the dose distribution of the contaminating electrons from the therapeutic beams.

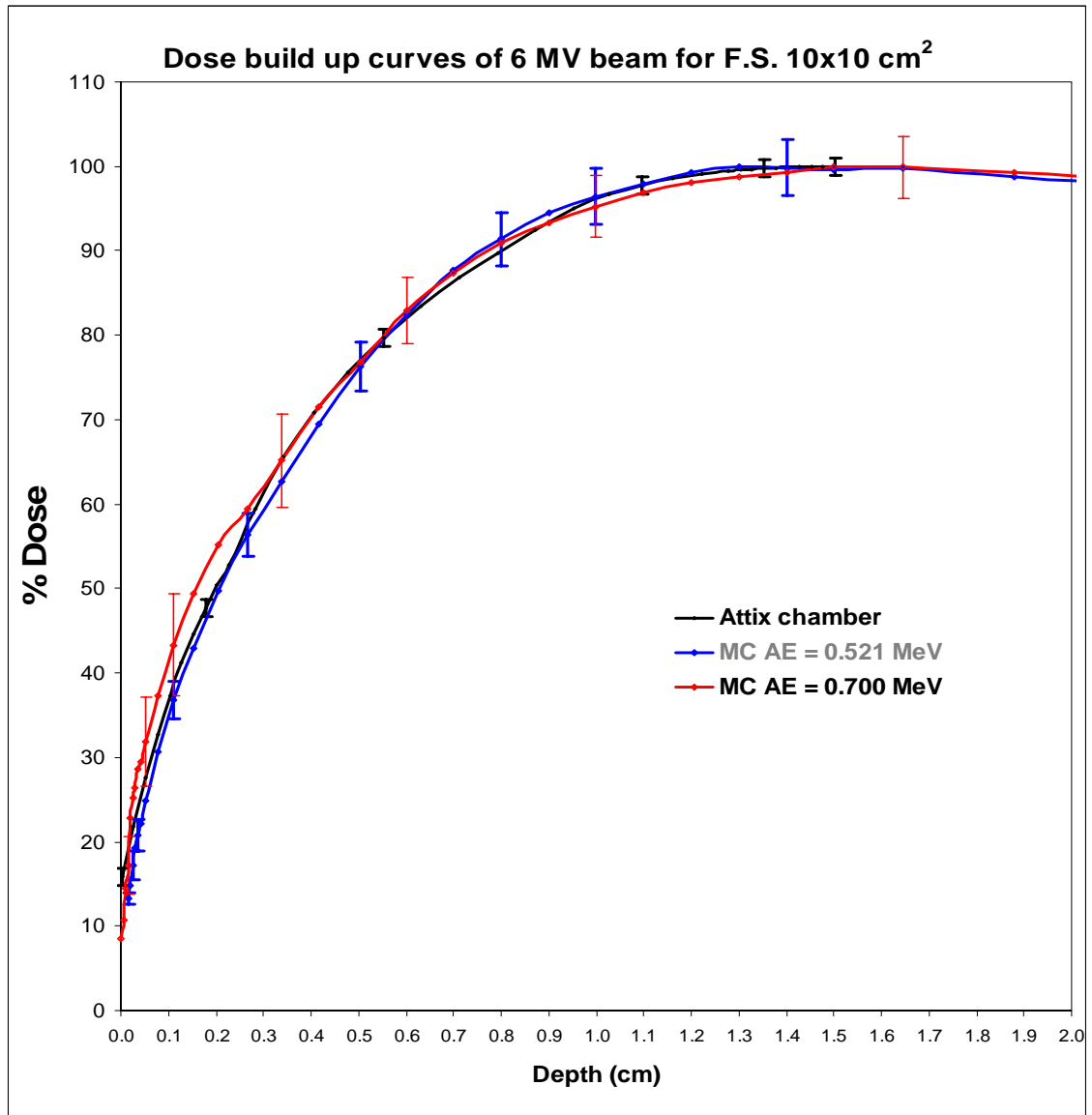


Figure 7.4. Match between experimental data and Monte Carlo calculation in the build-up region for 6 MV beam in a water phantom for a field size of 10 x 10 cm² for AE = 0.521 and 0.700 MeV.

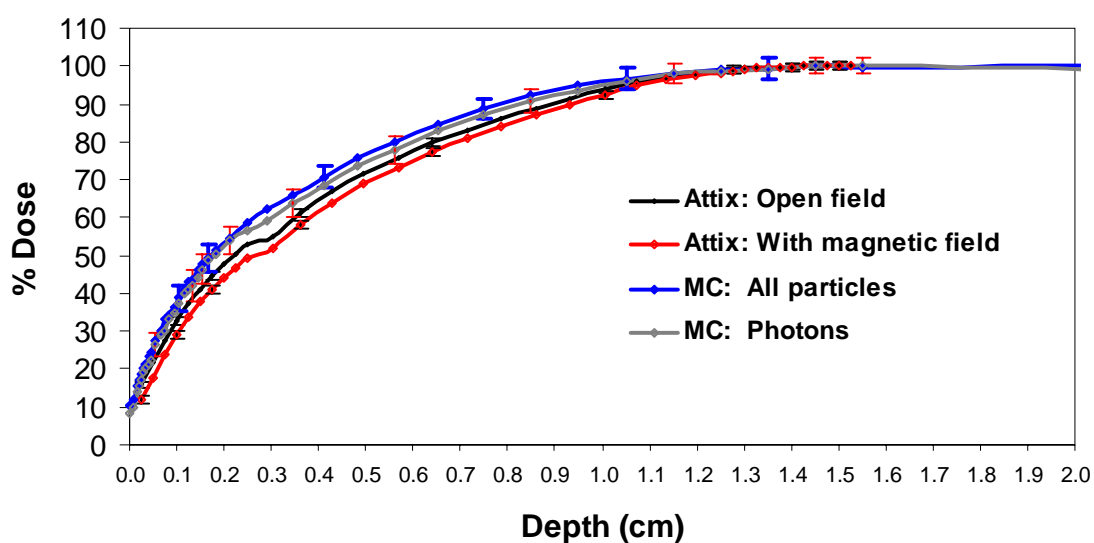
Figures 7.5 and 7.6 illustrate the results of measurements with the Attix chamber and Monte Carlo calculations in the build-up region for the 6 MV beam in a water phantom for field sizes of 10 x 10 cm² and 20 x 20 cm². Dose values with and without magnetic field are compared to the dose values from all particles and photons. The contamination comes from the difference between the dose values with and without magnetic field compared to the results from Monte Carlo calculations. Percentages of contamination

from the total dose also are shown in Figures 7.5 and 7.6 between the measurements and calculated results.

Dose values from Monte Carlo calculations with $AE = 0.700$ MeV in the build-up region for 6 MV beam in a water phantom for field size of $10 \times 10 \text{ cm}^2$ and $20 \times 20 \text{ cm}^2$ of open (without magnetic field) and magnetic field results for all particles and photons provide the higher dose than those obtained with Attix chamber with and without magnetic field. Whilst the dose difference between open and magnetic field results compared to the difference between all particles and photons, and percentage of contamination of the total dose, the result values with Attix chamber present the higher different dose than those obtained from Monte Carlo calculations for both field sizes of $10 \times 10 \text{ cm}^2$ and $20 \times 20 \text{ cm}^2$. Electron contamination can be determined from measured depth doses by subtracting the calculated photon dose; the result will be identified with the dose deposition due to contaminant electrons. From these data, the electron dose will be calculated in each clinical situation and added to the photon-dose calculation to determine the beam-dose deposition. Calculated dose could be fitted to a modified exponential curve beyond the first two millimetres, where uncertainty is difficult to estimate. As can be seen there is significant uncertainty in calculating build-up doses in megavoltage photon beams. Monte Carlo simulation used to obtain information that predict the dose distribution of the contaminating electrons from the clinical beams with good agreement to the measurement from Attix chamber at a few millimetres below the surface. Electron contamination is machine-dependent and dosimetry protocols state that beams should be calibrated at a depth beyond the range of charged particle contamination. The most energetic photons are generated in the direction of the electrons. Furthermore, the dose from charged particle contamination in the build-up region complicates the use of data from that region including the depth of dose maximum.

Monte Carlo calculations predicted the contamination dose in the build-up region to be lower than those obtained from measurements did. Percentage depth doses were calculated with DOSXYZnrc user code on radiographic film for the total dose and electron distribution of a 6 MV beam with $AE = 0.521$ and 0.700 MeV in Figures 7.7, 7.8 and 7.9.

a) Dose build-up curves of 6 MV beam for F.S. 10x10 cm²



b) Dose build-up curves of 6 MV beam for F.S. 10x10 cm²

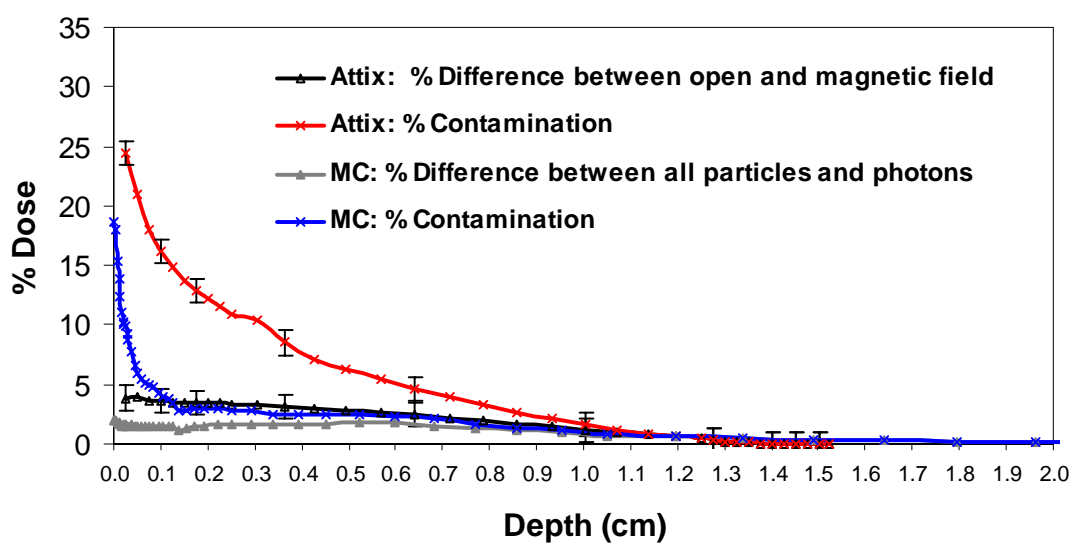
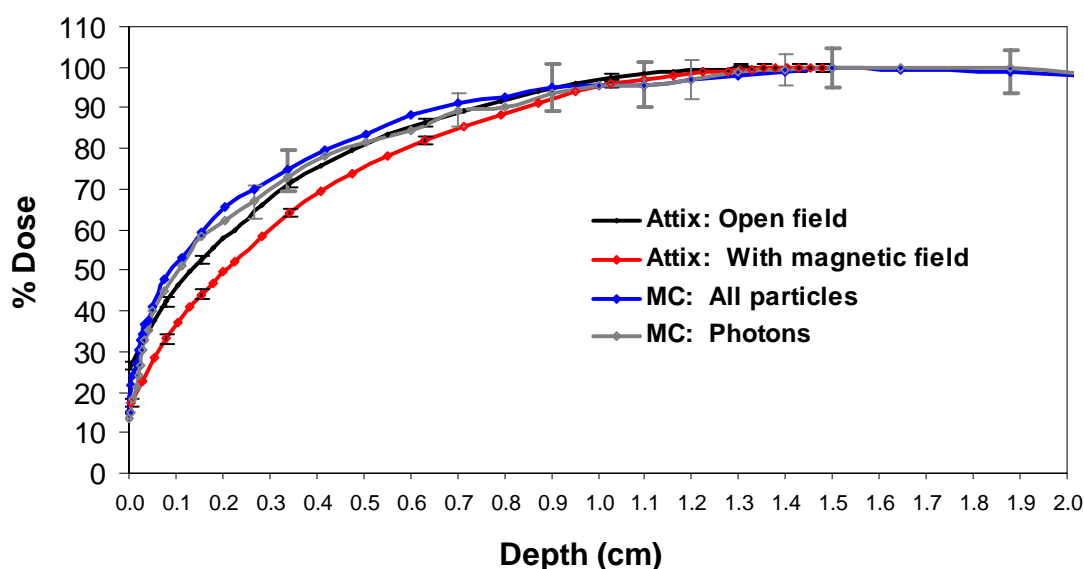


Figure 7.5. Dose values measured with Attix chamber and Monte Carlo calculations with AE = 0.700 MeV in the build-up region for 6 MV beam in a water phantom for field size of 10 x 10 cm²: a) Comparison of open (without magnetic field) and magnetic field results for all particles and photons, b) Difference between open and magnetic field results compared to difference between all particles and photons, and percentage of contamination of the total dose.

a) Dose build-up curves of 6 MV beam for F.S. 20x20 cm²



b) Dose build-up curves of 6 MV beam for F.S. 20x20 cm²

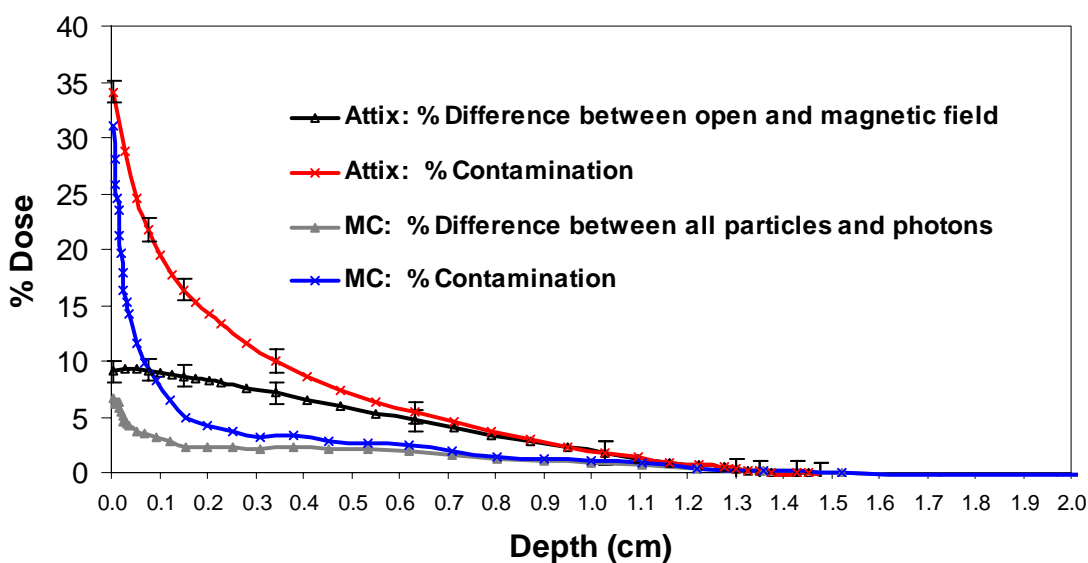


Figure 7.6. Dose values measured with Attix chamber and Monte Carlo calculations with $AE = 0.700$ MeV in the build-up region for 6 MV beam in a water phantom for a field size of 20×20 cm²: a) Open and magnetic field results are compared for all particles and photons, b) Difference between open and magnetic field results compared to difference between all particles and photons, and percentage contamination from the total dose.

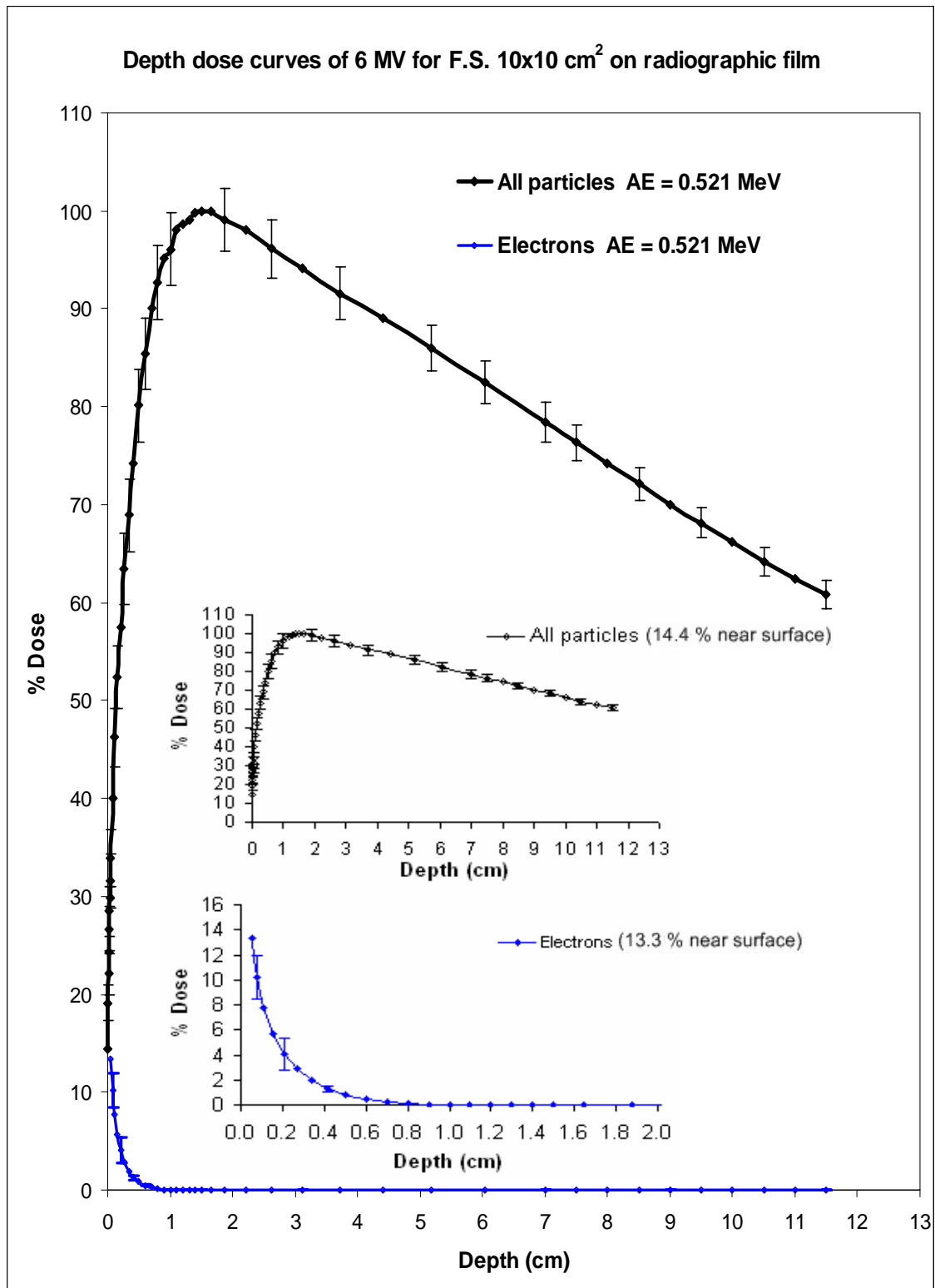


Figure 7.7. Depth dose curves from Monte Carlo results on simulated radiographic film for the energy cut-offs and AE = 0.521 MeV for 6 MV beam and field size of 10 x 10 cm²: a) depth dose curves of all particles, b) dose distribution of electrons.

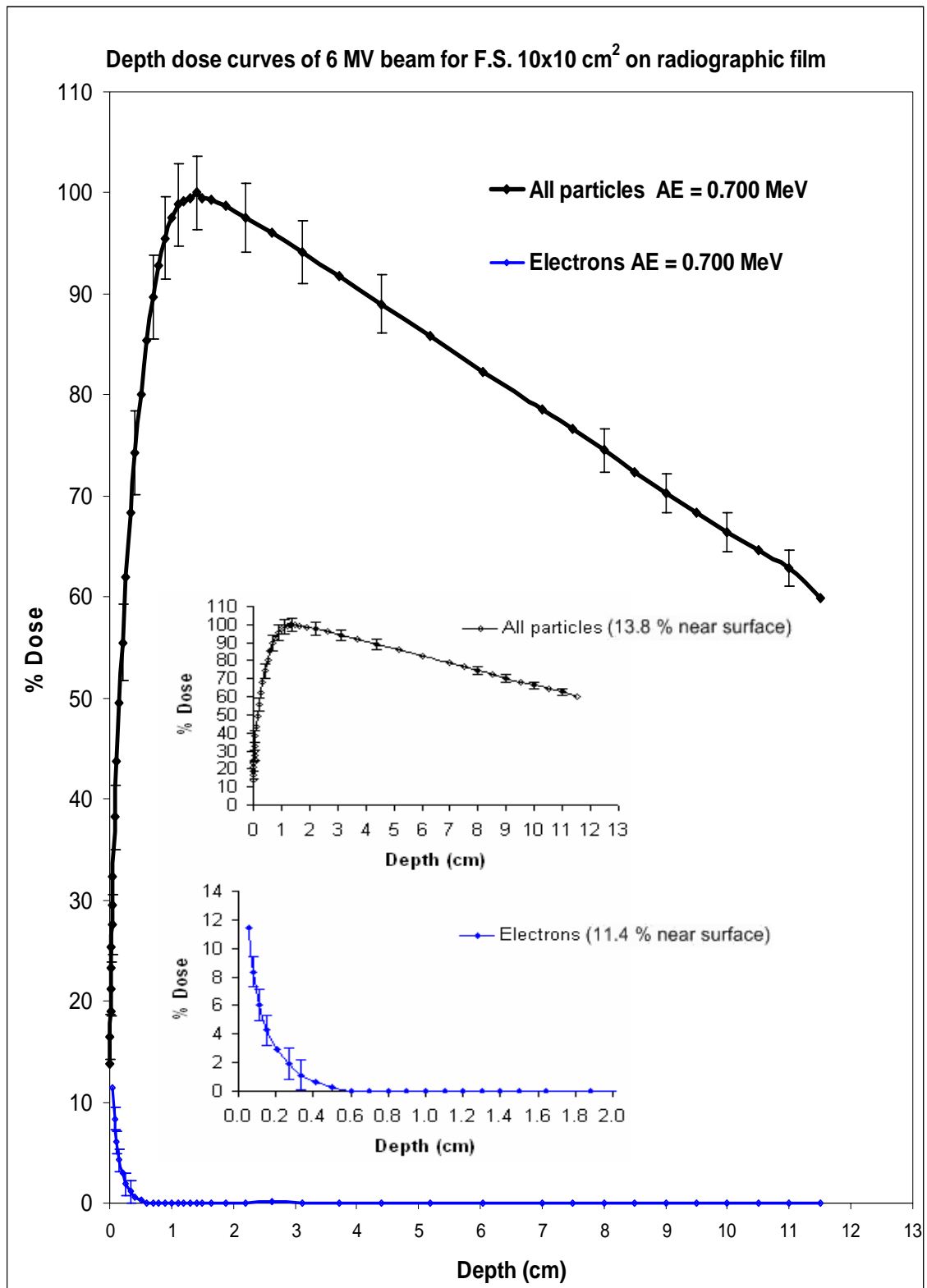


Figure 7.8. Depth dose curves from Monte Carlo calculations on simulated radiographic film for the energy cut-offs and AE = 0.700 MeV for 6 MV beam with field size of 10 x 10 cm²: a) depth dose curves of all particles, b) dose distribution of electrons.

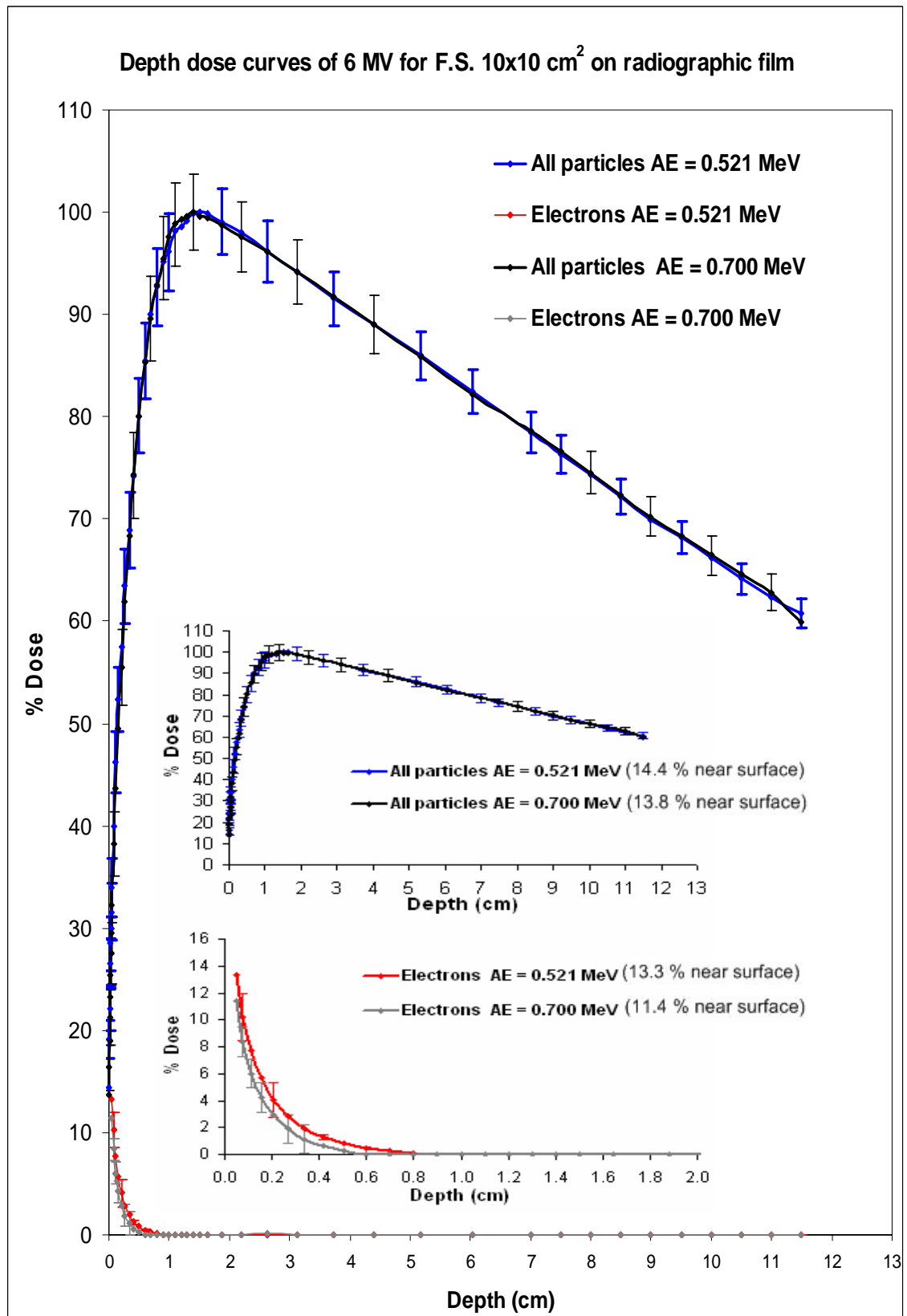


Figure 7.9. Comparison of depth dose curves from Monte Carlo calculations on simulated radiographic film using the different AE for 6 MV beam for field size of 10 x 10 cm²: a) depth dose curves of all particles, b) dose distribution of electrons.

The doses near the surface for total dose and electron dose using $AE = 0.521$ MeV are higher than those using 0.700 MeV because the lower fluences of electron contamination in the simulation are increased with the lower energy threshold AE condition. Thus, numerous secondary particles are accumulated in the top few millimetres from the surface of the phantom during the simulation process. The threshold of ECUT was selected to remove low energy electrons with kinetic energy of 10 keV from the simulation. So we used the AE, ECUT = 0.521 MeV in a simulation to study the doses at the surface and in the build-up region, because they involve not only the photon particles but also the dose from the electrons and positrons.

7.3.2 Surface dose

Figures 7.10-7.13 illustrate the dose profiles from the Monte Carlo calculated results with the data normalised at a depth of 10 cm for a field size of 10×10 cm² in a water phantom and on radiographic film along the cross-plane and in-plane distances (X and Y-axes) for $AE = 0.521$ and 0.700 MeV. As can be seen, the surface doses calculated on radiographic film are higher than the calculated dose in a water medium for both $AE = 0.521$ and 0.700 MeV along the X and Y-axes. There is a slight difference for surface doses in a water phantom between using $AE = 0.521$ and 0.700 MeV, while surface doses on radiographic film calculated using $AE = 0.521$ MeV are slightly higher than the calculated dose using $AE = 0.700$ MeV. To remove this inconsistency, we also performed the surface dose calculations using $AE = 0.700$ MeV on simulated radiographic film for field sizes of 5×5 , 10×10 , and 15×15 cm² compared to actual radiographic film measurements in Figure 7.14. Surface dose calculations using $AE = 0.521$ and 0.700 MeV on radiographic film for a field size of 10×10 cm² were compared to the real radiographic film measurements in Figure 7.15.

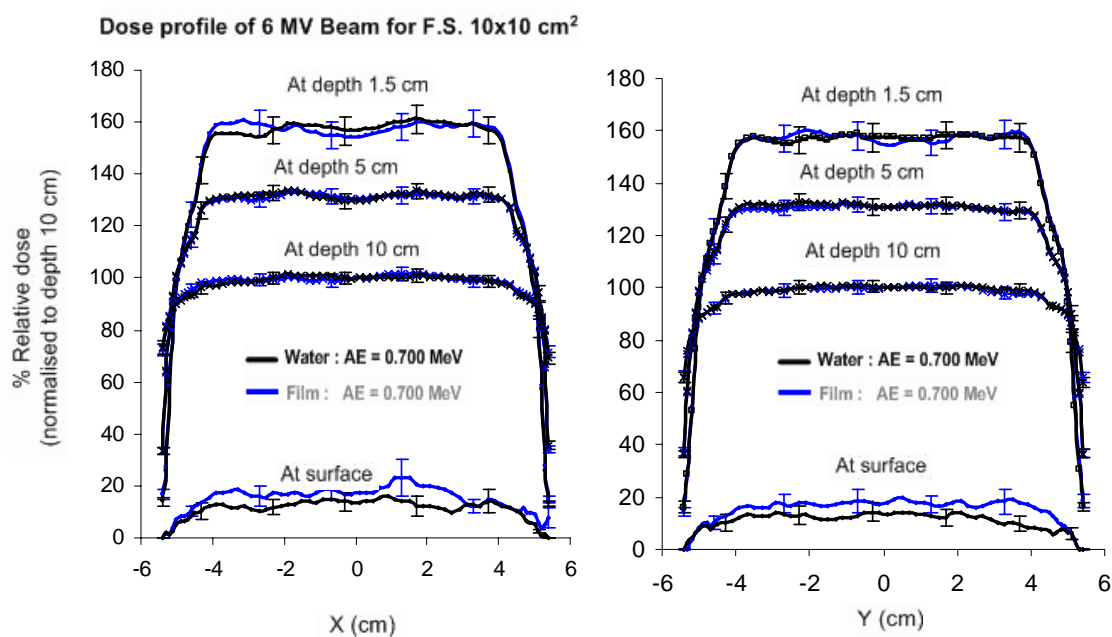


Figure 7.10. Simulated dose profiles compared between using $AE = 0.700$ MeV in a water phantom and radiographic film for 6 MV Clinac 2100 C with a field size of 10×10 cm² at different depths along X and Y – axis directions.

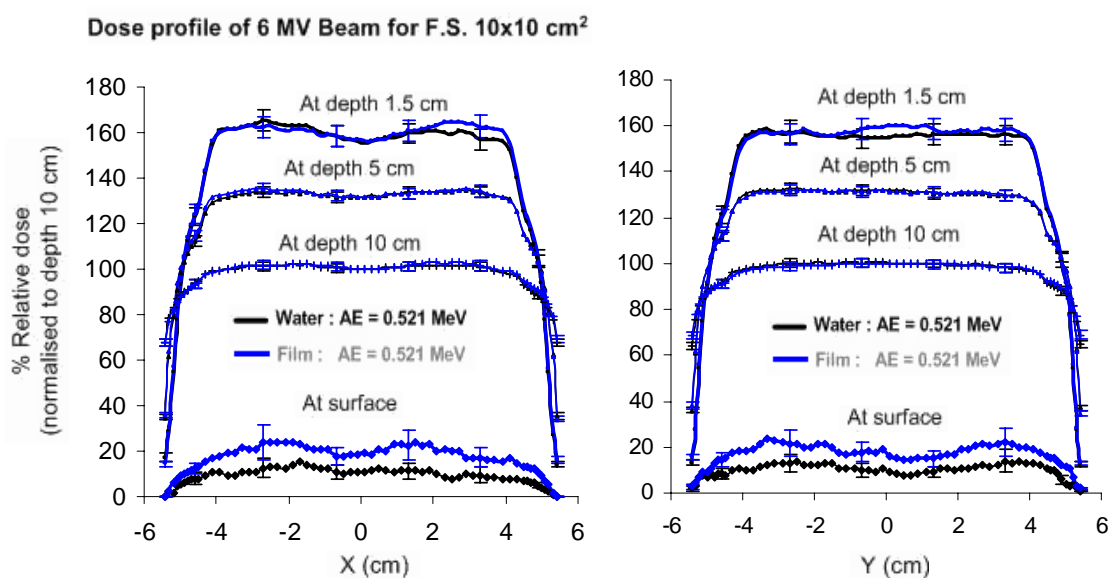


Figure 7.11. Simulated dose profiles compared between using $AE = 0.521$ MeV in a water phantom and radiographic film for 6 MV Clinac 2100 C for field size of 10×10 cm² at different depths along the X and Y – axes.

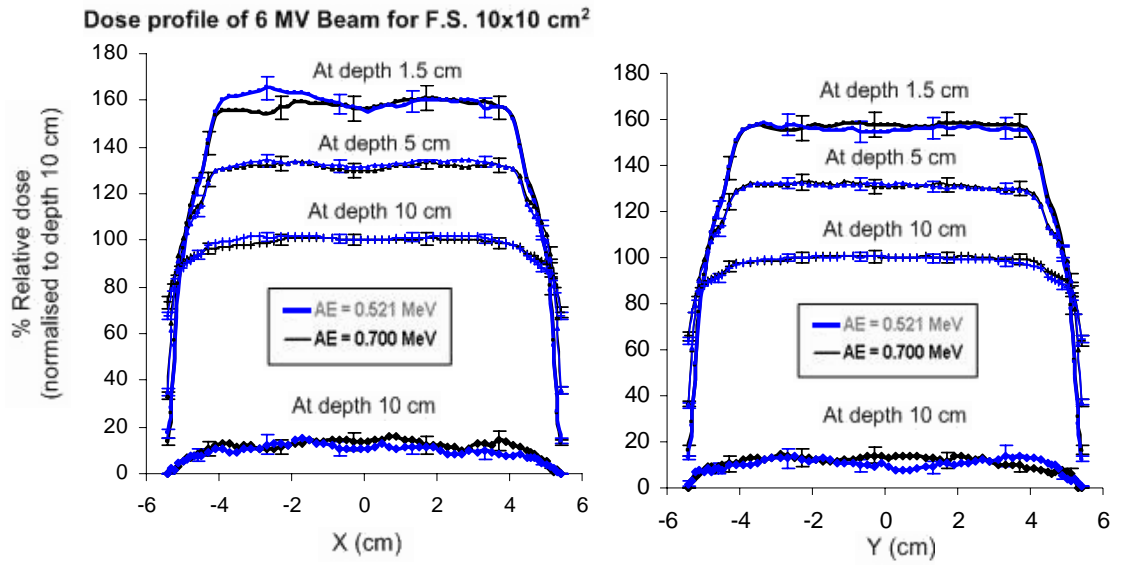


Figure 7.12. Simulated dose profiles compared between using $AE = 0.521$ MeV and $AE = 0.700$ MeV on a water phantom for 6 MV Clinac 2100 C for a field size of 10×10 cm² at different depths along the X and Y – axes.

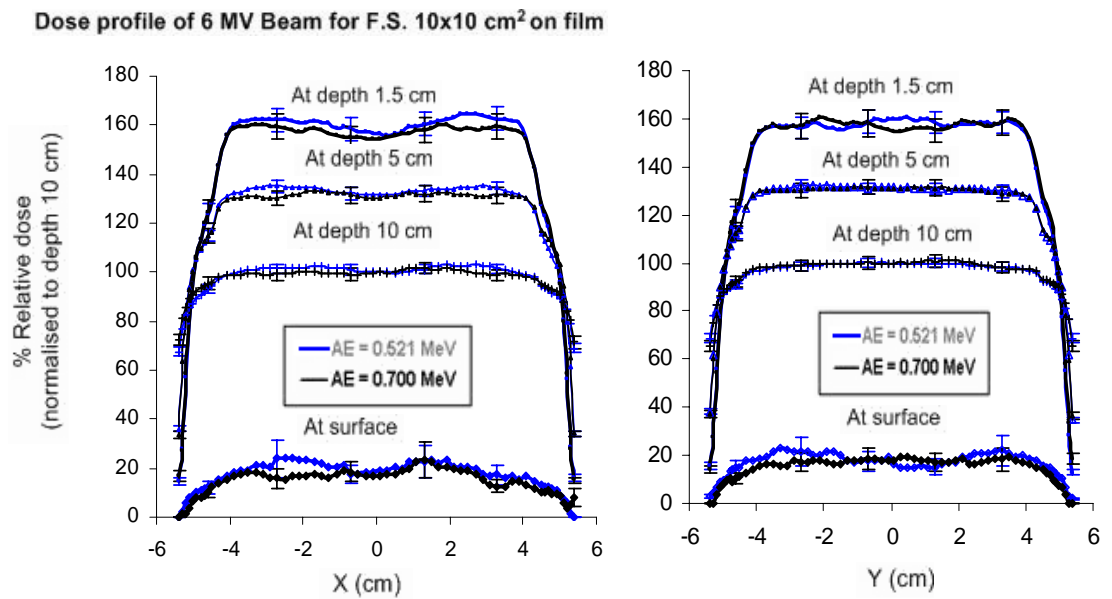
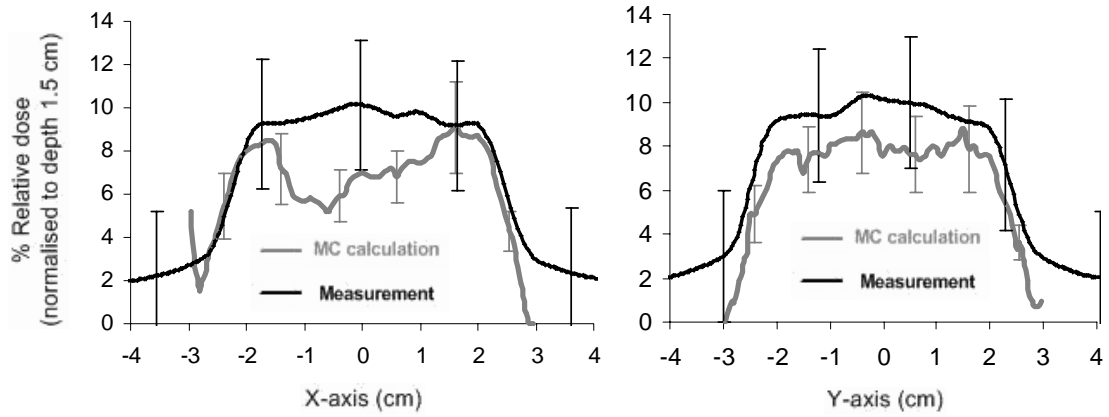
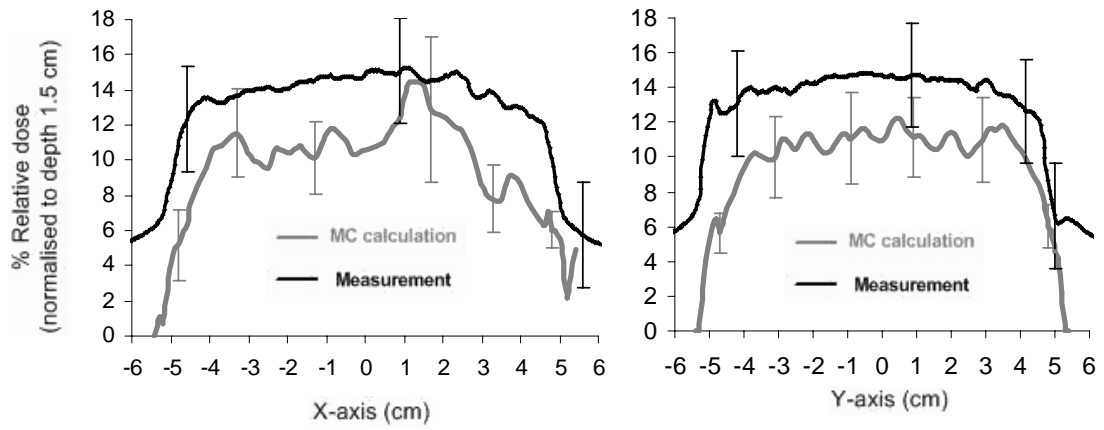


Figure 7.13. Simulated profiles compared between using $AE = 0.521$ MeV and $AE = 0.700$ MeV for radiographic film on a water phantom for 6 MV Clinac 2100 C for a field size of 10×10 cm² for different depths along the X and Y – axes.

a) Surface dose profile of 6 MV beam for F.S. $5 \times 5 \text{ cm}^2$



b) Surface dose profile of 6 MV beam for F.S. $10 \times 10 \text{ cm}^2$



c) Surface dose profile of 6 MV beam for F.S. $15 \times 15 \text{ cm}^2$

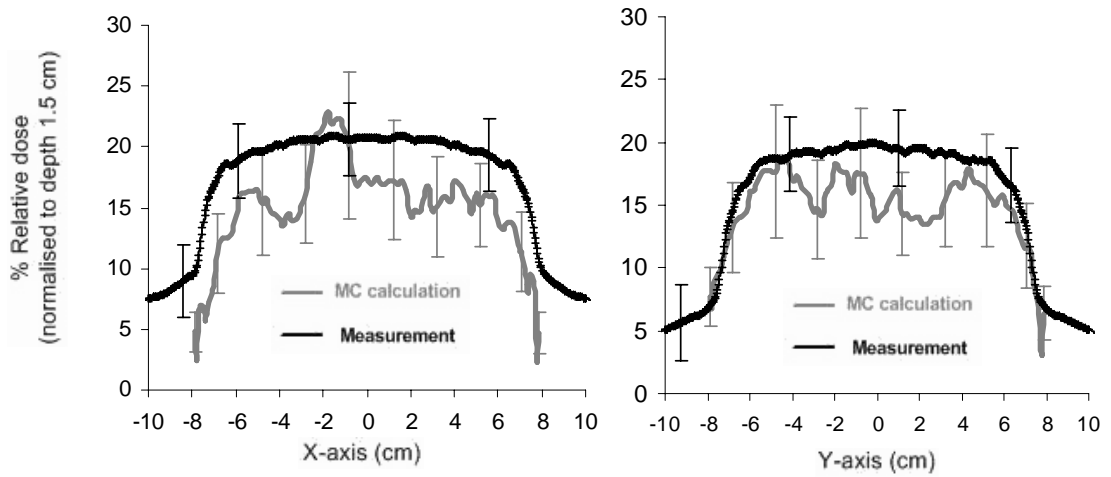


Figure 7.14. Surface dose profiles comparing the MC calculations with measurements on radiographic film using $AE = 0.700 \text{ MeV}$ for a 6 MV beam along the X and Y- axes for field sizes of: a) $5 \times 5 \text{ cm}^2$, b) $10 \times 10 \text{ cm}^2$, and c) $15 \times 15 \text{ cm}^2$.

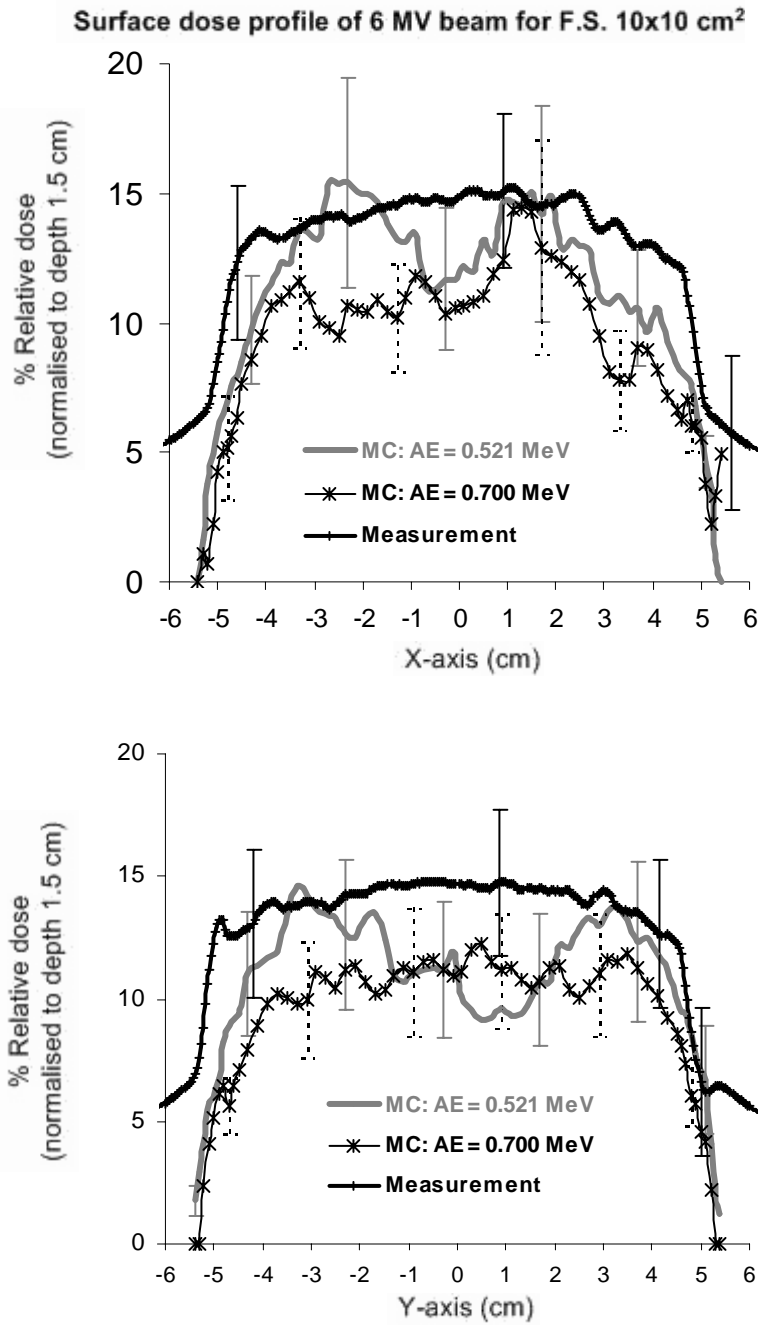


Figure 7.15. Surface dose profiles comparing the MC calculations with measurements on radiographic film using AE = 0.521 and 0.700 MeV for a 6 MV beam along the X and Y- axes for a field size of 10 x 10 cm².

Results measured on film compared to results from Monte Carlo calculation have shown similar agreement between using AE = 0.521 and 0.700 MeV. Using AE = 0.521 MeV, the calculated surface doses are higher than for the calculated surface doses from

using $AE = 0.700$ MeV. Dose profiles are from near the surface where the electron contamination contribution is significant. As can be seen from the strong variation of doses along the beam axis, along the X and Y-axes, in the larger field size, this is because the effect of scattered radiation increases with increasing field size. It is well known that dose is determined by the high-energy x-ray beam for depths greater than a few centimetres, but for the electrons, the deposited energy is limited to within a few centimetres. Thus, the contribution to the dose in this region is also comprised of the primary photons beam, backscattered radiation, and lepton contamination. As can be seen, the surface doses for a larger field size such as this are due to the lack of electronic equilibrium in this region. The larger the field size, the greater the presence of scattered radiation. Surface doses in this region are the primary photons, scattered photons, and contaminant radiation from the linear accelerator head, as well as from multiple scattering within the phantom. Monte Carlo calculations predicted a lower surface dose than those obtained from measurements, as shown in Table 7.3.

Table 7.3. Percentage of the surface dose from Monte Carlo calculations compared to the measurements on radiographic film.

Percentage of the surface dose						
MC calculations on film ($AE = 0.700$ MeV)				Radiographic film		
F.S.(cm ²)	All particles	Photons	% Reduction	open field	Magnetic field	% Reduction
10 x 10	13 ± 3	9 ± 3	31	14 ± 7	9 ± 7	36
15 x 15	19 ± 4	15 ± 4	21	19 ± 3	13 ± 3	32
20 x 20	20 ± 5	14 ± 4	30	27 ± 4	16 ± 4	41

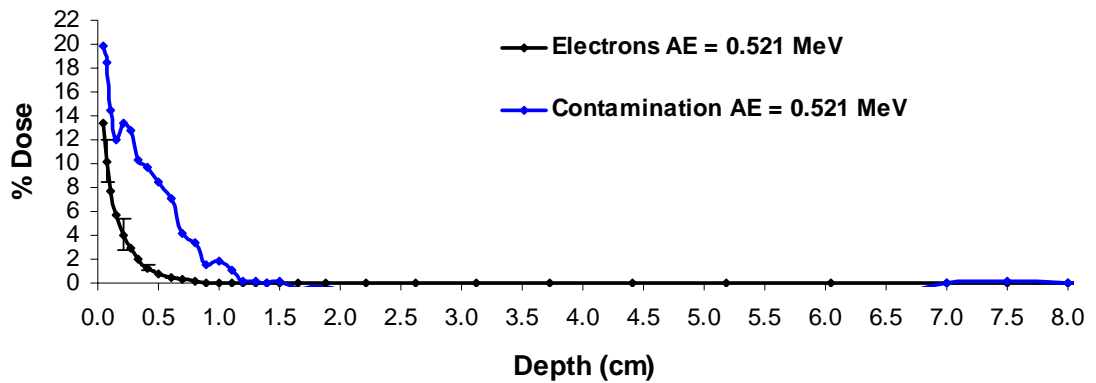
7.3.3 Electron and contamination doses

Figures 7.16, 7.17, 7.18 and 7.19 illustrate the electron and contamination depth dose curves from Monte Carlo calculations on radiographic film using different AE for a 6 MV beam and field sizes of 10×10 cm² and 20×20 cm². By subtracting the percentage dose results of the photons from the all particles results, the differences that represent contamination on the central axis of the beam are also presented. Dose calculations in a different medium with cross-section data also have a similar agreement between $AE =$

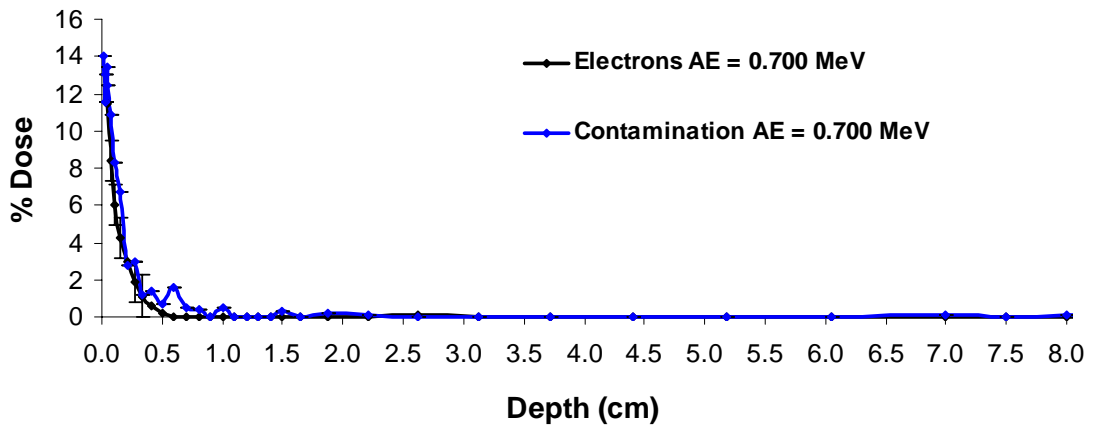
0.521 MeV and 0.700 MeV for the electron and contamination dose distributions. Detailed comparisons show that when $AE = 0.521$ MeV, results on doses of electrons and contamination are higher than for $AE = 0.700$ MeV. If the field sizes are larger, the electron and contamination doses are also higher. For several millimetres depth, the doses are different due to the involvement of scattering and contamination doses that have the lower energy. $AE = 0.521$ MeV is a lower energy threshold for production of electron interaction than $AE = 0.700$ MeV. The contributions to the dose in this region are comprised of the primary photons beam, backscattered radiation, and contamination. Contamination produced from the material in the treatment head will occur in each beam from the smaller field sizes to the larger field size. The jaws will stop most of the contamination produced above them when they are in a small field size configuration. However, as the field size is increased an enhanced effect occurs when the upper surface of the jaws allows more contamination produced in areas of the flattening filter and other components to pass through, so that a greater surface area of the sides of the jaws is exposed to the beam. Extra focal photons in particular may interact with these surfaces causing contamination; the air volume exposed to x-rays therefore increases the probability of contamination, so consequently as the field size is increased the contamination dose near the surface increases.

It is known that the dose delivered to the surface and down to 1 mm depth is the most important in terms of skin reactions within the basal cell and dermal layer. A high skin surface dose, which is undesired in many clinical situations, causes enhanced damage to skin. Thus, the information on dose build-up characteristics of the patient is important for proper treatment decisions. The Monte Carlo method is expected to evaluate lower energy electrons and contamination still present in this surface region. The threshold of the AE was selected to discard low-energy electrons with kinetic energy below 10 keV in the simulation, as they are the major concern in the study.

a) Depth dose distribution of 6 MV beam for F.S. 10x10 cm² on film



b) Depth dose distribution of 6 MV beam for F.S. 10x10 cm² on film



c) Depth dose distribution of 6 MV beam for F.S. 10x10 cm² on film

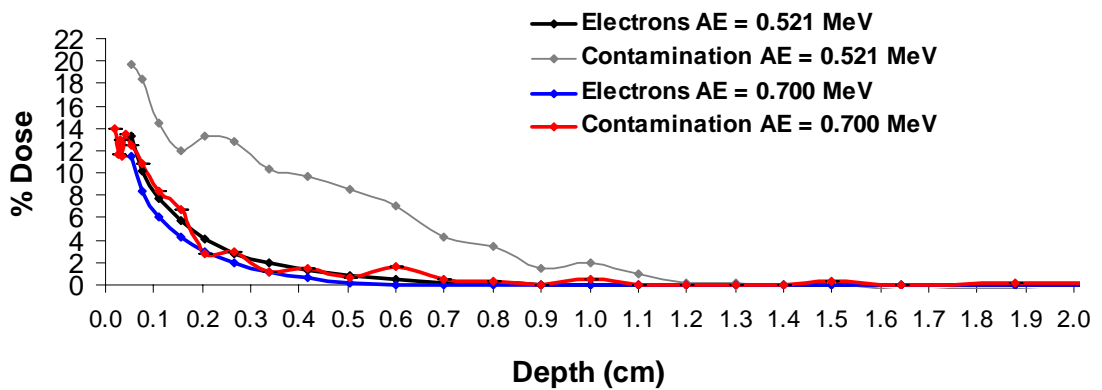


Figure 7.16. Comparison of electron and contamination depth dose curves from Monte Carlo calculations on radiographic film using the different AE for a 6 MV beam with a field size of 10 x 10 cm²: a) AE = 0.521 MeV, b) AE = 0.700 MeV, c) AE = 0.521 and 0.700 MeV. (Contamination is from the difference between all particles and photons.)

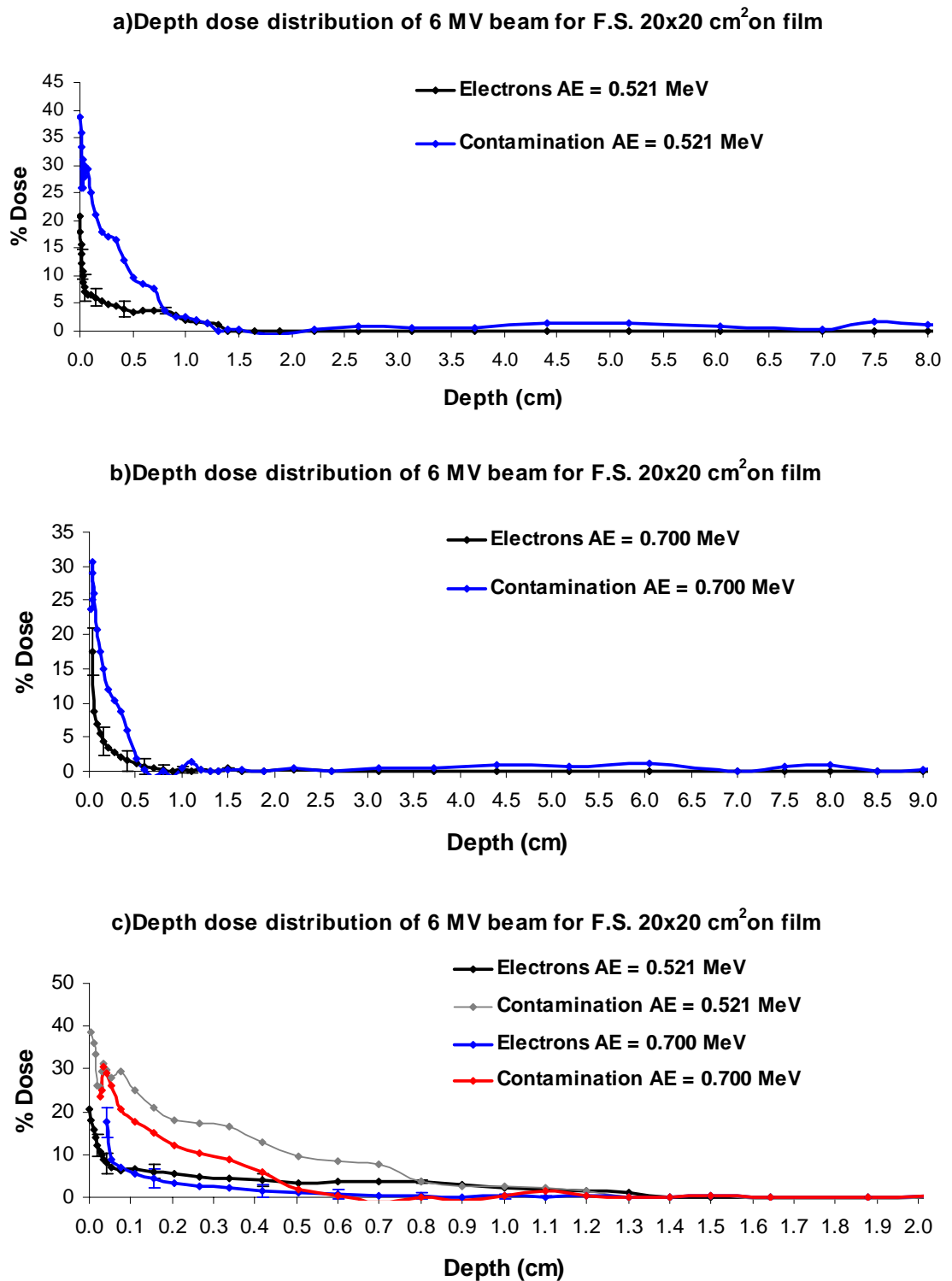
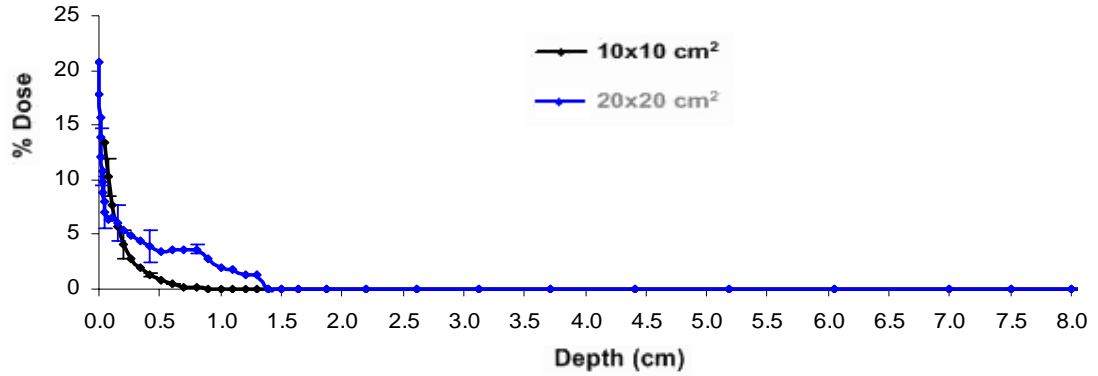
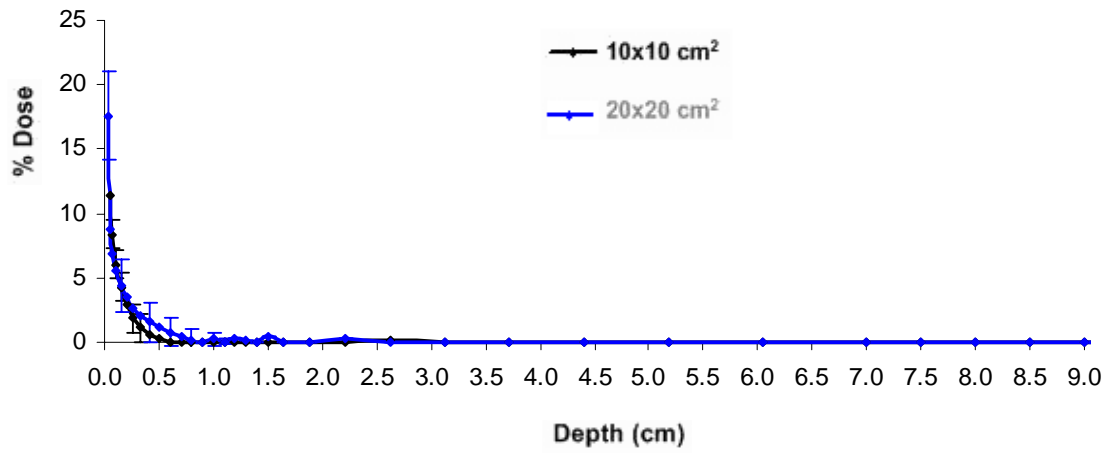


Figure 7.17. Comparison of electron and contamination depth dose curves from Monte Carlo calculations on radiographic film using the different AE for a 6 MV beam with a field size of 20 x 20 cm²: a) AE = 0.521 MeV, b) AE = 0.700 MeV, c) AE = 0.521 and 0.700 MeV. (Contamination is from the difference between all particles and photons.)

a) Electron dose distribution of 6 MV beam on film AE = 0.521 MeV



b) Electron dose distribution of 6 MV beam on film AE = 0.700 MeV



c) Electron dose distribution of 6 MV beam on film

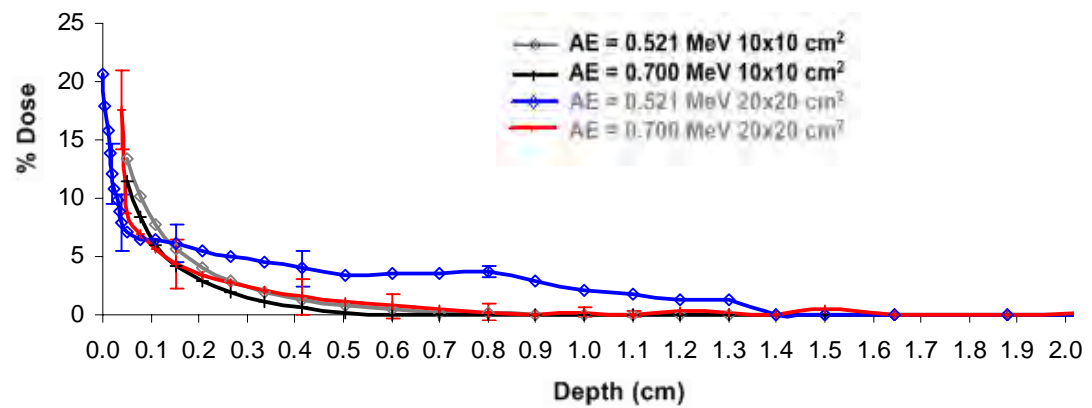
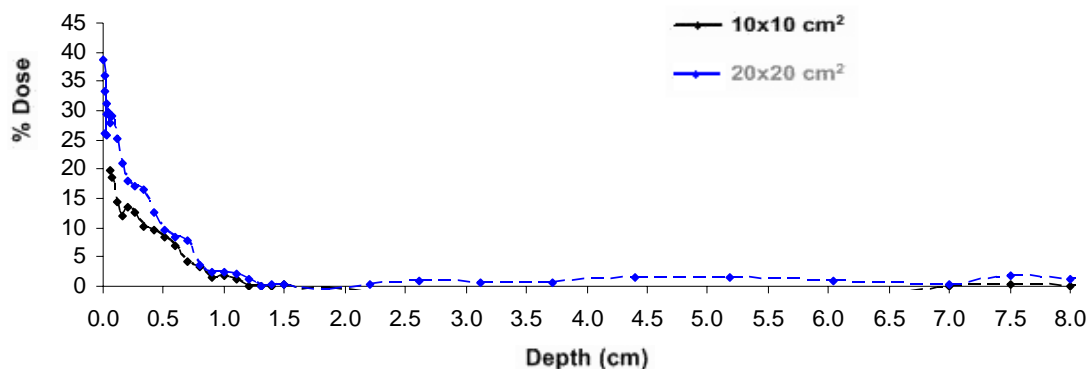
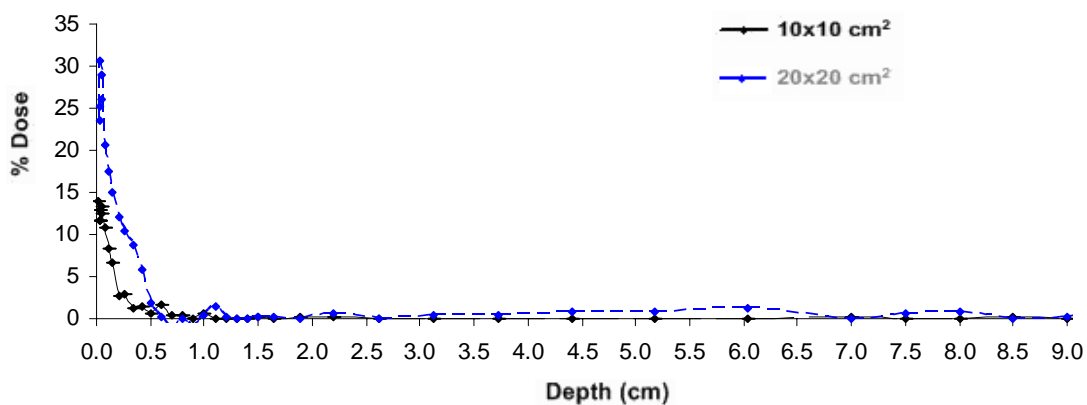


Figure 7.18. Comparison of electron depth dose curves from Monte Carlo calculations on radiographic film using the different AE: a) AE = 0.521 MeV for F.S. 10 x 10 and 20 x 20 cm², b) AE = 0.700 MeV for F.S.10 x 10 and 20 x 20 cm², c) AE = 0.521 and 0.700 MeV for F.S.10 x 10 and 20 x 20 cm².

a) Contamination dose distribution of 6 MV beam on film AE = 0.521 MeV



b) Contamination dose distribution of 6 MV beam on film AE = 0.700 MeV



c) Contamination dose distribution of 6 MV beam on film

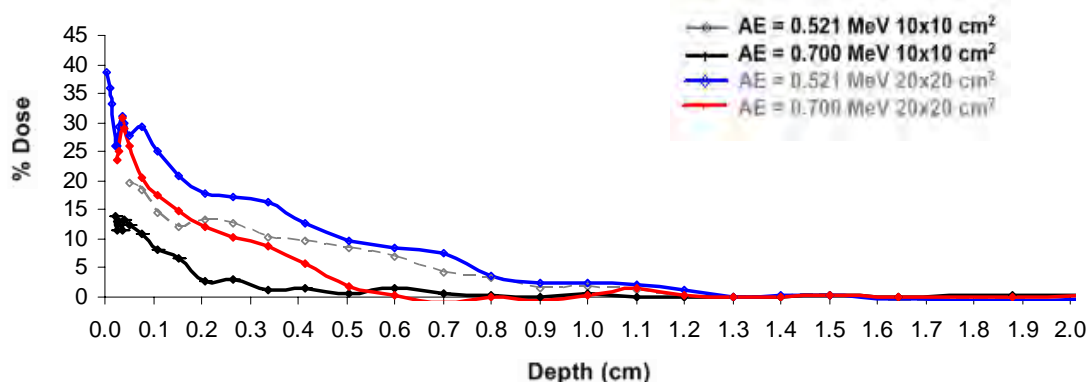


Figure 7.19. Comparison of contamination dose distribution curves from Monte Carlo calculations on radiographic film using the different AE: a) AE = 0.521 MeV for F.S. 10 x 10 and 20 x 20 cm², b) AE = 0.700 MeV for F.S. 10 x 10 and 20 x 20 cm², c) AE = 0.521 and 0.700 MeV for F.S. 10 x 10 and 20 x 20 cm².

7.4 Conclusions

The Monte Carlo method was used for simulation and measurements in this thesis work, specifically to simulate a photon beam of 6 MV from a Varian Clinac 2100 C linear accelerator. Results from the calculations and measurements have shown quite good agreement in dose distributions at the surface and in the build-up region, although the Monte Carlo results predicted dose distributions that were appreciably lower than those obtained from the measurements. Dose calculations using cross-section data in a different medium also showed good agreement between $AE = 0.521$ MeV and 0.700 MeV for the electron and contamination dose distributions. Investigation of the contamination offers important knowledge for developing methods for detection of electron contamination. The calculated fluence spectra for contaminant electrons is characterised by a sudden drop in the fluence of very low-energy electrons, due to the cut-off kinetic energy of 10 keV for the transport of electrons. The depth dose and profile comparisons between $AE = 0.521$ MeV and $AE = 0.700$ MeV for various field sizes indicated variation in the doses along the beam axis in the X and Y-axis directions at the surface and at a depth of 1.5 cm where the electron contamination has a more important influence on dose deposition.

CHAPTER 8

CONCLUSIONS

8.1 Magnetic field model

Radiation therapy procedures to control localised tumours may be affected by a number of factors, including variations in radiation sensitivity and the inability to apply an optimum tumour dose due to the limitations of the treatment technique. Applying an appropriate strong transverse magnetic field to a high-energy x-ray beam is one of the potential techniques to overcome the limitations of the conventional radiotherapy technique, which often involves a significant unwanted dose in a nearby region. In addition, it is often possible to direct the deflection of electrons and positrons in order to spare critical structures. The location and magnitude of this dose reduction are potentially adjustable by carefully designing the magnetic field configuration.

Implementing these methods requires building magnets to produce extremely strong and complex magnetic fields, hence our newly designed magnetic deflector device. Experimental results show that significant decreases in the skin dose with a strong magnetic field can still be achieved over the larger volume where the most of the deflection takes place. An enhancement of dose is never seen in the irradiated area. Due to the high magnetic field strength in the y-axis direction, which sets up the deflection process following the Lorentz force rule, the electron contamination is still present in the x-axis direction outside the treated area. However, material such as a 1.5 cm thick layer of wax could be placed next to the field to absorb the electron contamination during the radiation process. Although the magnetic deflector device is portable and clinically usable for x-rays, the weight of this device after adding more magnets has made attachment inconvenient. If the device was used clinically it would be best suited now to have a special table to carry the magnetic device to the linear accelerator machine for easy insertion in the treatment head.

An enhancement of the dose is never observed in the irradiated area, and a percentage reduction of the skin and subcutaneous dose up to 34 % with the NdFeB magnetic device was seen for a 20 x 20 cm² field size. The magnetic field strengths obtained by the magnetic deflector will theoretically give rise to electron deflection radii that should

cause the majority of electron contamination to exit the treatment field. The device can be located at any position between the target and the patient, depending on the deflector design, size, and purpose. In theory the ideal location tends to be closer to the patient surface than the x-ray source, as this potentially allows for removal of more contamination electrons, i.e. the only remaining contamination, which arises from the air column between the lowest part of the deflector and the patient surface. A simple magnetic field applied across the beam with its direction perpendicular to the beam axis will generate a sweeping action for any electrons passing through the region as described by the Lorentz Force rule. Such a magnetic field can be set up by a simple arrangement of permanent magnets that are mounted on either side of the x-ray beam. That is, the elimination of these doses due to contaminant electrons down to a depth of a few millimetres could be obtained with this magnetic deflector device.

Due to recent technological advances in manufacturing superconducting magnets that operate at higher temperature, such progress may be expected to continue to demonstrate the design and the feasibility of using strong transverse magnetic fields in photon beams to diminish electron contamination on the skin surface during the treatment for deep-seated tumours. Thus we have undertaken theoretical study on the transport of charged particles in magnetic fields and have qualitatively shown lepton dose reductions for photon beams in magnetic fields. Further work has been performed in an attempt to experimentally confirm the theoretical amount of electron deflection by monitoring the paths of the electron beams and the motions of electrons in a magnetic field as well as electron density distributions along the x, y, and z-directions for different magnetic profiles, which have been simulated by a Monte Carlo method.

8.2 Electron contamination from 6 MV x-ray beams

An advantageous feature of high-energy x-ray beams is the skin-sparing effect, but in some situations, this effect may be reduced or even lost if the beam is excessively contaminated with secondary electrons. Electrons are the major contaminants produced from Compton scattering and the pair production process. Thus, doses delivered in the skin surface are often dominated by electron contamination and can vary quite considerably within the first few millimetres of depth due to the build-up characteristics

of x-ray beams. These electrons arise from photon interactions with the collimating system and with any other scattering medium in the beam path. This is important, especially in the isocentric method of treatment in which these absorbers are brought close to the skin. The introduction of material into the beam path will increase the dose delivered to the patient's skin during treatment. Thus the pattern of behaviour of the skin dose can be attributed to variations in electron contamination caused by using accessory devices in radiotherapy treatment.

Contamination, which is usually produced by interactions of a high-energy x-ray beam from a medical linear accelerator, comes from Compton scattering and the pair production process. A large amount of electrons originate from Compton scattering and pair production, whereas a small percentage of positrons is generated from the pair production process. Thus, electron particles are the most important contaminants to study. These sources of contamination are ultimately responsible for the variation in contaminant doses caused by parameters such as the field size (Table 8.1) or the use of beam modifying devices (Table 8.2).

Table 8.1. Percentage of dose from the contamination and the percentage reduction for field sizes of 10 x 10 cm², 15 x 15 cm², and 20 x 20 cm² with the magnetic deflector device in place for a 6 MV x-ray beam in the build-up region.

Depth (mm)	F.S. 10 x 10 cm ²		F.S. 15 x 15 cm ²		F.S. 20 x 20 cm ²	
	% contamination	% Reduction	% contamination	% Reduction	% contamination	% Reduction
0	3.88	24.48	6.71	31.54	9.08	34.08
1	4.12	10.47	7.72	17.47	9.76	20.07
2	1.12	1.79	5.06	7.65	8.78	12.59
3	4.57	6.04	6.62	8.56	8.30	10.36
4	2.59	3.14	6.00	7.08	6.04	6.94
5	4.74	5.33	5.35	6.04	5.60	6.19
6	2.32	2.52	5.51	5.93	4.88	5.18
7	1.67	1.77	4.01	4.21	3.21	3.34
8	2.05	2.11	2.09	2.15	2.78	2.85
9	0.96	0.99	1.31	1.33	1.75	1.77
10	0.54	0.55	1.28	1.29	1.53	1.54
11	0.34	0.34	0.74	0.74	0.89	0.89
12	0.14	0.14	0.42	0.42	0.55	0.55
13	0.09	0.09	0.23	0.23	0.19	0.19
14	0.03	0.03	0.00	0.00	0.00	0.00
15	0.00	0.00	0.17	0.17	0.27	0.28

The secondary electrons that are set in motion and can accumulate in the skin surface are generated from the scattering interactions of the high-energy x-rays with many of the components in the medical linear accelerator head and in the air volume between the linear accelerator machine and the patient or phantom. Thus, doses delivered at the skin surface are often dominated by electron contamination and can vary quite considerably within the first few millimetres of depth due to the build-up characteristics of x-ray beams. In this thesis work, the surface dose increased as the field size increased both for an open field and when a Perspex tray was in the beam, and the increase was especially significant in case of a Perspex tray with larger field sizes. The Perspex tray and wedge filter eliminate secondary electrons, but generate new electrons at the same time. However, when these devices are used in combination with magnetic field, the surface dose is reduced significantly. A particularly effective way to reduce this unwanted dose is by using a magnetic deflector mounted into the lower part of the linear accelerator treatment head. The 6 MV x-ray beam data in Table 8.2 with and without the magnetic deflector show that a significant reduction of the skin dose by using magnetic field is practicable in clinical radiotherapy treatment.

Table 8.2. Percentage of dose absorbed at the surface for field sizes of 10 x 10 cm², 15 x 15 cm², and 20 x 20 cm² with the use of beam modifying devices and the magnetic deflector device in place for 6 MV x-ray beam from radiographic film.

Beam modifying devices	F.S. 10 x 10 cm ²		F.S. 15 x 15 cm ²		F.S. 20 x 20 cm ²	
	No deflection	Magnetic field	No deflection	Magnetic field	No deflection	Magnetic field
Open field	14 ± 7 %	9 ± 7 %	19 ± 3 %	13 ± 3 %	27 ± 4 %	16 ± 4 %
With 6 mm Perspex tray	15 ± 7 %	8 ± 7 %	-	-	33 ± 4 %	19 ± 4 %
15° Wedge	-	-	-	-	25 ± 7 %	18 ± 7 %
30° Wedge	-	-	-	-	38 ± 7 %	23 ± 7 %
45° Wedge	-	-	-	-	32 ± 7 %	20 ± 7 %
60° Wedge	-	-	23 ± 6 %	17 ± 6 %	-	-

Results are also shown in Fig. 8.2 for the surface dose profile in two dimensions (x and y-axis) where the surface dose is decreased at all sites within the treatment field with the

magnetic deflector device regardless of whether it is used with an open field, or whether a wedge or a Perspex tray are in place.

Although radiographic film has a composition that differs from that of tissue, it still is commonly used for radiation dosimetry because it can be used to obtain the dose distribution of the radiation field with high spatial resolution. Radiographic film offers a convenient medium for easily generating profiles and two-dimensional distributions as shown in Figure 8.1. We have proved that our new design of magnetic deflector attached to the accelerator head is sufficient to remove most of the contamination-scattered electrons from the photon field.

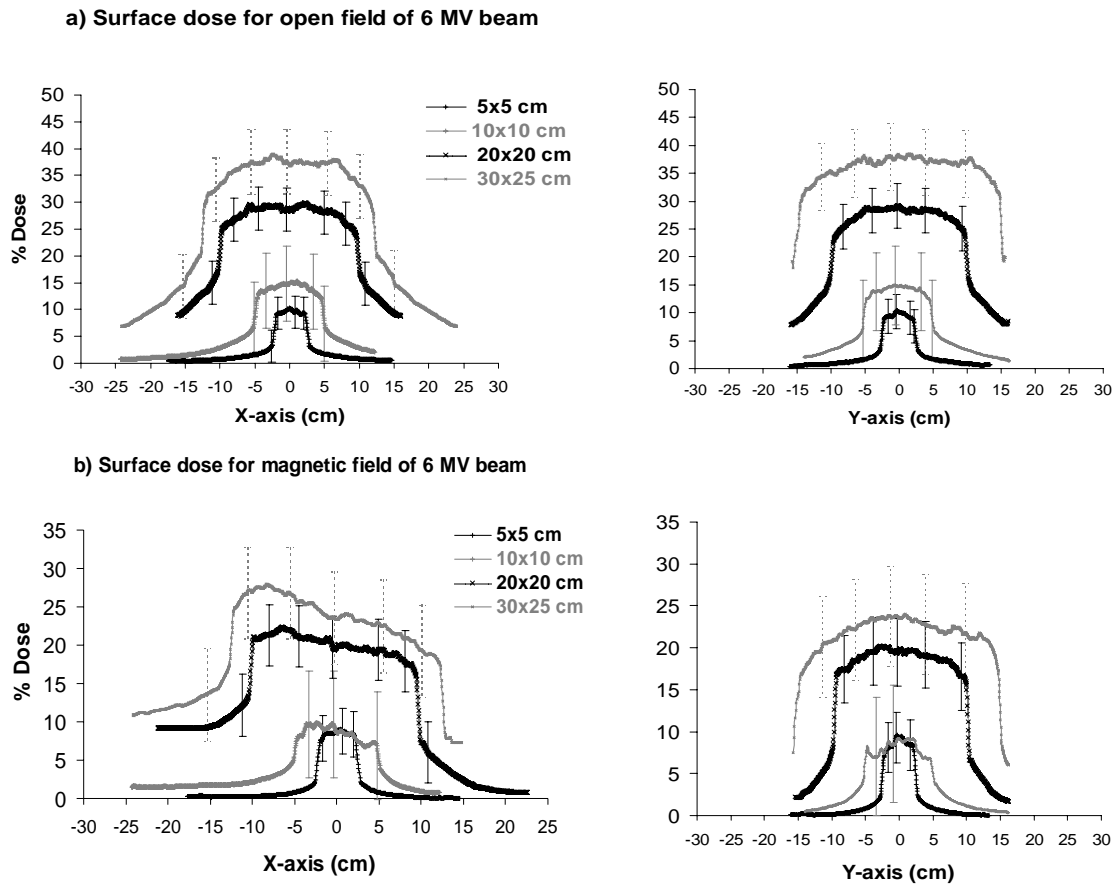


Figure 8.1. Extrapolated surface dose profile at central axis for 6 MV beam, measured cross-plane and in-plane: a) without (open field) magnetic field from the deflector for field sizes of $5 \times 5 \text{ cm}^2$, $10 \times 10 \text{ cm}^2$, $20 \times 20 \text{ cm}^2$, and $30 \times 25 \text{ cm}^2$, b) with magnetic field from the deflector for field sizes of $5 \times 5 \text{ cm}^2$, $10 \times 10 \text{ cm}^2$, $20 \times 20 \text{ cm}^2$, and $30 \times 25 \text{ cm}^2$.

Surface doses obtained by using radiographic film with an extrapolation technique for 6 MV x-rays match the Attix chamber results within 3 %. Using the extrapolation technique surface dose measurements could be obtained where the major source of the contributed dose came from electron contamination. Surface doses also change significantly with different treatment set-up parameters. A Perspex tray or a physical wedge eliminates secondary electrons and generate new electrons at the same time. The surface dose from the electron contamination in the treatment head can be reduced by using the new magnetic deflector device within the clinical treatment set-up.

8.3 Monte Carlo Simulation

8.3.1 Monte Carlo simulation model

Simulating a photon beam from a medical linear accelerator by BEAMnrc and DOSXYZnrc code allows us to determine the build-up depth dose curves and beam profiles. All these data have been compared with measurements in identical geometries. The geometrical description for Monte Carlo simulations of dose depositions in phantoms, including a full linear accelerator description, such as of the particle transport through the target and flattening filter, the ion monitor chamber, and the mirror, will enter the calculations in all simulations, while the only varying parts can be found in the jaw setting and the phantom. Therefore, the simulated geometry has been separated into a phantom and a linear accelerator section, which describes the treatment head of a Varian Clinac 2100C, as shown in Figure 8.2.

The simulation of a linear accelerator is carried out using two steps. The first step involves a detailed simulation of the components of the linear treatment head to score the bremsstrahlung energy spectra and fluence distribution as a function of radial position from the central axis of the beam. In the second step, the fluence distributions are reconstructed to create a source description that is used for subsequent simulations to calculate information related to the beam, such as the depth dose and profile characteristics from the machine to the phantom. The component modules are set up to output a simplified representation of the geometry for input to the EGS_Windows 4.0 graphic of three dimensional space as shown in Figure 8.3. The representations give considerable insight into the models being used with only a few histories to show how electrons and photons are tracked.

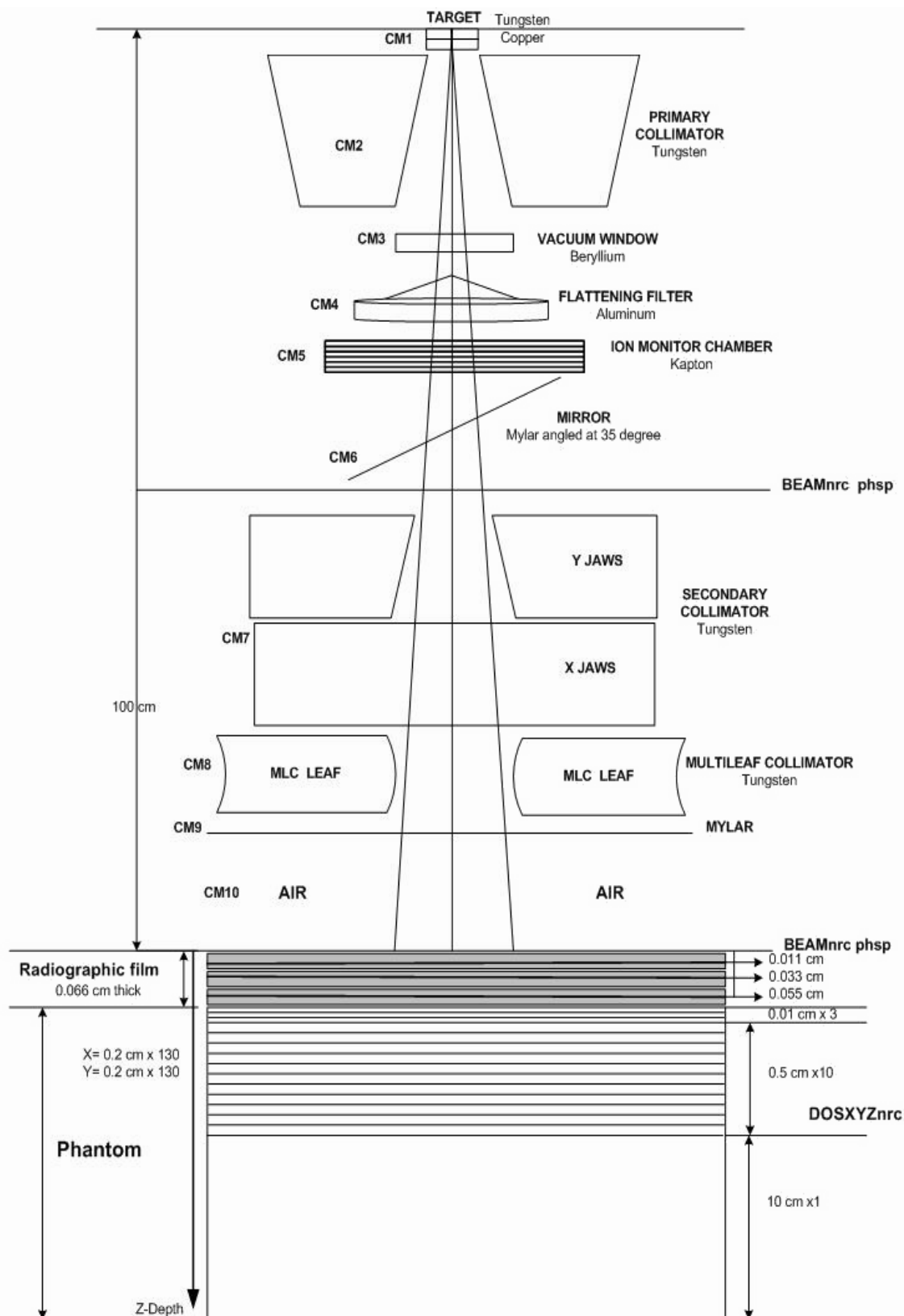


Figure 8.2. Schematic diagram of the Monte Carlo model used to simulate the Varian Clinac 2100 C for 6 MV x-ray beams.

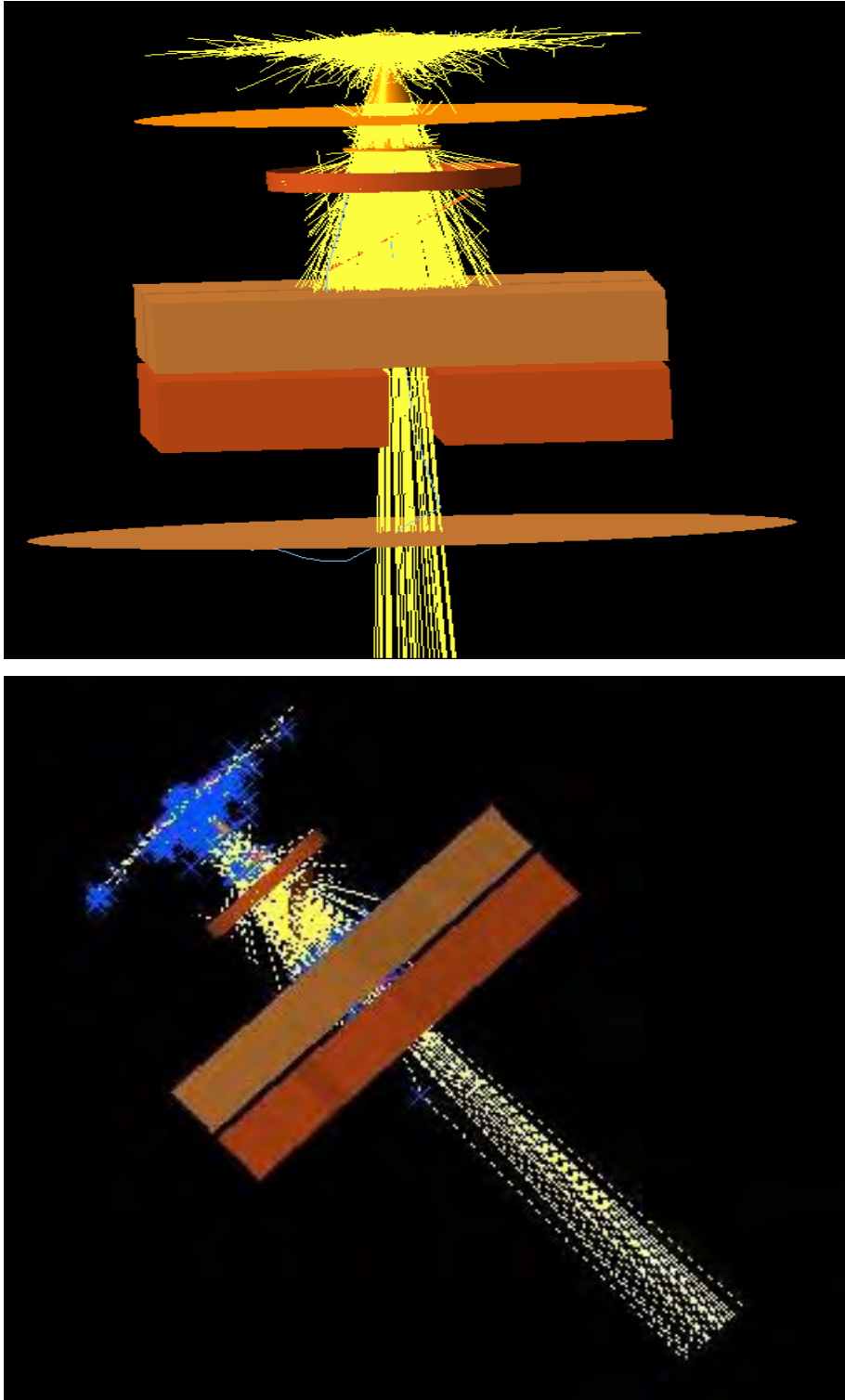


Figure 8.3. The geometry of the Clinac 2100 C accelerator head for 6 MV photon beam as shown by EGS_Windows 4.0 using 150-200 histories. Photons are represented by yellow lines, and electrons are represented by blue lines.

8.3.2 Determination of the transport model parameters

Selection of the transport parameters for a Monte Carlo calculation often depends on what aspects of the results are most important and how many resources are to be consumed by the calculation. Thus for complete and correct simulations, the particle transport parameters must be known. The particles transport model in EGSnrc is characterised by four parameters: AE, AP, ECUT, and PCUT. The parameters AE and AP define the threshold energy for the production of secondary electrons and photons, respectively. Low values of AE and AP increase the accuracy of the simulation at the expense of the calculation time. The parameters ECUT (electrons) and PCUT (photons) are cut-off energies for the termination of particle histories. When the energy of a particle falls below the selected values for ECUT and PCUT, the particle deposits its entire energy locally. For all simulations in our study the cut-off kinetic energy for terminating the transport of the electrons was set to ECUT = 0.521 and 0.700 MeV, while the cut-off energy for terminating the transport of photons was set to PCUT = 0.01 MeV. The threshold energy for production of secondary electrons were set to AE = 0.521 and 0.700 MeV, whereas the threshold energy for bremsstrahlung creation was set to AP = 0.01 MeV. These values were chosen based on the aims of our study and publications in the literature to achieve a compromise between accuracy and speed.

BEAMnrc was used for transport through the accelerator treatment head, and DOSXYZnrc was used for tallying dose in a water phantom. The user code BEAMnrc was used in this study for a photon beam of 6 MV. It is accepted that the various components of the accelerator treatment head present as sources of contaminating electrons. The interaction of the x-ray beam with the mechanical part of the linear accelerator and the air below the machine head produces a continuous spectrum. Investigation of the electron contamination sources offers important knowledge for developing methods for detection of electron contamination. Most of the photon beam originates directly from the target. The scattered photons are scattered from the primary collimator, the flattening filter or the field defining jaws. Most of the scattered photons appear to originate from the flattening filter, the primary collimator and other structures that the beam passes through and may interact with. The spectral shapes of particles from many component modules are generally similar. The calculated fluence spectra for contaminant electrons show a sudden drop in the fluence of very low-energy electrons, which is due to the cut-off kinetic energy of 0.010 MeV for the transport of electrons.

The photon doses have a higher dose distribution for $AE = 0.700$ MeV, whilst the electron doses have a higher dose distribution for $AE = 0.521$ MeV. A lower AE (value of $AE = ECUT$) was used to study the contamination in the high-energy x-ray beam. This is because the value of AE is used for the energy threshold for the production of the secondary electrons and the value of ECUT is used for the global cut-off energy for electron transport, below which the electron history terminates and energy is deposited in the current region. Thus the threshold of ECUT was selected to discard low-energy electrons with kinetic energy below 10 keV in the simulation in the electron contamination study.

The depth dose and profile comparisons between $AE = 0.521$ MeV and $AE = 0.700$ MeV in a water phantom for a field size of $10 \times 10 \text{ cm}^2$ found a variation in dose along the beam axis in the x and y-axis directions at the surface and at a depth of 1.5 cm, where the electron contamination has a more important influence on the dose. Electron dose profiles in a water phantom for the same field size along the x and y-axis directions have a higher electron dose when the lower AE is used.

In the Monte Carlo calculation EGSnrc code has been used in order to simulate the absorbed dose distribution given by a medical linear accelerator. The linear accelerator geometry was input into the Monte Carlo code using the accelerator manufacturer's specifications. The capability of the Monte Carlo program in evaluating dose distribution has been verified by comparison with measurements in the water phantom and on radiographic film. Ionisation measurements were made in a solid-water phantom by means of an Attix chamber for experiments on dose in the build-up region. The measurement of skin dose uses an Attix parallel plate ionisation chamber, which is primarily used as the benchmark chamber in solid-water phantom dose build-up measurements. A comparison between experiments and the Monte Carlo calculation makes it possible to estimate the contribution of contaminating electrons to the dose and to investigate the dose contribution due to secondary electrons.

From the Monte Carlo calculations and measurements on the surface and in the build-up region for 6 MV x-ray beams, we conclude that our optimised simulation model represents the beam emerging from the treatment head and the calculated percentage

depth doses with a satisfactory match to the experimental measurements for the same irradiation set-ups.

References

AMF Magnetics, Unit 1/26 Wenworth Ave Mascot NSW 2020 Australia.

Attix, F. H., Lopez, F., Owolabi, S. and Paliwal, B. R. (1983) Electron contamination in ^{60}Co gamma-ray beams *Med. Phys.*, **10** 301-6.

Beetson, J. S. *Vizimag 3.0 tutorial Copyright 2004.*

Biggs, P. J. and Ling, C. C. (1979) Electrons as the cause of the observed d_{max} shift with field size in high energy photon beams *Med. Phys.*, **6** 291-5.

Biggs, P. J. and Russell, M. D. (1983) An investigation into the presence of secondary electrons in megavoltage photon beams *Phys. Med. Biol.*, **28** 1033-43.

Bose, L. J., Danciu, C., Cheng, C. W., Brugmans, M. J., van der Horst, A., Minken, A. and Mijnheer, B. J. (2002) Interinstitutional variations of sensitometric curves of radiographic dosimetric films *Med. Phys.*, **29** 1772-80.

Butson, M. J., Cheung, T. and Yu, P. (2002a) Calculation of electron contamination doses produced using blocking trays for 6 MV X-rays *Radiation Measurements*, **35** 99-102.

Butson, M. J., Cheung, T. and Yu, P. (2002b) Lepton contamination and photon scatter produced by open field 18 MV X-ray beams in the build-up region *Radiation Measurements*, **35** 103-7.

Butson, M. J., Cheung, T., Yu, P. and Currie, M. (2004) Surface dose extrapolation measurements with radiographic film *Phys. Med. Biol.*, **49** N197-N201.

Butson, M. J., Mathur, J. N. and Metcalfe, P. E. (1996) Radiochromic film as a radiotherapy surface-dose detector *Phys. Med. Biol.*, **41** 1073-1078.

Butson, M. J., Wong, T. P. Y., Kron, T., Mathur, J. N., Clubb, B. and Metcalfe, P. E. (1994) Surface doses from combined electron/photon fields in radiotherapy *Australasian Physics & Engineering Sciences in Medicine*, **17** 14-22.

Butson, M. J., Yu, P., Kan, M., Carolan, M., Young, E., Mathur, J. N. and Metcalfe, P. E. (1997) Skin Dose Reduction by a Clinically Viable Magnetic Deflector *Australasian Physics & Engineering Sciences in Medicine*, **20** 107-110.

Butson, M. J., Yu, P. and Metcalfe, P. E. (1999) Extrapolated surface dose measurements with radiochromic film *Med. Phys.*, **26** 485-488.

Constantinou, C., Attix, F. H. and Paliwal, B. R. (1982) A solid water phantom material for radiotherapy x-ray and γ -ray beam calibrations *Med. Phys.*, **9** 436-441.

Danciu, C., Proimos, S., Rosenwald, J. C. and Mijnheer, B. J. (2001) Variation of sensitometric curves of radiographic films in high energy photon beams *Med. Phys.*, **28** 966-74.

- Deng, J., Jiang, S. B., Kapur, A., Li, J., Pawlicki, T. and Ma, C. (2000) Photon beam characterization and modelling for Monte Carlo treatment planning *Phys. Med. Biol.*, **45** 411-427.
- Gerbi, B. J. and Khan, F. M. (1990) Measurement of dose in the buildup region using fixed-separation plane-parallel ionization chambers *Med. Phys.*, **17** 17-26.
- Gerbi, B. J., Meigooni, A. S. and Khan, F. M. (1987) Dose buildup for obliquely incident photon beams *Med. Phys.*, **14** 393-9.
- Hubbell, H. and Seltzer, S. M. (1997) *Tables of x-ray mass attenuation coefficient and mass energy-absorption coefficients (version 1.03)*, available on <http://physics.nist.gov/xaamdi> (2004, Feb. 91), National Institute of Standards and Technology, Gaithersburg, MD.
- ICRP60 (1990) 1990 Recommendations of the International Commission on Radiological Protection **ICRP publication 60** 149-153.
- Jackson, W. (1971) Surface effects of high-energy x-rays at oblique incidence. *Br J Radiol*, **44** 109.
- Jursinic, P. A. and Mackie, T. R. (1996) Characteristics of secondary electrons produced by 6,10 and 24 MV x-ray beams *Phys. Med. Biol.*, **41** 1499-1509.
- Khan, F. M. (1994) *The physics of radiation therapy*, Williams & Wilkins, Baltimore.
- Khan, F. M., Moore, V. C. and Levitt, S. H. (1973) Effect of Various Atomic Number Absorbers on Skin Dose for 10-MeV X-Rays *Radiology*, **109** 209-12.
- Kim, S., Liu, C. R., Zhu, T. C. and Palta, J. R. (1998) Photon beam skin dose analyses for different clinical setups *Med. Phys.*, **25** 860-6.
- Klein, E. E. and Purdy, J. A. (1993) Entrance and exit dose regions for a CLINAC-2100C *Int. J. Radiation Oncology Biol. Phys.*, **27** 429-35.
- Klevenhagen, S. C. (1993) *Physics and Dosimetry of Therapy Electron Beams*, Medical Physics Publishing, Wisconsin.
- Klevenhagen, S. C., D'Souza, D. and Bonnefoux, I. (1991) Complications in low energy x-ray dosimetry caused by electron contamination *Phys. Med. Biol.*, **36** 1111-6.
- Krithivas, G. and Rao, S. N. (1985) A study of the characteristics of radiation contaminants within a clinically useful photon beam *Med. Phys.*, **12** 764-8.
- LaRiviere, P. D. (1983) Surface dose from 6 MV photon interactions in air *Phys. Med. Biol.*, **28** 285-7.
- Ling, C. C. and Biggs, P. J. (1979) Improving the buildup and depth-dose characteristics of high energy photon beams by using electron filters *Med. Phys.*, **6** 296-301.
- Mackie, T. R. and Scrimger, J. W. (1982) Contamination of a 15-MV photon beam by electrons and scattered photons *Radiology*, **144** 403-9.

- Malataras, G., Kappas, C. and Lovelock, D. M. J. (2001) A Monte Carlo approach to electron contamination sources in the Saturne-25 and -41 *Phys. Med. Biol.*, **46** 2435-46.
- Maximow, A. A. and Bloom, W. (1942) *Textbook of Histology*, PA:Saunders, Philadelphia.
- McGowan, H. C. E., Faddegon, B. A. and Ma, C.-M. (1995) *STATDOSE for 3D dose distributions*, NRCC Report PIRS-0509 (F).
- Mellenberg, D. (1990) Determination of build-up region over-response corrections for a Markus type chamber *Med. Phys.*, **17** 1041-4.
- Mellenberg, D. (1995) Dose behind various immobilization and beam-modifying devices *International Journal Radiation Oncology Biology Physics*, **32** 1193-1197.
- Mersseman, B. and de Wagter, C. (1998) Characteristics of a commercially available film digitizer and their significance for film dosimetry *Phys. Med. Biol.*, **43** 1803-12.
- Metcalfe, P., Kron, T. and Hoban, P. (1997) *The Physics of Radiotherapy X-Rays from Linear Accelerators*, Medical Physics Publishing, Wisconsin.
- Mohan, R., Chui, C. and Lidofsky, L. (1985) Energy and angular distributions of photons from medical linear accelerators *Med. Phys.*, **12** 592-597.
- Muench, P. J., Meigooni, A. S., Nath, R. and McLaughlin, W. L. (1991) Photon energy dependence of the sensitivity of radiochromic film and comparison with silver halide film and LiF TLDs used for brachytherapy dosimetry *Med. Phys.*, **18** 769-775.
- Nilsson, B. (1985) Electron contamination from different materials in high energy photons beams *Phys. Med. Biol.*, **30** 139-151.
- Nilsson, B. and Brahme, A. (1979) Absorbed Dose from Secondary Electrons in High Energy Photon Beams *Phys. Med. Biol.*, **24** 901-912.
- Nilsson, B. and Brahme, A. (1986) Electron contamination from photon beam collimators *Radiotherapy and Oncology*, **5** 235-44.
- Nilsson, B. and Montelius, A. (1986) Fluence perturbation in photon beams under nonequilibrium conditions *Med. Phys.*, **13** 191-5.
- Nizin, P. S. (1993) Electronic equilibrium and primary dose in collimated photon beams *Med. Phys.*, **20** 1721-1729.
- Padikal, T. N. and Deye, J. A. (1978) Electron contamination of a high-energy x-ray beam *Phys. Med. Biol.*, **23** 1086-92.

- Palm, A., Kirov, A. S. and LoSasso, T. (2004) Predicting energy response of radiographic film in a 6 MV x-ray beam using Monte Carlo calculated fluence spectra and absorbed dose *Med. Phys.*, **31** 3168-3178.
- Palm, A. and LoSasso, T. (2004) Influence of phantom material and size on radiographic film response *Med. Phys.*, **31** 1896.
- Petti, P. L. and Goodman, M. S. (1983) Investigation of buildup dose from electron contamination of clinical photon beams *Med. Phys.*, **10** 18-24.
- Petti, P. L., Goodman, M. S., Sisterson, J. M., Biggs, P. J., Gabriel, T. A. and Mohan, R. (1983) Sources of electron contamination for the Clinac-35 25-MV photon beam *Med. Phys.*, **10** 856-861.
- Purdy, J. A. (1986) Buildup/surface dose and exit dose measurements for a 6-MV linear accelerator *Med. Phys.*, **13** 259-262.
- Rao, B. M., Prasad, S. G., Parthasaradhi, K., Lee, Y., Ruparel, R. and Garces, R. (1988) Investigations on the near surface dose for three 10 -MV x-ray beam accelerators with emphasis on the reduction of electron contamination *Med. Phys.*, **15** 246-249.
- Rao, P. S., Pillai, K. and Gregg, F. C. (1973) Effect of shadow trays on surface dose and build-up for megavoltage radiation **117** 168-174.
- Rawlinson, J. A., Arien, D. and Newcombe, D. (1992) Design of parallel plate ion chambers for buildup measurements in megavoltage photon beams *Med. Phys.*, **19** 641-648.
- Rogers, D. W. O., Eewart, G. M., Bielajew, A. F. and van Dyk, G. (1985) *Calculation of Contamination of the Co Beam from an AECL Therapy Source*, NRC Report PXNR-2710.
- Rogers, D. W. O., Ma, C.-M., Walters, B., Ding, G. X., Sheikh-Bagheri, D. and Zhang, G. (2002) *BEAMnrc Users Manual PIRS-0509*.
- Sheikh-Bagheri, D., Rogers, D. W. O., Ross, C. K. and Seuntjens, J. P. (2000) Comparison of measured and Monte Carlo calculated dose distributions from the NRC linac *Med. Phys.*, **27** 2256-2266.
- Sixel, K. E. and Podgorsak, E. B. (1994) Buildup region and depth of dose maximum of megavoltage x-ray beams *Med. Phys.*, **21** 411-416.
- Sjogren, R. and Karlsson, M. (1996) Electron contamination in clinical high energy photon beams *Med. Phys.*, **23** 1873-1881.
- Suchowerska, N., Hoban, P., Butson, M. J., Davison, A. and Metcalfe, P. E. (2001) Directional dependence in film dosimetry: radiographic and radiochromic film *Phys. Med. Biol.*, **46** 1391-1397.

- Tannous, N. B., Gagnon, W. F. and Almond, P. R. (1981) Buildup region and skin-dose measurements for the Therac 6 Linear Accelerator for radiation therapy *Med. Phys.*, **8** 378-381.
- Van der Zee, W. and Welleweerd, J. (1999) Calculating photon beam characteristics with Monte Carlo techniques *Med. Phys.*, **26** 1883-1892.
- Velkley, D. E., Manson, D. J., Purdy, J. A. and Oliver, J., G. D. (1975) Build-up region of megavoltage photon radiation sources *Med. Phys.*, **2** 14-19.
- Walters, B. R. B., Kawrakow, I. and Rogers, D. W. O. (2002) History by history statistical estimators in the BEAM code system *Med. Phys.*, **29** 2745-52.
- Williamson, J., Khan, F. M. and Sharma, S. (1981) Film dosimetry of magavoltage photon beams: a practical method of isodensity to isodose curve conversion *Med. Phys.*, **8** 94-8.
- Yang, J., Li, J., Qin, L., Xiong, W. and Ma, C. (2004) Modelling of electron contamination in clinical photon beams for Monte Carlo dose calculation *Phys. Med. Biol.*, **49** 2657-2673.
- Zhu, T. C. and Palta, J. R. (1998) Electron contamination in 8 and 18 MV photon beams *Med. Phys.*, **25** 12-19.